CHEMICAL ENVIRONMENT SELECTIVITY IN MÖSSBAUER DIFFRACTION

Thesis by

Tab A. Stephens

In Partial Fulfillment of the Requirements
for the Degree of Doctor of Philosophy

California Institute of Technology
Pasadena, California

1996

(Defended May 14, 1996)

to Keri Keilberg Stephens

Acknowledgments

I would like to thank the following people:

- Dr. Brent Fultz, my thesis advisor, who has provided guidance and direction to this Texan for last six years;
- Dr. Werner Keune, who performed some of the initial experiments on his 1991 summer sabbatical at Caltech;
- my previous advisors: Drs. Donald Naugle, Paul Shlichta, and Daya Rathnayaka, who have taught me to appreciate science in all of its many forms;
- Lawrence Anthony, Dave Lee, Channing Ahn, and Carol Garland, who have always lended a helping hand, ear, and mind;
- Pam Albertson, Laura Nagel, Heather Frase, Luibo Hong, Zheng-Qiang Gao, Chuck Witham, Adrian Hightower, Peter Bogdanoff, and the other "inhabitants" of Keck Labs;
- Parker Altice, Paul Watson, Steve "Slick" Means, and the rest of the Texas A&M physics crew;
- The truly exceptional teachers at Breckenridge High School: Weldon Edwards; James and Becky Isabel; and Phil Dye;
- My extended family: Tommy and Sharon Wimberley; Jim and Frances Wilkerson; Sarah Ellis; Ray, Karen, Kori, and Lauren Wilkerson; and Eddie and Dr. Leslie Keilberg; and
- My family: my wife Keri and my cats, Mikasa and MacGyver.

This work was supported by the U.S. National Science Foundation under contract DMR-9415331. I was also supported by an Office of Naval Research Graduate Fellowship for my first three years at Caltech.

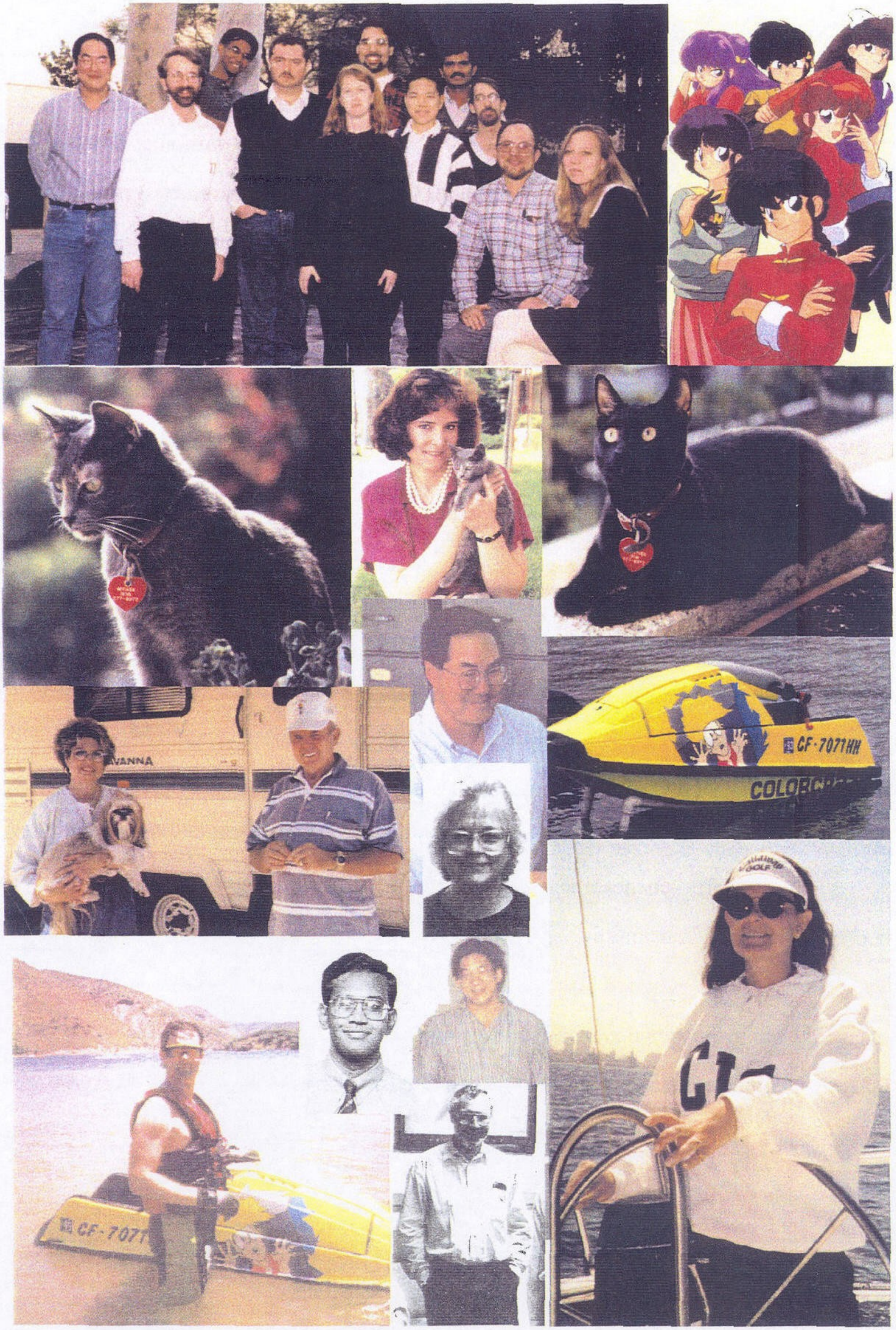
AVANNA
CF-7071HH
CF-7071
GOLF

Abstract

We demonstrate a new feature of Mössbauer diffraction that is useful for studies of atomic arrangements in materials — that Mössbauer diffraction can measure the autocorrelation function of ^{57}Fe atoms as a function of their chemical environment. To acquire the experimental data, we built a Debye-Scherrer type powder diffractometer with a ^{57}Co radiation source and a large angle position sensitive detector. By working with polycrystalline materials near the kinematical limit of diffraction, the broadening of nuclear energy levels is not severe, so the spectroscopic capabilities of Mössbauer scattering are preserved. The sample was polycrystalline ^{57}Fe$_3$Al with the ordered D0$_3$ structure. The two sites for the ^{57}Fe atoms, the Wyckoff 4(b) and 8(c) sites, differ in both their chemical environment (0Al versus 4Al 1nn) and in their spatial arrangement (face-centered cubic, fcc, with lattice parameter $2a_0$ versus simple cubic, sc, with lattice parameter a_0). Diffraction peaks from the fcc structure were detected when the incident radiation was tuned to the Mössbauer resonance of the Wyckoff 4(b) Fe site, but not for tuning to the 8(c) site, thereby distinguishing the spatial arrangements of these two Fe sites. Thus, the validity of chemical environment selectivity was proven.

The phase change of the Mössbauer scattering near resonance affects the interference of diffracted waves from different chemical environments. Interference effects between x-ray Rayleigh scattering and Mössbauer scattering from the ^{57}Fe$_3$Al sample were observed, as were interference effects involving the different components of the Mössbauer spectra. A simple oscillator model was used successfully to calculate the interference effects seen in the experimental data.

Table of Contents

List of Figures

Chapter 1 Diffraction and Mössbauer diffraction

Most of our knowledge about atomic arrangements in materials comes from diffraction experiments, where an incident wave is directed into a material and a detector is used to observe the angles and intensities of the outgoing diffracted waves. The incident waves must have wavelengths comparable to the spacings between atoms, and three types of waves have proved useful. X-ray diffraction, conceived by Laue and the Braggs, was first [1]. The electric field of the incident x-rays causes the electrons about an atom to oscillate, and their accelerations generate an outgoing wave. The same Rayleigh scattering mechanism has also been used for γ-ray diffraction. In electron diffraction, originating with Davisson and Germer, the charge of the incident electron interacts with the positively charged core of the atom, thus diverting the electron wavevector. In neutron diffraction, the incident neutron interacts with the nuclei in the samples or with magnetic electrons. These three diffraction methods occur by very different physical mechanisms, so they often provide complementary information about atom arrangements in materials. For example, x-ray diffraction can be used to determine long range crystallographic order in a sample, while electron diffraction is used to determine defect structure.

The possibility of a fourth type of diffraction mechanism was found in 1960 [2,3]. The incident wave is a γ-ray emitted during the decay of an excited state of a ^{57}Fe nucleus. The wavelength of this γ-ray is 0.86 Å, so it can undergo the same atomic scattering as an x-ray. It may, however, undergo a second type of scattering that was discovered in 1957 by Rudolph Mössbauer [4]. In the Mössbauer effect, a γ-ray can be emitted by one nucleus and then excite another when both nuclei are embedded in solids, so minimal energy is lost by nuclear recoil. The lifetime of the excited state of the ^{57}Fe nucleus is 140 ns, which is a comparatively long time. In this time the front of the γ-ray wave packet will have traveled far beyond the specimen, so there are many questions about the time dependence of the scattering process and the effect of diffraction angle. These questions have provided excellent topics for fundamental physics research in Mössbauer diffraction (discussed in § 2.4). Owing to the exotic nature of the method and its experimental difficulties, however, Mössbauer diffraction has not yet been used successfully for studies of atomic arrangements in materials, although there was a previous attempt to do so [5,6]. Furthermore, the chemical environment selectivity experiments performed here involved polycrystalline samples, rather than the single crystal samples that form the bulk of the Mössbauer diffraction physics experiments to date. The use of powder diffraction experiments will allow a wider range of materials to be examined.

The purpose of this thesis research is to test if Mössbauer diffraction can be used as an analytical tool for materials science. The plan is to use the chemical sensitivity of the Mössbauer effect, obtained through hyperfine interactions, to turn on and off the Mössbauer scattering by selected ^{57}Fe nuclei. In principle, for a given tuning of the incident γ-rays, only those ^{57}Fe nuclei in one particular chemical environment can contribute, through Mössbauer scattering, to the diffraction pattern. For comparison, the methods of anomalous scattering in x-ray diffraction and isotopic substitution in neutron diffraction are capable of providing a diffraction pattern from a selected atom species. The diffraction experiments described in this thesis should take this selectivity to the new level of obtaining a diffraction pattern from a selected chemical environment of the selected atom. Concisely stated, chemical environment selective diffraction can provide independent autocorrelation functions for Fe atoms in different chemical environments. Although chemical environment selective diffraction is a method specialized to ^{57}Fe, no other diffraction technique has this capability.

1.1 Chemical environment selective diffraction

Chemical environment selective diffraction will now be described in terms of the D0$_3$-ordered Fe$_3$Al samples that are used in the experiments. Fe$_3$Al was chosen to test chemical environment selectivity for a number of reasons. First, the D0$_3$-ordered structure possesses two different chemical environments, and these two crystallographic sites have different spatial periodicities on the underlying bcc lattice. If these two ^{57}Fe sites could be selected independently for Mössbauer diffraction, we would expect them to produce different diffraction patterns. The hyperfine magnetic fields of these two chemical environments were sufficiently different to provide well-separated absorption peaks in the Mössbauer absorption spectra. This strong separation of peaks in the energy spectrum made us optimistic that we could select each environment independently. Second, Fe_3Al has been extensively studied by our group [7-12], so we are very familiar with the processing requirements needed to obtain good samples. Third, assuming chemical environment selectivity is possible, Fe_3Al samples can provide further experiments using Mössbauer diffraction (see § 1.2). Fourth, Fe_3Al-based alloys possess a number of desirable properties (including excellent oxidation and sulfidation resistance) and commercial applications (for service in chemical processing equipment) [13].

The $D0_3$ structure for Fe_3Al is shown in Figs. 1.1 and 1.2. The bcc-based $D0_3$ structure has the following properties [14,15]:

(1) Pearson symbol: cF16
(2) Structure prototype: BiF_3
(3) Space group: $Fm\bar{3}m$
(4) 1nn coordination number: 8
(5) 2nn coordination number: 6
(6) 3 Wyckoff crystallographic sites: Al atoms on the 4(a) sites; Fe atoms on the 4(b) and 8(c) sites.

The $D0_3$ structure can also be expressed as four interpenetrating face centered cubic (fcc) sublattices, indicated in Fig. 1.1 by α, β, γ, and δ. The Al atoms on the 4(a) sites occupy the δ sublattices, while the Fe atoms are subdivided into two groups. The Fe atoms with only Fe atoms in their first nearest neighbor shell (1nn) occupy the 4(b) sites and the γ

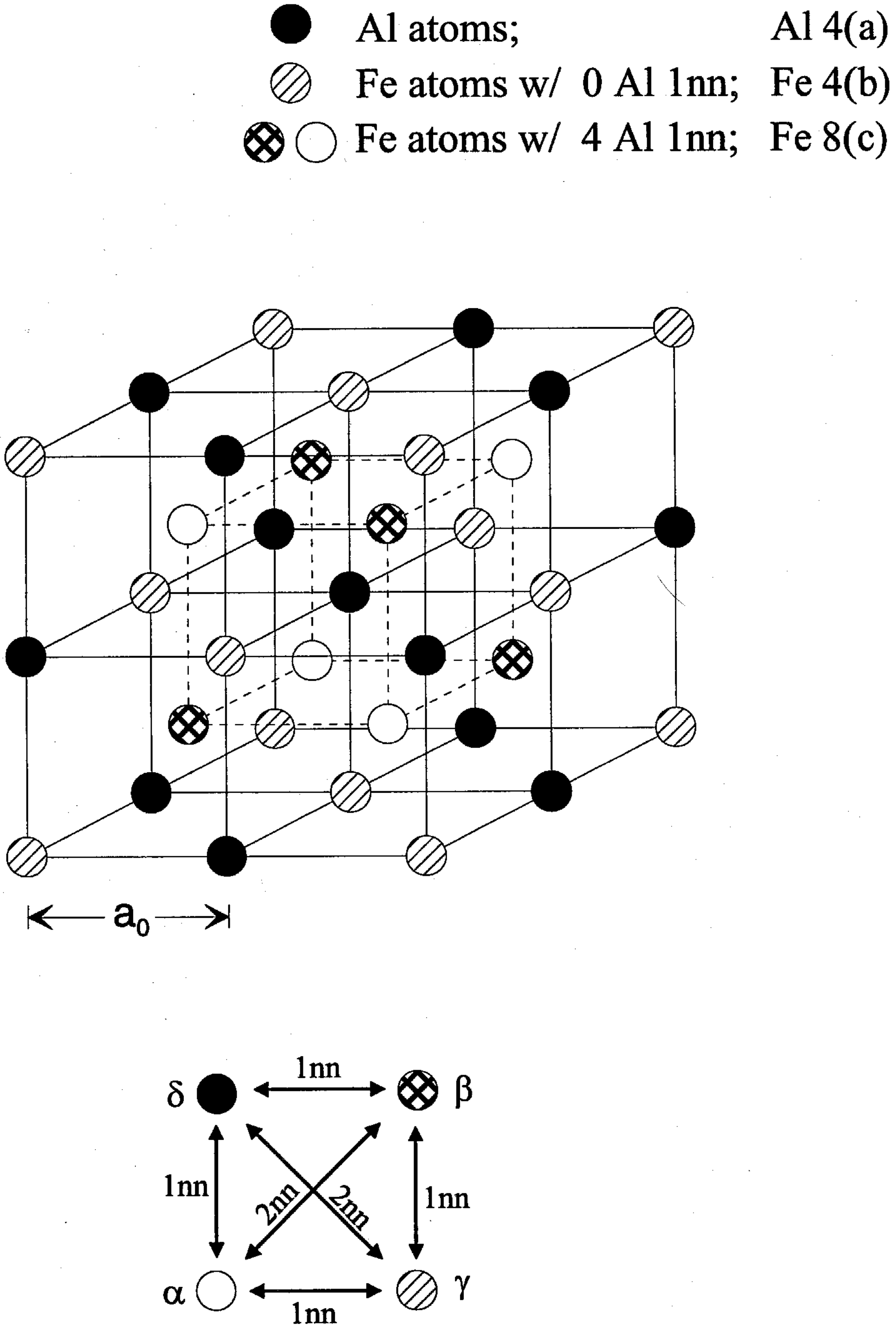

Figure 1.1 The $D0_3$ structure for Fe_3Al.

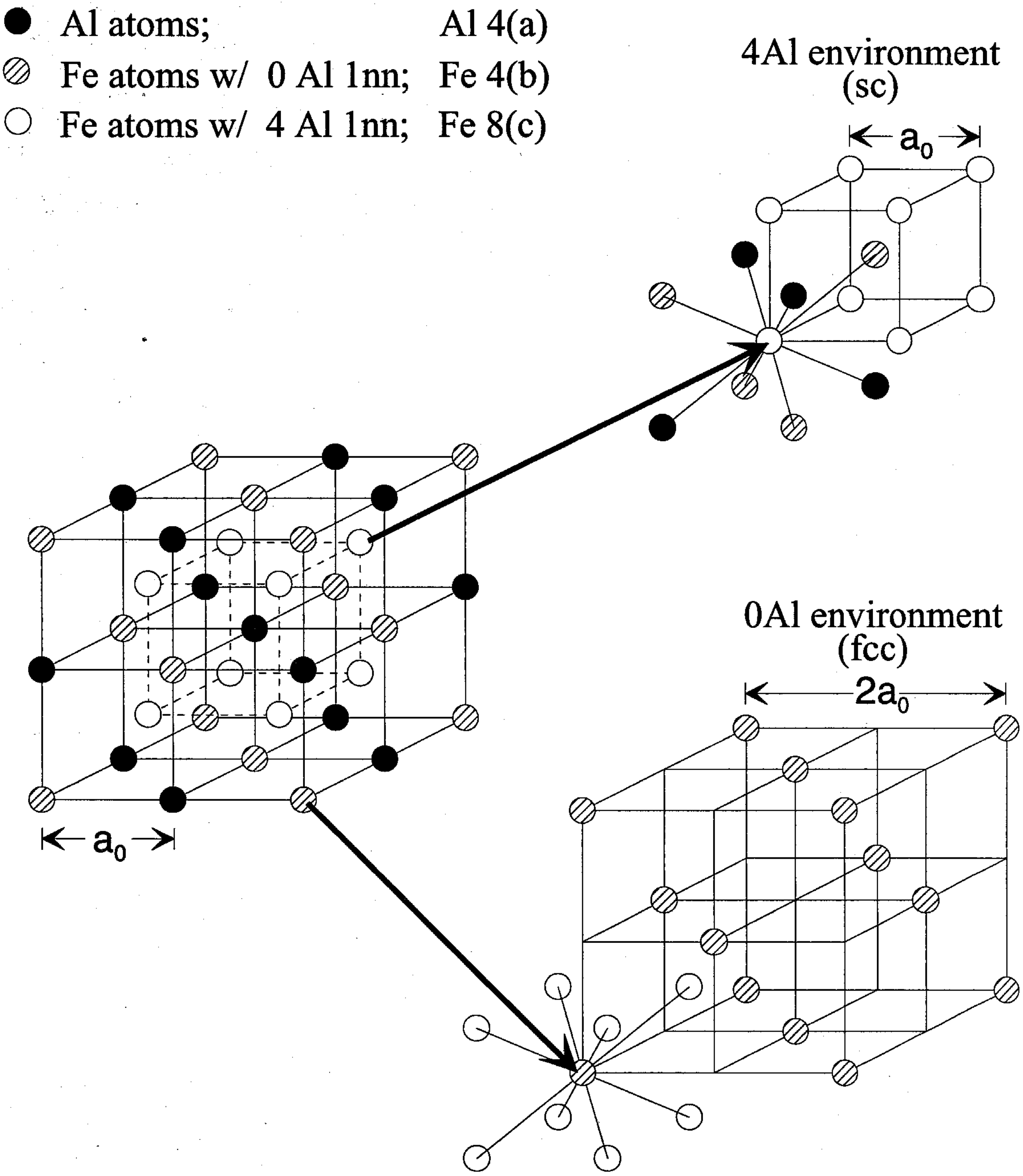

Figure 1.2 The $D0_3$ structure and its associated simple cubic (sc) and face centered cubic (fcc) sublattices.

sublattice. These Fe atoms have the "0Al" (no Al atom neighbors) environment. The remaining Fe atoms have 4 Al atoms and 4 Fe atoms in their 1nn shell and occupy the 8(c) sites and both the α and β sublattices (the sites on the α and β sublattices are crystallographically equivalent). These Fe atoms have the "4Al" (4 Al atom neighbors) environment.

Figure 1.2 shows two sublattices for the Fe atoms in Fe_3Al with perfect $D0_3$ order. The Fe atoms with the 4Al environment form a simple cubic (sc) sublattice with a lattice parameter of $a_0 = 2.86$Å. The Fe atoms with the 0Al environment form a face centered cubic (fcc) lattice (the γ sublattice) with a lattice parameter of $2a_0$. The structure factor rules for selection of diffraction peaks are different for these two Fe environments [16]. Thus, we can expect different diffraction patterns from each environment.

As the Fe_3Al sample will also scatter the incident photons by x-ray Rayleigh scattering, x-ray Bragg peaks will be seen in the diffraction pattern. However, the Bragg peak intensities for x-ray diffraction are different from the Mössbauer diffraction from both the 0Al and 4Al environments. The three families of Bragg diffraction peaks are the bcc fundamentals, the $\left(\frac{1}{2}\frac{1}{2}\frac{1}{2}\right)$-family of superlattice peaks, and the (100)-family of superlattice peaks. The x-ray structure factor intensities for $D0_3$ Fe_3Al predicts the superlattice peaks to have only 6% of the structure factor intensities for bcc fundamental diffractions. On the other hand, since the 0Al environment is fcc with $a = 2a_0$, the 0Al environment should have all three types of diffraction peaks of equal intensity. The 4Al environment is sc, and should not have $\left(\frac{1}{2}\frac{1}{2}\frac{1}{2}\right)$-family peaks, but the 4Al environment should have (100)-family and bcc fundamental diffractions of equal intensity. Table 1.1 summarizes these results.

Table 1.1 Allowed diffraction peaks for the three resonance conditions for $^{57}Fe_3Al$ samples.

		Diffraction Peaks	
Resonance cond.	bcc fundamental	$\left(\frac{1}{2}\frac{1}{2}\frac{1}{2}\right)$-family	(100)-family
0Al	yes	yes	yes
4Al	yes	no	yes
off	yes	no*	no+

* 6.0 % of bcc fundamentals
\+ 3.0 % of bcc fundamentals

Figures 1.3 through 1.5 show the design of the experiment and the expected results for the 0Al environment, the 4Al environment, and x-ray diffraction, respectively. The Mössbauer absorption spectra are calculated spectra for a sample with perfect $D0_3$ order, where only the sextets of peaks corresponding to the 0Al and 4Al environments are present. The dark curves in the Mössbauer spectra of Figs. 1.3 and 1.4 are the sextets of absorption peaks corresponding to the 0Al and 4Al environments, respectively. In the plan for the experiment, the Mössbauer diffractometer is tuned on-resonance to peak 6 of each sextet. The condition for x-ray diffraction by Rayleigh scattering alone (Fig. 1.5) is produced by tuning off the Mössbauer absorption peaks. The simulated diffraction peaks are meant to show peak positions and types and approximate intensity, although the peaks have not been scaled to account for form factors, Debye-Waller factors, multiplicity, and other intensity-altering mechanisms. The exception is that the diffraction peaks for the 4Al environment are shown as having twice the intensity of those for the 0Al environment because twice as many Fe atoms are available for diffraction. The ratio of the x-ray diffraction peak intensity to the Mössbauer diffraction peak intensity is not set.

The preceding description of chemical environment selectivity is rather simplistic, as it does not account for interference effects between x-ray scattered and Mössbauer scattered photons (chapter 5 addresses the interference effects). However, as we will see

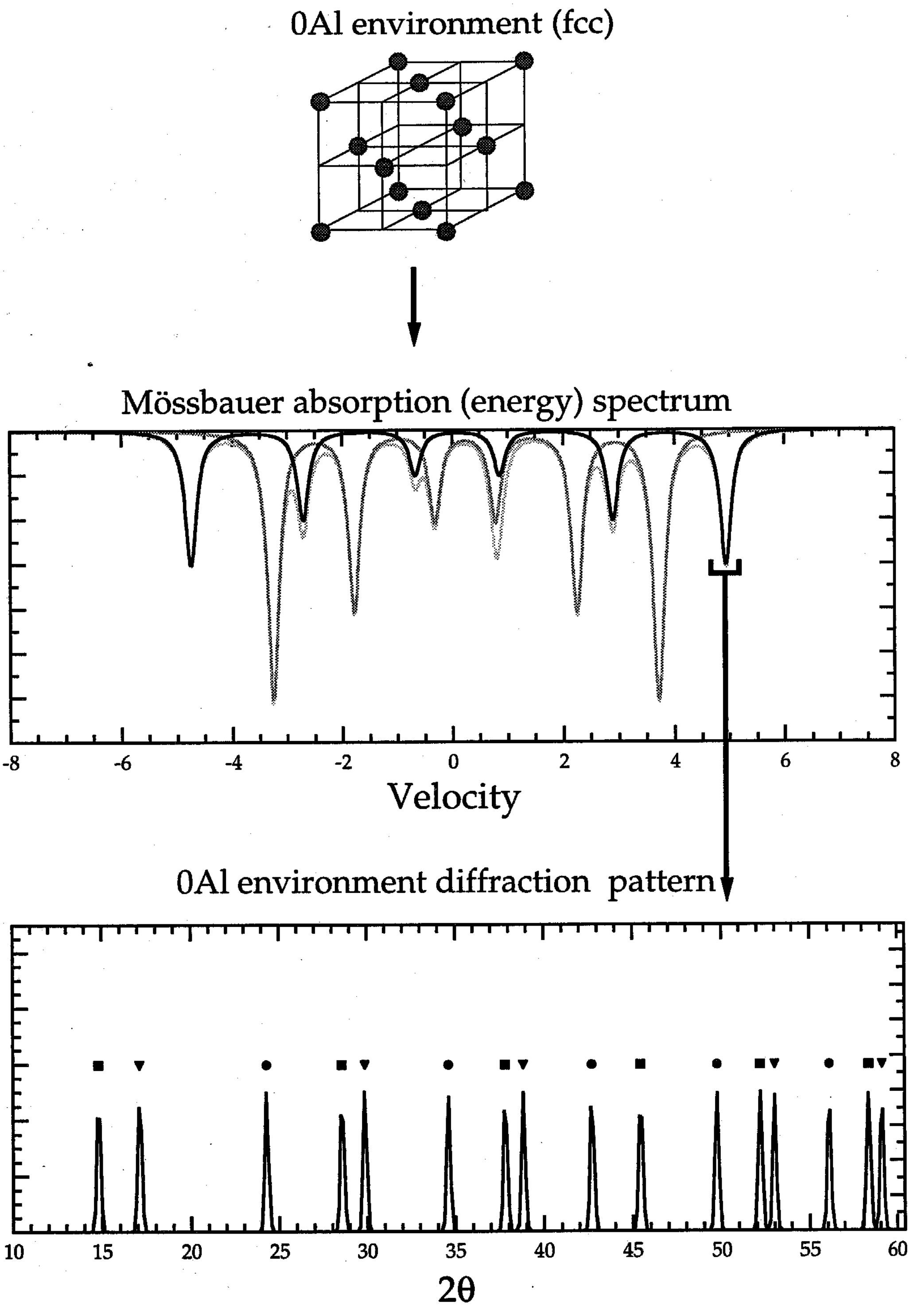

Figure 1.3 Chemical environment selective diffraction from the 0Al environment of $D0_3$-ordered Fe_3Al. The circles indicate bcc fundamental peaks, the squares indicate (1/2 1/2 1/2)-family superlattice peaks, and the inverted triangles indicate (100)-family superlattice peaks.

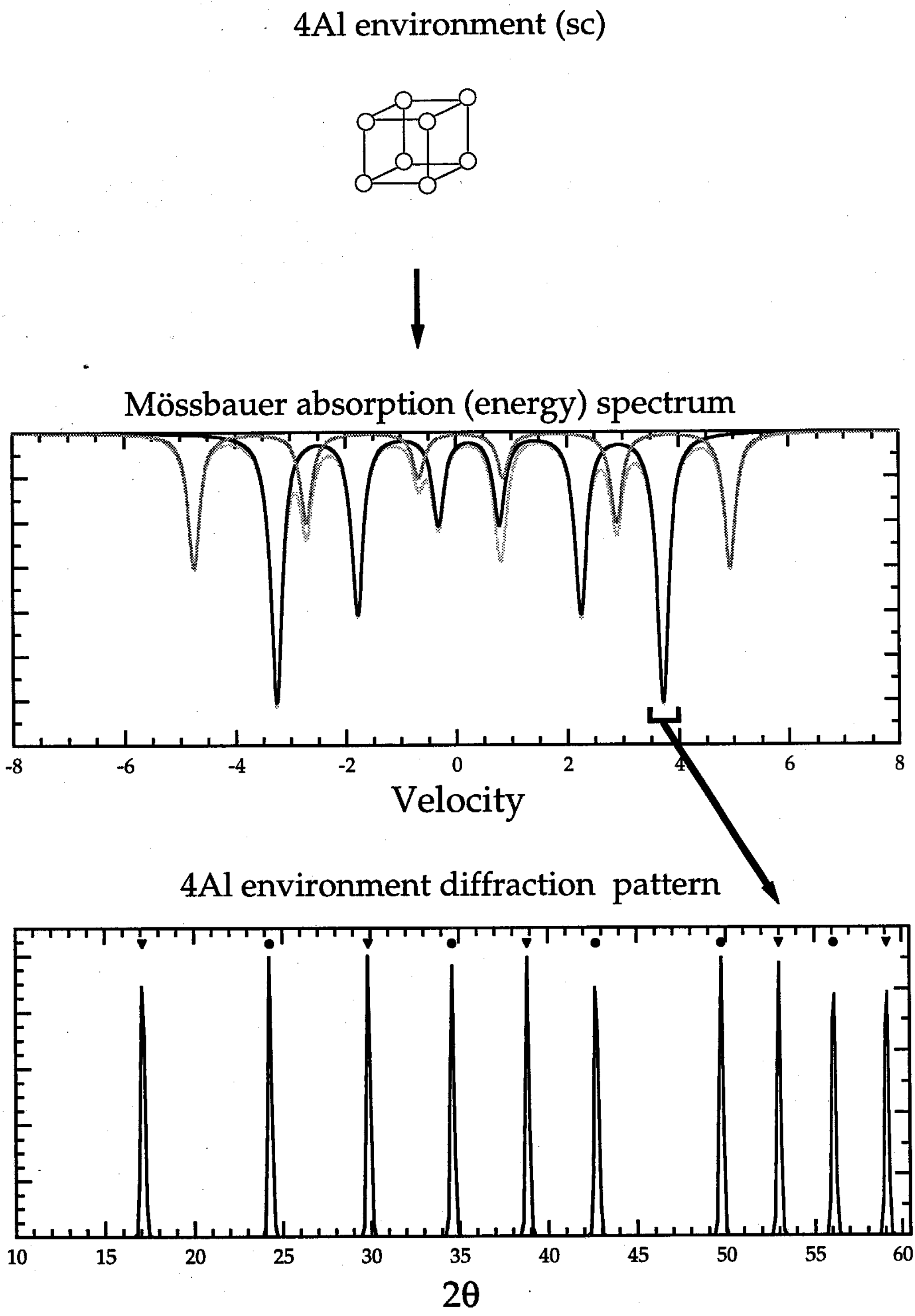

Figure 1.4 Chemical environment selective diffraction from the 4Al environment of $D0_3$-ordered Fe_3Al. The circles indicate bcc fundamental peaks and the inverted triangles indicate (100)-family superlattice peaks.

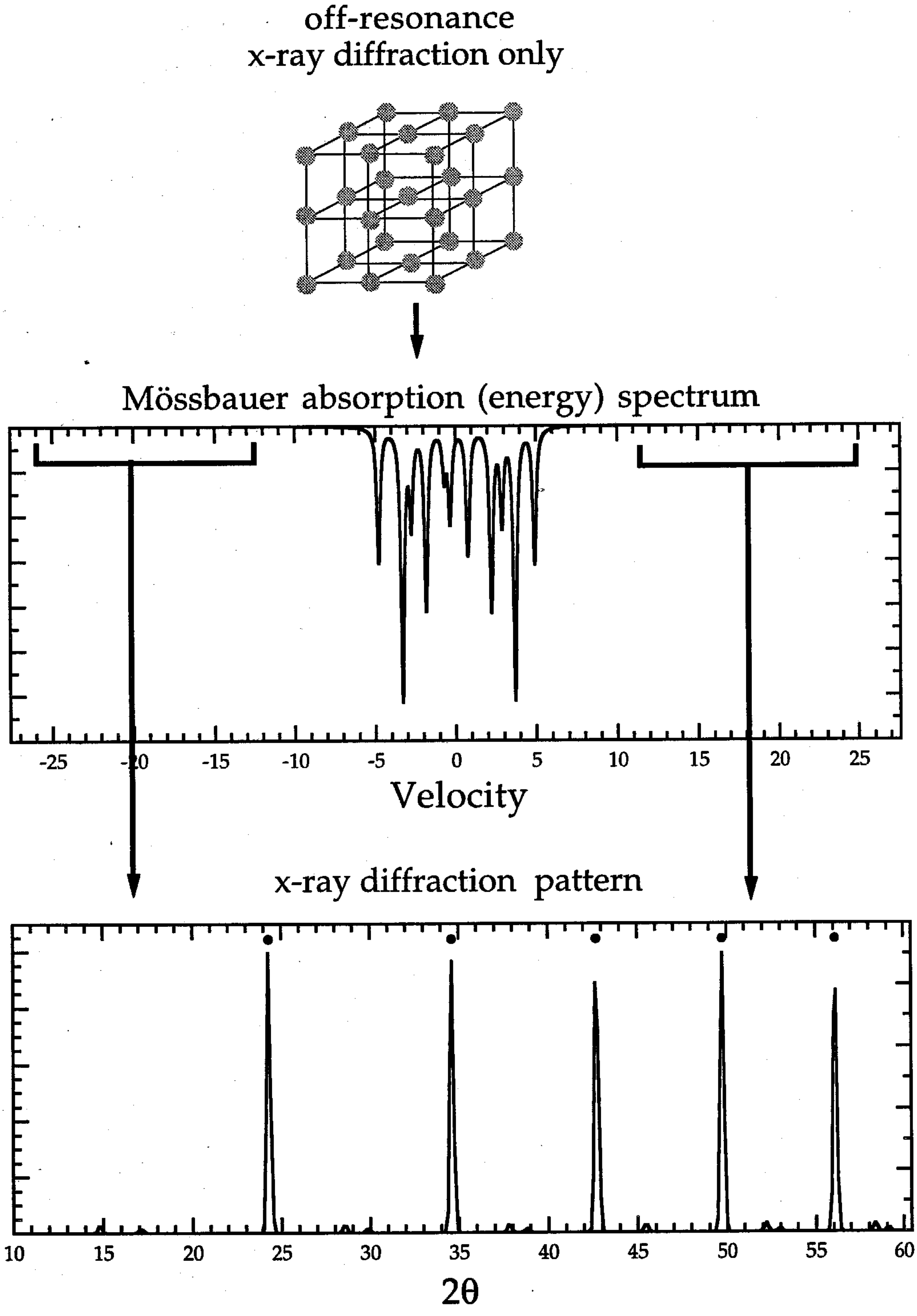

Figure 1.5 Chemical environment selective diffraction from the off resonance condition (x-ray diffraction only) of $D0_3$-ordered Fe_3Al. The circles indicate bcc fundamental peaks.

in chapter 4, the superlattice peaks do not suffer from interference effects, owing to the weakness of their x-ray structure factor intensities. Our simple description is reasonably accurate for the intensities of the superlattice diffractions, since they originate primarily with Mössbauer scattering.

1.2 Possible uses of chemical environment selectivity

If the chemical environment selective powder diffraction technique proves successful, many new experiments will be possible in principle, but not all will be immediately possible in practice. The principle limitation will be counting statistics, as the countrates generated during the experiments are very low♦. However, even modest countrate capabilities should make practical some important experiments on crystalline materials.

For illustration, two types of experiments of immediate interest are available in the study of polycrystalline, partially-ordered alloys. First, chemical environment selectivity should make it easy to distinguish between the case of weak homogeneous order and the case of ordered regions within a disordered matrix. Second, chemical environment selective diffraction should permit new studies of antisite defects in ordered alloys (individual atoms on the wrong sublattice), which are involved in a variety of phase transformation in intermetallic compounds including amorphization [17-24].

There are two reports of transient B32 order during the disorder-order transformation in Fe-Al [8,25]. In one study, disordered alloys of Fe_3Al annealed at 300^0C developed an excess amount of B32 order that is comparable to the amount of $D0_3$ order [8], and the other study found even more B32 order [25]. The formation of so much B32 order is a surprise since the Fe-Al phase diagram (Fig. 1.6) contains a large region of B2

♦ For example, countrate limitation suggest that in the foreseeable future it will be impractical to examine an Fe-B metallic glass and determine independent radial distribution functions for Fe atoms with different numbers of B neighbors.

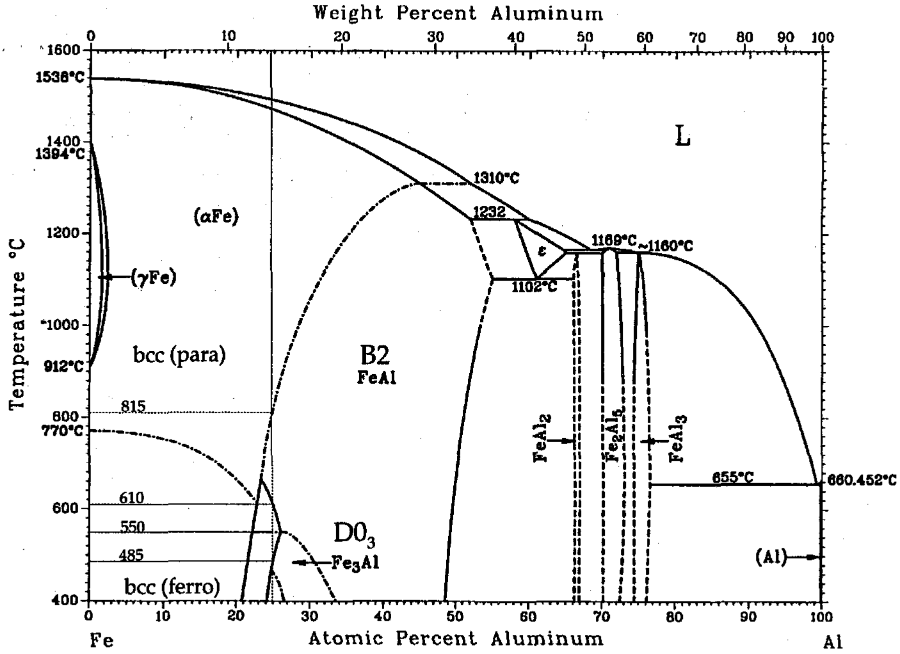

Ref. 30, p. 148

Figure 1.6 The Al-Fe phase diagram.

order, and the B2 and B32 ordered structures require very different types of interatomic interactions [26,27]. The formation of B32 order may occur for reasons of kinetics, as theoretical work suggests [28,29]. Experimentally, however, there remains the question of where the B32 is located. The B32 regions are small, ~5 nm as determined from x-ray superlattice linewidths. Identifying their location is therefore difficult, even with transmission electron microscopy [8]. Mössbauer diffraction could determine if these regions are homogeneous modifications of the $D0_3$ ordered regions, or if they exist heterogeneously as distinct regions between the $D0_3$ domains. If the B32 order develops homogeneously, the ^{57}Fe atoms with 0Al 1nn through 4Al 1nn environments would all tend to exhibit similar excesses in their $\left(\frac{1}{2}\frac{1}{2}\frac{1}{2}\right)$-type diffraction peaks. Were the B32 order in distinct regions, however, the 4Al environment of ^{57}Fe may not show such strong $\left(\frac{1}{2}\frac{1}{2}\frac{1}{2}\right)$-type diffraction peaks.

Large local distortions are associated with antisite defects in many alloys, such as Fe-Al where there is a big difference in metallic radii of the Fe and Al atoms (1.24Å versus 1.43Å). It is almost certain that antisite defects in Fe_3Al will interact, and will probably repel each other♦. Elimination of antisite defects involves some intermediate-range diffusion, which is not instantaneous. It is possible that an early stage of relaxation of a disordered solid solution of Fe_3Al involves the redistribution of antisite defects. One antisite Al atom can affect the HMF at up to 8 1nn Fe atoms, so many perturbed ^{57}Fe atoms (e.g., the 3Al and 5Al environments) would be available for chemical environment selective diffraction.

♦ When large numbers of antisite defects are present, they may be expected to undergo long-range secondary ordering, such as the formation of $D0_3$ order in B2 order.

References, Chapter 1

[1] H.P. Klug and L.E. Alexander, X-ray Diffraction Procedures (Wiley–Interscience, New York, 1974), 2nd edition.

[2] P.J. Black and P.B. Moon, Nature **188**, 481 (1960).

[3] P.J. Black, G. Longworth, and D.A. O'Conner, Proc. Phys. Soc. **83**, 925 (1964).

[4] R.L. Mössbauer, Z. Physik **151**, 124 (1958).

[5] Y. Kakai, M. Hirano, Y. Ooi, and N. Kunitomi, J. Phys. Soc. Jpn. **51**, 929 (1982).

[6] Y. Kakai, Y. Ooi, and N. Kunitomi, J. Phys. Soc. Jpn. **57**, 3172 (1988).

[7] B. Fultz and Z.Q. Gao, Nucl. Instrum. Methods in Phys. Res. B **76**, 115 (1993).

[8] Z.Q. Gao and B. Fultz, Philos. Mag. B: Cond. Mat. **67**, 787 (1993).

[9] B. Fultz, H.H. Hamdeh, S.A. Oliver, and Z.Q. Gao, Phys. Rev. B **49**, 6312 (1994).

[10] L. Anthony, L.J. Nagel, J.K. Okamoto, and B. Fultz, Phys. Rev. Lett. **73**, 3043 (1994).

[11] C. Bansal, Z.Q. Gao, L.B. Hong, and B. Fultz, J. Appl. Phys. **76**, 5961 (1994).

[12] L. Anthony and B. Fultz, Acta Metall. Mat. **43**, 3885 (1995).

[13] C.G. McKamey, J.H. DeVan, P.F. Tortorelli, and V.K. Sikka, J. Mater. Res. **6**, 1779 (Aug. 1991).

[14] J.L.C. Daams, P. Villars, and J.H.N. van Vucht, *Altas of Crystal Structure Types for Intermetallic Phases* (ASM International, Materials Park, OH, 1991), Vol. 4, p. 6814.

[15] P. Villars and L.D. Calvert, *Pearson's Handbook of Crystallographic Data for Intermetallic Phases* (ASM International, Materials Park, OH, 1991), Vol. 1, p. 815.

[16] B.E. Warren, *X-ray Diffraction* (Dover, New York, 1990), p. 31.

[17] L.M. Di, P.I. Loeff, and H. Bakker, J. Less-Common Metals **168**, 183 (1991).

[18] J.A. Horton, I. Baker, and M.H. Yoo, Philos. Mag. A **63**, 319 (1991).

[19] M.J. Sabochick and N.Q. Lam, Phys. Rev. B **43**, 5243 (1991).

[20] J.R. Shoemaker, R.T. Lutton, D. Wesley, W.R. Wharton, M.L. Oehrli, M.S. Herte, and M.J. Sabochick, J. Mater. Res. **6**, 473 (1991).

[21] R.A. Johnson and J.R. Brown, J. Mater. Res. **7**, 3213 (1992).

[22] L.M. Di, H. Bakker, and F.R. DeBoer, Physica B **182**, 91 (1992).

[23] C.L. Fu, Y.Y. Ye, M.H. Yoo, and K.M. Ho, Phys. Rev. B **48**, 6712 (1993).

[24] Y.S. Cho and C.C. Koch, J. Alloys and Compounds **194**, 287 (1993).

[25] W. Schweika, Mater. Res. Soc. Symp. Proc. **166**, 249 (1990).

[26] M.J. Richards and J.W. Cahn, Acta Metall. **19**, 1263 (1971).

[27] S. M. Allen and J.W. Cahn, Acta Metall. **20**, 423 (1972).

[28] L. Anthony and B. Fultz, J. Mater. Res. **4**, 1132 (1989).

[29] L. Anthony and B. Fultz, J. Mater. Res. **9**, 348 (1994).

[30] U.R. Kattner, in *Binary Alloy Phase Digrams*, editor-in-chief T.B. Massalski (ASM Internation, 1990), 2nd edition, p. 147.

Chapter 2 The Mössbauer effect

While working on his doctoral thesis in 1957, Rudolf L. Mössbauer discovered the effect that now bears his name. He found that, under the right conditions, ^{191}Ir nuclei could absorb gamma rays without individually recoiling [1]. He was awarded the 1961 Nobel Prize in Physics for his discovery.

This chapter will describe the Mössbauer effect and its various features. Furthermore, this chapter will discuss Mössbauer diffraction and the previous work that is important to the development of chemical environment selectivity. The chapter consists of four sections. Section 2.1 describes the Mössbauer effect in general, while § 2.2 lists the important quantities for the ^{57}Fe Mössbauer effect. Section 2.3 describes the hyperfine interactions and perturbations of the energies of nuclear transitions. Finally, § 2.4 describes some aspects of Mössbauer diffraction.

2.1 The Mössbauer effect

The Mössbauer effect is the recoilless resonant emission and absorption of gamma ray photons by the nuclei of specific isotopes. While theoretically possible in all elements, only a few isotopes show the effect strongly. Figure 2.1 shows the elements used in Mössbauer spectroscopy. Fortunately, Fe (in the form of the isotope ^{57}Fe) is included in this list.

Figures 2.2abc depicts the Mössbauer effect. A photon of energy E_0 is generated by the decay of the nuclear excited state of energy E_e to the ground state of energy E_g. During the recoil, the atom may recoil with the energy E_R (Fig. 2.2a). The photon emitter, or source, creates a photon with energy $E_0 - E_R$. The photon is then absorbed by a nucleus in the sample (absorber), if the photon has the energy $E_0 + E_R$ to overcome any recoil energy of the absorbing nucleus. The nuclear excited state has certain properties — besides

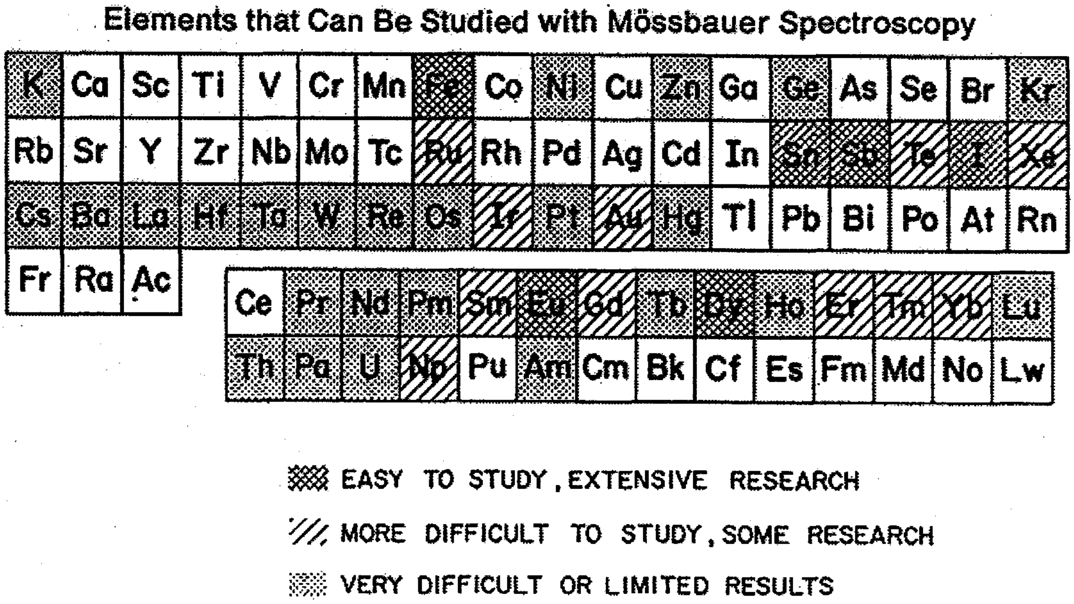

Elements that Can Be Studied with Mössbauer Spectroscopy

░ K	Ca	Sc	Ti	V	Cr	Mn	▩ Fe	Co	░ Ni	Cu	░ Zn	Ga	░ Ge	As	Se	Br	░ Kr
Rb	Sr	Y	Zr	Nb	Mo	Tc	▨ Ru	Rh	Pd	Ag	Cd	In	▩ Sn	▩ Sb	▨ Te	▩ I	▨ Xe
░ Cs	░ Ba	░ La	░ Hf	░ Ta	░ W	░ Re	░ Os	▨ Ir	░ Pt	▨ Au	░ Hg	Tl	Pb	Bi	Po	At	Rn
Fr	Ra	Ac															
			Ce	░ Pr	░ Nd	░ Pm	▨ Sm	▩ Eu	▨ Gd	░ Tb	▩ Dy	░ Ho	▨ Er	▨ Tm	▨ Yb	░ Lu	
			░ Th	░ Pa	░ U	▨ Np	Pu	░ Am	Cm	Bk	Cf	Es	Fm	Md	No	Lw	

▩ EASY TO STUDY, EXTENSIVE RESEARCH

▨ MORE DIFFICULT TO STUDY, SOME RESEARCH

░ VERY DIFFICULT OR LIMITED RESULTS

Ref. 6, p. 9

Figure 2.1 Elements that may be studied using Mössbauer spectrscopy.

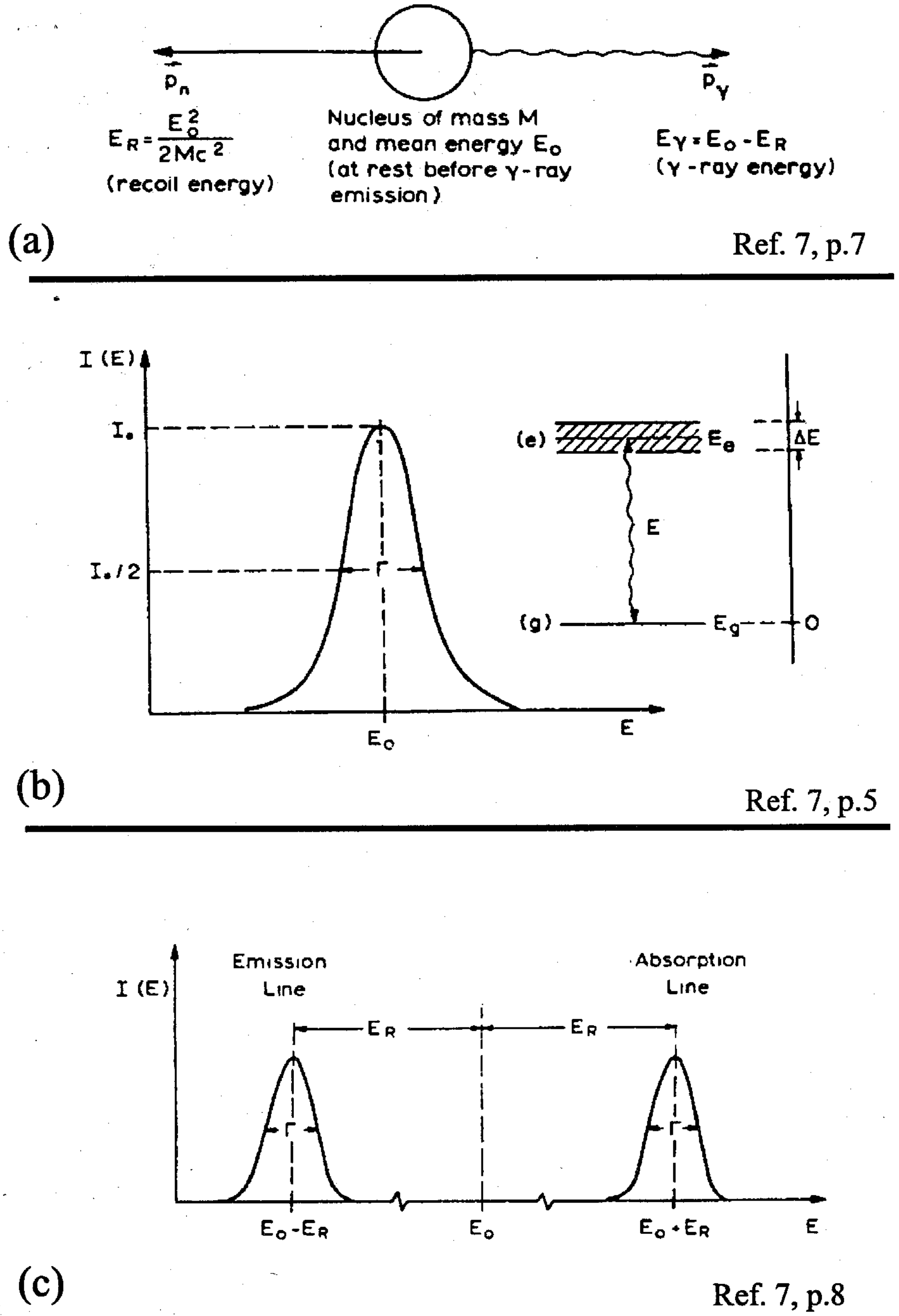

Ref. 7, p.7

Ref. 7, p.5

Ref. 7, p.8

Figure 2.2 (a) Recoil of the nucleus during emission. (b) The Mössbauer line shape from the decay of the nuclear excited state. (c) Separation of the Mössbauer lines by the recoil of the nucleus. The Mössbauer effect is only possible in the absence of this recoil.

its transitional energy, $E_0 = E_e - E_g$: it has an energy linewidth, Γ, which is proportional to ΔE (Fig. 2.2b). An important feature of nuclear resonant absorption is that both the emitter (source) and the absorber of the photon have transition energies between the ground and excited states that are precise to $\sim 10^{-9}$ eV. Resonant absorption occurs only when these two lines overlap to within 10^{-9} eV. Recoil generated during the emission and/or absorption by a free nucleus is of order 10^{-3} eV and will prevent the overlap (Fig. 2.2c). Thus, the source nucleus must emit the γ-ray without free recoil or energy loss to phonons for resonant
lattice vibrations
absorption to occur.

The primary feature of the Mössbauer effect is that the atoms containing the nuclei are embedded in solid matrices that allow for emission and absorption with zero energy loss to phonons or free recoil. This requires that the entire matrix that contains the atom will recoil as a unit. Because the mass of the matrix exceeds that of the atom by many orders of magnitude, the recoil energy will be much less than the linewidth ($E_R \ll \Gamma$), allowing resonant absorption to occur. Quantified by the recoil-free fraction, *f* (described in § 2.1.2), this zero phonon process is analogous to the fraction of scatterings of x-rays without phonon excitation.

Fortunately for materials science, factors other than recoil can affect the energies of the emission and absorption lines. These include, but are not limited to, the isomer shift, magnetic hyperfine interactions, and electronic quadrupole interactions. Conveniently for ^{57}Fe, the scale of these energies is larger than the energy of the transitional linewidth, but not too much larger. Thus, small changes can be made to tune the energy of the photon to compensate for the differences between the lines, allowing the acquisition of a spectrum of nuclear energy transitions. The energy changes are made by inducing a Doppler shift for either the source or absorber with a precision velocity transducer. The transducer typically scans a small velocity range on the order of a few millimeters per second. The velocity needed is derived from:

$$\nu = c \cdot \frac{\Gamma}{E_\gamma} = \frac{c}{Q} \qquad (2.1)$$

where c is the speed of light and Q is the ratio of the energy of the transition to its linewidth. Very large Q is characteristic of the Mössbauer effect; typical values are 10^{12}. For comparison, x-ray transitions have intrinsic Q's of 10^3 - 10^4. Figure 2.3 provides a graphical demonstration of the effects of the Doppler shift, including the resulting Mössbauer spectrum.

This rest of this section describes general properties of the Mössbauer effect, and then presents specific properties of the ^{57}Fe isotope. Only the properties most important to the present work are discussed. The references given at the end of the chapter should be consulted for a more complete description of the Mössbauer effect. [2-10]

2.1.1 Facts about the Mössbauer effect

Important properties of the Mössbauer effect are:

(1) It is a nuclear effect: only the energy levels in the atom's nucleus are involved.

(2) The nuclei involved are not in isolated atoms such as a gas; they must be embedded in a matrix.

(3) Scale of energies involved (all in eV):

Mössbauer gamma-rays, E_γ	10^4 - 10^5
Lattice binding energies	1 - 10
Free-atom recoil, E_R	10^{-4} - 10^{-1}
Lattice vibrations (phonons)	10^{-3} - 10^{-1}
Transition linewidths, Γ	10^{-9} - 10^{-6}

(4) The nuclear transitions are well defined by the quantum mechanics of the nuclear spins and selection rules.

(5) Absorption and/or emission of quanta by the nuclei may occur *recoillessly*: without the excitation of phonons. Effective mass is thus the entire sample

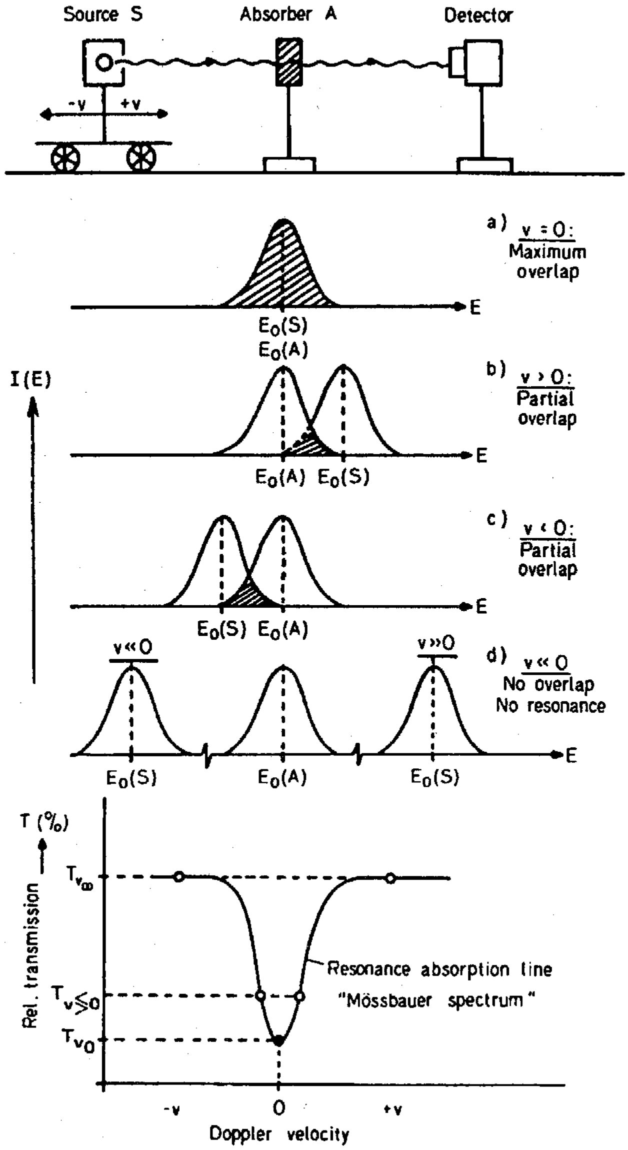

Ref. 7, p. 11

Figure 2.3 Explanation of Mössbauer Effect absorption as a function of the Doppler-derived energy ($E_R = 0$ is assumed).

rather than individual atoms. The recoil-free fraction, *f*, quantifies this zero phonon process.

(6) Lifetimes and energy widths of the excited states are related through Heisenberg's Uncertainity Principle: $\Delta E \Delta t \geq \hbar$. Since the excited states decay exponentially, we can use the relationship: $\Gamma\tau = \Gamma\left(t_{1/2}/\ln 2\right) = \hbar$, where τ is the mean lifetime of the state and Γ is the FWHM of the transitional spectral line (which has Lorentzian shape).

(7) Nuclear excited states that are candidates for the Mössbauer effect have $\tau \sim 10^{-6}$ to 10^{-11} s. Shorter and longer lifetimes will not work, as they are experimental unfeasible and smear the transitional lines, respectively.

(8) Anything that can change the energy or energy width of the nuclear states will affect the Mössbauer effect. Herein lies the physics that may be exploited by the materials scientist.

(9) Chemically, crystallographically, or magnetically inequivant sites in an absorber cause differences in the Mössbauer spectra. These are the effects that make chemical environment selective diffraction possible.

2.1.2 Recoil-free fraction

The scale of energies given in (3) above provides important information on how resonant absorption occurs. The energy of a recoiling nucleus is approximately two orders of magnitude smaller than the binding energy of the atom in the crystal. Thus, the photons that are absorbed and/or emitted are insufficient to kick the atom out of the sample. On the other hand, phonons are approximately 10^6 times more energetic than the transition linewidths. Any phonon excitation will destroy the Mössbauer effect by preventing resonant absorption.

Determining the probability of emission processes where there is no change in lattice phonons is paramount to understanding the Mössbauer effect. We start with Fermi's

Golden Rule from quantum mechanical radiation theory, which relates transitional probabilities to the initial and final states of the system:

$$W = \text{const.} \times |\langle f|H|i\rangle|^2 \tag{2.2}$$

where W is the probability of generating a phonon, H is the interaction Hamiltonian operator (which depends upon the position of the nucleus and the momenta and spins of the particles within the nucleus), and $|i\rangle$ and $|f\rangle$ are the initial and final states of the system, respectively. The nuclear decay is independent of the vibrational state due to difference in the range of their respective forces [2,5]. As we are interested only in the vibration state, the nuclear part can be separated and discarded. The "recoil-free fraction," *f*, which is the fraction of emissions with no phonon excitation, is [5]:

$$f = W_{rff} = \exp\left[-\frac{4\pi^2\langle x^2\rangle}{\lambda^2}\right] = \exp\left[-\kappa^2\langle x^2\rangle\right] \tag{2.3}$$

$$\kappa = 2\pi/\lambda = E/\hbar c$$

where $\langle x^2\rangle$ is the mean squared vibrational amplitude of the atom and κ is the wave vector of the emitted photon. The wavelength of the photon is λ, $2\pi\hbar$ is Planck's constant, and c is the speed of light. Equation 2.3 predicts that when the vibrational amplitude of the nucleus is comparable to the γ-ray wavelength, there will be significant coupling of the nuclear decay to phonon modes.

At this point a model is needed for lattice vibrations. The delta-function, single frequency Einstein model yields [2]:

$$f = \exp\left(\frac{-E_R}{k\theta_E}\right) = \exp\left(\frac{-E_R}{\hbar\omega_E}\right) \tag{2.4}$$

θ_E and ω_E are the Einstein temperature and frequency, and E_R is the recoil energy of the nucleus. The more complicated but more accurate Debye model predicts [7]:

$$f = e^{-2M} \quad , \qquad (2.5)$$

where:

$$M = \frac{6h^2}{m_a k_B \theta_D}\left[\frac{\phi(x)}{x} + \frac{1}{4}\right]\frac{\sin^2\vartheta}{\lambda^2}$$

$$\phi(x) = \frac{1}{x}\int_0^x \frac{\zeta d\zeta}{e^{\zeta} - 1} \qquad \text{(The Debye function)}$$

$$x = \frac{\theta_D}{T}$$

The mass of the atom is m_a, k_B is Boltzmann's constant, and ϑ is the angle of the Bragg peak. The $\sin^2\vartheta$ term causes a decrease in the intensity of the Mössbauer diffraction peaks for increasing ϑ (see § 5.3.6). In Mössbauer spectroscopy the Debye model reduces to the following approximations:

$$f = \begin{cases} \exp\left[\dfrac{-E_R}{k_B\theta_D}\left\{\dfrac{3}{2} + \dfrac{\pi^2 T^2}{\theta_D{}^2}\right\}\right] & T \ll \theta_D \\ \exp\left[\dfrac{-6E_R T}{k_B \theta_D{}^2}\right] & T \geq \theta_D \end{cases} \qquad (2.6)$$

where θ_D (= 414K for Fe_3Al) and T are the Debye and ambient temperatures, respectively. The Debye model introduces temperature dependence, as should be expected. This temperature dependent f is also known as the Lamb-Mössbauer factor. While very similar to the Debye-Waller factor in x-ray scattering, the Lamb-Mössbauer factor has an important difference. X-ray scattering processes occur rapidly compared to the time scale for lattice vibrations; the lifetime of the Mössbauer excited state is long compared to the same vibrations. This impacts Mössbauer scattering by requiring two f terms (one for absorption by the sample, the other for re-emission), $f_{L-M} = e^{-4M}$, to correctly model the intensity, while the x-ray scattering only requires one. These two factors will be used in the interference model chapter, § 5.

In summary, the important effects governing the recoil-free fraction, f, are:

1) E_R, the recoil energy
2) the stiffness of the binding of the atom in the crystal, as represented by θ_D
3) the ambient temperature

The recoil-free fraction, f, is higher for lower ambient temperatures, less energetic photons, and higher θ_D.

2.1.3 Absorption cross section

A high recoil-free fraction does little good without a sufficient concentration resonant absorption in the energy range of interest. For ideally thin sources and samples, both the emission and absorption energy distribution are Lorentzian (the Fourier transform of the exponentially-decaying excited state). The recoilless source energy distribution is:

$$N(E)dE = \frac{f_s\Gamma_s}{2\pi}\frac{dE}{(E-E_\gamma)^2+(\Gamma_s/2)^2} \qquad (2.7)$$

where f_s and Γ_s are the recoil-free fraction and linewidth of the source, respectively. The resonant absorption cross-section, $\sigma(E)$, has the form:

$$\sigma(E) = \sigma_0 \frac{(\Gamma_a/2)^2}{(E-E_\gamma)^2 + (\Gamma_a/2)^2} \tag{2.8}$$

where:

$$\sigma_0 = 2\pi\lambda^2 \left(\frac{2I_e+1}{2I_g+1}\right)\left(\frac{1}{1+\alpha}\right)$$

Γ_a = linewidth of the source
α = total internal conversion coefficient (described in § 2.1.4)
λ = wavelength of photon
I_e = nuclear spin quantum number (ground state)
I_g = nuclear spin quantum number (excited state)

For ideally thin samples and sources, $\Gamma = \Gamma_s = \Gamma_a$, and the resonance distribution (the convolution of the emission and absorption distributions) will itself be a Lorentzian function with $\Gamma_r = 2\Gamma$. For the remainder of the thesis, the linewidth Γ will refer to the full width at half maximum (FWHM) of the resonant absorption peak ($\Gamma = \Gamma_r$) unless otherwise noted. With increasing thickness of the sample, where *T* is the characteristic thickness [11]:

$$T = f_a n_a a_a \sigma_0 t_a, \tag{2.9}$$

$$\frac{\Gamma_r}{\Gamma} = 2.00 + 0.27 \cdot T \qquad 0 < T \leq 5$$

$$\frac{\Gamma_r}{\Gamma} = 2.02 + 0.29T - 0.005 \cdot T^2 \qquad 4 < T \leq 10$$

where:

f_a = recoil-free fraction of the absorber
n_a = number of atoms per cm^3 in the absorber
a_a = fractional abundance of the isotope
t_a = absorber thickness in cm

2.1.4 Alternate decay mechanisms (channels)

Excited states in the nucleus can decay by methods other than re-emitting a photon with the energy of the nuclear transition. These methods include electron excitations in atomic orbitals, which then give rise to x-rays or electron emission, decay products known as conversion x-rays and conversion electrons. Figure 3.8b shows the various products for the decay of the ^{57}Fe excited state. The internal conversion coefficient, α, is the ratio of electron excitation channels to the gamma-ray photon emission channel. Obviously, photon production will be more efficient for smaller α. In processes of Mössbauer scattering involving multiple photon absorptions and emissions from the nuclear excited states, photon emission efficiency may be suppressed by several orders of magnitude when $\alpha \sim 10$.

2.2 Important values for the ^{57}Fe Mössbauer effect

All of the experiments performed in this thesis involve the ^{57}Fe isotope Mössbauer effect. Table 2.1 lists the important quantities.

Table 2.1 Important quantities of the ^{57}Fe Mössbauer transition @ 14.41 keV.

Symbol	Value (units)	Quantity
α_T	8.21	total internal conversion coefficient
f	0.8	Lamb-Mössbauer factor (@ 300K)
$t_{1/2}$	9.77×10^{-8} sec	half-life of the excited state
Γ	4.55×10^{-9} eV	energy width of the transition
Γ_v	0.095 mm/sec	velocity equivalent of Γ
σ_0	2.38×10^{-18} cm^2	maximum absorption cross section
E_0	14.41 keV	energy of transition
E_R	1.95×10^{-3} eV	free atom recoil energy of nucleus
λ	0.86 Å	wavelength of γ-ray
I_g	1/2	nuclear spin quantum number (ground state)
I_e	3/2	nuclear spin quantum number (excited state)
τ_{Co}	270 days	half-life of the ^{57}Co

2.3 Hyperfine interactions and perturbations

As stated in § 2.1.1, for materials science the interesting and exploitable physics of the Mössbauer effect is in the perturbations and interactions of the nuclear states by external agents. The ^{57}Fe nucleus has a positive charge, has a finite radius with a distorted (non-spherical) shape when excited, and has spin. Thus, interactions of a ^{57}Fe nucleus with electric field, an electric field gradient, and a magnetic field will perturb the energy of the nuclear transitions and lead to hyperfine splittings and shifting of transition energies. The three most important interactions for the ^{57}Fe Mössbauer effect are the electric monopole (E0), electric quadrupole (E2), and magnetic dipole (M1). Figure 2.4a shows how the interactions may affect the energy levels, while Fig. 2.4b shows how the interactions may be used in different fields of science.

2.3.1 Isomer shift, E0

The isomer shift is the electric monopole (E0) contribution to the hyperfine interaction of the ^{57}Fe nucleus with the atomic electrons. The isomer shift is caused by interactions of the nuclear charge with the atomic electron density inside the nucleus. As the electrons must have a finite probability of being inside the nucleus for this effect to occur, direct interactions are limited to s-electrons (and relativistic 2p electrons). Other electrons (p-, d-, and f-) interact indirectly by affecting the shapes of the s-electron wavefunctions. The isomer shift is:

$$\delta = const \cdot \left(\tfrac{\delta R}{R}\right) \cdot \left[|\psi(0)|_A^2 - |\psi(0)|_S^2 \right] \tag{2.10}$$

where:

δ = the isomer shift
R = radius of assumed spherical atomic nuclei
$\delta R = R_e - R_g$

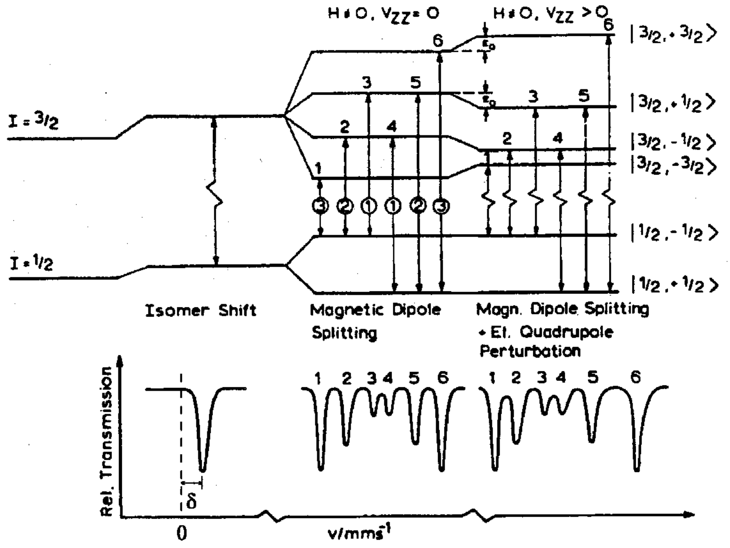

(a)

Ref. 7, p. 27

Relationship between Variables Measured Using Mössbauer Spectroscopy and Various Research Fields

Measured variable	Nuclear physics	Solid state physics	Chemistry	Metallurgy	Biology	Analytical
Isomer shift	Nuclear radius change	Electronic structure	Valence state and covalency	Electronic structure	Valence changes	
Magnetic hyperfine structure	Nuclear moments	Magnetic structure, electronic configuration of magnetic ions	Electronic configuration of magnetic ions	Order–disorder, precipitate identification	Ligand conformation	Chemical or phase identification by comparison with spectra of known materials
Electric quadrupole hyperfine structure		Electronic configuration	Ligand symmetry, bonding orbitals			Particle size information via superpara-magnetism
Recoil-free fraction		Phonon spectrum, anisotropic binding	Anisotropic binding	Force constants and anharmonic binding	Free or bound complex	

(b)

Ref. 6, p. 8

Figure 2.4 (a) The hyperfine parameters and (b) their relationships in various research fields.

$|\psi(0)|^2$ = probability density of the s-electrons at the nucleus
A, S, e, g subscripts -> absorber, source, excited, ground.

The factor $\left(\frac{\delta R}{R}\right)$, the nuclear part of the isomer shift, is the relative difference in the nuclear radius in the excited and ground states. Were there no such difference in nuclear radii, the electrostatic energy (E0) would be equal in both the excited and ground states, and there would be no change in electrostatic energy for the nuclear transition. A positive isomer shift shows that the electron density at the absorber nucleus is lower than that of the source for negative $\left(\frac{\delta R}{R}\right)$, which for ^{57}Fe is ~5 x 10^{-4}.

The atomic part of the isomer shift, $\left[|\psi(0)|_A^2 - |\psi(0)|_S^2\right]$, is very sensitive to chemical influences, such as changes in oxidation or spin state and bonding. The s-electron density at the nucleus is changed directly by changing the s-electron population in the valence shell and indirectly through screening by the other electrons. Consequently, the isomer shift can provide useful information about bond properties, valency, and oxidation state of a Mössbauer atom. Typical isomer shifts range from 0 to $\pm$ 0.5 mm/sec.

A knowledge of both source and absorber is necessary to determine the measured isomer shift. Our sources were ^{57}Co in Rh at room temperature, which has an isomer shift of -0.114 mm/sec with respect to metallic iron [12].

Rather than just changing the position of the energy levels, it is also possible to split them according to the nuclear spins, I (as is the case with both E2 and M1 interactions). This splitting is due to transition degeneracies (2I+1) being partially or fully broken and leads to a number of possible absorption energies and their corresponding lines in the Mössbauer spectra.

2.3.2 Electric quadrupole hyperfine interactions, E2

The nuclear electric quadrupole moment, which reflects the deviation of the nucleus from spherical symmetry, may interact with an inhomogeneous electric field to create electric quadrupole hyperfine interactions. These interactions depend on the orientation of the nuclear spin of the excited state of ^{57}Fe with respect to the orientation of the electric field gradient. Small local electric field gradients are generated when ^{57}Fe atoms have Al atoms as nearest neighbors. However, the axis of quantization of the nuclear spin is dominated by the strong hyperfine magnetic field in the material. In a polycrystalline sample, the orientations of electric field gradients will be averaged over all directions to the first neighbor Al atoms. The result is only a weak broadening of the absorption lines, so I will not discuss this topic further.

2.3.3 Magnetic dipole hyperfine interactions, M1

Magnetic dipole hyperfine interactions are of considerable importance to the work done in this thesis. The interaction, which is also called the nuclear Zeeman effect, arises through the interaction of the nuclear magnetic moment and a magnetic field at the nucleus. The interaction Hamiltonian is

$$\mathcal{H}_m = \vec{\mu} \cdot \vec{H}, \tag{2.11}$$

where $\vec{\mu}$ is the magnetic dipole moment and $\vec{H}$ is the total magnetic field at the nucleus. The field can be caused internally by the sample or externally by an applied field.

The nuclear Zeeman effect splits the nuclear energy levels into 2I+1 equally spaced and nondegenerate substates, where I is the spin quantum number. Splitting the $I_e = \frac{3}{2} \rightarrow I_g = \frac{1}{2}$ transition in ^{57}Fe creates eight possible transitions, of which only six are allowed by the M1 selection rules: $\Delta I = 1$; $\Delta m = 0, \pm 1$. Figure 2.4a shows the allowed sextet of peaks.

The relative intensities of the peaks seen in the Mössbauer spectra depend on the probabilities of the transitions occurring; these can be calculated using the square of the Clebsch-Gordon coefficients. The normalized intensities for ^{57}Fe, assuming no thickness distortions, are listed in Table 2.2.

Table 2.2 Relative Mössbauer peak intensities for ^{57}Fe.

Absorption Peaks	Normalized Intensities
3 and 4	1
1 and 6	3
2 and 5	varies from 0 to 4 depending on moment projection on magnetic field; isotropic average yields 2.

2.3.4 Hyperfine interactions affecting $^{57}Fe_3Al$

The two chemical environments of the D0$_3$-ordered ^{57}Fe$_3$Al samples (described in § 1.1) are each responsible for a sextet of absorption peaks. These two distinct sextets originate with the magnetic dipole Zeeman splitting with different values of the hyperfine magnetic field — the ^{57}Fe atoms with 0 Al neighbors experience an HMF of -310 kG while the ^{57}Fe atoms with 4Al neighbors experience an HMF of -220 kG. Figure 3.5 shows the HMF probabilities for the experimental ^{57}Fe$_3$Al samples (the presence of other Al environments indicates the samples are not fully ordered). The differences in the HMF's as a function of Al environment can be understood in terms of the additive perturbation model [10], where the HMF at a specific ^{57}Fe atom in an Fe-X alloy (X is the solute) is:

$$H = H_0 + \Delta H \tag{2.12}$$

$$\Delta H = n_1 \Delta H_1^X + n_2 \Delta H_2^X + \kappa c$$

where:

H_0 = -330 kG at 300K for an ^{57}Fe nucleus in pure iron metal

n_1, n_2 = the number of 1st nearest neighbor (1nn) and 2nn solute atoms, respectively

ΔH_1^X, ΔH_2^X = the HMF perturbations caused by each 1nn and 2nn solute atom, respectively

κ = HMF perturbation caused by 3nn and more distant solute atoms

c = solute concentration in the Fe-X alloy

The phenomenological additive perturbation model describes the changes of the ^{57}Fe HMF caused by nearest neighbor solute atoms. It assumes that the combined effects of several solute atoms are approximately additive.

The chemical origin of the HMF perturbations is better understood with the magnetic polarization model [10]. In the magnetic polarization model, the HMF perturbation, *ΔH*, is the sum of two components, H_L and H_{NL} (local and nonlocal). The first component, H_L, is caused by the unpaired *3d* electrons local to the ^{57}Fe atom, which polarize all of the *s*-like electrons at the same ^{57}Fe atom. Changes in H_L are:

$$\Delta H_L = \alpha \Delta \mu(0) \tag{2.13}$$

where α is a constant of proportionality, and $\Delta\mu(0)$ is the change in the local magnetic moment at the ^{57}Fe atom. Aluminum atoms do not change the magnetic moment at adjacent ^{57}Fe atoms. Thus, for Fe-Al alloys, $\Delta\mu(0) = 0$ and $\Delta H_{\mathrm{L}} = 0$.

The second component, H_{NL}, is comprised of the transferred HMF and arises from spin polarizations of nonlocal 4*s* electrons at the ^{57}Fe nucleus. These spin polarizations are in response to changes in magnetic moments at the neighbor lattice sites. Changes in H_{NL} are further separated into two terms, ΔH_{DNL} and ΔH_{INL}. The direct nonlocal term, ΔH_{DNL}, comprises the contributions from the lattice sites occupied by solute atoms. The indirect nonlocal term, ΔH_{INL}, comprises the contributions from those lattice sites occupied by iron atoms, but whose magnetic moments are perturbed by nearby solute atoms. For Fe-Al alloys, $\Delta H_{\mathrm{INL}} = 0$ because the Fe atoms do not have a change in magnetic moment when they have Al atom neighbors. Thus, for ordered Fe-Al alloys (where only the 1nn solute atoms are important) [10]:

$$\Delta H = \Delta H_{DNL} = -\alpha_{CEP} \sum_{n=0}^{8} \delta(r_n) f(r_1) \mu_{Fe}(0) \qquad (2.14)$$

where α_{CEP} is the constant of proportionality for the conduction electron polarization mechanisms and $\delta(r_n)$ is the Kroneker delta (which equals one if the site is occupied by an Al solute atom and zero otherwise). The term $f(r_1)$ is the fraction of conduction electron polarization at the ^{57}Fe nucleus produced by a change in the magnetic moment at *r*, with respect to the conduction electron polarization produced by the same change in the magnetic moment at $r = 0$. Finally, the $\mu_{Fe}(0)$ term is the magnetic moment of an iron atom in pure iron. For constant $f(r_1)$, the magnetic polarization model reduces to the additive perturbation model and:

$$\Delta H_1^{Al} = -\alpha_{CEP} f(r_1) \mu_{Fe}(0) \qquad (2.15)$$

The product $\alpha_{CEP} f(r_1)$ = -11.5 kG/μ_B, so the magnitude of the HMF of an ^{57}Fe atom is decreased when 1nn Al atoms are present. The distinction between the sextets of the 0Al and 4Al environments allows each environment to be selected independently, which allows acquisition of the unique diffraction patterns.

The D0$_3$-ordered ^{57}Fe$_3$Al samples also possess a small isomer shift. The isomer shift helps to separate peak 5 of the 0Al environment and peak 6 of the 4Al, which is why peak 6 of both environments was chosen for data acquisition. Figure 3.16 shows the sextets of the experimental samples.

2.4 Mössbauer diffraction

Mössbauer diffraction involves the coherent scattering of gamma rays from a crystal containing nuclei that are capable of resonant absorption and re-emission. The spatial coherence was first observed by Black and Duerdoth [13]. Since its discovery in the early 1960's [14,15], Mössbauer diffraction has focused primarily on diffraction from single crystals to maximize the intensity of the Mössbauer scattering. Dynamical diffraction theories have replaced the original kinematical approximations [16-18] as Laue geometries and forward scattering experiments have replaced simpler scattering experiments. While several of the phenomena seen in single crystal experiments will not be seen in our polycrystalline samples, a brief overview of single crystal Mössbauer diffraction experiments is instructive. A recent paper by Smirnov [19] provides such an overview.

The first evidence of coherent Mössbauer scattering was seen in the experiments of Black and Moon [14], where interference was observed between the x-ray Rayleigh scattering and Mössbauer scattering. The interference proved that resonant Mössbauer scattering retained coherence through the decay of the excited nuclear state. Studies of the interference effects in Mössbauer energy spectra continue to be actively pursued [20-25]. Kovalenko *et al.* [26] have studied the interference effects from crystallographically nonequivalent sites, but they saw the effects in the Mössbauer energy spectra.

The limit between kinematic and dynamic diffraction theory is set by the size of the crystal of coherently scattering nuclei. Kinematical diffraction theory is limited to small crystals ($d \ll 1/\mu_r$, where d is the characteristic crystal size and μ_r is the linear nuclear absorption factor at resonance[•]). The crystallite sizes of our polycrystalline samples (^{57}Fe and Fe_3Al) are ≤ 35 nm, which is the grain size determined by x-ray diffraction. The ^{57}Fe samples have the largest μ_r at 60 nm, but this represents the total Mössbauer cross section (only a small fraction of the total cross section will be available in our experimental data; see § 3.2.1). Thus, kinematical diffraction theory along the lines of O'Conner and Black [27] is sufficient for our polycrystalline samples. This is the subject of chapter 5. However, the strength of the interference between the Mössbauer and x-ray scattering in our Fe_3Al samples (§ 5) refutes a prediction of Ref. 15 that interference would not be seen in the diffraction pattern.

Central to the theory of nuclear resonance scattering is the concept of the nuclear exciton. The nuclear exciton is the superposition state of the delocalized, spatially- and time-phased nuclear excitation from the Mössbauer excited states. The existence of the nuclear exciton is surprising, as the coherence must be preserved for the lifetime of the excited state (10^{-5} to 10^{-9} seconds). The scattered radiation from the nuclear exciton is also coherent with the x-ray scattering processes in the sample, giving rise to interference effects that are addressed in chapter 5.

[•] The linear nuclear absorption factor sets the most restrictive limit on kinematical validity, as the coherence length needed for dynamical diffraction is also dependent on the internal conversion coefficient. Larger coefficients cause shorter coherence lengths as fewer photons are "available" per unit length.

In the dynamical limit, there is an enhancement of the coherent channel decay [28,29], resulting in a strong speedup in the rate of nuclear decay [30-32]. There is also a corresponding suppression of the incoherent decay channels. The nuclear exciton is responsible, with the enhancement predominately occurring in the spatially coherent (forward and Bragg) directions. While the speedup effect is primarily seen in the time domain experiments with synchrotron experiments, energy domain experiments such as ours could be adversely affected through broadening of the Mössbauer transition lines [33]. Fortunately, the speedup effects are limited by spatial coherence [34,35]. Thus, highly perfect crystals are needed to directly observe the speedup effects (a speedup factor of 200 resulted in a linewidth broadening factor of 30 [33]). Even in the kinematical limit, however, the coherent enhancement can cause some linewidth broadening, but we estimate it to be less than 10%. Thus, we do not expect the enhancement of the coherent decay channels to cause problems for our polycrystalline sample experiments.

In recent years Mössbauer diffraction experiments began using synchrotron radiation (SR) sources instead of radioisotope sources [36,37]. Synchrotron radiation experiments are conducted in the time domain rather the energy domain used by radioisotope sources. The pulsed nature of SR and its timing capabilities compensate for its lack of precise energy resolution.

There are a number of good review articles on Mössbauer diffraction. There are reviews covering both theoretical [16-18] and experimental work (radioisotope [38-41] and synchrotron radiation [42-45]). The reader is referred to Ref. 19 for a more complete explanation of Mössbauer diffraction through SR.

References, Chapter 2

[1] R.L. Mössbauer, Z. Phys. **151**, 124 (1958).

[2] H. Frauenfelder, *The Mössbauer Effect* (W.A. Benjamin, New York, 1962).

[an excellent early book; contains a number of important reprints]

[3] G.K. Wertheim, *Mössbauer Effect: Principles and Applications* (Academic Press, New York, 1964).

[very basic]

[4] P.G. Debrunner and H. Frauenfleder, in *An Introduction to Mössbauer Spectroscopy*, edited by L. May (Plenum Press, New York, 1971), Chapter 1.

[very basic]

[5] N.M. Greenwood and T.C. Gibb, *Mössbauer Spectroscopy* (Chapman and Hall, London, 1971).

[very good description of the Mössbauer effect; large number of applications]

[6] R.L. Cohen, *Applications of Mössbauer Spectroscopy* (Academic Press, New York, 1976) Volume I.

[Short introduction; Applications include: Metallurgy, Colloid and Interface Chemistry, Biological Studies, and Solid State Chemistry]

[7] P. Gütlich, R. Link, and A. Trautwein, *Mössbauer Spectroscopy and Transition Metal Chemistry* (Springer-Verlag, New York, 1978).

[good description]

[8] R.L. Cohen, *Applications of Mössbauer Spectroscopy* (Academic Press, New York, 1980) Volume II.

[Applications include: Additional Colloid and Interface Chemistry, Biological Studies, and Metallurgy]

[9] D.P.E. Dickson and F.J. Berry, *Mössbauer Spectroscopy* (Cambridge University, New York, 1986).

[Applications only]

[10] B.T. Fultz, in *Mössbauer Spectroscopy Applied to Magnetism and Materials Science*, edited by G.J. Long and F. Grandjean (Plenum Press, New York, 1993), Chap. 1.

[Discusses hyperfine magnetic field (HMF) spectra — examples include Fe_3Al short range order]

[11] S. Margulies and J.R. Ehrman, Nucl. Instrum. Methods **12**, 131 (1961).

[12] A.H. Muir, K.J. Ando, and H.M. Coogan, *Mössbauer Effect Data Index, 1958-1965* (Interscience, New York, 1967), p. 26.

[13] P.J. Black and I.P. Duerdoth, Proc. Phys. Soc. 84, 169 (1964).

[14] P.J. Black and P.B. Moon, Nature **188**, 481 (1960).

[15] P.J. Black, G. Longworth, and D.A. O'Conner, Proc. Phys. Soc. **83**, 925 (1964).

[16] Yu. Kagan and A.M. Afanas'ev, *Proc. Int. Atomic Energy Agency Symp. on Mössbsauer Spectroscopy and its Applications* (IAEA, Vienna, 1972), p. 143.

[17] V.A. Belyakov, Usp. Fiz. Nauk **115**, 553 (1975) [Sov. Phys.-Usp. **18**, 267 (1975)].

[18] U. van Bürck, Hyperfine Inter. **27**, 219 (1986).

[19] G.V. Smirnov, Hyperfine Inter. **97/98**, 551 (1996).

[20] G. Faigel and M. Tegze, Hyperfine Inter. **92**, 1137 (1994).

[21] M. Tegze and G. Faigel, Hyperfine Inter. **92**, 1143 (1994).

[22] J.G. Mullen, R.A. Wagoner, and G. Schupp, Hyperfine Inter. **83**, 147 (1994).

[23] R.A. Wagoner and J.G. Mullen, Phys. Rev. B **49**, 12425 (1994).

[24] R.A. Wagoner, J.G. Mullen, and G. Schupp, Phys. Rev. C **47**, 1951 (1993).

[25] J.G. Mullen, A. Djedid, B. Bullard, G. Schupp, D. Cowan, Y. Cao, M.L. Crow, and W. Yelon, Hyperfine Inter. **40**, 123 (1988).

[26] P.P. Kovalenko, V.G. Labushkin, A.K. Ovsepyan, É.R. Sarkisov, G.V. Smirnov, and I.G. Tolpekin, Zh. Eksp. Teor. Fiz. **88**, 1336 (1985) [Sov. Phys. JETP **61**, 793 (1985)].

[27] D.A. O'Conner and P.J. Black, Proc. Phys. Soc. **83**, 941 (1964).

[28] G.T. Trammell, *Proc. Int. Atomic Energy Agency Symp. on Chemical Effects of Nuclear Transformations*, Prague 1960 (IAEA, Vienna, 1961), Vol. 1, p. 75.

[29] A.M. Afanas'ev and Yu. Kagan, Pis'ma Zh. Eks. Teor. Fiz. **2**, 130 (1965) [JETP Lett. **2**, 81 (1965)].

[30] Yu. Kagan, A.M. Afanas'ev, and V.G. Kohn, J. Phys. C: Solid State **12**, 615 (1979).

[31] J.P. Hannon and G.T. Trammel, Physica B **159**, 161 (1989).

[32] A.M. Afanas'ev and Yu. Kagan, Zh. Eksp. Teor. Fiz. **52**, 191 (1967) [Sov. Phys. JETP 25, 124 (1967)].

[33] U. Van Bürck, G.V. Smirnov, R.L. Mössbauer, and Th. Hertrich, J. Phys.: Condens. Matter **2**, 3989 (1990).

[34] H.J. Lipkin, Phys. Rev. Lett. **58**, 1176 (1987).

[35] G.T Trammel and J.P. Hannon, Phys. Rev. Lett. **61**, 653 (1988).

[36] S.L. Ruby, J. Phys. (Paris) **35**, C6-209 (1974).

[37] E. Gerdau, R. Rüffer, H. Winkler, W. Tolksdorf, C.P. Klages, and J.P. Hannon, Phys. Rev. Lett. **54**, 835 (1985).

[38] G.V. Smirnov, Hyperfine Inter. **27**, 203 (1986).

[39] H. de Waard, Hyperfine Inter. **68**, 143 (1991).

[40] G.V. Smirnov, Hyperfine Inter. **72**, 63 (1992).

[41] G.V. Smirnov and A.I. Chumakov, in *Resonant Anomalous X-ray Scattering*, edited by G. Materlik, C.J. Sparks, and K. Fisher (Elsevier, Amsterdam, 1994), p. 604.

[42] E. Gerdau, R. Rüffer, H.D. Rüter, and J.P. Hannon, Hyperfine Inter. **40**, 49 (1988).

[43] J. Arthur, D.E. Brown, S.L. Ruby, G.S. Brown, and G.K. Shenoy, J. Appl. Phys. **67**, 5704 (1990).

[44] R. Rüffer, Synchrotron Radiation News **5**, 25 (1992).

[45] E. Gerdau and U. van Bürck, in *Resonant Anomalous X-ray Scattering*, edited by G. Materlik, C.J. Sparks, and K. Fisher (Elsevier, Amsterdam, 1994), p. 589.

Chapter 3 Instrumentation

This chapter deals with the experimental equipment, samples, and procedures that were necessary to collect the data shown in § 4[♦]. As my thesis work progressed, the instrumentation has evolved and improved. While these improvements will be discussed in the appropriate sections, this chapter will focus on the equipment used to collect the most recent data.

The chapter is broken into five sections: § 3.1 provides an overview of the equipment, § 3.2 describes the samples, § 3.3 discusses the photon sources and their velocity transducer, § 3.4 describes the INEL (Instrumentation Électronique) detector and electronics, and § 3.5 explains the collimator and shielding. Additional information can be found in Appendix B, which explains issues such as the calibration procedures.

The data sets mentioned in this chapter, such as Fe95 (^{57}Fe sample data) and Fe_3Al95 ($^{57}Fe_3Al$ sample data), are described in § 4.1.

3.1 An overview of the Mössbauer diffractometer

There are many different parts to the instrument, so a quick overview should prove useful. Figures 3.1 through 3.3 provide a visual tour of the experimental equipment. Unless noted otherwise, the equipment and procedures are the most current.

Figure 3.1 shows a top view of the detector and source arrangement. The two rulers, one 6" long and the other 12", provide the scale. The figure does not show the Pb shielding that is normally placed above the source (removed so that the drive can be seen).

[♦] In a nutshell, the equipment consists of mating a radioactive Mössbauer source to a position sensitive x-ray diffractometer. As we will see, the marriage was a bit rocky at first, but has ultimately proven successful.

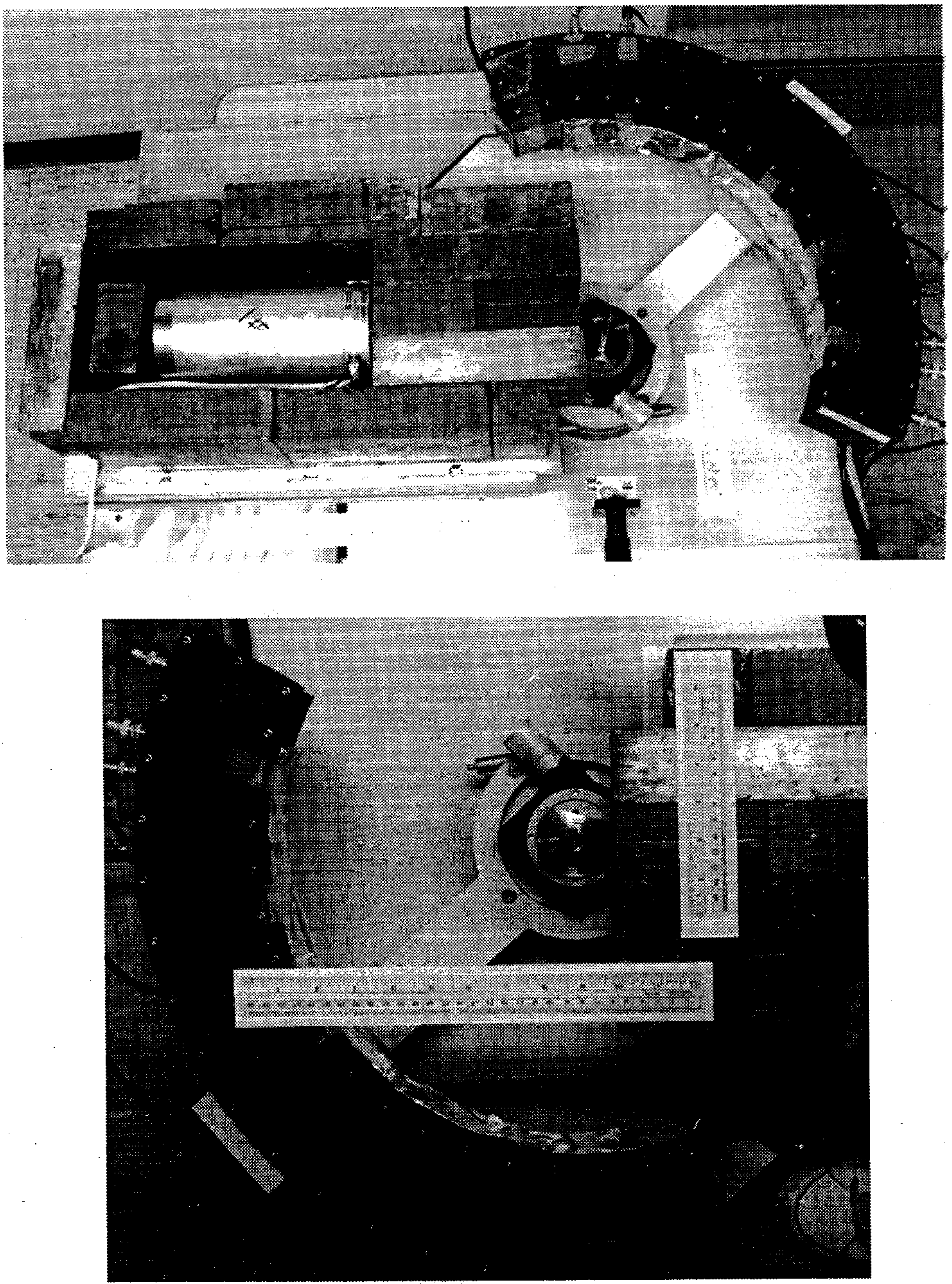

Figure 3.1 Top views of the INEL detector and source arrangement.

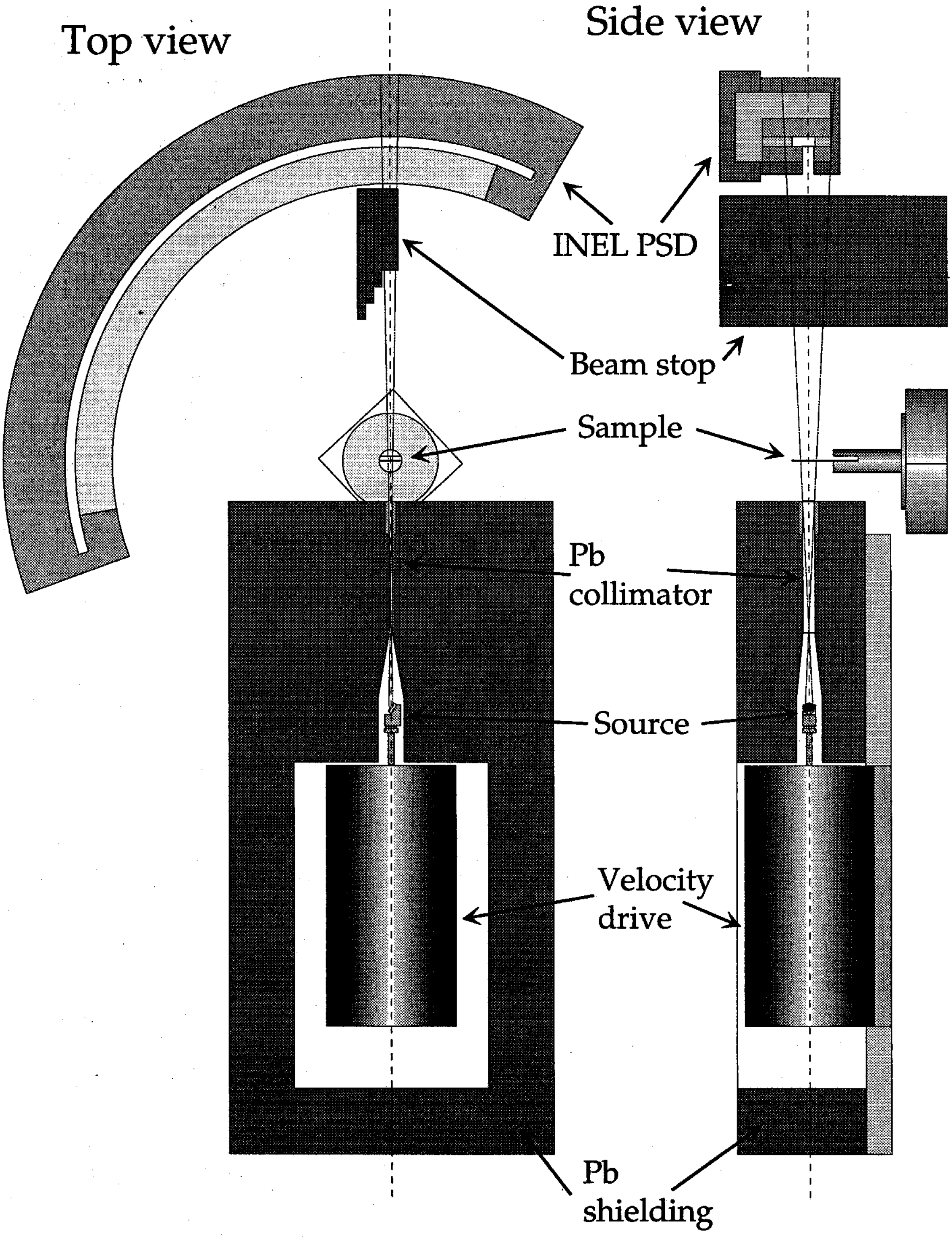

Figure 3.2 Schematic views of the INEL detector and source arrangement. The solid lines indicate the line of sight of the 6 mm diameter tilted source through the collimator. The drawing is at a 1:5 scale.

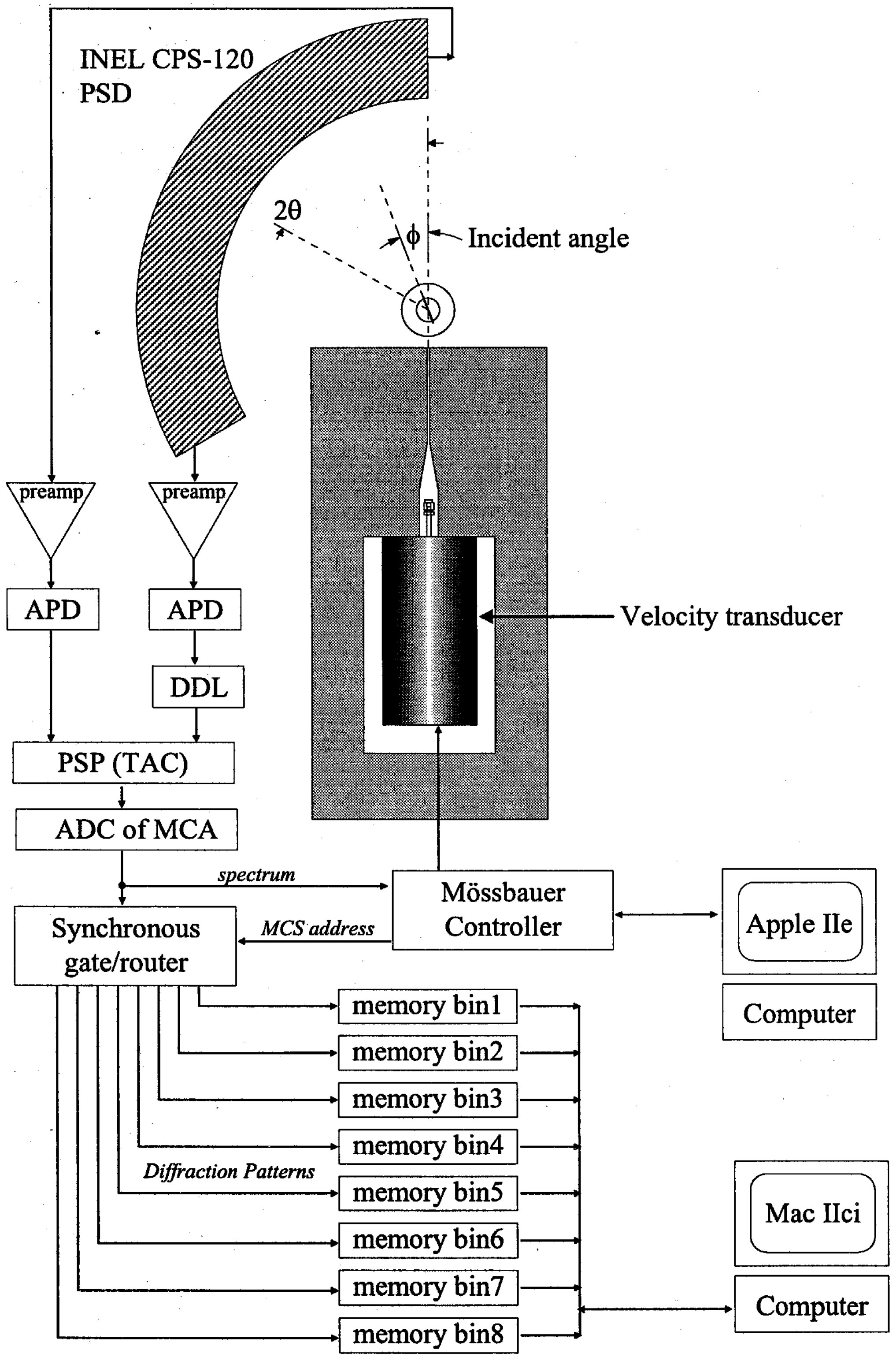

Figure 3.3 Data flow diagram for the INEL detector and its electronics. The acronyms are defined in section 3.4.

(The x-ray beamline originally used with the detector can be seen in the lower part of the top photograph.)

Figure 3.2 displays the top and side schematic views of the Mössbauer diffractometer. All items are to scale, with the figure printed at a reduction of 1:5. The dashed and solid lines provide the axis and line of sight of the source through the collimator, respectively. The divergence of the solid lines indicates the size of the transmitted beam and the size of the sample needed to fully intercept it. The side view also shows that a taller detector window would be useful.

Figure 3.3 shows the flow and control of the data. The detector and its electronics, which are described in § 3.4.1–2, collect and process the photons scattered by the sample, thus providing the spatial information necessary to form the diffraction patterns. The velocity transducer (§ 3.3.3) is operated in a region-of-interest mode around selected peaks in the energy spectrum. The synchronous router (§ 3.4.3) then stores up to eight independent diffraction patterns corresponding to different sub-ranges in the energy spectrum.

3.2 Samples

In § 1.1 it is explained why $^{57}Fe_3Al$ was chosen as the sample for the experiments performed in this thesis research. This section describes the desired characteristics of the samples and sample preparation, and my success in achieving the desired characteristics.

3.2.1 Desired sample characteristics

Several characteristics are desirable for the samples used in our experiments. The samples should have:

(1) high enrichment in the Mössbauer isotope (^{57}Fe),
(2) full crystallographic ordering,

(3) a controlled, homogeneous composition,
(4) a controlled thickness to maximize Mössbauer scattering while minimizing x-ray scattering,
(5) a proper sample area for the geometry of the detector,
(6) a low level of contamination and oxidation, and
(7) low cost.

As ^{57}Fe accounts for only ~2.2% of natural iron, all of the samples must be made with artificially enriched ^{57}Fe to maximize resonant absorption. More importantly, all non-resonant Fe nuclei will lead to incoherent scattering, so high enrichment is required. This leads to expensive samples, as 95%-enriched ^{57}Fe costs US $10 per mg. Efforts were made to minimize the amount of ^{57}Fe needed to make the samples.

The optimum thickness for the sample is determined by several considerations. The ^{57}Fe resonant absorption cross-section for 14.41 keV photons is typically several hundred times larger than that for x-rays. As the x-ray characteristic thickness is approximately 20 microns, the samples should have a maximum thickness of a few microns to suppress x-ray scattering. Even this thickness would seem to be too large, as the sample is approximately 50 times the characteristic thickness for the Mössbauer absorption. However, the breadth of the Mössbauer spectra and the method of data collection allows only a small fraction of the total resonant absorption cross-section to be applied to each diffraction pattern. Chapter 5, which describes the modeling of the data, provides greater detail on the effects of sample thickness and cross sections.

The size and shape of the INEL detector and the collimator for the incident beam set the geometrical requirements for the samples to be 1 cm wide by 2 cm tall.

3.2.2 bcc ^{57}Fe samples

Our first experiments were performed on two 95%-enriched ^{57}Fe foils obtained from NEN (New England Nuclear) DuPont and arranged to make a sample of 2 cm high by

1 cm wide. Each foil was initially 2.75 microns thick, but they were etched to 2.55 microns to check for surface texture effects and to remove possible surface oxides. Both the Fe91 and Fe95 data sets were acquired from the post-etched samples.

Figure 3.4a shows conventional x-ray diffraction patterns from the ^{57}Fe samples before and after etching. The patterns were made on the INEL CPS-120 diffractometer with Co Kα radiation and an incident angle of 15 degrees. The absence of the (200) and (220) peaks and the extreme reduction of intensity in the (110) peak indicates the presence of crystallographic texture in the sample. More information on this crystallographic texture can be found in § 3.2.7. The grain size was estimated to be 32 nm by the Scherrer formula for x-ray line broadening caused by small grain size.

3.2.3 D0$_3$ ^{57}Fe$_3$Al samples

The samples for the ^{57}Fe$_3$Al experiments were made at Caltech, as described here. Several means of preparing the ^{57}Fe$_3$Al samples were examined; these included evaporation, piston-anvil quenching, rolling, and diffusion between closely-coupled foils of ^{57}Fe and Al. Natural iron was first used to test methods of sample preparation.

Evaporation should be the most desirable method of sample preparation, as we can "grow" flat samples to arbitrary thickness. However, the evaporators we have available cannot ensure proper composition. The geometric requirements to evaporate evenly-thick sub-micron films require a small solid angle, and thus a large amount of starting material with potentially large amounts of isotope loss. A more "directed" form of evaporation is needed to prevent isotope loss.

The diffusion method involved taking thin (1-2 micron) foils of Al and Fe, folding them over each other several times, and then cold rolling the resulting "sandwich" to approximately 2 microns. The process of folding and rolling was repeated several times to ensure close contact between foils. The sample was then annealed at a high temperature to promote interdiffusion of the Fe and Al. This method was stopped, as very high

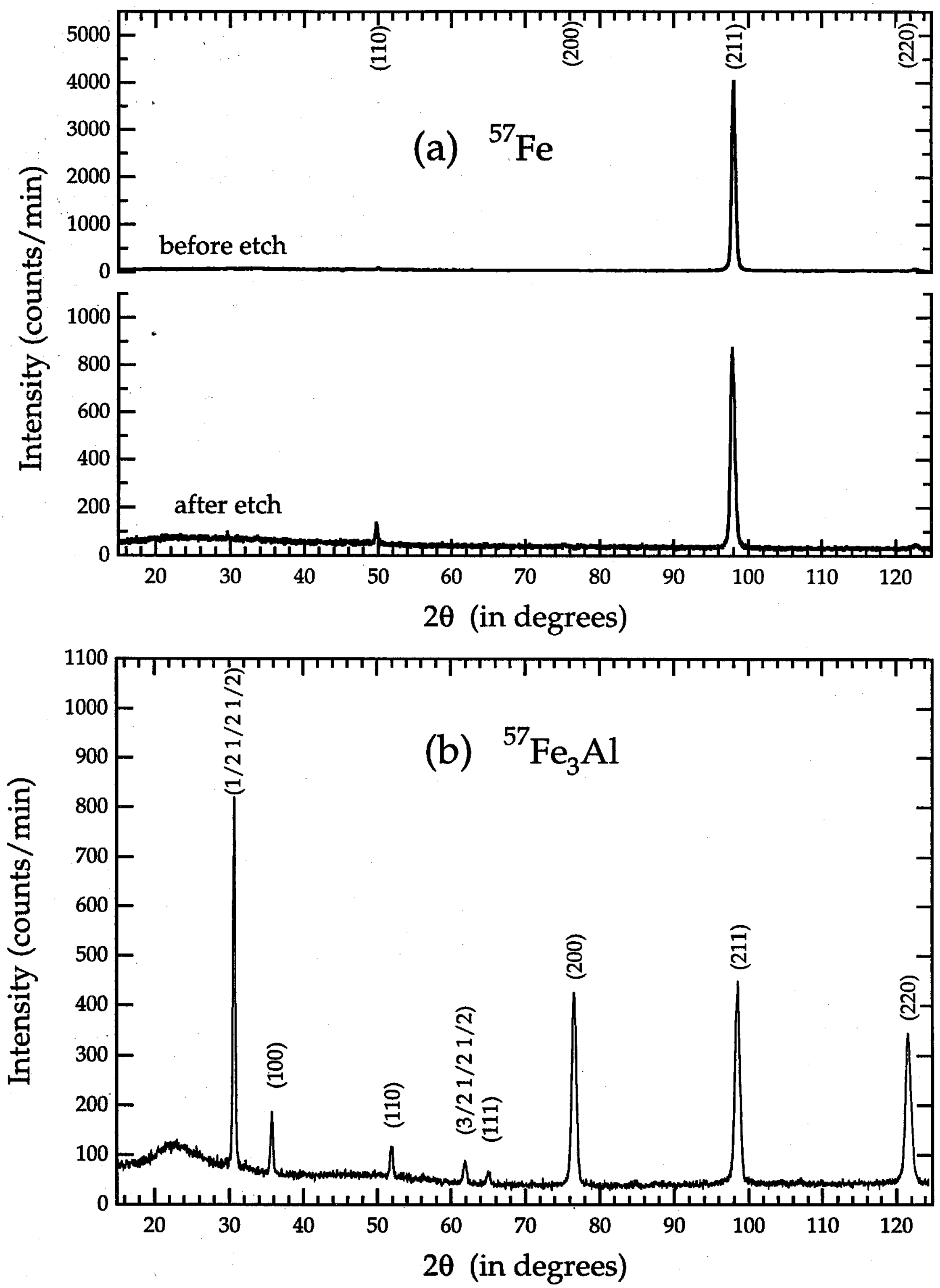

Figure 3.4 X-ray diffraction patterns of (a) ^{57}Fe and (b) ^{57}Fe$_3$Al used in the texture work. Data was acquired with INEL CPS-120 PSD with Co Kα x-ray radiation. The incident angle was set at 15 degrees.

temperatures were needed to properly interdiffuse the two elements, threatening oxidation and contamination. Furthermore, both the sample composition and homogeneity were in doubt.

A combination of arc-melting, splat-quenching, and rolling was chosen for sample preparation because of (1) the low level of isotope loss during preparation (<20% loss of starting material), (2) the composition preservation from ingot to final sample, (3) the low level of contamination, and (4) the high degree of crystallographic texture that can be exploited to enhance the intensity of certain diffraction peaks.

3.2.4 Procedure for $^{57}Fe_3Al$ sample preparation

The $^{57}Fe_3Al$ samples were prepared by arc-melting ingots comprising 95%-enriched ^{57}Fe with Al (99.999 %) in a three psi overpressure of Ar. The chamber, an Edmund Bühler D-7400, was cleaned prior to melting by Ar purging and Ti gettering. The resulting $^{57}Fe_3Al$ ingots were small: 50 to 100 mg total weight. The samples were inverted and remelted to ensure homogeneity. Mass loss was evidenced by the black soot left on the Cu hearth, but was only a few percent. The small spherical ingots were ideal for the next step of piston-anvil quenching.

Piston-anvil (splat) quenching was performed with an Edmund Bühler Ultra Rapid Quencher (URQ). The splat quencher levitates and melts a small ingot through use of a radio frequency (RF) power supply in an 3 psi over-pressure of Ar gas. Upon turning off the power supply, the molten ingot falls between two Cu anvils that accelerate towards each other by electromagnetically-driven pistons. Contact between the molten ingot and the Cu anvils results in rapid cooling (~10^6 K/sec) and pancake-shaped samples. While the high cooling rate is not required, the quenching process does provide an ideal shape for further sample processing. The 50 mg $^{57}Fe_3Al$ ingots were transformed into pancake-shaped "splats" with a thickness of 35 microns and a diameter of 1.5 cm. Rolling was then performed to achieve the desired final thickness.

Samples were cold rolled from both ingot and splat-quench form to achieve the desired thickness. Rolling was performed by placing the sample in a half-sandwich of 24 gauge AISI 304 stainless steel plate and progressively passing it through the rolling mill. Fe_3Al is somewhat brittle, so care was taken to prevent fracture of the sample. Rolling was performed slowly, with many passes through the roller. While hot rolling (heating the sample/plate combination in a furnace and then rolling while still hot) may offer improved ductility, fear of oxidation led to all of the samples being cold rolled at room temperature. The samples rolled after splat quenching (final thickness ~ 2.5 microns) fared better than the samples rolled directly from ingot (~ 6 microns), probably because the splat samples were disordered bcc, which is more ductile than the B2 or $D0_3$ ordered forms of Fe_3Al. The crystallographic texture of the samples was different, as described below.

All samples required annealing to develop $D0_3$ order. The $D0_3$ structure transforms to a B2 structure at 550^0C, so all annealing was done below this temperature. The samples used in the diffraction experiment were annealed for 100+ hours at 450^0C and then allowed to cool in the furnace. Test samples indicated that additional time and temperature did not make a noticeable improvement to the degree of $D0_3$ ordering.

3.2.5 $^{57}Fe_3Al$ sample designations

The samples prepared by splat-quenching followed by rolling are designated $^{57}Fe_3Al$ #1(*) or #1(*), where * is a letter designation for each particular sample. The samples rolled directly from ingots are designated $^{57}Fe_3Al$ #2(*) or #2(*). My preferred samples are #1(C) and #2(A). While these samples were annealed by a similar procedure, they differed in their crystallographic textures and thus favored different diffraction peaks.

3.2.6 Sample composition and chemical order

Because the $^{57}Fe_3Al$ samples were made from unusually small ingots, care was taken to determine if the samples had the proper composition and chemical order. Long range order (LRO) and grain size were determined by x-ray powder diffractometry, which also showed the samples to have a high degree of crystallographic texture. Section 3.2.7 will describe the texture in more detail. Conversion electron Mössbauer spectroscopy (CEMS) was used to measure the short range order (SRO), as the samples were too highly enriched with ^{57}Fe to allow transmission Mössbauer spectroscopy. Electron microprobe analysis was used to measure the chemical composition of the samples.

Figure 3.4b shows an x-ray powder diffraction pattern from an $^{57}Fe_3Al$ sample. The rolling direction of the foil was parallel to the axis of the goniometer and perpendicular to the plane of the scattered radiation. The strong crystallographic texture suppresses the intensity of the (110) peak, which normally would be the most intense peak in the diffraction pattern. The strong superlattice peaks, the $\left(\frac{1}{2}\frac{1}{2}\frac{1}{2}\right)$ and the (100), indicate a very high degree of order. Unfortunately, the strong crystallographic texture of the foils made it impossible to quantify the long range order (LRO) parameter by x-ray diffractometry, but similar heat treatments on filed powders produced LRO parameters of close to unity. The grain size of the $^{57}Fe_3Al$ foils was estimated to be 23 nm by the Scherrer formula.

Figure 3.5a displays Mössbauer CEMS data, while Fig. 3.5b displays the hyperfine magnetic field (HMF) probability distribution extracted from the CEMS data. The extraction is performed by the method of LeCäer and Dubois [1]. Table 3.1 provides the probabilities associated with each environment: these data were calculated by fitting five Gaussian peaks to the HMF probability distributions in Fig. 3.5c.

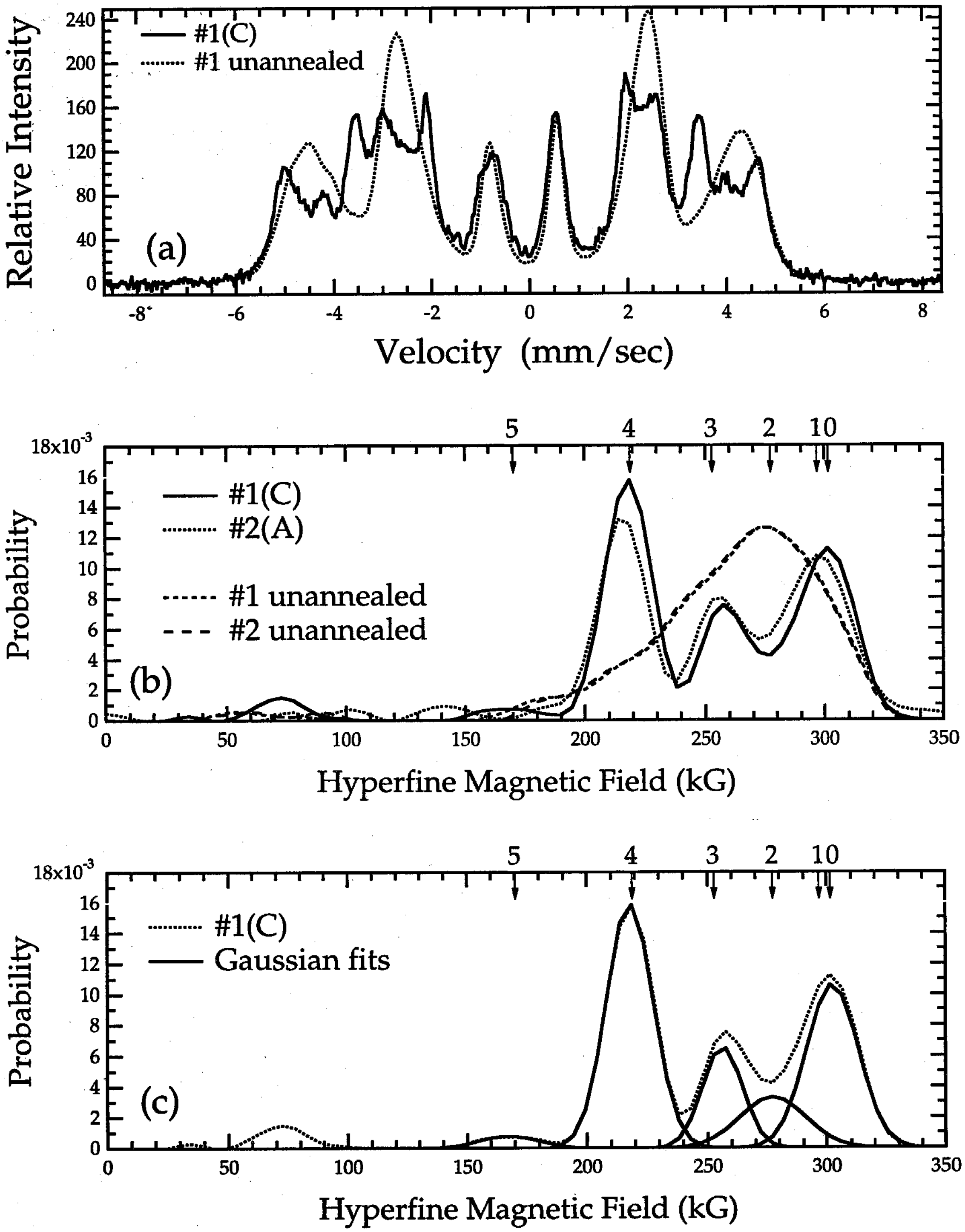

Figure 3.5 (a) Conversion electron Mössbauer spectroscopy (CEMS) and (b) hyperfine magnetic field (HMF) probability distributions of the ^{57}Fe$_3$Al samples. (c) Gaussian fits to the HMF's. The numbers on the top of figures (b) and (c) indicate the HMFs of the various Al 1nn environments.

Table 3.1 CEMS results for the $^{57}Fe_3Al$ samples. Results for both experimental samples and their unannealed base material are shown.

	% occupancy of each 1nn				
sample	0,1 Al	2 Al	3 Al	4 Al	5 Al
splat and rolled	23.32	37.74	32.40	4.14	8.12
rolled from ingot	15.97	45.73	30.77	6.51	4.17
#1(C)	29.02	11.58	13.79	38.84	2.54
#2(A)	35.30	9.50	12.92	32.70	2.95

Table 3.2 Expected occupancies of the various 1st nearest neighbor sites (Al atoms in the 1nn shell of the Fe) for the $^{57}Fe_3Al$ as a function of order. The disordered case is based on the binomial distribution for a 25% alloy with 8 possible 1nn sites [2]. Sites above 5 Al 1nn are not included due to insignificant occupation.

	% occupancy of the 1st nn sites					
Type of order	0	1Al	2Al	3Al	4Al	5Al
disorder	10.01	26.71	31.15	20.76	8.65	2.31
DO_3	33.33	0	0	0	66.67	0

We compare the distributions of Al neighbors from the data in Table 3.1 to the binomial probabilities expected of a random alloy or an alloy with DO_3 chemical order (Table 3.2). The 2Al and 3Al environments are much more prevalent than expected in both the unannealed (binomial probabilities) and annealed data (DO_3 order). We initially were concerned that this could be due to an Al deficiency in the sample. However, the electron microprobe results below showed that the composition of the samples was accurate. Two other causes are possible. First, the samples are not fully ordered and therefore have ^{57}Fe atoms with 2Al and 3Al environments. However, this does not explain the excess of 2Al and 3Al environments in the unannealed samples. Second, the extractions of the HMF distributions were not perfect. This is possible due to line broadening in the CEMS data caused by the high degree of ^{57}Fe enrichment in the samples. Even allowing for these problems, however, the results should be adequate for our needs.

The chemical composition of the samples of $^{57}Fe_3Al$ from both preparation methods (#1 and #2) was measured at the Caltech Geology and Planetary Sciences Analytical facility with a JEOL Superprobe 733 electron microprobe. The samples were prepared identically to those used in the diffraction experiments. To increase the quantitative reliability of the analysis, several Fe_3Al standards of known composition were used. Each sample was examined in at least five different areas. The average compositions and standard deviations of these measurements are shown in Table 3.3. The $^{57}Fe_3Al$ sample compositions are very close to the desired 25% Al.

Table 3.3 JEOL 733 microprobe results on the Fe_3Al samples. Both bulk ingots were 5 grams in mass (they were prepared with natural Fe).

Sample	Expected %'s	meas. Fe %	meas. Al %	std. dev. %
type #1 (splat-then-rolled)	Fe75Al25	74.6	25.4	0.40
type #2 (rolled-from-ingot)	Fe75Al25	74.9	25.1	0.39
Bulk ingot A	Fe75Al25	74.9	25.1	0.13
Bulk ingot B*	Fe74Al26	74.1	25.9	*

*Bulk ingot B was sampled only once and was solved for as an unknown after the microprobe was calibrated against the bulk ingot A.

We calculated the effect of chemical disorder on the intensities of superlattice diffractions. Only one of the four crystallographic sites in the Fe_3Al $D0_3$ structure should contain Al atoms: the δ sites in Fig. 1.1. In the case of an Al deficiency, antisite Fe atoms will occupy the vacant Al sites. The 4Al sites, α and β, which contain Fe atoms, can be used to probe for antisite Fe atoms. If we assume these antisite Fe atoms are distributed at random over the δ sites, we can compare the ratio of the binomial distributions for the number of 3Al 1nn and 4Al 1nn to the CEMS results and determine the Al deficiency. Using the data from Table 3.1, we determined that the experimental samples are 23% Al.

We used this composition with the Lazy Pulverix[♦] computer program to calculate the superlattice intensities when 6% of the δ site atoms were Fe. Compared to an alloy with perfect stiochiometry, we calculate a 20% decrease in intensity of the superlattice peaks. The disorder in the samples may have caused a significant decrease in the superlattice peak intensities.

3.2.7 Crystallographic texture

Cold rolling the samples to decrease thickness introduces crystallographic texture. Texture in this sense is the preferential orientation of the crystallites that compose the sample. The preferential orientation is chosen by the active slip systems in the sample, which allows for easier plastic deformation along certain crystallographic planes than others [3]. Because texture aligns certain planes parallel to the plane of the sample, the intensity of the Bragg peaks in the diffraction pattern corresponding to these planes is enhanced. Conversely, the intensities of the Bragg peaks of the unfavored crystallographic planes are reduced. Thus, through careful sample selection, we can enhance the intensity of the superlattice Bragg peaks that are interesting for measurement of chemical environment selectivity.

All samples exhibited at least some crystallographic texture. To quantify the texture, x-ray powder diffraction patterns were obtained from the sample over a range of angles of the incident beam with the INEL x-ray diffractometer described in § 3.4. The crystallographic texture makes the intensity of the Bragg peaks highly sensitive to the incident angle of the radiation. By measuring Bragg peak intensities as a function of

---

[♦] Lazy Pulverix [4] calculates theoretical x-ray and neutron diffraction powder patterns. The diffraction patterns are calculated using the lattice parameters, space-group symbol, and coordinates and chemical symbols of the atoms in the unit cell. The calculation includes atom form factors, Lorentz-polarization factors, and geometrical features of a Bragg-Brentano powder diffractometer.

incident angle, we made a simple texture map of the samples. Figures 3.6 and 3.7ab show the crystallographic texture of the ^{57}Fe and ^{57}Fe$_3$Al samples. The figures display the areas of the various peaks versus the incident angles used to acquire the diffraction patterns. Figure 3.6 shows the crystallographic texture of the ^{57}Fe sample both before and after the surface was etched. The two most prominent peaks, the (200) and the (211), show a substantial decrease in intensity after the etch, indicating that surface of the foils was more textured than the interior.

Results of diffraction peak intensities versus incident angle for ^{57}Fe$_3$Al #1(C) are displayed in Fig. 3.7a. Results for sample #2(A) are displayed in Fig. 3.7b. Two differences are seen upon comparison to the ^{57}Fe results. First, the peak areas are more than an order of magnitude smaller than those of the Fe. Second, the data (diffraction intensity versus incident angle) show broader peaks, which indicates less crystallographic texture. The texture is a more pronounced for the ^{57}Fe sample than the ^{57}Fe$_3$Al samples. The abrupt decrease in intensity of the $\left(\frac{1}{2}\frac{1}{2}\frac{1}{2}\right)$ peak at an incident angle of 30^0 occurs because the incident angle has exceeded the 2θ angle of the peak.

Comparing the texture effects of the ^{57}Fe$_3$Al samples shows that the #1(C) sample favors the $\left(\frac{1}{2}\frac{1}{2}\frac{1}{2}\right)$-type superlattice diffractions, while the #2(A) sample favors the (100)-type superlattice diffractions and the (200) fundamental. Thus, both samples should prove useful in the chemical environment selectivity experiments, as both types of superlattice peaks are needed to prove the effects.

It turns out that the differences in crystallographic texture between the surface and the interior of the sample do not cause problems in the interpretation of the ^{57}Fe$_3$Al data. The texture effects in ^{57}Fe$_3$Al are not strong. Furthermore, as we will see in § 5, the effective cross sections for Mössbauer and x-ray scattering are very similar. Therefore, any depth dependence of the crystallographic texture will affect both types of scattering in the same manner.

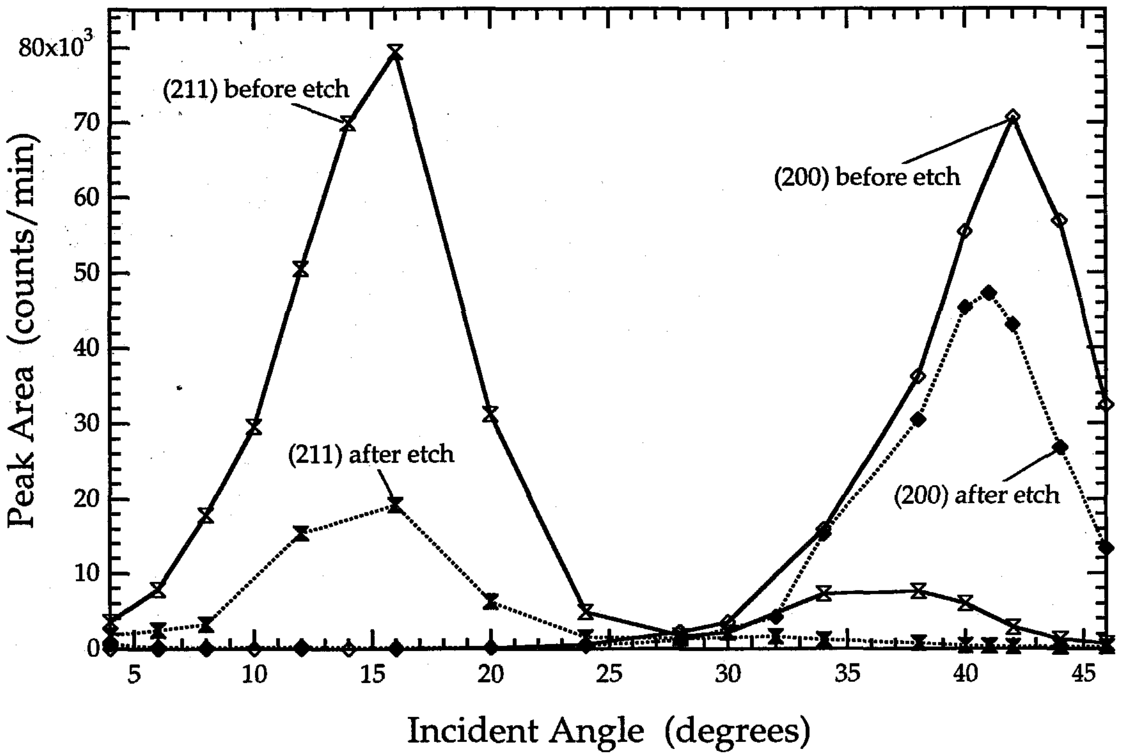

Figure 3.6 Crystallographic texture of the bcc ^{57}Fe NEN foil before and after etching. Only the two most prominent peaks are shown.

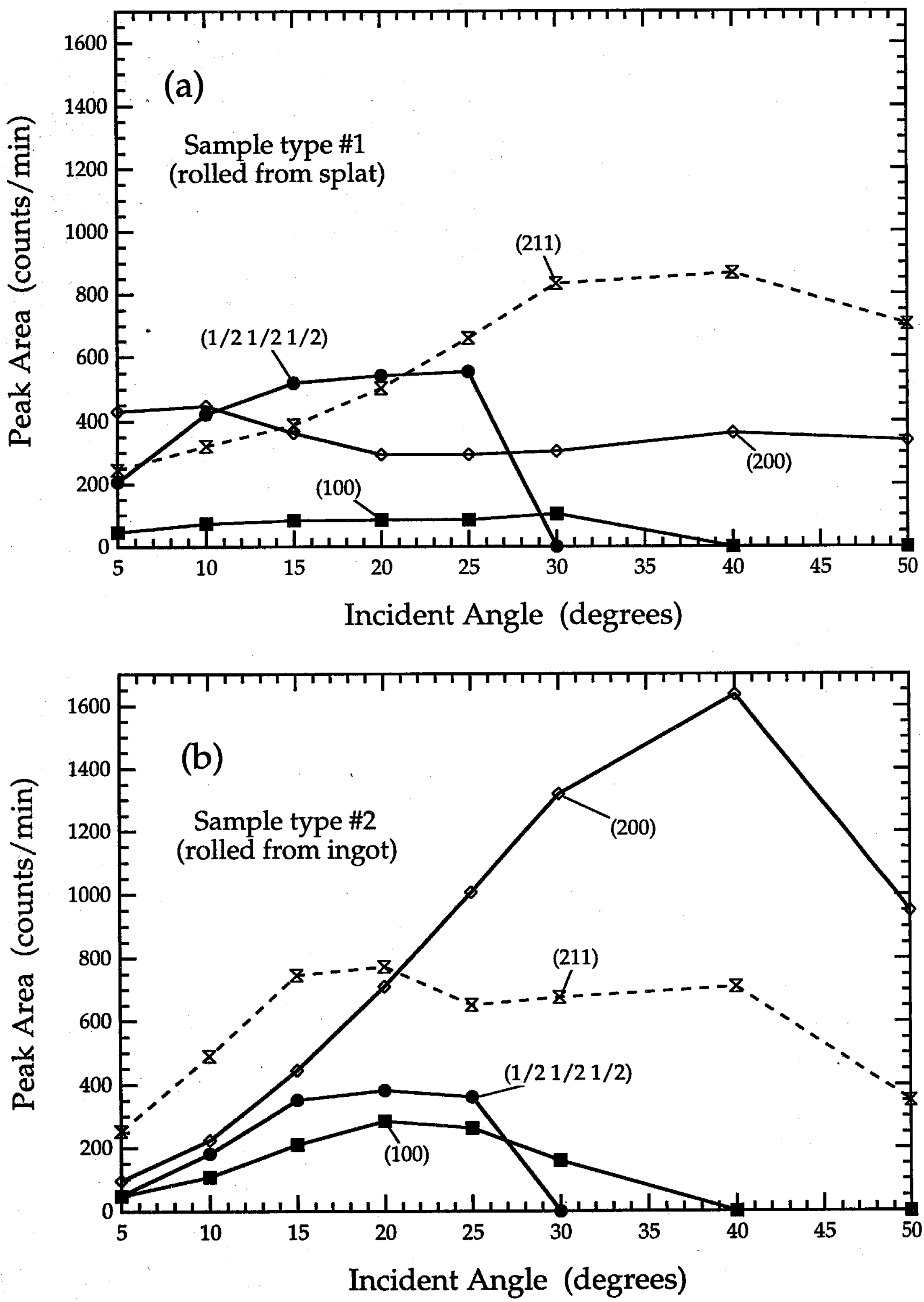

Figure 3.7 $^{57}Fe_3Al$ sample texture for both types of samples.

3.2.8 Sample holder

A mechanical support was needed to hold the samples in the goniometer. An ideal support would have low absorption and weak scattering. We tested a variety of sample supports to find one that gave minimal effects on the diffraction data. We chose 1/16 inch Plexiglas. For the foil samples, a thin layer of vacuum grease on top of the Plexiglas dropped the background counts considerably and also held the foil in place.

3.3 Photon sources

Radioactive ^{57}Co sources are used to provide 14.41 keV photons for our experiments. The ^{57}Co source has a half-life of 270 days; new sources must be purchased on a yearly basis for optimal results. Commercial sources include American, European, and Russian suppliers. Our main suppliers have been Amersham (UK-based) and NEN (New England Nuclear) Dupont.

Figures 3.8ab show decay schemes for ^{57}Co sources and the corresponding ^{57}Fe absorbers. The desired 14.41 keV photons account for only a small percentage of the photons that are incident upon the absorber. In a conventional transmission Mössbauer experiment, only the resonant absorption of the 14.41 keV photons is important. The subsequent decay of the excited states in the absorber is through the full 4π solid angle, with re-emission of the resonant photons accounting for ~10 % of those absorbed. Very few of the re-emitted 14.41 keV photons will enter the detector, so the absorption peaks of a transmission Mössbauer spectrum are representative of the actual absorption taking place in the sample.

Table 3.4 lists the photons of concern in our diffraction experiment. This list includes the photons of Fig. 3.8a plus those from source impurities and fluorescent x-rays from Pb scattering and the source matrix material. The 85 keV photons from the Pb fluorescence originate from the collimator and the shielding. Known radioactive impurities

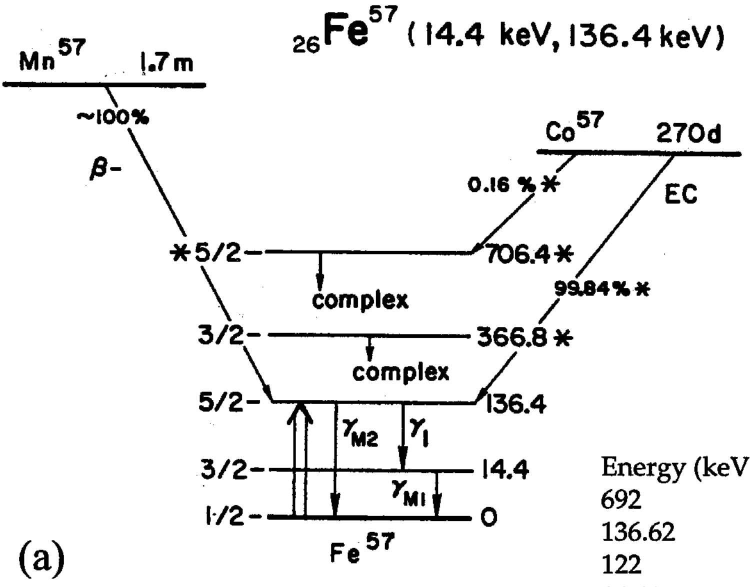

Ref. 10, p. 24

Energy (keV)	emitted	relative int.
692	0.16%	0.2
136.62	10.8%	13
122	85.5%	100
14.41	9.5%	11
6.5 (Fe Kα Xray)	~55%	65

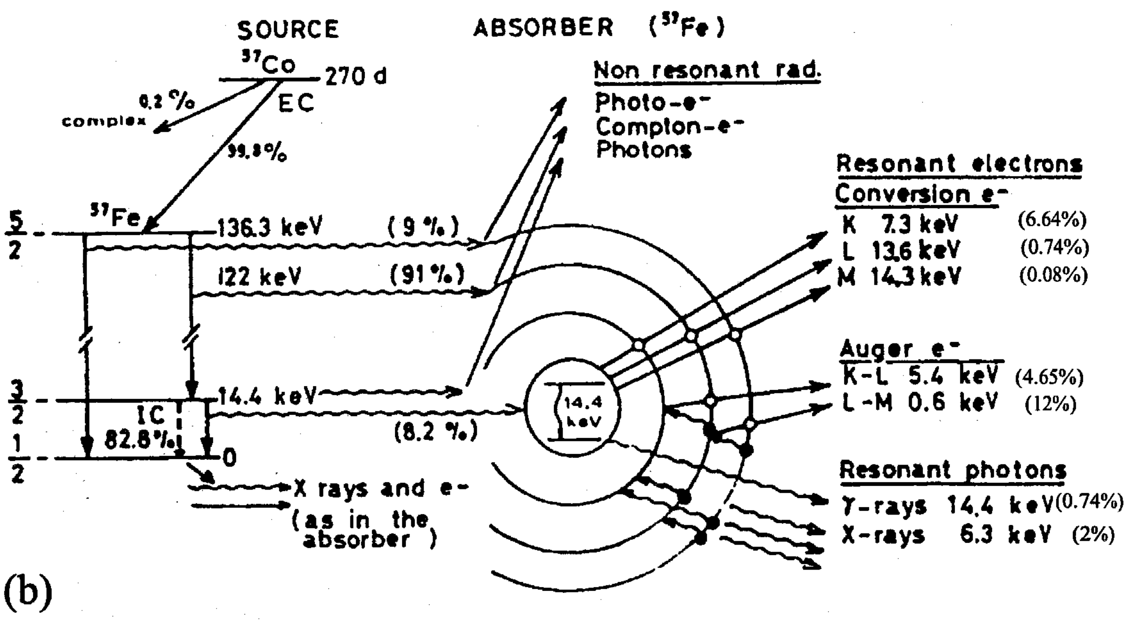

Ref. 11, p. 84

Figure 3.8 Decay schemes for (a) the ^{57}Co source and (b) the first excited state of the ^{57}Fe isotope.

produced in the source during fabrication include ^{58}Co and ^{60}Co. In a newly purchased source, 0.3% of the photons from the source come from these impurity isotopes. After 15 weeks, this decreases to 0.15% [5]. Because these impurities provide a relatively small percentage of photons and also because of the extremely low efficiency of the INEL detector at their high energies, the source impurities were not a serious concern in the experiment. Nevertheless, with so many undesirable photons incident on the specimen, it is clear that some energy discrimination of the detector pulses would be desirable.

Table 3.4 Expected photon energies [6] for a ^{57}Co source in a Rh matrix with collimation and sample.

Expected Radiation (in keV)	Origin	Comment
1173, 1332	^{60}Co	source impurity
811	^{58}Co	source impurity
692	^{57}Co	non-EC decay channel
136.32	^{57}Co	E2 transition
122	^{57}Co	pre-cursor to M1 transition
~85	Pb edge	fluorescence (shielding)
20.2	Rh x-rays	embedding matrix
14.41	^{57}Co	Mössbauer transition (M1)
6.4	Kα Fe x-rays	internal conversion decay

Figure 3.8b shows the emissions from the decay of the excited state of ^{57}Fe. Many ^{57}Fe Mössbauer spectroscopy experiments rely on products of the non-resonant decay channel, as they are more plentiful than the re-emitted 14.41 keV photons. One example is the conversion electron Mössbauer spectroscopy (CEMS) technique mentioned in § 2 and used as an analytical tool in § 3.2.6. Conversion electron Mössbauer spectroscopy uses the relatively plentiful (6.6% of the decaying ^{57}Co nuclei) K-shell conversion electrons to form backscatter Mössbauer spectra. Similarly, the very low energy (0.6 keV) Auger electrons (12%) and the 6.3 keV Fe Kα x-rays (2%) can be

detected to form backscatter spectra. In comparison, the 14.41 keV photons account for 0.74% of the decaying ^{57}Co nuclei.

The ^{57}Co source isotope is embedded in a matrix to provide a high recoil-free fraction during photon emission. The sources are made by diffusing the ^{57}Co into a foil of Rh metal. In practice, sources have a maximum radioisotope loading. If source loading exceeds 1 Ci/cm^2, there will be problems with line broadening due to self-absorption. These problems worsen as the source ages, as more of the ^{57}Co turns to ^{57}Fe. This effective maximum is 280 mCi for our source with a 6 mm diameter. Table 3.5 lists information on the sources used in the experiments. All sources had a linewidth of 0.11 mm/sec and a recoil-free fraction of 0.75.

Table 3.5 ^{57}Co sources used with the Mössbauer diffraction experiments.

Start Date	Start Activity	Supplier	Matrix	Active Diam.	Used With
5/18/90	54.0 mCi	Amersham	6 µm Rh	6 mm	pre-Fe91
8/14/91	44.5 mCi	NEN	12 µm Rh	3 mm	Fe91
5/26/93	45.6 mCi	Amersham	6 µm Rh	6 mm	Fe_3Al93
3/22/94	53.0 mCi	Amersham	6 µm Rh	6 mm	Fe_3Al94
2/17/95	145 mCi	Amersham	6 µm Rh	6 mm	Fe_3Al95

3.3.1 Source holder

The source foil was epoxied to a threaded Al block. The circular source was tilted by 60^0 with respect to the direction of the incident beam (see Fig. 3.2). The tilting gave a foreshortening of the source profile that provided a width of the incident beam that was half its height. By tilting the source we measured a 25% reduction in the width of the transmitted beam with respect to the untilted source. Improved intensity in the beam was also measured.

3.3.2 Velocity transducer

A Ranger Scientific MS-900 velocity transducer provided the Doppler shifts for the ^{57}Co source. The MS-900 drive controller allows the transducer to be operated in either constant acceleration mode or in a flyback mode that "zooms" into a narrow velocity range of interest. The MS-900 is interfaced to an Apple IIe computer. The velocity range is set by two controls: an offset that defines the start velocity of the scan and a scan range that sets the velocity window of interest.

The 1024 channel multichannel scalar/analyzer provides three functions for the Mössbauer diffraction experiment. First, the scalar provides the reference signal for the velocity waveform. Second, the scalar signal provides the synchronous router with the timing information necessary to collect diffraction patterns at different Doppler shifts. Third, the analyzer memory is used to collect Mössbauer transmission spectra necessary to set the velocity conditions and router control. This third function is used only when the transmitted beam is allowed into the INEL detector. The transmitted beam is normally blocked to suppress the detector background when acquiring Mössbauer diffraction patterns.

The following facts pertain to the operation of the MS-900:

(1) the sweep rate, or dwell time, per channel for all operations is 250 microseconds,
(2) all of the off-resonance data were acquired in constant acceleration mode,
(3) all of the on-resonance data were acquired in flyback mode,
(4) the on-resonance data were acquired with the best possible approximations to a constant velocity mode, and
(5) the drive response becomes increasingly nonlinear as the size of the velocity window is decreased.

Point (5) could be a serious problem, but the nonlinearity is highly repeatable and therefore correctable with a careful velocity calibration. Figure 3.14c shows this non-linearity in the ^{57}Fe sample. Figures 3.14ab show how the nonlinear velocity was mapped onto a linear velocity scale to provide a normal Mössbauer transmission spectrum. Appendix B describes the calibration procedure.

3.4 Detector and electronics

This section describes the INEL CPS-120 position sensitive detector, its original electronics, and our modifications to the electronics. Figures 3.1 through 3.3 should be consulted throughout.

3.4.1 Detector

An INEL (Instrumentation Électronique) CPS-120 large angle position sensitive detector (PSD) is the heart of our Mössbauer diffractometer. Along with its associated electronics, the INEL detector provides the ability to simultaneously collect diffraction data over a 120 degree, one-dimensional arc with a spatial resolution of 0.03 degrees. When used as part of an x-ray powder diffraction system, data acquisition can sometimes be performed in only a few minutes, compared to hours for more traditional scanning θ-2θ diffractometers. The detector system uses a Debye-Scherrer geometry common to powder diffraction with old film cameras, with the PSD taking the place of the camera film [7]. The incident angle of the photon beam with respect to the plane of the sample, ϕ, is fixed, and data are collected simultaneously over the entire 120 degree range of the detector. Figure 3.3 shows this geometry. This geometry differs from that of a normal Bragg-Brentano x-ray powder diffractometer, where the sample is placed at an incident angle of θ and a detector intercepts a small range around the angle 2θ. The INEL Debye-Scherrer system provides diffraction intensities different from those of a Bragg-Brentano diffractometer owing to differences in its geometry [8].

Figures 3.9abc show three sets of diffraction patterns from a powdered Si standard. All data are from x-ray scattering only. These patterns provide an interesting

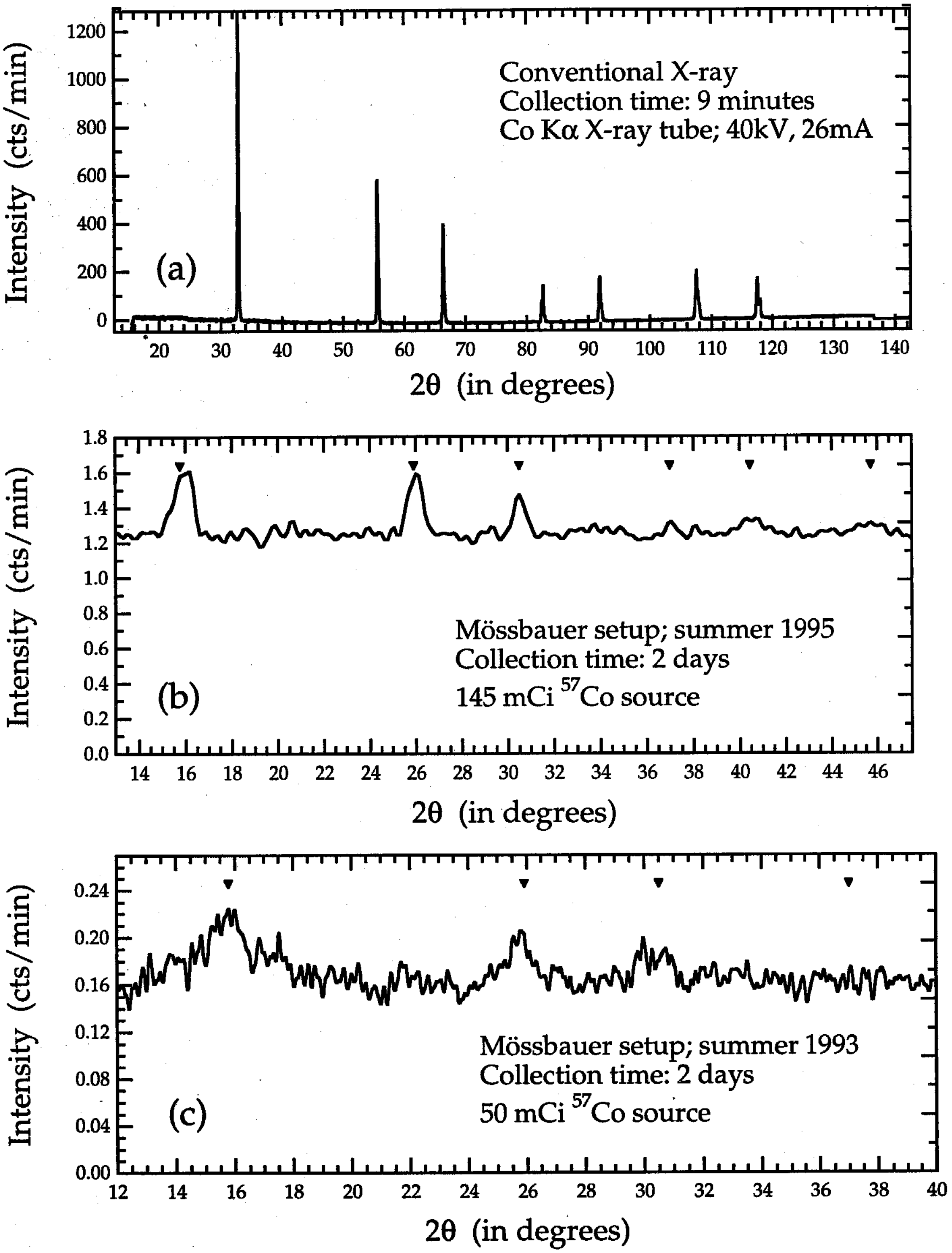

Figure 3.9 Si standard calibration files for a conventional x-ray diffractometer and the Mössbauer diffractometer.

comparison of the normal operation of the INEL system with a sealed x-ray tube source operated at 1040 W versus the Mössbauer setup with radioisotope sources.

Figure 3.10 shows a cross section of the CPS-120 detector. Photons enter the detector through a Mylar window and are absorbed in an 8 mm distance. The detector is operated at a high bias voltage of 9.3 kV. The gas ions provide a current to the positively-charged cathode readout strips. The approximately 500 cathode readout strips are linked together with capacitors and inductors to form a delay line, which delivers the signal to both ends of the detector. The full line has a 1.2 μsec delay, which sets the maximum rate of data acquisition. The detector signals are amplified by matched preamplifiers and sent to the rest of the electronics for time-to-voltage conversion.

The detector operates in a "self-quenching streamer" mode, which provides good spatial resolution but poor energy resolution. Unfortunately, operating the detector as a gas-filled proportional counter, which would provide better energy resolution, delivers poor spatial resolution [9].

The detector operates with a high pressure (6.2 bar) of noble gas to provide the ionization efficiency of the detector. The gas mixture includes 15% ethane as a quench gas with a noble gas balance. Since the gas flows continuously through the detector, Ar is preferred for cost reasons over Kr (3x the cost of Ar) or Xe (15x the cost of Ar). Table 3.6 shows the absorption efficiencies of the noble gases used. Krypton would normally be preferred over Ar because of its larger absorption cross section. Unfortunately, commercially available Kr gas contains a radioactive isotope (^{85}Kr), which generates additional noise in the detector. We tried using an $Ar_{0.9}Kr_{0.1}$ mixture to increase efficiency while limiting cost. The signal increased by the expected factor (> 2), but the background noise unfortunately increased by a factor of 3.25. Thus, further work with the Kr-based gas was discontinued. Matheson Gas is our primary supplier. The ethane is "CP grade"; the argon is "Matheson purity."

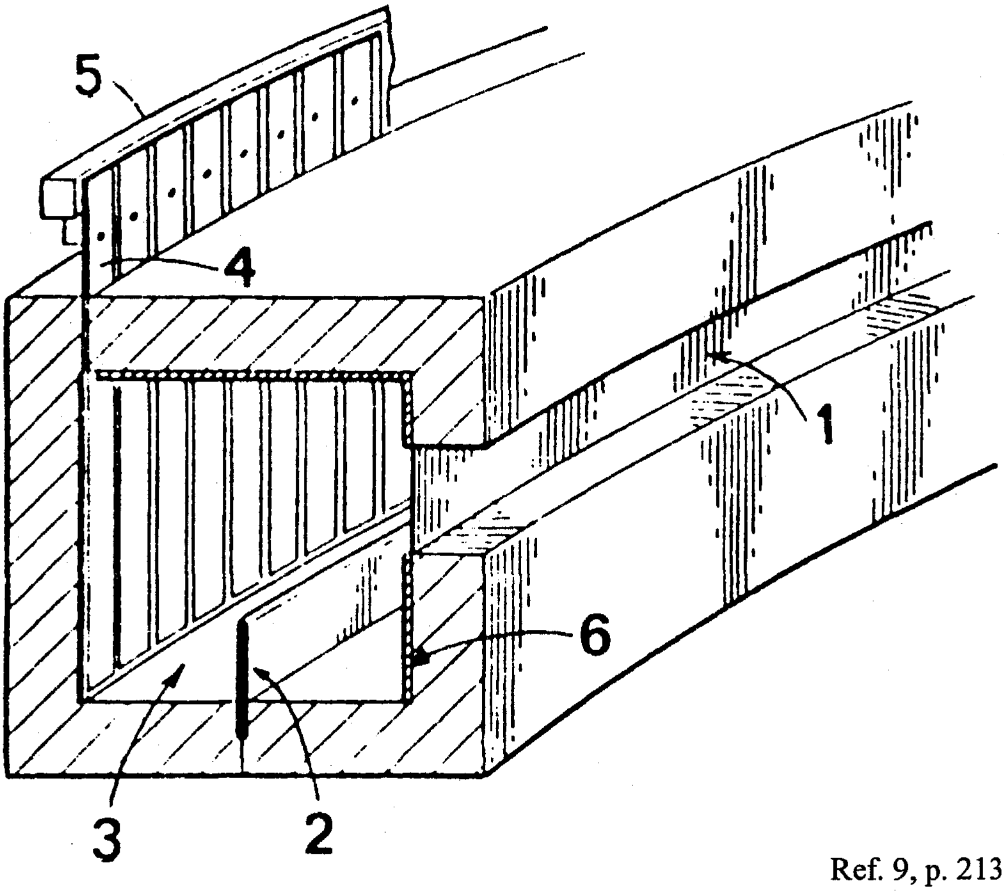

Ref. 9, p. 213

Figure 3.10 Cross section of INEL Detector.

1) Entrance Window
2) Anode blade
3) Gas volume
4) Cathode readout strip
5) Delay line
6) Other cathode electrode

The ambient noise of the detector is quite low: 3.5 Hz over the entire detector with no external photon source present. This is the equivalent of 0.153 cts/(mCi·hr·deg) over the 120 degree detector.

Table 3.6 Calculated absorption efficiencies of the INEL detector.

Energy (keV)	100% Ar	90% Ar, 10% Kr	100% Kr
6.4	79.85%	81.90%	93.12%
14.41	14.72%	35.57%	94.83%
20.2	5.57%	12.42%	55.51%
85	0.17%	0.31%	1.56%
122	0.12%	0.17%	0.65%

3.4.2 Detector electronics

This subsection briefly describes the electronics which process the signals received from the detector. Please refer to Fig 3.3. The two signals from the preamplifiers are sent to a pair of analog pulse discriminators (APD), which shape the signals for better position resolution. One of the signals is then sent directly to the start channel of the position sensitive processor (PSP), while the other signal goes through a digital delay line (DDL) before arriving at the stop channel of the PSP. The DDL is necessary to ensure that the stop signal always arrives after the start signal. The PSP is a time-to-amplitude converter (TAC); it creates a single pulse (0 to 10 V) which is proportional to the time difference between the start and stop signals. The amplitude of the PSP output pulse is thus directly related to the detector position where the event occurred. The PSP output pulse is sent to an analog to digital converter (ADC), a Silena 7423/UHS, which is directly linked to a memory buffer, a Silena 7328/S. The ADC/memory buffer combination acts as a multichannel analyzer (MCA); the analog PSP pulse is converted and stored in the proper MCA address. The ADC provides 13 bits of resolution with a conversion time of 3 microseconds. As the counts accumulate, a diffraction pattern is formed and stored in the memory buffer. The memory buffer contains its own microprocessor and memory, allowing the controlling computer to be free for other work. Our modifications to the MCA are described in § 3.4.3.

The data in the memory buffer are retrieved through an IEEE-488 interface to a Macintosh IIci computer. The computer uses the program Igor Pro with a custom Igor external operation program (XOP) to control the MCA functions. The retrieved data are then stored on the computer for analysis.

3.4.3 Synchronous router

Chemical environment selective Mössbauer diffraction experiments require that different diffraction patterns are acquired in synchronization with the Doppler drive. Ideally, each diffraction pattern would be collected at only one velocity. However, the MS-900 drive was unable to select a velocity range less than three linewidths wide. This did prove advantageous, however, in identifying the velocity range from the spectrum itself. An electronic means for routing the detector signals is used to compensate. Diffraction patterns corresponding the different sub-intervals of velocity were routed to different memory buffers, so several different diffraction patterns were collected simultaneously.

The synchronous memory gate/router is shown in Fig 3.3. The gating works by controlling the MCA of the INEL with output from the MCS (multichannel scaler) of the Ranger MS-900 drive controller. As the Ranger cycles through the velocity ranges, it advances the MCS as previously described in § 3.3.2. We tap the MCS address lines and run them to a homemade router box, which compares the current MCS value to preset numbers, configured via hardware switches. When the number of the MCS address matches that of the switches, a signal is sent to a counter chip, advancing the current number in the chip and changing its output value. The counter chip output consists of three TTL output signals, which are buffered and sent to the MCA of the INEL. Figures 3.11

and 3.12 show the gating board and its logic design. The MCA of the INEL provides an 8K (13 bits) buffer to store the data. We modified the MCA to pass the lowest 10 bits as diffraction data, reserving the three most significant address lines as a means of receiving routing signals from the gating box. Thus, up to eight different diffraction patterns corresponding to energy regions chosen by the gating box can be stored in the 8K buffer simultaneously. Using eight 1K diffraction patterns raises the minimum angular resolution to 0.12 degrees, but this is not a problem because the diffraction peaks are much wider than this.

The eight memory locations that correspond to the different velocity regions will be referred to as "bins." Each bin holds one diffraction pattern; each pattern is a single component of the acquired data. The component diffraction patterns and their corresponding memory locations are labeled by the tags "bin#," where # ranges from 1 to 8. Not all of the eight component diffraction patterns are useful. Memory bin1 and bin8, the first and last, were set to receive diffraction information at undesirable times, when the drive was making large changes in velocity. Each of the three resonance conditions (0Al, 4Al, and off) required additional bins to store undesired data outside of the desired velocity regions.

Figure 3.13 shows the settings for the velocity bins used for acquiring off-resonance diffraction patterns from bcc ^{57}Fe for the Fe95 data set. Good off-resonance diffraction patterns were collected in bin2, bin4, bin5, and bin7. These bins lie at least 10Γ (FWHM) away from the center of the closest Mössbauer absorption peak, so any peaks seen in the diffraction pattern are from x-ray scattering only. Figures 3.14abc show the on-resonance conditions for the Fe95 (^{57}Fe) data. Figure 3.14a shows the raw data, the peaks fitted to the data, and the gating bins. The raw and fitted data were obtained in a normal transmission run acquired by allowing the transmitted beam to enter the detector. Figure 3.14b is an enlargement of Fig. 3.14a. Absorption peak 6 is sampled by bin2, bin3, bin4, and bin5, while peak 1 is sampled by bin7. The asymmetric placement of bin7 over its

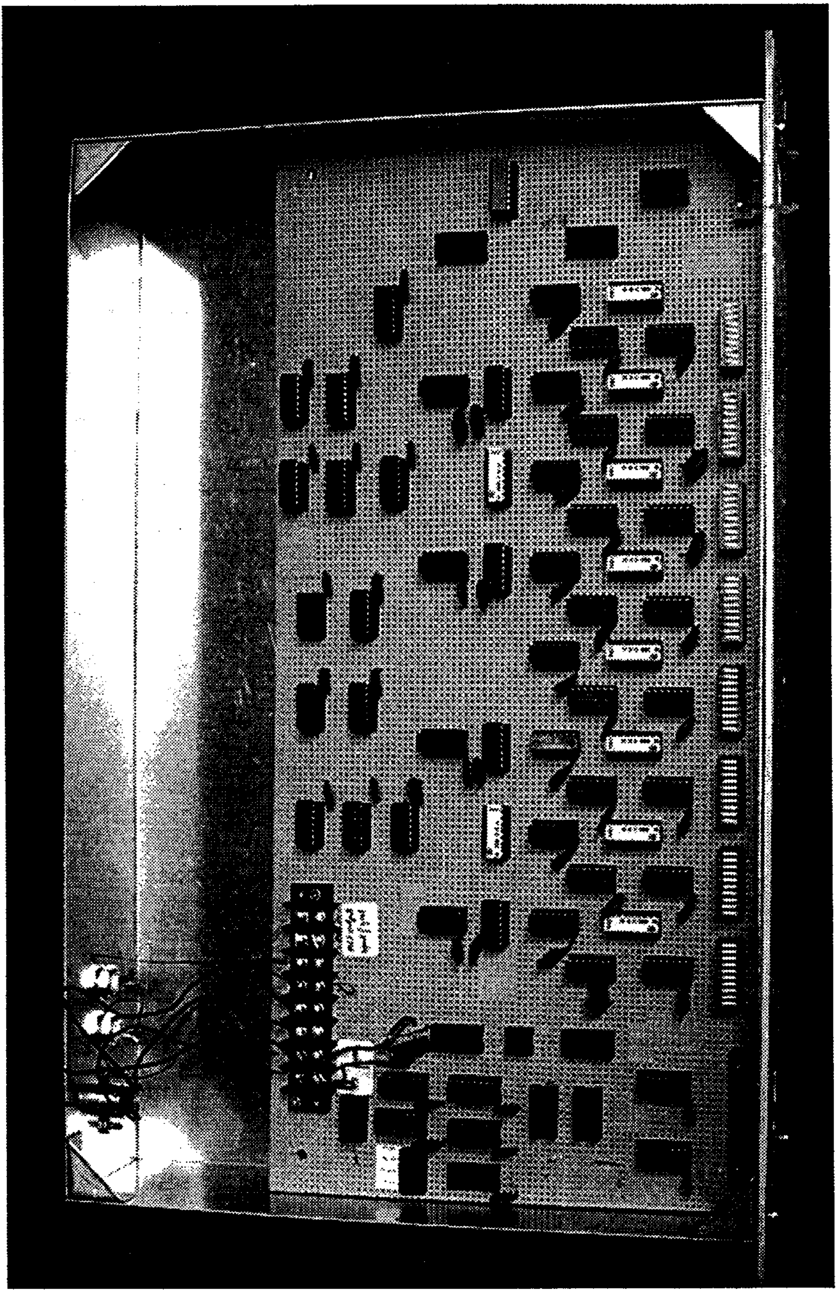

Figure 3.11 The synchronous router.

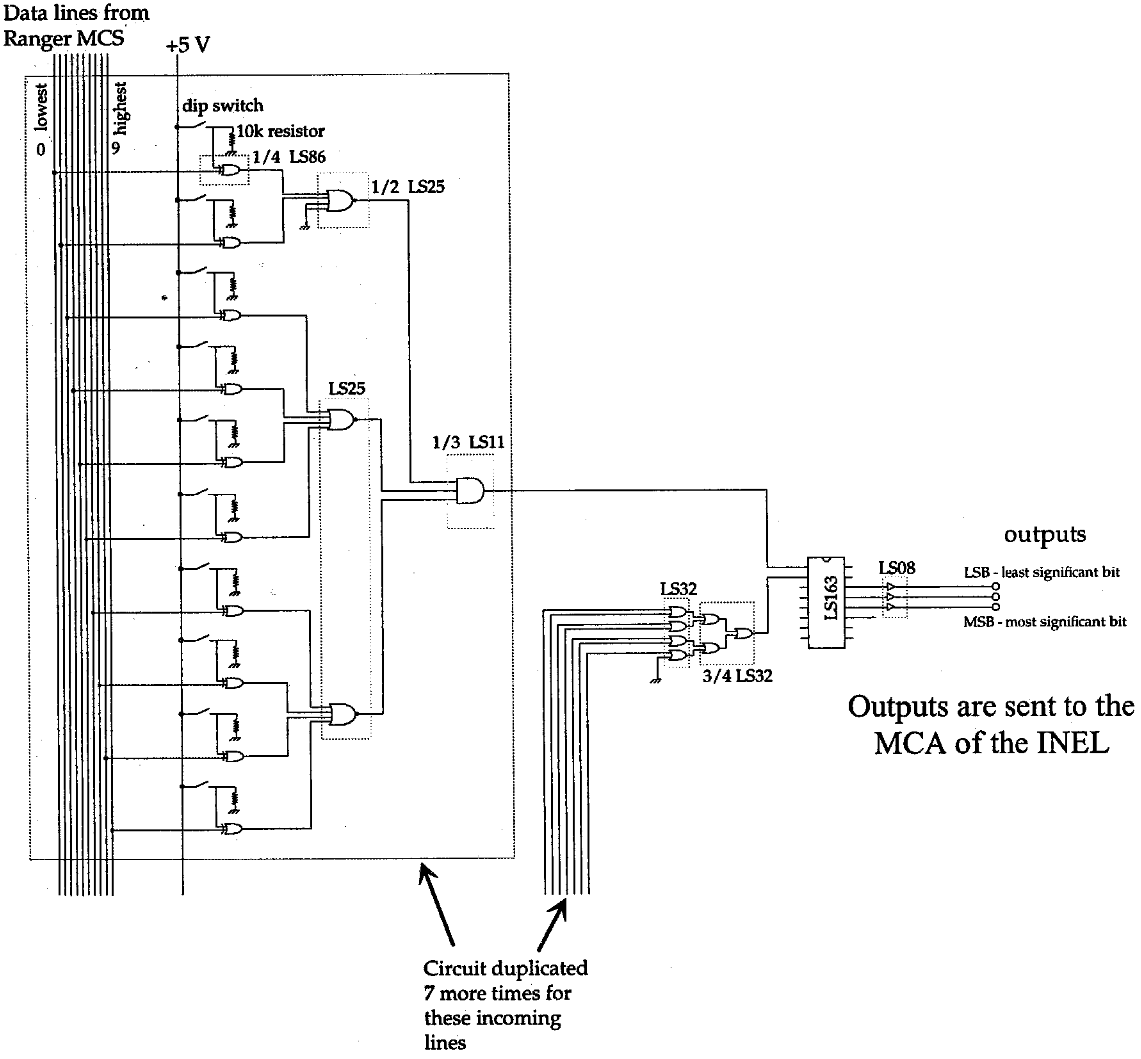

Outputs are sent to the MCA of the INEL

Circuit duplicated 7 more times for these incoming lines

Figure 3.12 Basic logic and schematic diagram of the synchronous router.

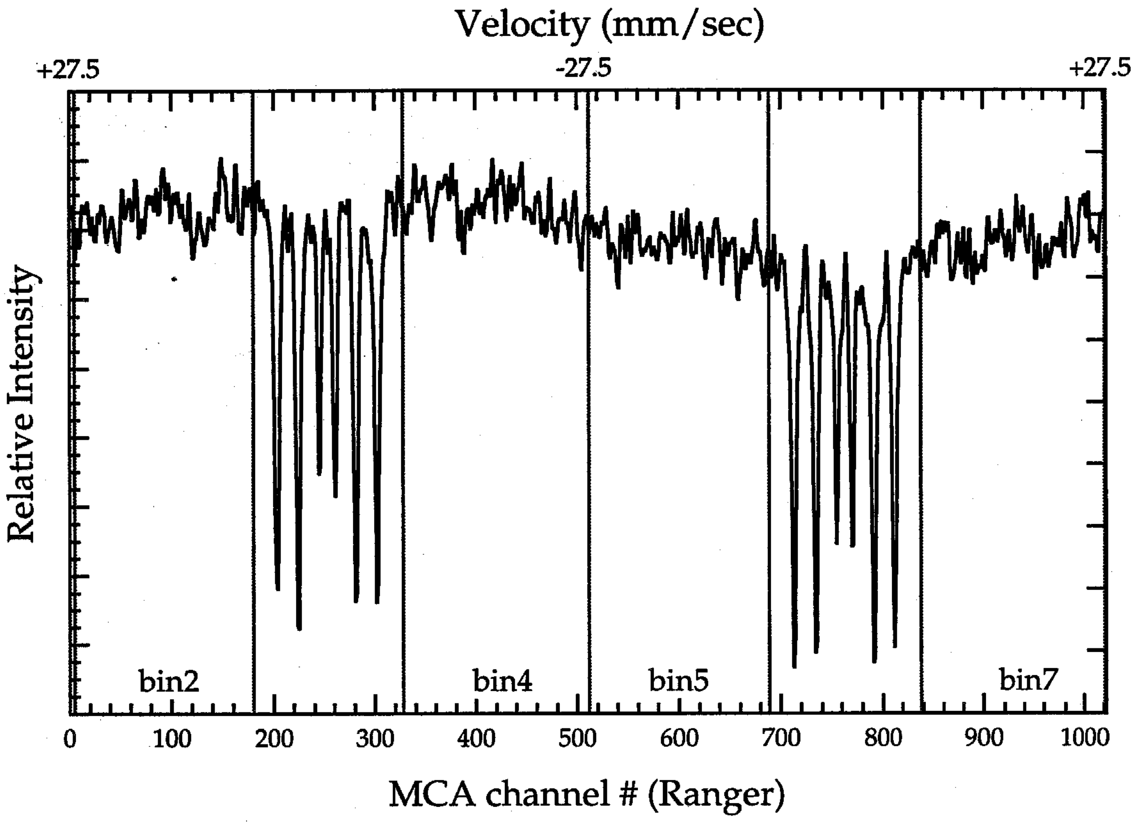

Figure 3.13 ^{57}Fe Mössbauer energy spectra for the off-resonance velocity conditions shown. The "bin#" (where # = 1 to 8) tags indicate which memory location will store the respective diffraction pattern.

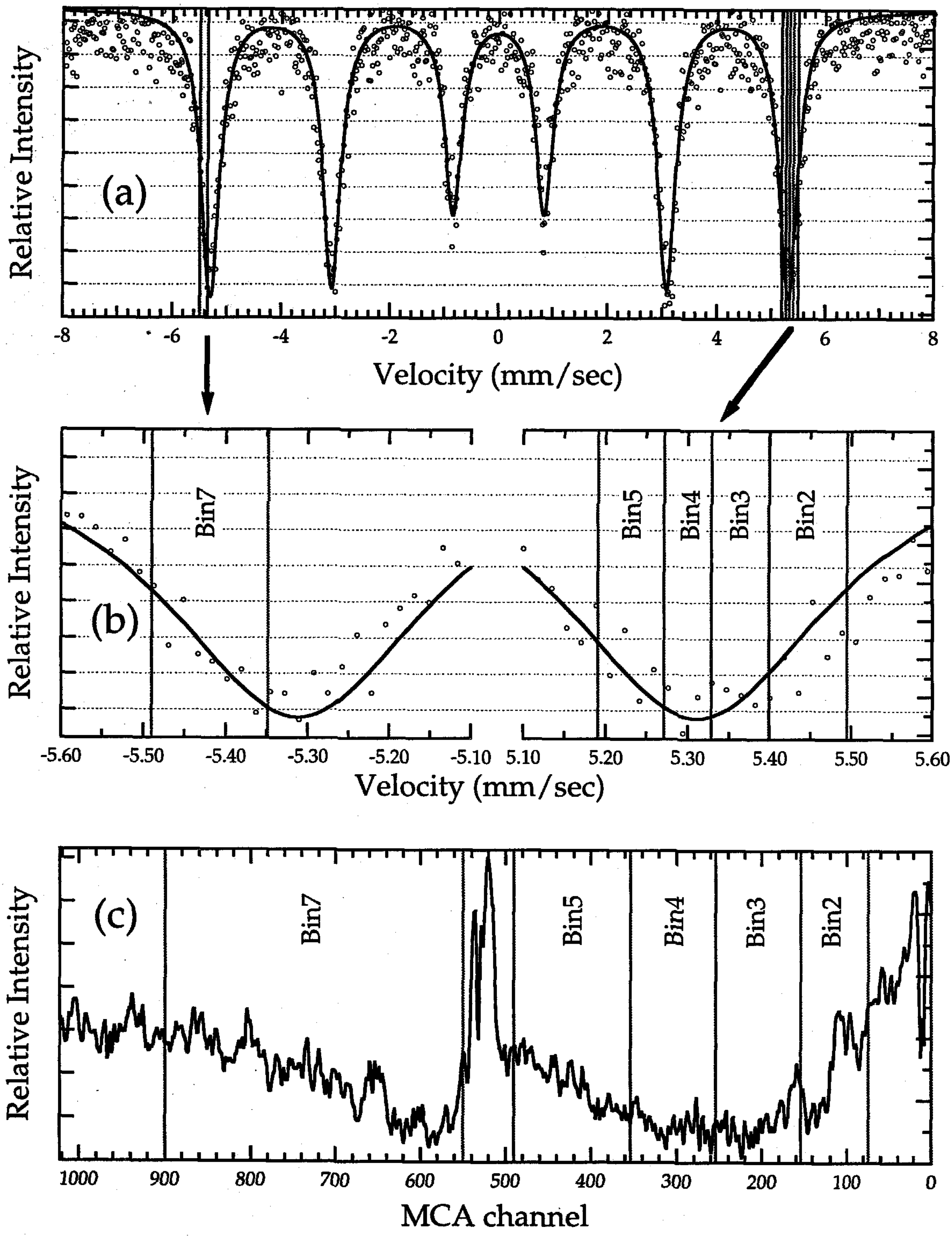

Figure 3.14 ^{57}Fe Mössbauer energy spectra for the on-resonance gating conditions shown. The text explains the three graphs.

absorption peak caused bin7 to be sacrificed to improve the velocity ranges in the other four useful bins. Figure 3.14c shows the actual Mössbauer transmission data acquired and used to set the positions of the bins. As mentioned in § 3.3.2, the drive response is non-linear but repeatable.

Figures 3.15ab show the $^{57}Fe_3Al$ velocity conditions. Figure 3.15a shows the raw data for a normal transmission run. The velocity bins for both the 0Al and 4Al resonance conditions are labeled and shown in their actual locations. Figure 3.15b shows the off-resonance velocity bins used with the $^{57}Fe_3Al$ samples. Figures 3.16ab provide an enlarged view of the two on-resonance conditions for $^{57}Fe_3Al$ samples. Both figures show the individual sextet environments as well as their sum. The five sextets are the result of fit to the raw data by the method of LeCäer and Dubois (see § 3.2.6), and they correspond to the Gaussian peaks fit to the HMF distributions of Fig. 3.5c. The summed trace is the solid black line; the 0Al sextet, the small dash line; the 4Al sextet, the large dash line; and the 2Al, 3Al, and 5Al sextets, the solid gray lines. The implications of the overlap between these different absorption peaks will be explored in § 5.

3.4.4 Detector placement

Before the collection of the final data set, $Fe_3Al95v2$, the INEL detector was moved closer to the sample to capture a larger solid angle and increase the number of detected photons. Figure 3.17 shows the new position of the detector. The detector was moved along its center line from 250 mm (detection chamber to goniometer center distance) to 125 mm. The shielding around the sample had to be reduced to accommodate the detector, but the increased background occurred primarily in an unimportant region of the detector. However, other problems were observed and are discussed in § 4.4.

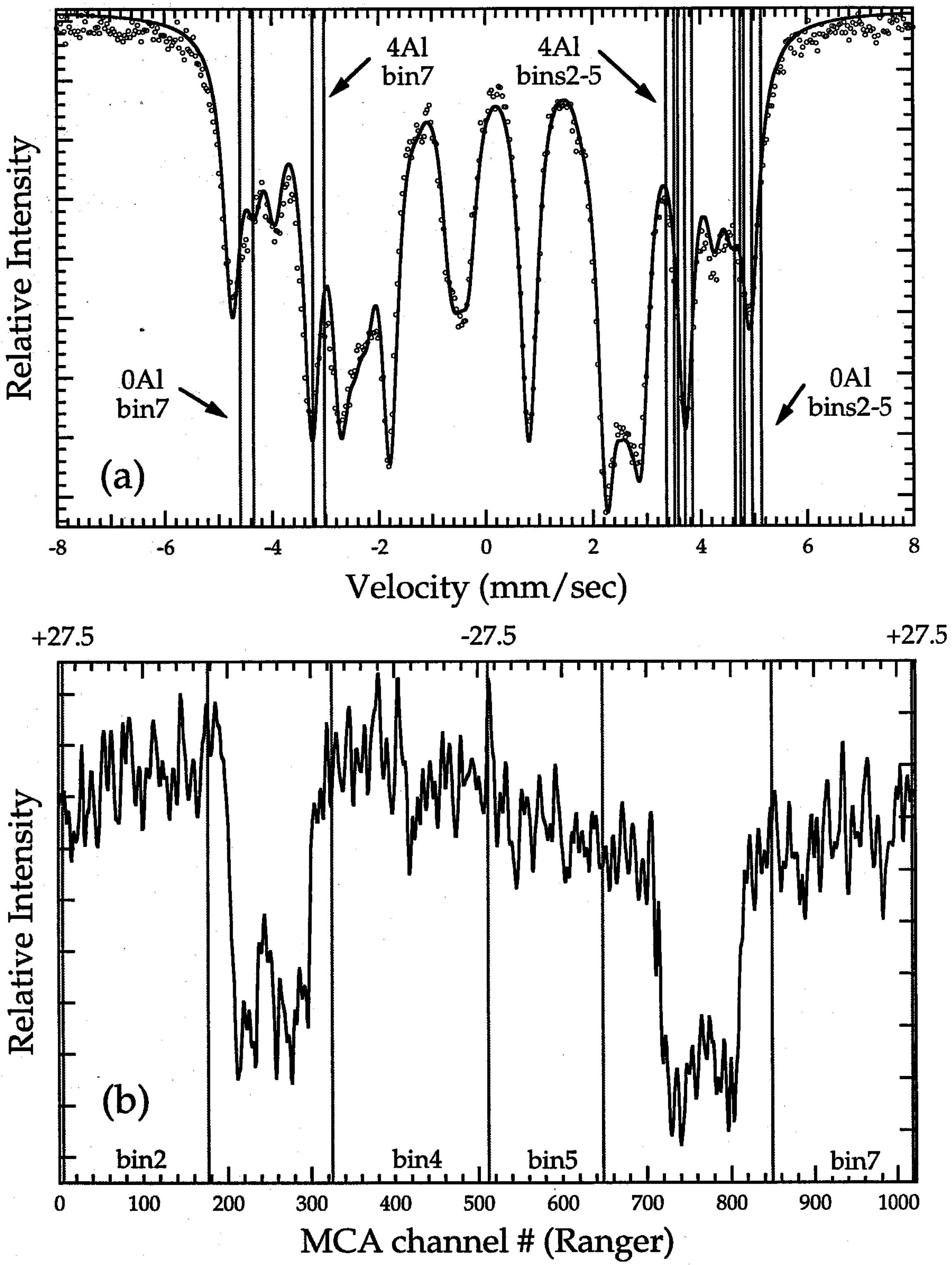

Figure 3.15 $^{57}Fe_3Al$ Mössbauer energy spectra for both the (a) on- and (b) off-resonance gating conditions.

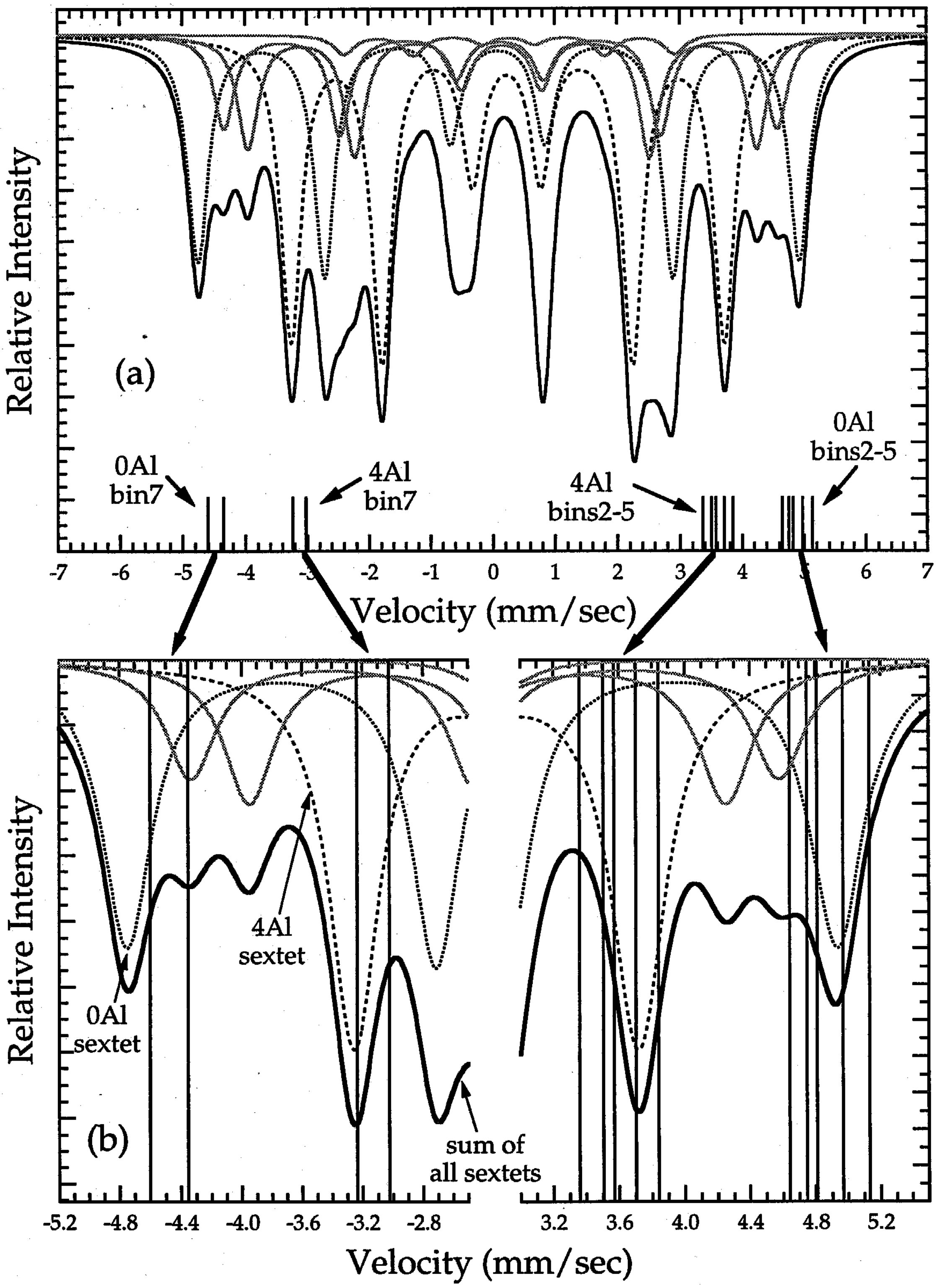

Figure 3.16 $^{57}Fe_3Al$ Mössbauer energy spectra for the on-resonance conditions. The traces shown are the modelled fits to the real sample. All five sextets are shown along with their sum.

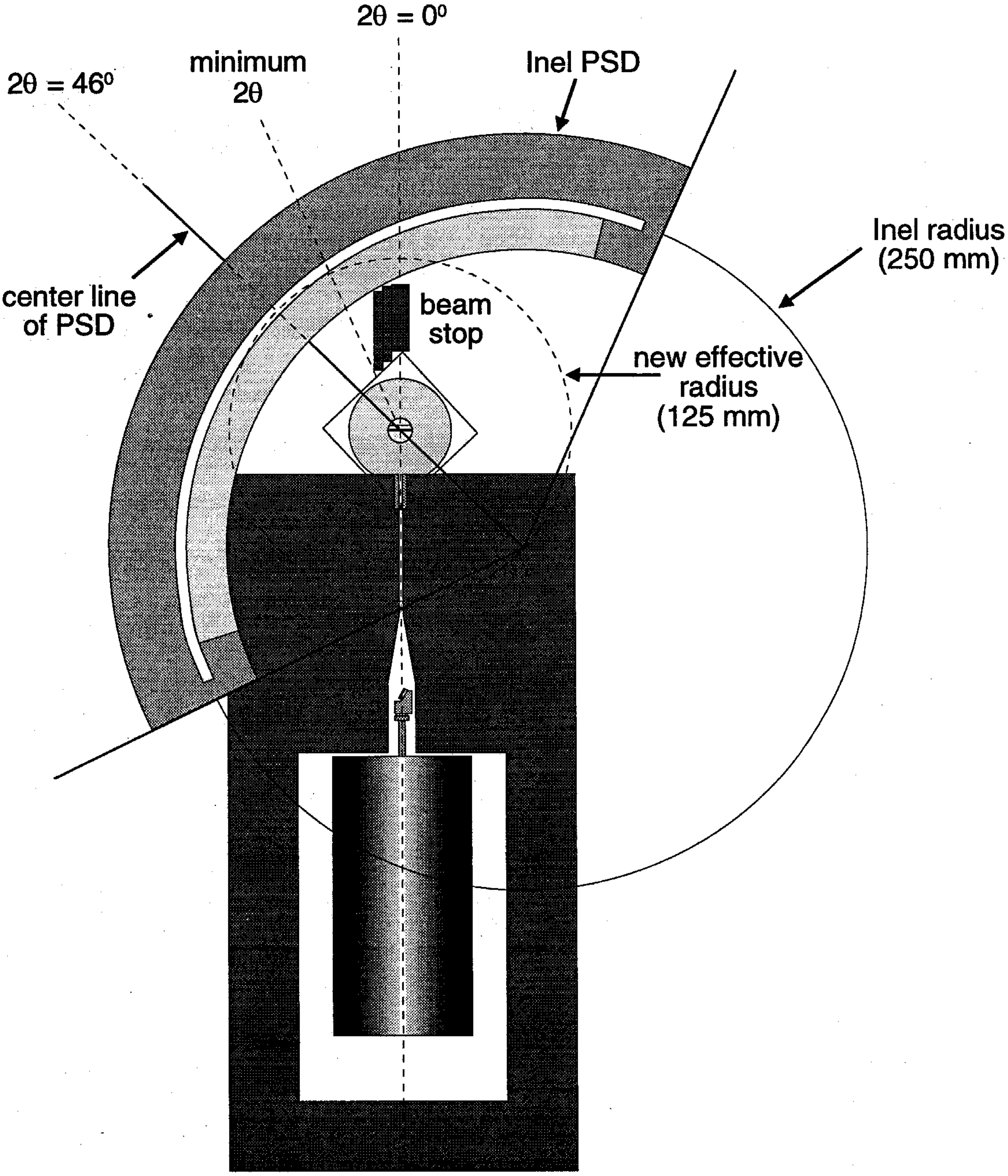

Figure 3.17 Change of the INEL detector position for the $Fe_3Al95v2$ ($^{57}Fe_3Al$) data set. The effective radius of the detector was changed from 250 mm to 125 mm.

3.5 Collimator and shielding

The Pb collimator being used is shown in Fig. 3.18. It was precision milled from solid Pb bricks. The collimator is lined with Al plates to suppress some Pb fluorescence. The collimator provides an incident beam of $\sim 1^0$ in width. Figure 3.1 shows overhead photographs of the INEL detector and collimator arrangement. The large amount of Pb on the sides of the collimator effectively screens the detector from all stray radiation from the source. Please note that additional Pb, in the form of thin bricks and sheets, is normally placed above the collimator and drive to reduce the radiation hazard to users of the system.

The beam transmitted directly through the sample was blocked from entering the detector. We found that the beam block removed much background in the data. The shape of the beam block was found to be important, as scattering from the block can be a substantial part of the detector background. For example, the stray photon background was reduced by more than a factor of three (from 7.1 to 2.3 Hz) between collecting the Fe95 data set and the Fe_3Al95 data set by simply reshaping the beam block. The reshaping involved creating a staggered-edge to the Pb block to prevent the front edge of the block from scattering into the rest of the detector. Figures 3.2 and 3.17 show the beam blocks used while acquiring the Fe_3Al95 and $Fe_3Al95v2$ data sets, respectively.

Sample's view of the source

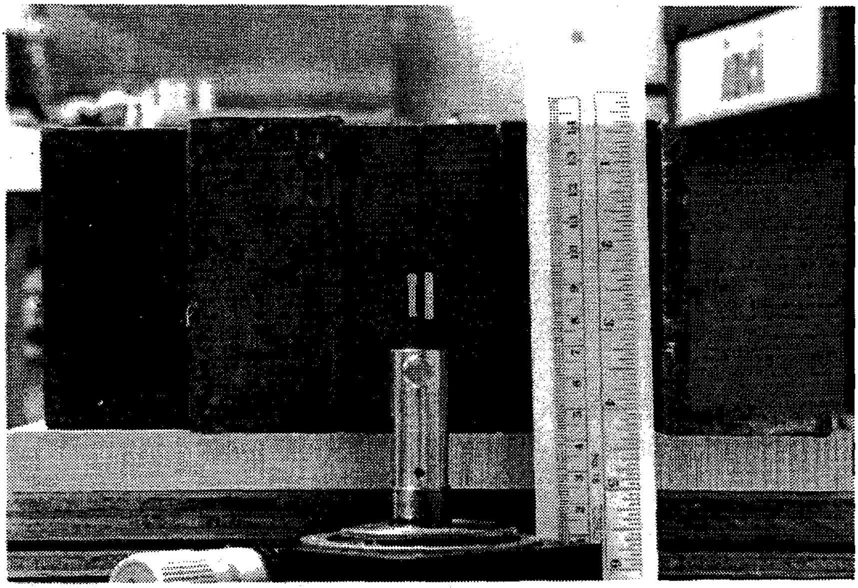

Source's view of the sample

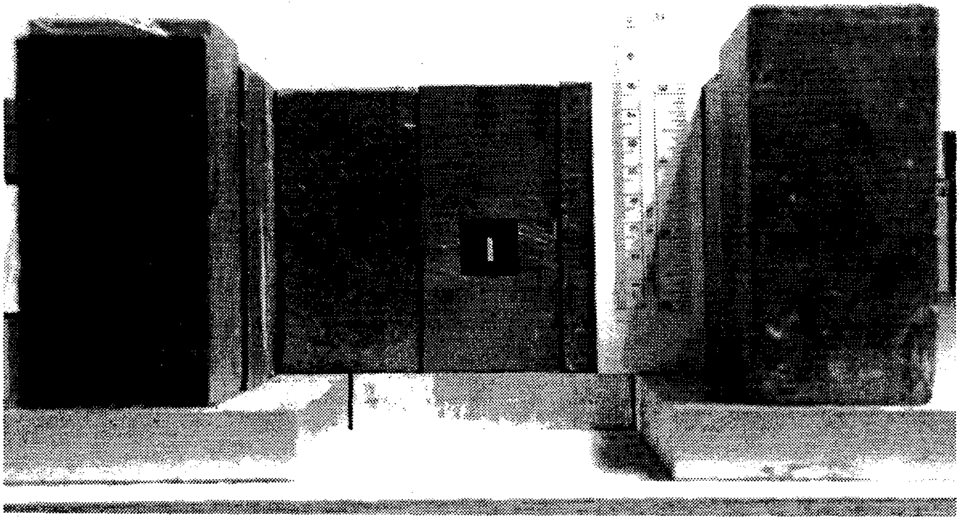

Figure 3.18 Front and back views of the Pb collimator.

References, Chapter 3

[1] G. LeCaer and J.M. Dubois, J. Phys. E: Sci. Instrum. **12**, 1083 (1979).

[2] W.H. Beyer, *CRC Standard Mathematical Tables* (CRC Press, Boca Raton, FL, 1978), 25th edition, p. 525.

[3] G.Y. Chin, in *Metals Handbook*, edited by T. Lyman *et al.*, (American Society for Metals, Metals Park, OH, 1973), Vol. 8, 8th edition, p. 229.

[4] K. Yvon, W. Jeitschko, and E. Parthe, computer code Lazy Pulverix, Laboratory of X-ray Crystallography, University of Geneva, Geneva, Switzerland, 1989.

[5] Amersham technical support (private communication).

[6] R.L. Heath, in *CRC Handbook of Chemistry & Physics*, edited by R.C. Weast (CRC Press, Boca Raton, FL, 1978), 64th edition, p. B-232.

[7] H.P. Klug and L.E. Alexander, *X-ray Diffraction Procedures (for Polycrystalline and Amorphous Materials)*, (Wiley-Interscience, New York, 1974), 2nd edition, p. 177.

[8] Z.Q. Gao and B. Fultz (unpublished).

[9] J. Ballon, V. Comparat, and J. Pouxe, Nucl. Instrum. Methods 217, 213 (1983).

[10] A.H. Muir, K.J. Ando, and H.M. Coogan, *Mössbauer Effect Data Index, 1958-1965* (Interscience, New York, 1967).

[11] J.R. Gancedo, M. Gracia, and J.F. Marco, Hyperfine Inter. **66**, 83 (1991).

Chapter 4 The experimental data

Chapter 4 presents the experimental data collected with the equipment described in chapter 3. As the equipment and data collection techniques have improved, so has the data. While the earlier data sets are interesting, as they show a continuing level of improvement, emphasis will be on the most recent data.

Chapter 4 is subdivided into five sections. Section 4.1 describes the nomenclature for distinguishing the data sets from each other. Section 4.2 describes the techniques of data collection and manipulation. Sections 4.3 and 4.4 describe data from the $^{57}Fe_3Al$ samples and demonstrate how the data proves chemical environment selectivity. Section 4.5 presents data on ^{57}Fe and uses it to explain the improvements in our experimental technique.

4.1 Data set nomenclature

A total of two ^{57}Fe and four $^{57}Fe_3Al$ data sets were collected. This section provides their nomenclature. The $^{57}Fe_3Al$ sets use the letters <u>Fe_3Al</u> as a prefix; the ^{57}Fe sets, <u>Fe</u>. The numbers in the names indicate the year when collection started for the data set. The most important of these sets are:

(1) Fe_3Al95	$^{57}Fe_3Al$ data set collected using the 145 mCi source; fully described in § 4.3,
(2) $Fe_3Al95v2$	a repeat of Fe_3Al95 with the INEL detector moved closer to the sample, fully described in § 4.4, and
(3) Fe95	the best ^{57}Fe data set to date; fully described in § 4.5.

The older data sets can be found in Appendix C, but comments will be made on them in this chapter as appropriate. They are:

(4) Fe91	the first good ^{57}Fe data set; acquired with a simple electronic gate,
(5) Fe_3Al93	the first $^{57}Fe_3Al$ data set; the milled collimator was introduced, and
(6) Fe_3Al94	the second $^{57}Fe_3Al$ data set; the synchronous router was used.

4.2 Data acquisition and manipulation

This section describes the techniques used to acquire and process the data. As the signal to noise ratio (S/N) of the diffraction peaks is low, all of the efforts to collect and process the data have been to improve this important ratio. While most of the improvement has been caused by stronger sources and better hardware, the importance of the data processing should not be overlooked.

4.2.1 Noise

The noise comes primarily from three sources: (1) random detector discharges, (2) background from non-14.41 keV photons from the radioisotope source, and (3) sensitivity variations across the INEL detector. Sensitivity variations across the INEL detector do not cause real noise, but their shape can lead to the appearance of spurious peaks, and are thus included in this discussion.

The noise caused by random detector discharges is due to ambient room radiation (cosmic gamma-rays, isotopes in building materials, etc.) and electrical breakdowns in the detector gas (caused by dust and other particles in the gas). This type of ambient noise is the hardest to control. We observed that the level of noise is intrinsically linked to the high voltage bias of the detector. Unfortunately, decreasing the high voltage on the detector decreases not only the noise but also the useful signal sensitivity. In addition, detector shielding did not completely remove the ambient background. Fortunately, the INEL detector is very "quiet," with a background of ~2 to 5 Hz over the entire detector. In a series of test trials, we optimized the detector bias at 9.3 kV, which provided the best S/N (the ambient background is ~3.5 Hz at this setting). Unfortunately, this level of noise is still much higher than we would like.

The noise caused by the non-14.41 keV photons from ^{57}Co source would not present a problem if the INEL had better capabilities for electronic energy discrimination. To help compensate for this deficiency, we used an Al filter in front of the detector to suppress 6 keV x-rays from the sample, resulting in a 99% reduction in their intensity. We also found that the judicious use of shielding made an important improvement in the background from stray radiation from the radioisotope source. Nevertheless, even with the strong 145 mCi source used for collecting the 1995 data sets, the noise in the area of the diffraction peaks was comparable to the ambient noise level from random discharges.

The sensitivity variations across the INEL detector cause the same number of photons in two different areas of the detector to register as slightly different numbers of events. Thus, the background of the detector is not flat, but instead varies up and down with periods of several data channels. It is possible to mistake these modulations for weak diffraction peaks. The reasons for the sensitivity variations are not known. Fortunately, since the sensitivity variations are reproducible, these problems can be removed as detailed below.

4.2.2 Factors and conditions affecting data collection

Several factors are necessary to consider when collecting data. These include:

(1) sample choice and incident angle (which affects the intensity of diffraction peaks owing to sample texture),
(2) detector background and position (used to remove detector gain variations and isolated bad points),
(3) velocity range of the transducer (used to achieve the desired resonance conditions),

(4) synchronous router operation (used to collect data from particular resonance conditions), and
(5) blocking or passing the transmitted beam into the detector (passing increases background noise at low angles).

The choice of incident angle may be used to exploit the crystallographic texture of the sample to favor certain diffraction peaks over others. However, varying the incident angle slightly (a degree or so) between different data collection runs helps to ensure that any individual large crystallites within the sample do not improperly skew the intensities. In the case of the Fe_3Al95 and Fe_3Al93 data sets, both types of samples (rolled from splat and rolled from ingot) were used, and the results summed for at least two different incident angles each. These data sets therefore contain diffraction peaks enhanced by texture, but without the distortion caused by a few strongly diffracting crystallites.

Data sets Fe_3Al94, Fe_3Al95, Fe_3Al95v2, and Fe95 include background patterns acquired with everything except the actual sample. These background files are used to remove detector gain variations and individual bad points. The background files are used to normalize the real data sets, resulting in reasonably flat backgrounds. The bad points in the detector are seen as sharp peaks in the background. Thus, the bad points can be avoided to prevent false peak detection. Fortunately, most of the bad points are located away from the interesting diffraction peaks. An exception was the bad points near $2\theta=64.5^0$ in the Fe_3Al95 data that prevented detection of the $\left(\frac{7}{2}\frac{1}{2}\frac{1}{2}\right)\left(\frac{5}{2}\frac{5}{2}\frac{1}{2}\right)$ superlattice peak at 64.1^0. Figures 4.8 and 4.9 show a region of bad points that required the data to be discarded.

The counts in the background data (obtained without sample) were typically ten times larger than the individual diffraction patterns. Nevertheless, owing the limited statistical quality of the background, we found it advantageous to filter severely the high frequency Fourier components (see appendix B) in it before subtracting the background from the individual diffraction patterns. This severe filtering suppressed nicely the statistical scatter of the background, but left some residual background variations that are seen as "ripples" in the background-corrected data of Fig. 4.1.

All of the data sets except the Fe91 were obtained with at least two different detector positions (the detector is rotated by 2.0 degrees). Comparisons of data acquired at multiple detector positions identify detector gain variations and bad points, which move with the detector. Since some of the detector gain variation had a periodicity of 4.0 degrees, this background component was averaged away when the data sets were summed.

4.2.3 Data processing

The 1995 data sets [Fe_3Al95, $Fe_3Al95v2$, and Fe95] were collected with the synchronous router, which results in several useful diffraction patterns per run. The diffraction patterns from each of the useful velocity bins are normalized by the intensity [source strength x collection time (in $\mathrm{mCi \cdot hr}$)] and are corrected by the appropriate background file. The data sets are then summed with each component properly weighted by its intensity (in $\mathrm{mCi \cdot hr}$). Bad points in the data are noted and removed, and the data are smoothed with the Igor binomial smoothing function[♦] [1] to give the final results.

Smoothing is preferred to the noise reduction techniques used on the background files, as explained in appendix B.

4.3 The Fe_3Al95 $^{57}Fe_3Al$ data

The Fe_3Al95 data set possesses the best counting statistics for the $^{57}Fe_3Al$ samples. Data were acquired for all three resonance conditions using a very strong ^{57}Co source

---

[♦] The binomial smoothing operation is a Gaussian filter. It convolves the data with normalized coefficients derived from Pascal's triangle at a level equal to the smoothing parameter (we used a parameter of 2) [2].

whose initial activity was 145 mCi. The other factors used for collecting this data set include:

(1) three sample incident angles,
(2) two detector positions,
(3) transmitted beam blocked for all data collection,
(4) both types of samples (rolled from ingot and rolled from splat) for some averaging over the crystallographic texture of the sample,
(5) approximately equal intensities (mCi·hr) from both sample types,
(6) incident angle set to maximize the intensity of the $\left(\frac{3}{2}\frac{3}{2}\frac{3}{2}\right)$ superlattice peak, and
(7) the best equipment to date, as described in § 3.

Aspects of the Fe_3Al95 data are displayed in the following figures. Figure 4.1 shows the composite diffraction patterns for the three resonance conditions, and Fig. 4.3 shows the differences between them. Figures 4.4 and 4.6 show the diffraction patterns of the components of the two on-resonance conditions along with their respective sums. Diffraction patterns from velocity bin2 through bin5 (inclusive) were summed to provide the data in Fig. 4.1. Figures 4.5 and 4.7 provide the velocity gating information for interpreting the component data shown in Figs. 4.4 and 4.6, respectively. The data shown in Fig. 4.1 were acquired over a time and source intensity of 50,000 mCi·hr. The lines are all Gaussian peaks with a FWHM of 0.67 degrees; only the peak positions and heights are varied when fitting to the data. The fundamental peaks (200), (211), and (222) are clearly seen, which is expected from the samples' texture. In addition the important Fe_3Al95 superlattice peaks from Fig. 4.3 are shown: the $\left(\frac{3}{2}\frac{3}{2}\frac{3}{2}\right)\left(\frac{5}{2}\frac{1}{2}\frac{1}{2}\right)$ peak at 45.5 degrees and the (300)(221) peak at 53 degrees.

Table 4.1 Allowed diffraction peaks for the three resonance conditions for $^{57}Fe_3Al$ samples.

Resonance cond.	Diffraction Peaks bcc fundamental	 $\left(\frac{1}{2}\frac{1}{2}\frac{1}{2}\right)$-family	 (100)-family
0Al	yes	yes	yes
4Al	yes	no	yes
off	yes	no	no

As previously described in § 1.1, Mössbauer diffraction patterns acquired with the three resonance conditions should have the diffraction peaks listed in Table 4.1. The principal peaks of interest are also labeled, while a full peak position list can be found in Table A.1.

The peaks of interest in the diffraction patterns have been fit with Gaussian functions to obtain basic information on their width and area in the number of counts in the peak. The peak areas are reported in Table 4.2 in terms of the total peak counts and units of standard deviation above the noise level set by the statistics. The noise level is found by summing the total background counts within the full width at half maximum (FWHM) of the peak and taking the square root of this number. Thus, the noise level is based on the counts in the region of the peak and is in fact the standard deviation of those counts. In cases where two or more sets of data are being compared, the noise level is constructed using the least significant statistics available. The noise level, now called σ, is divided into the fitted area of the peak to obtain the peak area in units of σ. When generating the difference between two peak areas in diffraction patterns of comparable statistics, the corrected peak area is further divided by $\sqrt{2}$. The resulting corrected peak areas represent the lower limit of the statistics and set a minimum confidence level in the peaks [3].

Table 4.2 Peak areas for the Fe_3Al95 data in Fig. 4.1. The numbers listed in parentheses are the total numbers of counts in the peak. The peaks listed with zero counts were not fit.

Resonance Condition	(200)	(211)	$\left(\frac{3}{2}\frac{3}{2}\frac{3}{2}\right)\left(\frac{5}{2}\frac{1}{2}\frac{1}{2}\right)$	(300)(221)	(222)
0Al (0Al counts)	7.4 σ (980)	7.0 σ (960)	2.0 σ (250)	$<$ 1.0 σ (100)	3.1 σ (350)
4Al (4Al counts)	6.9 σ (1050)	4.9 σ (750)	0.0 σ (0)	2.1 σ (270)	3.2 σ (350)
off (off counts)	12.2 σ (1040)	7.0 σ (600)	0.0 σ (0)	0.0 σ (0)	3.6 σ (240)

The left side of Fig. 4.3 shows the differences of the diffraction patterns in Fig. 4.1. The difference patterns are formed by simple subtractions as indicated in the graph. An advantage of working with the differences of diffraction patterns is that they have a better correction for the detector background. As before the line traces are Gaussian fits to the data. The solid lines indicate peaks with high confidence levels; the dashed lines indicate low confidence peaks. Unfortunately, interpreting the data is not a simple matter of subtracting the on- from the off-resonance data. Two effects are primarily to blame: (1) the loss of x-ray scattering intensity in the presence of strong Mössbauer absorption and (2) interference effects between the Mössbauer and x-ray scattering. Nevertheless, as shown in § 5.2, when the x-ray superlattice diffractions are weak, it is possible to identify chemical environment selectivity directly in differences of on- and off-resonance diffraction patterns.

Two sets of superlattice peaks in Fig. 4.3 show chemical environment selective diffraction effects. The $\left(\frac{3}{2}\frac{3}{2}\frac{3}{2}\right)\left(\frac{5}{2}\frac{1}{2}\frac{1}{2}\right)$ peak at 45.5 degrees can be seen in the 0Al data but not in the 4Al or off-resonance data. This is as predicted, as $\left(\frac{1}{2}\frac{1}{2}\frac{1}{2}\right)$-type diffractions are allowed only for the 0Al condition. The peak has an area of 2.0 σ, which exceeds the $\left(\frac{3}{2}\frac{3}{2}\frac{3}{2}\right)\left(\frac{5}{2}\frac{1}{2}\frac{1}{2}\right)$ peak area of the two earlier $^{57}Fe_3Al$ data sets: the Fe_3Al94 area is 1.2 σ, and the

Fe_3Al93 area is ~0.5 σ. The $\left(\frac{5}{2}\frac{3}{2}\frac{1}{2}\right)$ peak at 52.2 degrees and the (300)(221) peak at 53 degrees form the second set of superlattice peaks. Both peaks are expected for the 0Al condition, while only the latter peak is expected for the 4Al condition. The 0Al data shows two possible peaks of low confidence (< 1.0 σ). The 4Al shows the allowed peak at 53 degrees (2.1 σ), but it also shows intensity in the $\left(\frac{5}{2}\frac{3}{2}\frac{1}{2}\right)$ peak (< 1.0 σ).

While there are a number of possible explanations for the weak $\left(\frac{5}{2}\frac{3}{2}\frac{1}{2}\right)$ peak in the 4Al resonance condition, the most probable, interference, will be explored in the next chapter. Unlike the fundamental peaks, the high-order superlattice peaks do not suffer from interference with x-ray scattering. However, they can suffer from interference with other Mössbauer scattering, and the 4Al environment is particularly susceptible. This susceptibility arises from the large number of chemical environments whose Mössbauer absorption peaks overlap the 4Al. Even allowing for these problems, the two sets of superlattice peaks in Fig. 4.3 demonstrate the sought-after chemical environment selective diffraction. The 0Al environment is seen in the 45.5 degree peak and the 4Al environment in the 53 degree peak. Other examples are reported in the data set described next.

4.4 The $Fe_3Al95v2$ $^{57}Fe_3Al$ data

The $Fe_3Al95v2$ data set was a repeat of the Fe_3Al95 data with two important differences: (1) the INEL detector was moved closer to the sample, as described in § 3.4.4, and (2) only one sample was used [the $^{57}Fe_3Al$ #1(C), rolled from a splat sample] to maximize crystallographic texture effects. Moving the detector closer allowed a larger solid angle to be collected. We switched to using only the sample rolled from a splat, since it shows the most favorable texture for the $\left(\frac{1}{2}\frac{1}{2}\frac{1}{2}\right)$-type superlattice peaks. The sacrifice in this case is the other fundamental peaks; only the (211) diffracts strongly for this sample.

However, since the Fe_3Al95 data shows clearly the various fundamental peaks, the sacrifice seemed reasonable.

Several problems arose from moving the INEL detector closer to the sample. First, parallax problems are induced when the detector is moved from its fixed distance from the sample, as seen in Fig. 3.17. The linear relationship used for calibrating the detector's 2θ position is also broken. Second, the angular resolution of the detector is reduced by a factor of two when the detector is moved to half its previous distance. Third, increasing the strength of the useful signal is done at the expense of increasing the noise background. The source shielding was less effective, as the new geometry permits less Pb to be used than before. Fourth, the beam stop size has to be reduced to prevent it from blocking the signal into the detector in the desired angular range ($2\theta > 30$ degrees). These problems cause an increase in the photon noise background [7.8 Hz vs. 2.3 Hz for the Fe_3Al95 data, a factor of 3.4 increase][♦] and larger background variations as a function of 2θ angle. The first two problems were easily overcome: the 2θ angular positions became non-linear, but this was handled through careful recalibration. The detector resolution increased to 0.12 degrees per channel, but the diffraction peaks possessed FWHM's greater than 0.6 degrees. Although the noise level increased significantly, so did the signal for certain important diffraction peaks.

Figure 4.2 displays the diffraction pattern from the summed $Fe_3Al95v2$ data sets for the three resonance conditions. The data were processed identically to the Fe_3Al95 data in § 4.3. The intensity average is 22,500 mCi·hr, or approximately half that of the Fe_3Al95 data. The lower angular resolution is seen as a lower density of data points when compared to Fig 4.1. The Gaussian fits are used again to identify the important peaks. The strong fundamental peak in Fig. 4.2 is the (211). Other fundamental peaks can be seen, but the only one that bears mentioning is the (222).

[♦] The total background noise was 5.8 Hz for Fe_3Al95 and 11.3 Hz for $Fe_3Al95v2$, a factor of ~ 2 increase.

Chemical environment selective diffraction effects are best seen in differences of diffraction patterns obtained in different resonance conditions. Figure 4.3 presents differences between the two on-resonance conditions and the off-resonance condition. The 0Al condition diffracts more strongly than the other two conditions, indicating a large amount of Mössbauer scattering into this peak. It is important to note that Fe_3Al95v2 peak areas are calculated with half the counts of the Fe_3Al95 data set. Summing the areas of the fundamental peaks for both data sets yields almost identical results: the Fe_3Al95v2 peak areas contain 3% more counts than Fe_3Al95 (6500 counts). Moving the detector to half its original distance increases the signals in the peaks by a factor of 2 (a r^{-1} dependence since the solid angle is increased with height of the detector only). Of course the actual gain is less because of the increase in noise, but moving the detector has definitely lead to an improvement in the data. Table 4.3 provides the areas for the important peaks in the Fe_3Al95v2 data set.

Table 4.3 Peak areas for the Fe_3Al95v2 data in Fig. 4.2 [(211) peak] and Fig. 4.3 [(222) and $\left(\frac{7\,1\,1}{2\,2\,2}\right)\left(\frac{5\,5\,1}{2\,2\,2}\right)$]. The numbers listed in parentheses are the total numbers of counts in the peak. The peaks listed with zero counts were not fit.

Resonance Condition	(211)	(222)	$\left(\frac{7\,1\,1}{2\,2\,2}\right)\left(\frac{5\,5\,1}{2\,2\,2}\right)$
0Al	18.8 σ	3.0 σ	3.0 σ
(0Al counts)	(1820)	(340)	(350)
4Al	15.9 σ	0 σ	0 σ
(4Al counts)	(2130)	(0)	(0)
off	18.3 σ	0 σ	0 σ
(off counts)	(2560)	(0)	(0)

Figure 4.2 also shows a Gaussian fit for the $\left(\frac{7}{2}\frac{1}{2}\frac{1}{2}\right)\left(\frac{5}{2}\frac{5}{2}\frac{1}{2}\right)$ superlattice peak. The line trace shown at 64.1 degrees represents the $\left(\frac{7}{2}\frac{1}{2}\frac{1}{2}\right)\left(\frac{5}{2}\frac{5}{2}\frac{1}{2}\right)$ peak, which is 3.0 σ in area. Both this peak and the 0Al (222) are more clearly seen on the right side of Fig. 4.3, which displays the differences of the diffraction patterns in Fig. 4.2. The $\left(\frac{7}{2}\frac{1}{2}\frac{1}{2}\right)\left(\frac{5}{2}\frac{5}{2}\frac{1}{2}\right)$ superlattice peak is of $\left(\frac{1}{2}\frac{1}{2}\frac{1}{2}\right)$-type, so it should be seen only in the 0Al resonance condition. The lack of corresponding peaks in the 4Al and off resonance conditions is very encouraging. Unfortunately, the $\left(\frac{7}{2}\frac{1}{2}\frac{1}{2}\right)\left(\frac{5}{2}\frac{5}{2}\frac{1}{2}\right)$ superlattice peak was not seen in the Fe_3Al95 data because it was obscured by bad points in the detectors. Moving the detector also moved the bad points, allowing this magnificent peak to be observed. The $\left(\frac{7}{2}\frac{1}{2}\frac{1}{2}\right)\left(\frac{5}{2}\frac{5}{2}\frac{1}{2}\right)$ superlattice peak in the Fe_3Al95v2 data set is our best evidence for chemical environment selectivity.

4.5 The Fe95 ^{57}Fe data

This section data uses data collected from the ^{57}Fe samples to show how changes in the experimental equipment and data processing techniques have improved the quality of our data. The Fe91 ^{57}Fe data, described in Ref. 4 and Appendix C, was the first data showing Mössbauer diffraction peaks from a polycrystalline sample. The Fe95 ^{57}Fe data was collected just prior to the Fe_3Al95 data, and it benefits from all our experimental improvements, including the 145 mCi ^{57}Co source.

Figure 4.8 shows the Fe95 diffraction patterns. The incident angle was set to maximize the (400) peak, and three peaks are seen in the data: the (222), the (400), and the (332). All three peaks are apparently from Mössbauer scattering only, as no x-ray scattering is seen in the off-resonance data. The range of data from 75 to 82 degrees was removed due to bad regions in the detector. Table 4.4 presents the areas of the diffraction peaks found in Fig. 4.8. The on-resonance data in Fig. 4.8 are summed from all five component diffraction patterns (bin2 through bin5 and bin7) in Fig. 4.9. Figures 3.13 and 3.14 show the velocity gating bins used for acquiring the component patterns.

Table 4.4 Peak areas for the Fe95 data in Fig. 4.8. The numbers listed in parentheses are the total numbers of counts in the peak. The peaks listed with zero counts were not fit.

resonance condition	(222)	(400)	(332)
on	6.5 σ	16.9 σ	15.6 σ
(on counts)	(400)	(1080)	(1040)
off	0 σ	0 σ	0 σ
(off counts)	(0)	(0)	(0)

A quick comparison shows that the statistical quality of the on-resonance Fe95 peaks exceed the Fe91 peaks by a factor of 3.3. As we are measuring the areas in terms of noise background, the Fe95 peak areas exceed the Fe91 by a factor of 10.9.

The difference in collection time accounts for a factor of 1.5 (75 hours versus 50 hours), while the Fe95 radiation source was 3.7 times stronger. The remaining factor of 2 can be attributed to improvements in the experimental equipment.

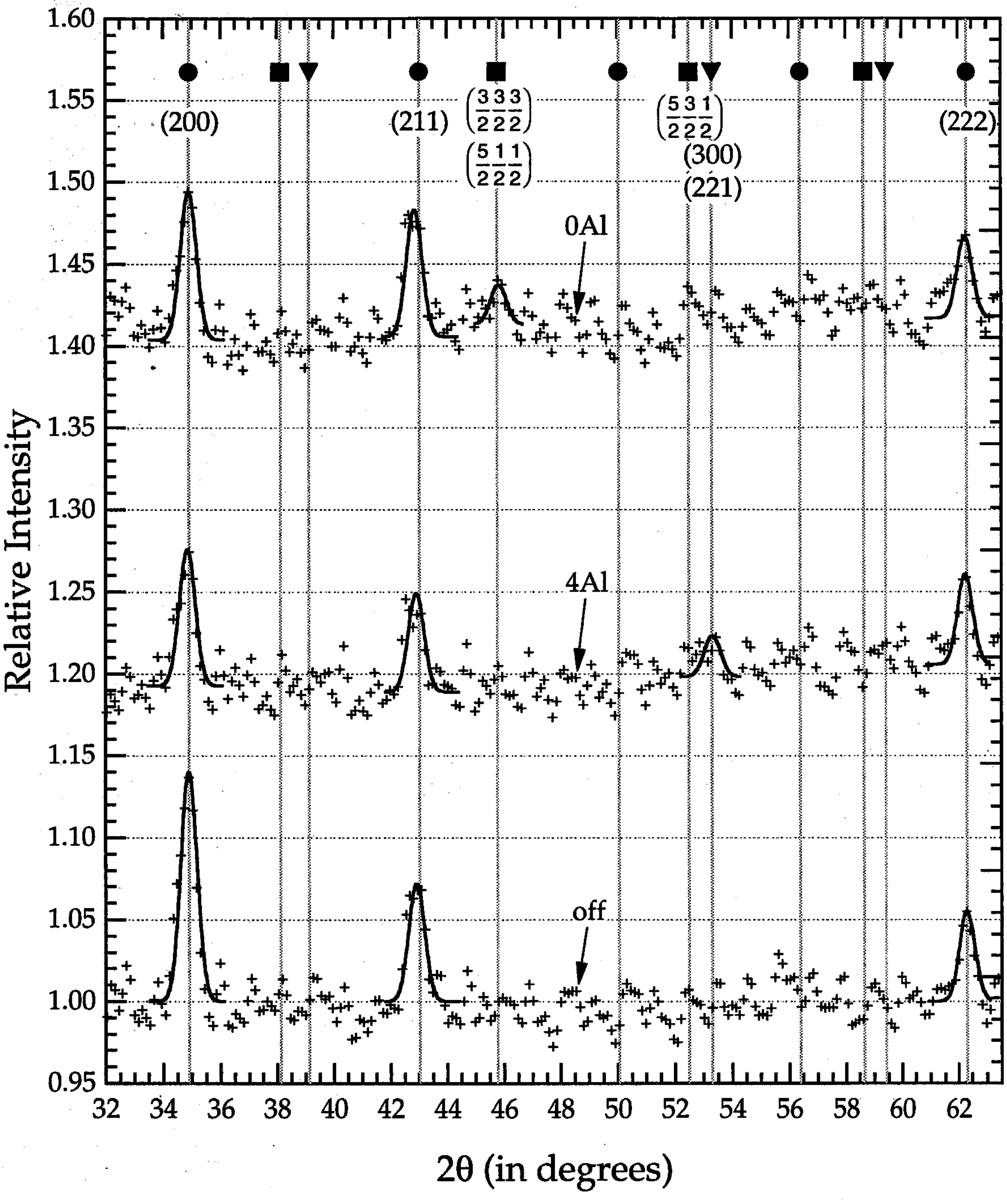

Figure 4.1 The three resonance conditions for the $^{57}Fe_3Al$ sample (Fe_3Al95 data set). The two on-resonance diffraction patterns are summed from velocity bin2 through bin5. The circles indicate bcc fundamental peaks, the squares indicate (1/2 1/2 1/2)-family superlattice peaks, and the inverted triangles indicate (100)-family superlattice peaks.

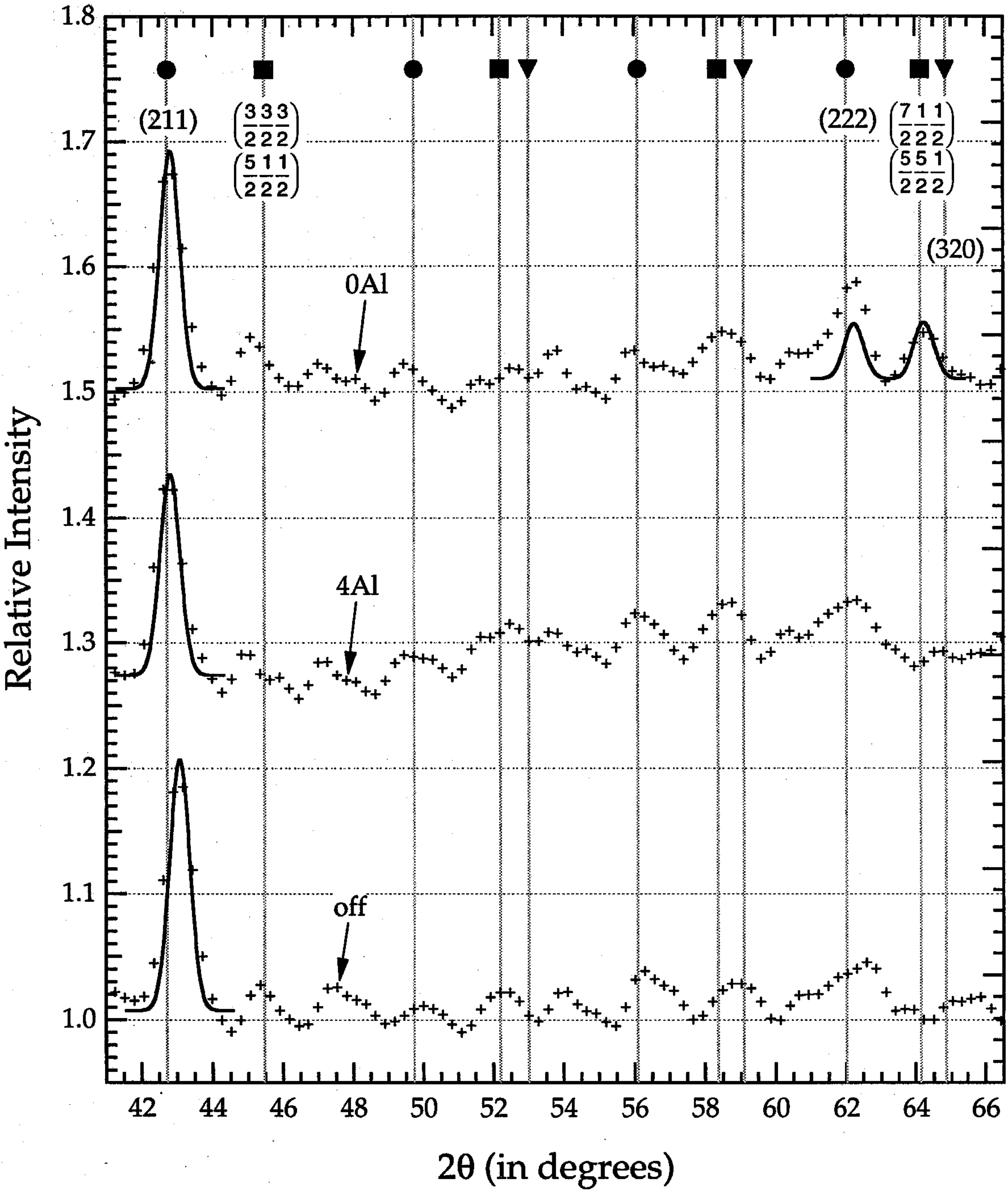

Figure 4.2 The three resonance conditions for the $^{57}Fe_3Al$ sample ($Fe_3Al95v2$ data set). The two on-resonance diffraction patterns are summed from velocity bin2 through bin5.

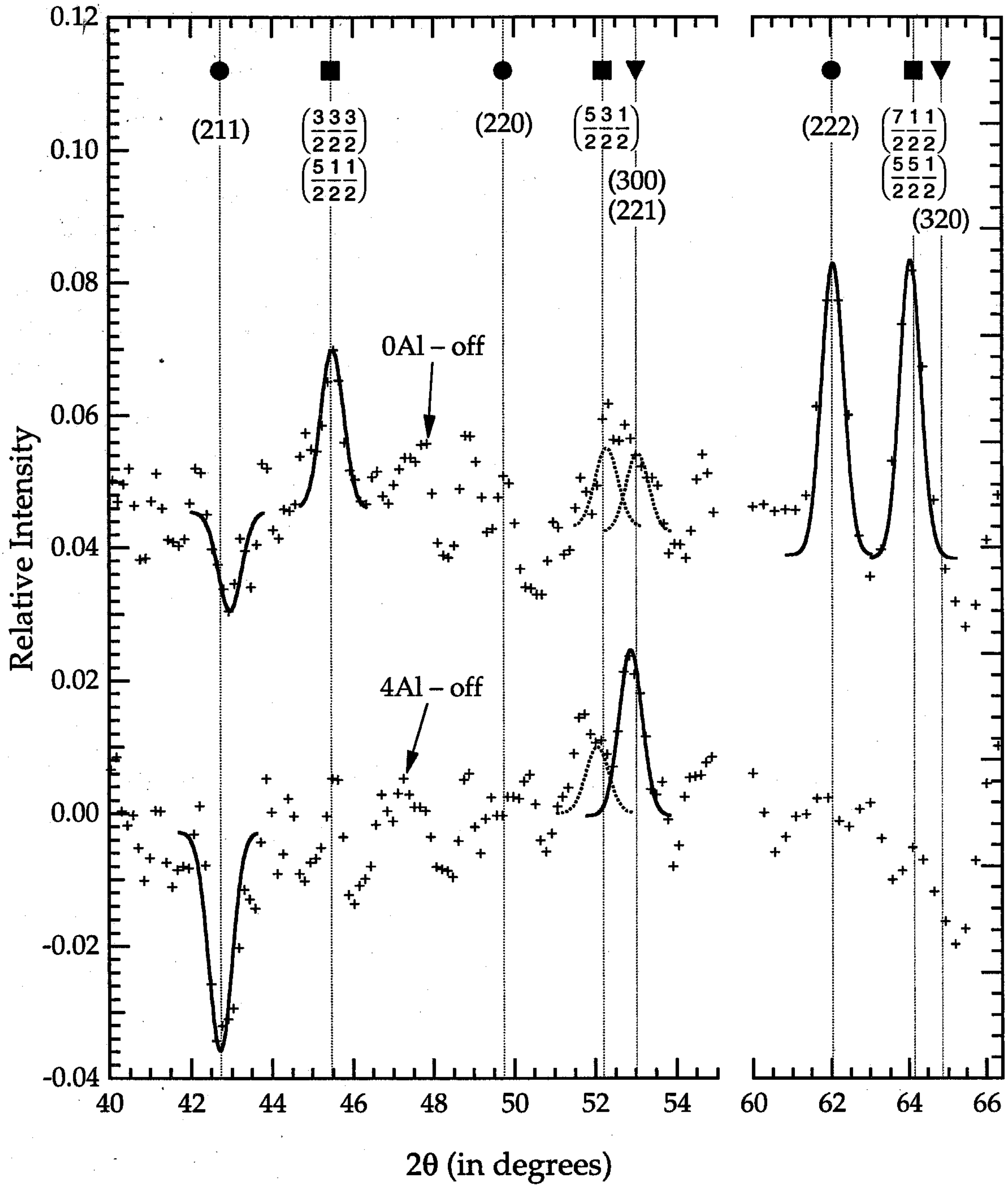

Figure 4.3 Differences between the three resonance conditions for the $^{57}Fe_3Al$ sample. The Fe_3Al95 data set is displayed on the left side of the graph; the $Fe_3Al95v2$, the right side. The solid lines are high confidence peaks; the dashed lines, low confidence.

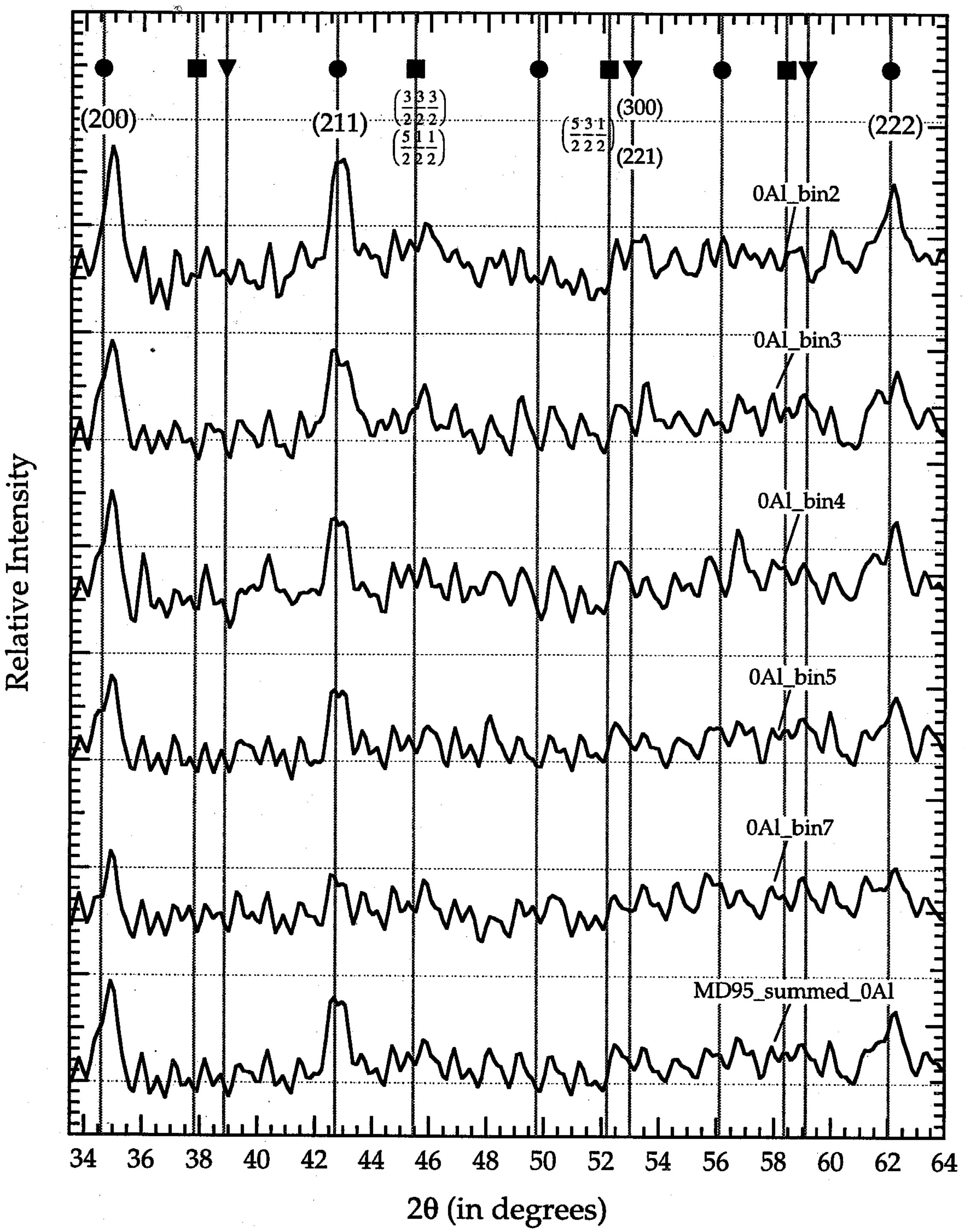

Figure 4.4 Fe_3Al95 data set for the 0Al condition. Data from the individual velocity bins and the sum of bin2 through bin5 are displayed.

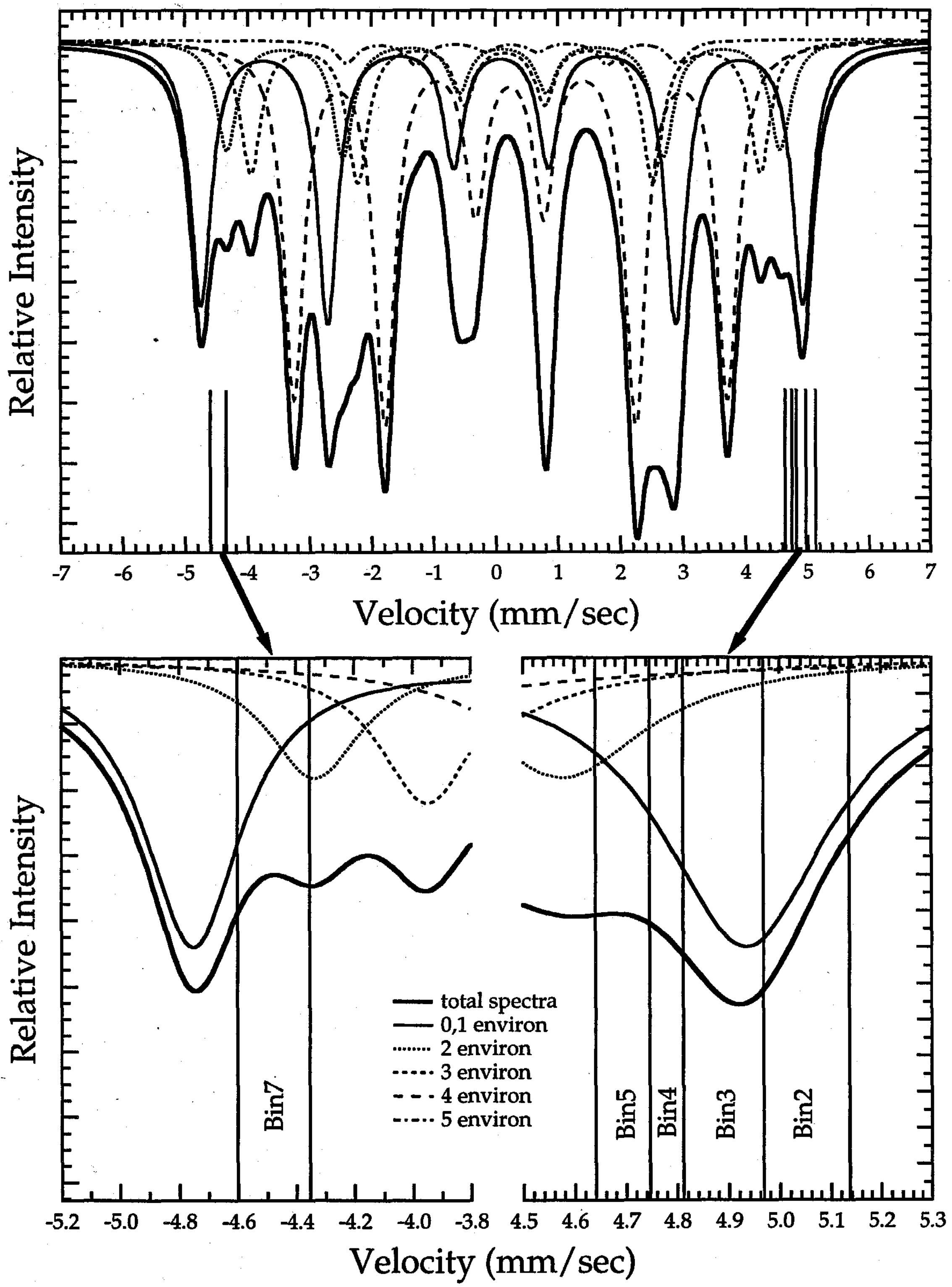

Figure 4.5 The 0Al velocity bins for the Fe_3Al95 data set in figure 4.4.

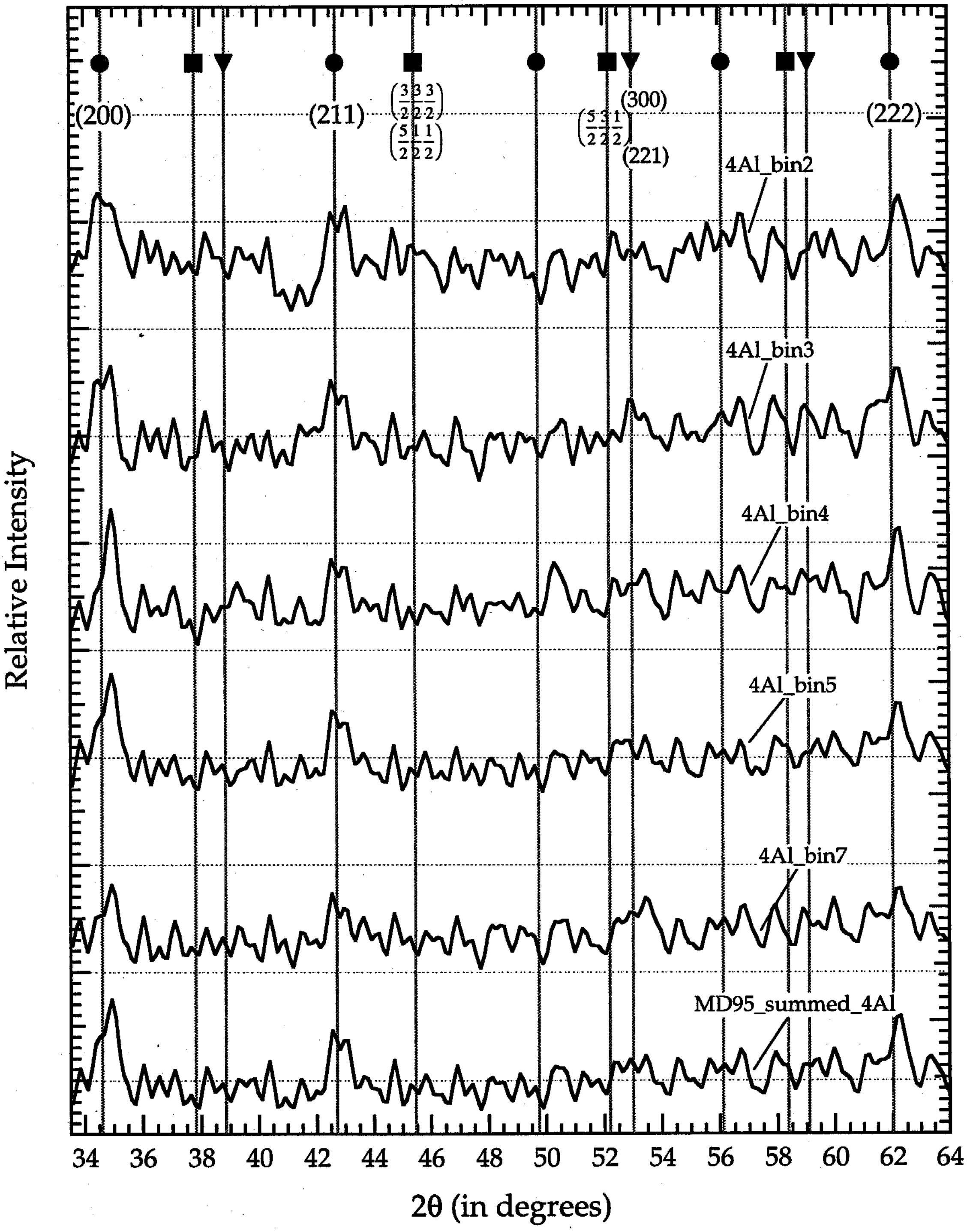

Figure 4.6 Fe_3Al95 data set for the 4Al condition. Data from the individual velocity bins and the sum of bin2 through bin5 are displayed.

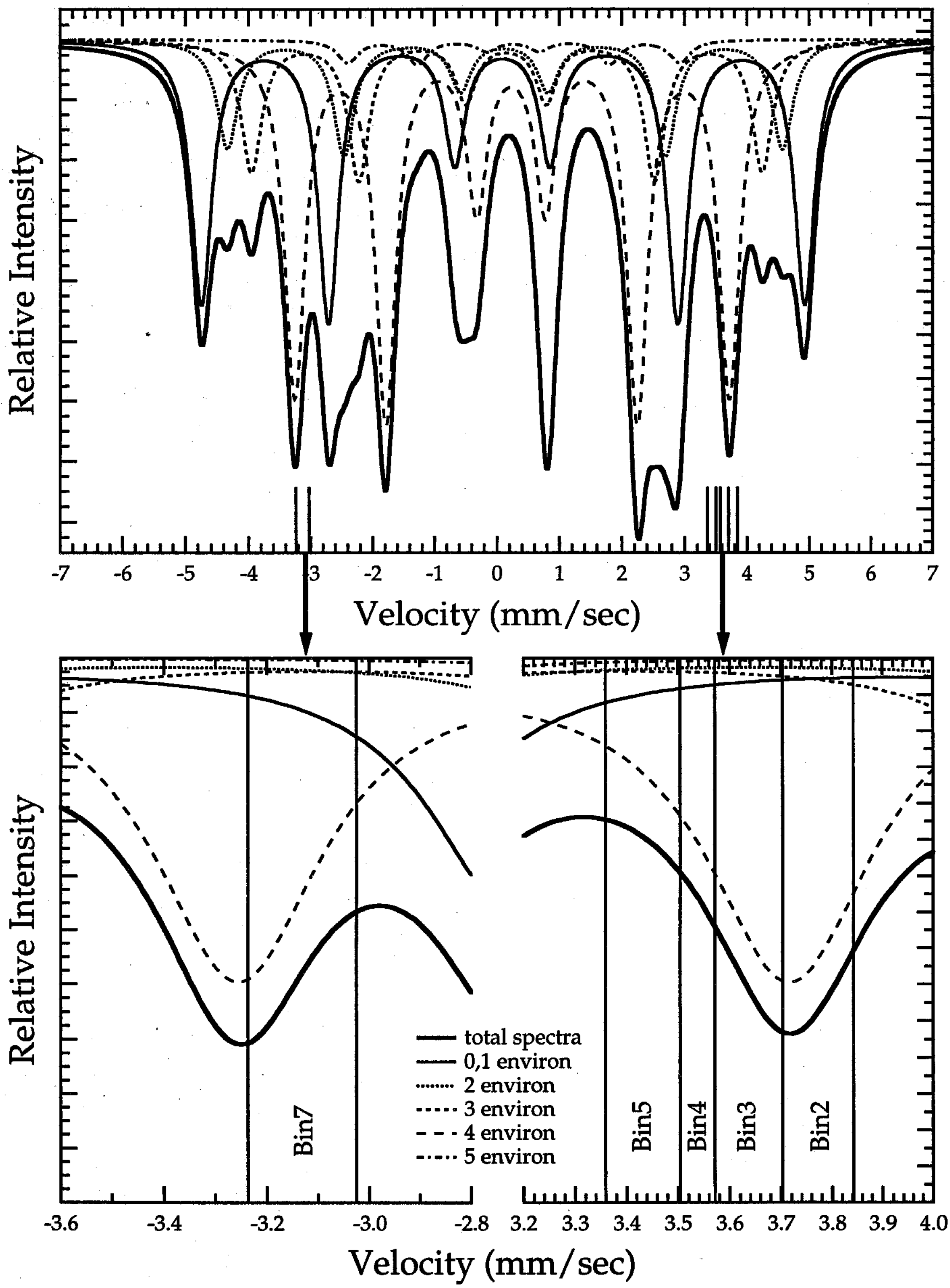

Figure 4.7 The 4Al velocity bins for the Fe_3Al95 data set in figure 4.6.

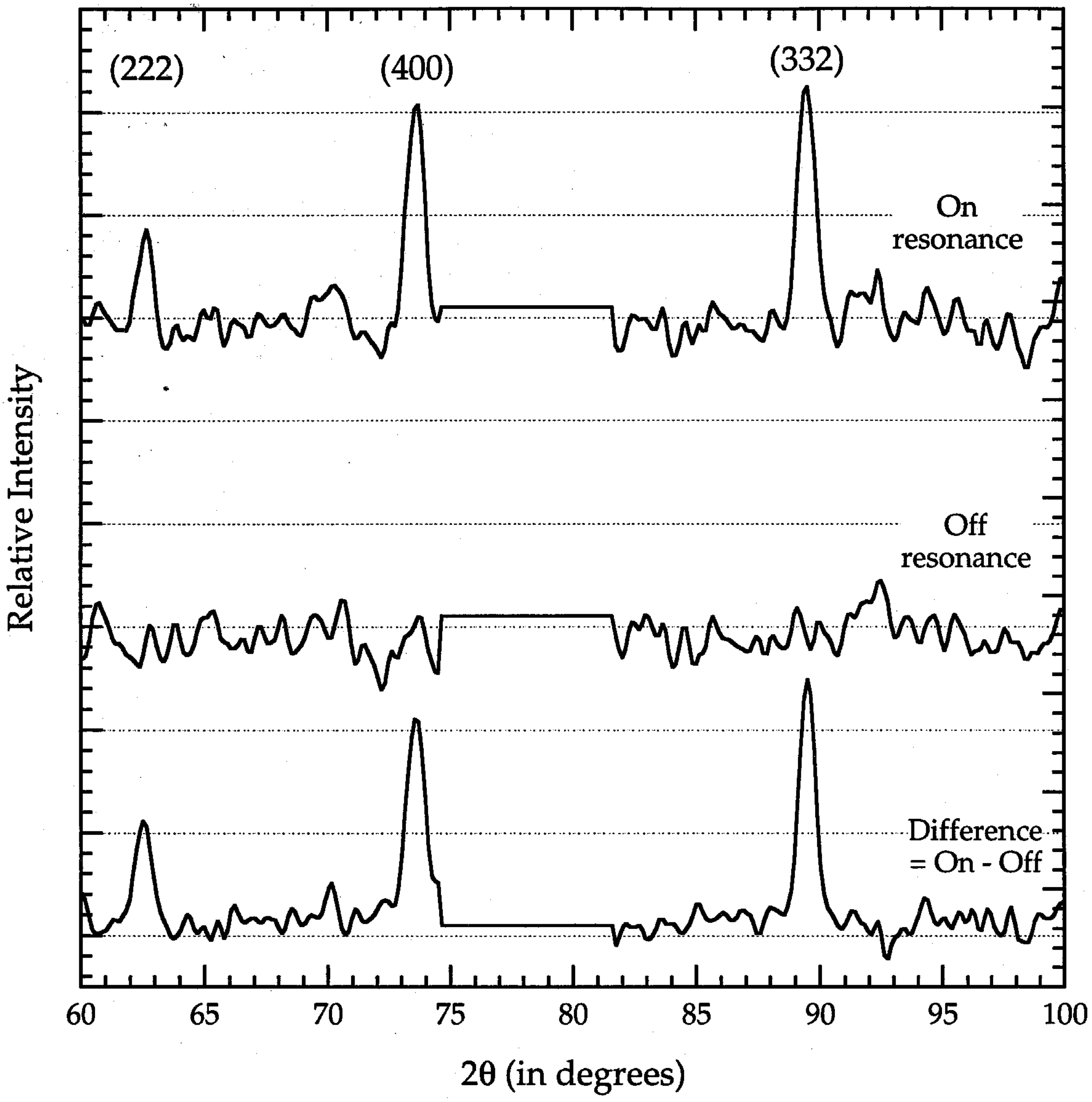

Figure 4.8 The Fe95 (^{57}Fe) data set acquired using the 145 mCi ^{57}Co source. The zeroed region from 75 to 82 degrees occurs in a bad region of the detector.

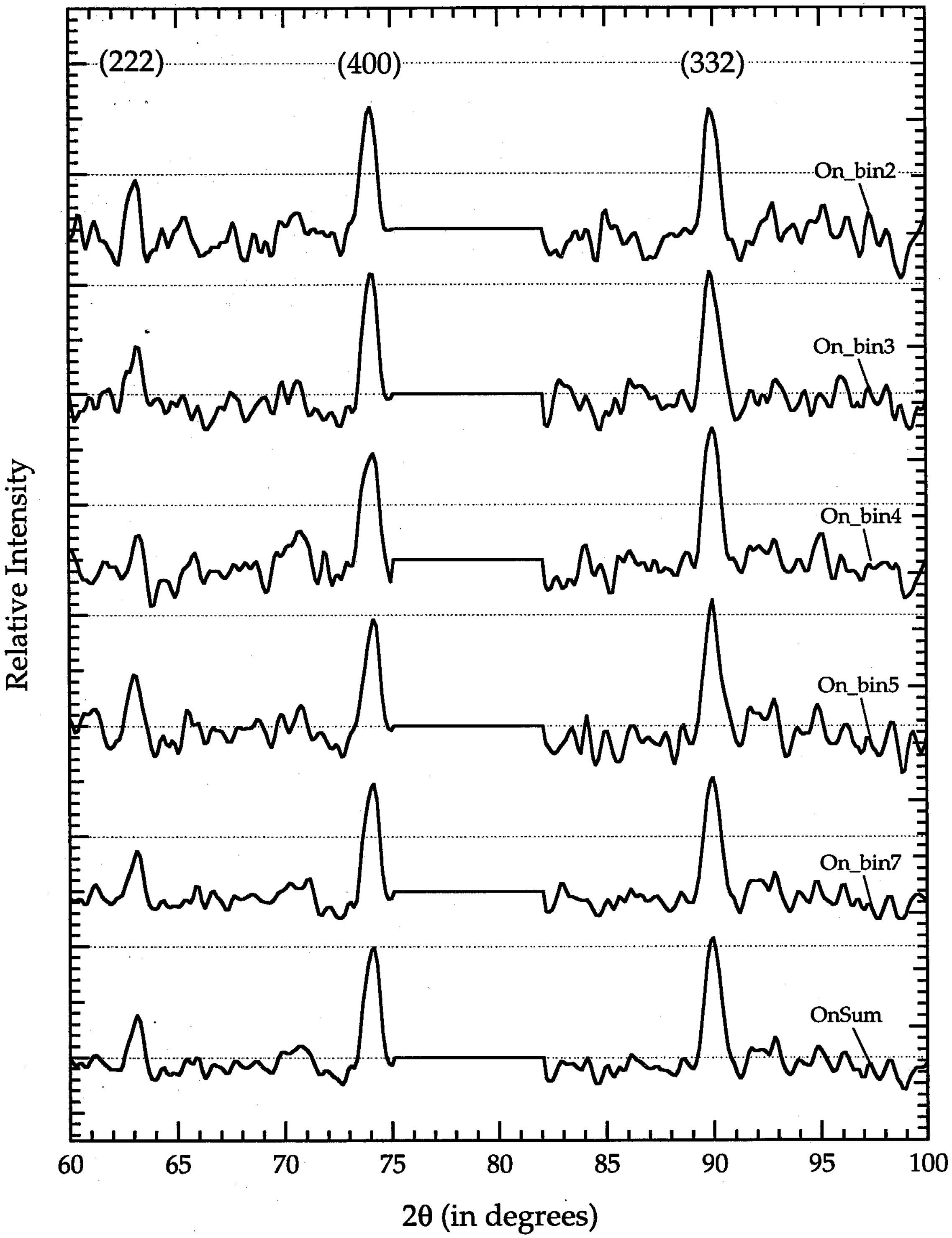

Figure 4.9 The ^{57}Fe on-resonance component data (Fe95 data set). The OnSum curve is the sum of all five useful bins.

References, Chapter 4

[1] Wavemetrics, Inc., *Igor Pro User's Guide*, (Lake Oswego, OR, 1996), p. II-593.

[2] P. Marchand and L. Marmet, Rev. Sci. Instrum. **54**, 1034 (1983).

[3] J.R. Taylor, *An Introduction to Error Analysis* (University Science Books, Sausalito, CA, 1982), Chap. 5.

[4] T.A. Stephens, W. Keune, and B. Fultz, Hyperfine Inter. **92**, 1095 (1994).

Chapter 5 Interference effects in Mössbauer and x-ray scattering

This chapter describes a generalized kinematical diffraction theory for both Mössbauer and x-ray Rayleigh scattering. The theory is implemented numerically in a multislice computer code and is used to predict the interference effects that occur because of the energy dependence of the Mössbauer scattering.

This chapter comprises five sections. Section 5.1 describes qualitatively the origin of interference phenomena. Section 5.2 describes the kinematical diffraction theory and scattering factors. Section 5.3 describes the multislice calculations performed to justify using the kinematic diffraction theory and to determine the free parameters needed to model the interference effects. Section 5.4 describes a Monte Carlo simulation of chemical environment selective diffraction from the ^{57}Fe$_3$Al sample. Finally, § 5.5 compares the calculated interference and absorption effects to those in the experimental data.

5.1 Interference phenomena in resonance scattering

The Bragg peak intensities were seen to vary in the different component diffraction patterns of Figs. 4.4, 4.6, and 4.9. Intensity variations are expected, since the amount of resonant Mössbauer absorption differs for each of the diffraction patterns. However, interference between the x-ray scattering and Mössbauer scattering may also cause the variations. Thus, we propose a scattering model that handles properly the interference among scattering from different processes and calculates the effects on the intensities of the diffraction peaks.

Our model uses a set of oscillators to track the changes in the phase and amplitude of the scattered photons. The oscillators are damped and driven; the Mössbauer oscillators are driven close to resonance while the x-ray oscillator is driven well above resonance [1].

Figure 5.1 shows an oscillator phase response as a function of its driving frequency. The regions A, B, C, and D correspond to energy ranges for the respective velocity bins (explained in § 3.4.3). The Mössbauer oscillator response shows the rapid phase change as the driving frequency passes through resonance. The x-ray response, however, is always out-of-phase as the driving frequency is far above the x-ray absorption edges for both Fe and Al. The change from in-phase scattering below resonance to out-of-phase scattering above gives rise to strong interference effects, not only between the Mössbauer and x-ray components, but between the individual Mössbauer components themselves. The latter is due to the overlaps between the various absorption peaks in the Mössbauer spectrum of $^{57}Fe_3Al$. Finally, the model then uses the phase shifts of scattered waves as predicted from the Mössbauer energy spectra to predict intensities of the Bragg peaks seen in the diffraction pattern.

5.1.1 Phase–amplitude diagram of interference

Figures 5.2a through 5.3b illustrate the basic effects of interference in resonance scattering. The figures graphically show how the calculated Mössbauer scattering spectrum is compared to the experimental data. The demonstration uses one x-ray and one Mössbauer oscillator for clarity.

Figure 5.2a shows a phase amplitude (PA) diagram for x-ray scattering, Mössbauer scattering, and their sum. The PA diagram displays the real and imaginary components of the scattering factor. The x-ray scattering factor is indicated by the dotted line. The Mössbauer scattering factor is a vector added to the tip of the x-ray vector. Depending on the velocity bin and its phase shift, the sum of the x-ray and Mössbauer phase factors will touch a point on the dashed circle in Fig. 5.2a. The total scattering factor, which is the sum of two, starts at the origin and ends on the circle. Increasing energy (velocity) is indicated by tracing the circle in a clockwise direction. The regions A, B, C, and D correspond to

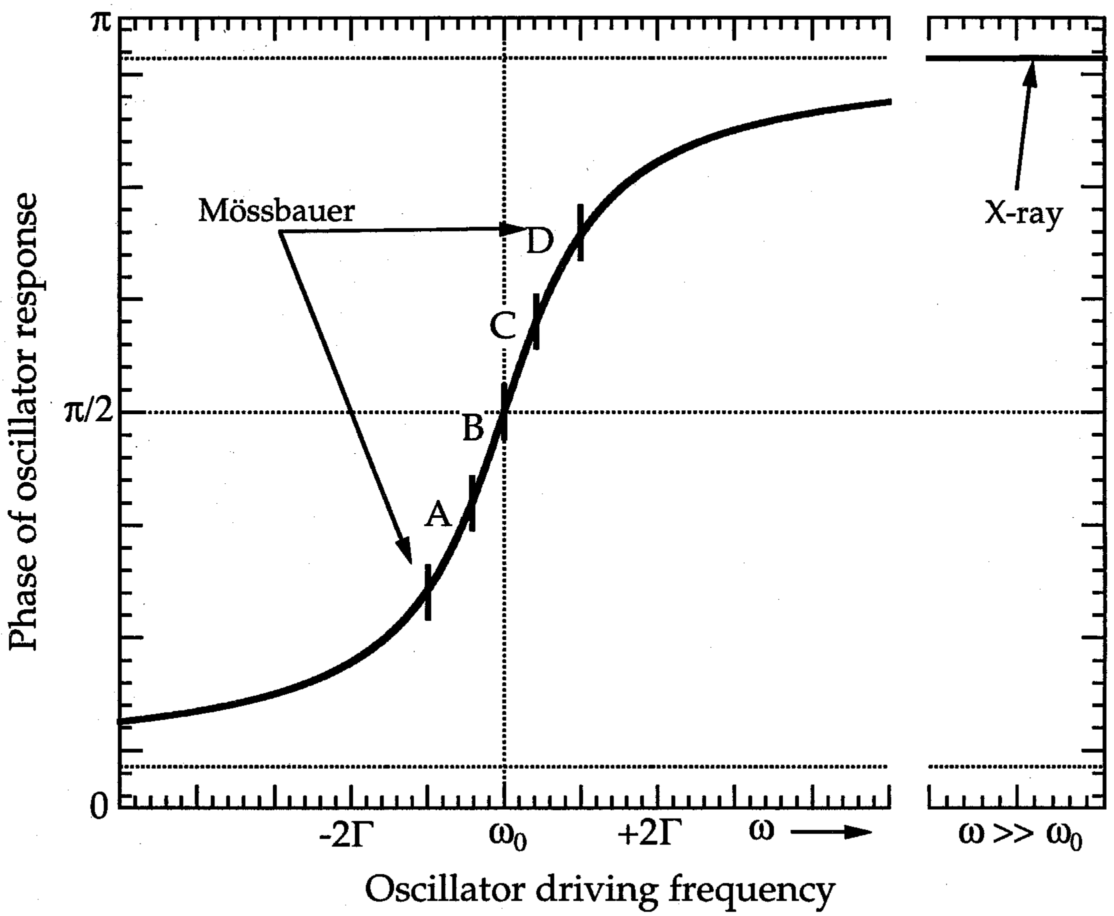

Figure 5.1 Oscillator phase response as a function of its driving frequency. The energy is given in terms of linewidths, Γ.

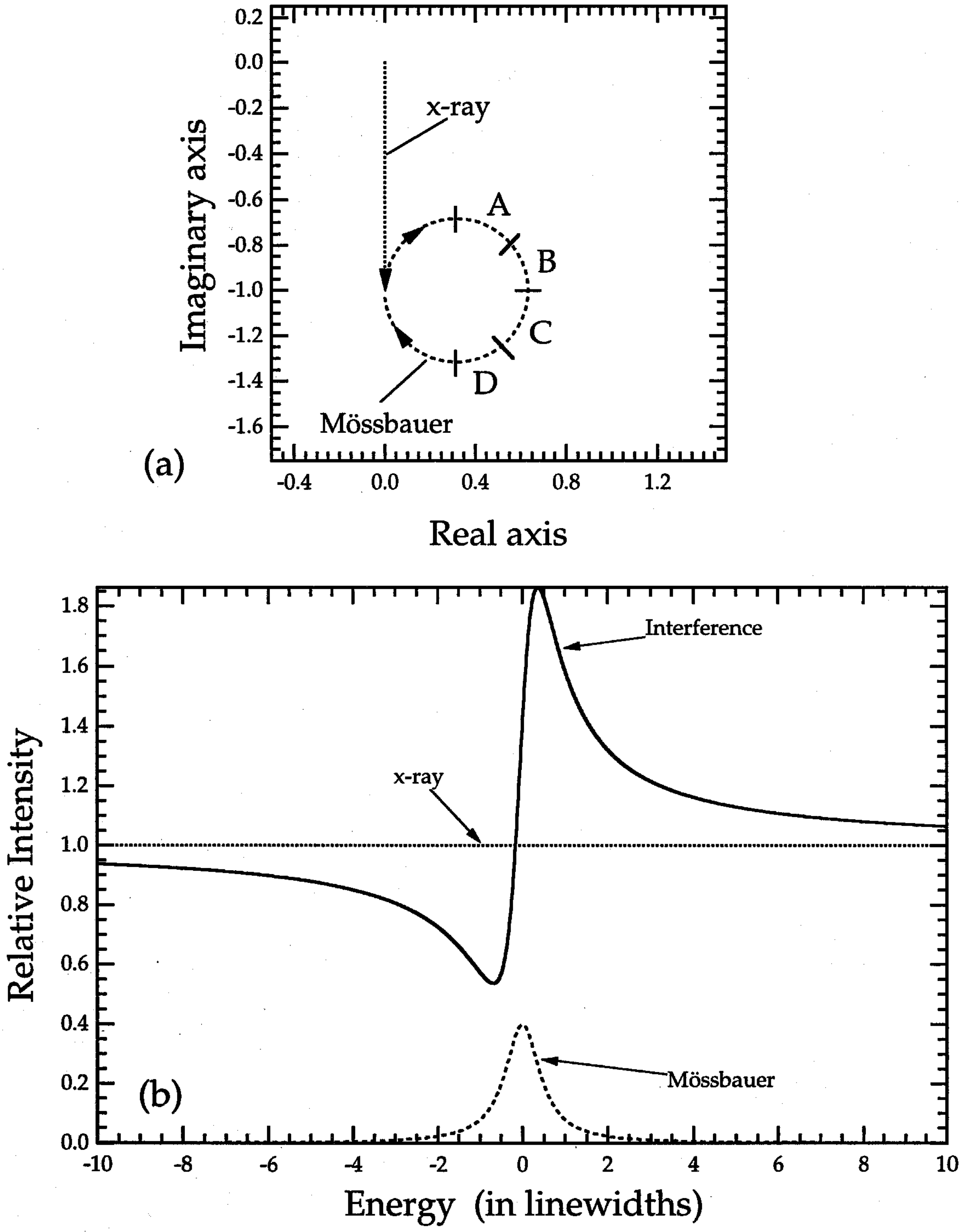

Figure 5.2 (a) Phase-amplitude diagram for the intensity curves below. (b) Intensity versus energy for Mössbauer scattering, X-ray scattering, and their interference. The letters A through D indicate different gating bins; see Figure 5.3a.

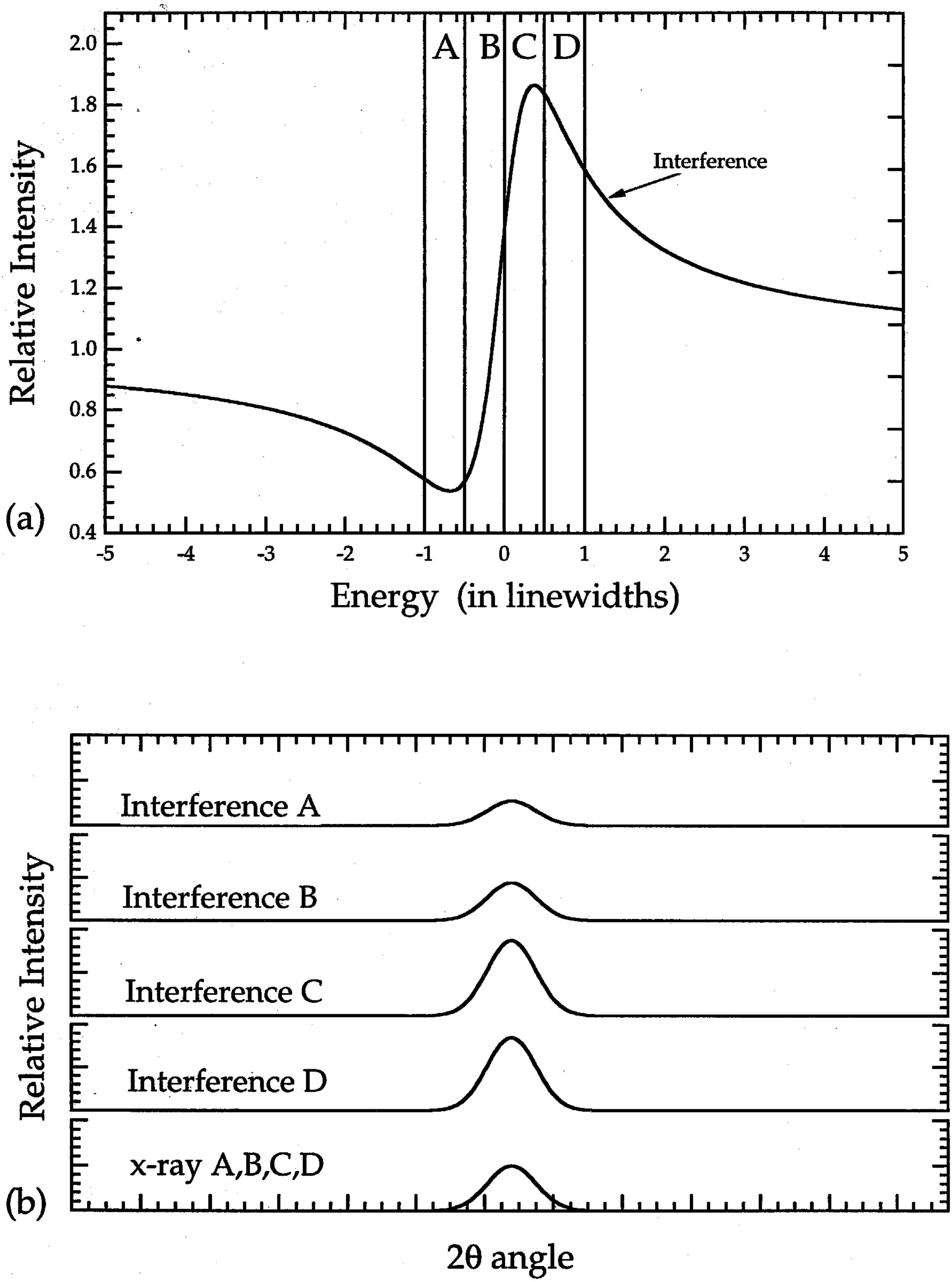

Figure 5.3 (a) Interference curve replotted from figure 5.2a. The letters A through D indicate different gating bins. (b) Simulated diffraction peaks corresponding to the gating bins above. Peaks are scaled by the normalized intensities of the bins.

the energy ranges of Fig 5.1.. These can be related to our different velocity bins and the diffraction patterns they collect.

Figure 5.2b shows the energy dependence of the intensities of scattering. Figure 5.2b was obtained as *f*f*, where *f* is the scattering factor shown in Fig 5.2a for Mössbauer scattering, x-ray scattering, and the coherent sum of the two. The interference curve shows decreased intensity at negative velocities and increased intensity at positive velocities. This behavior is caused by the phase change in the Mössbauer scattering as it goes through resonance, leading to destructive interference with x-ray scattering at low energies and constructive interference at high energies.

Figure 5.3a shows how the modeled data are related to the diffraction peaks. The four velocity bins are displayed in addition to the interference intensity curve of Fig 5.2b. The interference curve is integrated over each of the bins and normalized by the energy width of the bin. This yields a ratio of numbers for the velocity bins that corresponds to the amount of scattering for each resonance condition.

Figure 5.3b shows simulated diffraction peaks, similar to those expected in the real data. All of these peaks are identical in width, and scaled in height by the intensities provided by Fig. 5.3a. These modeled results can be compared to experimental data. The ratios of the diffraction peak areas from the different velocity bins of the experimental data are compared to the ratios of scattering from the velocity bins in the model.

5.2 Diffraction theory

We use a kinematical diffraction theory because multiple scattering processes are negligible in our samples. Justification will be presented in § 5.3.

5.2.1 Kinematical diffraction theory

The photon wave, ϕ, that is scattered by an atom at $\vec{r}$ will include contributions from both Mössbauer and x-ray scattering. It is not obvious that these two contributions will be coherent, but interference between x-ray and Mössbauer scattering was first identified in Mössbauer energy spectra [2,3]. We write:

$$\phi\left(\vec{r},\Delta\vec{k},\delta\varepsilon_{\mathrm{i}'}^{\mathrm{m}'}\right) = e^{-i\Delta\vec{k}\cdot\vec{r}}\left[f_X(\vec{r}) + f_M\left(\vec{r},\delta\varepsilon_{\mathrm{i}'}^{\mathrm{m}'}\right)\right] \quad , \tag{5.1}$$

where:

$$\delta\varepsilon_{\mathrm{i}'}^{\mathrm{m}'} = \mathrm{E} - \varepsilon_{\mathrm{i}'}^{\mathrm{m}'} \quad . \tag{5.2}$$

Here E is the precise energy of the incident γ-ray. The energy of a particular excited state of a particular nucleus is $\varepsilon_{\mathrm{i}'}^{\mathrm{m}'}$, where i' denotes the chemical environment of the nucleus, and m' denotes the transition within the nucleus. For ^{57}Fe there are six allowed nuclear transitions, so that $1 \leq \mathrm{m}' \leq m$, where $m = 6$. We assume a total of $\imath$ chemical environments that provide distinct hyperfine magnetic fields (HMF's), so that $1 \leq \mathrm{i}' \leq \imath$. The diffraction vector, $\Delta\vec{k}$, is defined in the usual way [4]:

$$\Delta\vec{k} = \vec{k} - \vec{k}_0 \quad , \tag{5.3}$$

where the wavevector of the scattered wave is $\vec{k}$, and the incident wavevector is $\vec{k}_0$.

The total diffracted wave, $\psi\left(\Delta\vec{k},\mathrm{E}\right)$, is the sum of the $\phi\left(\vec{r},\Delta\vec{k},\delta\varepsilon_{\mathrm{i}}^{\mathrm{m}}\right)$ over all atoms, chemical environments, and nuclear transitions:

$$\psi\left(\Delta\vec{k},\mathrm{E}\right)=\sum_{\vec{r}}e^{-i\Delta\vec{k}\cdot\vec{r}}\left[f_X(\vec{r})+\sum_{\mathrm{i}}^{i}\sum_{\mathrm{m}}^{m}f_M\left(\vec{r},\delta\varepsilon_{\mathrm{i}}^{\mathrm{m}}\right)\right] \tag{5.4}$$

There are, of course, correlations between the position of the atom, $\vec{r}$, and its chemical environment, i, but we include this information within $f_M\left(\vec{r},\delta\varepsilon_{\mathrm{i}}^{\mathrm{m}}\right)$ rather than writing the correlation as an explicit function.

The intensity, $I\left(\Delta\vec{k},\mathrm{E}\right)$, of the diffracted wave is:

$$I\left(\Delta\vec{k},\mathrm{E}\right)=\psi\left(\Delta\vec{k},\mathrm{E}\right)\psi^{*}\left(\Delta\vec{k},\mathrm{E}\right) \quad , \tag{5.5}$$

$$\begin{aligned}I\left(\Delta\vec{k},\mathrm{E}\right)=&\left\{\sum_{\vec{r}}e^{-i\Delta\vec{k}\cdot\vec{r}}\left[f_X(\vec{r})+\sum_{\mathrm{i=1}}^{i}\sum_{\mathrm{m=1}}^{m}f_M\left(\vec{r},\delta\varepsilon_{\mathrm{i}}^{\mathrm{m}}\right)\right]\right\}\\&\times\left\{\sum_{\vec{r}'}e^{i\Delta\vec{k}\cdot\vec{r}'}\left[f_X^{*}(\vec{r}')+\sum_{\mathrm{j=1}}^{i}\sum_{\mathrm{n=1}}^{m}f_M^{*}\left(\vec{r}',\delta\varepsilon_{\mathrm{j}}^{\mathrm{n}}\right)\right]\right\} \quad ,\end{aligned} \tag{5.6}$$

$$\begin{aligned}I\left(\Delta\vec{k},\mathrm{E}\right)=&\sum_{\vec{r}}\sum_{\vec{r}'}e^{-i\Delta\vec{k}\cdot(\vec{r}-\vec{r}')}\left\{f_X(\vec{r})f_X^{*}(\vec{r}')+f_X(\vec{r})\left[\sum_{\mathrm{j=1}}^{i}\sum_{\mathrm{n=1}}^{m}f_M^{*}\left(\vec{r}',\delta\varepsilon_{\mathrm{j}}^{\mathrm{n}}\right)\right]\right.\\&\left.+\left[\sum_{\mathrm{i=1}}^{i}\sum_{\mathrm{m=1}}^{m}f_M\left(\vec{r}',\delta\varepsilon_{\mathrm{i}}^{\mathrm{m}}\right)\right]f_X^{*}(\vec{r}')+\sum_{\mathrm{i=1}}^{i}\sum_{\mathrm{j=1}}^{i}\sum_{\mathrm{m=1}}^{m}\sum_{\mathrm{n=1}}^{m}f_M\left(\vec{r},\delta\varepsilon_{\mathrm{i}}^{\mathrm{m}}\right)f_M^{*}\left(\vec{r}',\delta\varepsilon_{\mathrm{j}}^{\mathrm{n}}\right)\delta\left(\Delta\mathrm{I_m},\Delta\mathrm{I_n}\right)\right\}.\end{aligned} \tag{5.7}$$

The Kroneker delta, $\delta\left(\Delta\mathrm{I_m},\Delta\mathrm{I_n}\right)$, is required in the last term because within a uniform magnetic domain, nuclear transitions with different changes in angular momentum cannot scatter the same photon. Figure 2.4 shows the transitions in ^{57}Fe that yield $\delta\left(\Delta\mathrm{I_m},\Delta\mathrm{I_n}\right)=1$: absorption peaks 1 and 4 ($\Delta\mathrm{I}=-1$), peaks 2 and 5 ($\Delta\mathrm{I}=0$), and peaks 3 and 6 ($\Delta\mathrm{I}=+1$). With the definition:

$$\vec{R} \equiv \vec{r} - \vec{r}' \quad , \tag{5.8}$$

$$I\left(\Delta\vec{k},\mathrm{E}\right) = \sum_{\vec{R}} e^{-i\Delta\vec{k}\cdot\vec{R}} \left\{ P_{XX}\left(\vec{R}\right) + P_{XM}\left(\vec{R},\mathrm{E}\right) + P_{MX}\left(\vec{R},\mathrm{E}\right) + P_{MM}\left(\vec{R},\mathrm{E}\right) \right\} \tag{5.9}$$

where we have defined the four Patterson functions:

$$P_{XX}\left(\vec{R}\right) \equiv \sum_{\vec{r}} f_X(\vec{r}) f_X^*\left(\vec{r}+\vec{R}\right) \tag{5.10}$$

$$P_{XM}\left(\vec{R},\mathrm{E}\right) \equiv \sum_{\vec{r}} \sum_{\mathrm{i=1}}^{i} \sum_{\mathrm{m=1}}^{m} f_X(\vec{r}) f_M^*\left(\vec{r}+\vec{R},\delta\varepsilon_{\mathrm{i}}^{\mathrm{m}}\right) \tag{5.11}$$

$$P_{MX}\left(\vec{R},\mathrm{E}\right) \equiv \sum_{\vec{r}} \sum_{\mathrm{i=1}}^{i} \sum_{\mathrm{m=1}}^{m} f_M\left(\vec{r},\delta\varepsilon_{\mathrm{i}}^{\mathrm{m}}\right) f_X^*\left(\vec{r}+\vec{R}\right) \tag{5.12}$$

$$P_{MM}\left(\vec{R},\mathrm{E}\right) \equiv \sum_{\mathrm{i=1}}^{i} \sum_{\mathrm{j=1}}^{i} \sum_{\mathrm{m=1}}^{m} \sum_{\mathrm{n=1}}^{m} f_M\left(\vec{r},\delta\varepsilon_{\mathrm{i}}^{\mathrm{m}}\right) f_M^*\left(\vec{r}+\vec{R},\delta\varepsilon_{\mathrm{j}}^{\mathrm{n}}\right) \delta\left(\Delta\mathrm{I}_{\mathrm{m}},\Delta\mathrm{I}_{\mathrm{n}}\right) \quad . \tag{5.13}$$

Note that $P_{XX}\left(\vec{R}\right)$ is the well-known Patterson function for x-ray diffraction [5].

The Patterson functions $P_{XM}\left(\vec{R},\mathrm{E}\right)$ and $P_{MX}\left(\vec{R},\mathrm{E}\right)$ are the spatial correlation functions for a photon that is scattered by Mössbauer scattering from one atom and by x-ray scattering from another atom. It can be shown that when the crystal has inversion symmetry, $P_{XM}\left(\vec{R},\mathrm{E}\right) = P_{MX}^*\left(\vec{R},\mathrm{E}\right)$, so the sum $P_{XM}\left(\vec{R},\mathrm{E}\right) + P_{MX}\left(\vec{R},\mathrm{E}\right)$ is a real number. This interference between x-ray scattering and Mössbauer scattering has been studied previously. There is a large phase shift of the Mössbauer scattering when E is tuned through resonance, but not so for the x-ray scattering. Therefore, this interference has usually been observed in Mössbauer energy spectra, obviating the need to build a Mössbauer diffractometer. Since x-ray scattering is independent of E, it may be possible to isolate the Mössbauer scattering through energy-dependent diffraction studies. Note that if the x-ray scattering could be removed as a constant factor, the diffracted *intensity* would be proportional to $\sum_{\vec{R}} e^{-i\Delta\vec{k}\cdot\vec{R}} f_M(\vec{R})$. Such x-ray/Mössbauer interference-type diffraction experiments have therefore been proposed as a solution to the phase problem in diffraction (see for example [6]). In principle, the interference between x-ray scattering and Mössbauer scattering can be used to obtain chemical environment selectivity in diffraction experiments. Unfortunately for $^{57}Fe_3Al$, the x-ray scattering into superlattice diffractions is too weak to provide useful chemical environment selectivity by the interference of x-ray and Mössbauer scattering. We have, however, performed an extensive analysis of the interference phenomena observed in the bcc fundamental diffractions, for which x-ray scattering is strong. Section 5.3 describes this work.

The Patterson function $P_{MM}(\vec{R},\mathrm{E})$ of Eq. 5.13 is the basis for our chemical environment selective diffraction experiments on $^{57}Fe_3Al$. Since the x-ray scattering into the superlattice diffractions is very weak, the superlattice peaks are determined primarily by $P_{MM}(\vec{R},\mathrm{E})$. This is convenient because it is then possible to identify chemical environment selectivity directly in differences of on- and off-resonance diffraction patterns (see § 4.3).

5.2.2 Mössbauer and x-ray scattering factors

The Patterson functions (Eqs. 5.10 through 5.13) are defined in terms of the Mössbauer and x-ray scattering factors. We now address the energy dependence of the scattering factors, which provide the phase and amplitude information necessary to understand the interference terms. The Mössbauer scattering factor, $f_M(\vec{r},\delta\varepsilon_{\mathrm{i}}^{\mathrm{m}})$, is:

$$f_M(\vec{r},\delta\varepsilon_{\mathrm{i}}^{\mathrm{m}}) = -G_{\mathrm{i}}^{\mathrm{m}}\rho(\vec{r},\mathrm{i})\left(\frac{2(\delta\varepsilon_{\mathrm{i}}^{\mathrm{m}})}{\Gamma}+i\right)^{-1} \tag{5.14}$$

where $G_{\mathrm{i}}^{\mathrm{m}}$ includes all the information regarding the Mössbauer transition probability such as spin levels, internal conversion coefficient, Clebsch-Gordon coefficients, polarization factors, and Lamb-Mössbauer factors [6-8]. Here $\rho(\vec{r},\mathrm{i})$ is the probability of finding an ^{57}Fe nucleus with chemical environment i at position $\vec{r}$. The last factor in Eq. 5.14 describes the energy dependence of the phase [largest when $\delta\varepsilon_i^{\mathrm{m}} = 0$ (at resonance)]. The full natural linewidth is represented by Γ.

The x-ray scattering factor, $f_X(\vec{r},\mathrm{E})$, is:

$$f_X(\vec{r},\mathrm{E}) = f_{X0}(\vec{r}) = -i\left(f_{Fe}\rho_{Fe}(\vec{r}) + f_{Al}\rho_{Al}(\vec{r})\right) \tag{5.15}$$

where f_{Fe} and f_{Al} contain all of the x-ray scattering information [4]. The negative *i* term is needed to preserve the phase information of the scattered radiation: the scattered photons are 180^0 out-of-phase with the incident radiation, which is assumed to have the phase of +*i*. Here $\rho_{Fe}(\vec{r})$ is the probability of finding an Fe atom at position $\vec{r}$, and $\rho_{Al}(\vec{r})$ is the probability for Al atoms.

Writing $f_{M0} = -\sum_{\mathrm{m}=1}^{m}\sum_{\mathrm{i}=1}^{i} G_{\mathrm{i}}^{\mathrm{m}}\rho(\vec{r},\mathrm{i})$ provides another useful quantity, the ratio of Mössbauer to x-ray scattering, r_{MX}:

$$r_{MX} = \frac{f_{M0}}{f_{X0}}\mathcal{R} \quad , \tag{5.16}$$

where:

$$\mathcal{R} = \frac{\displaystyle\int_{E_{\min}^{bin\#}}^{E_{\max}^{bin\#}} \sum_{m=1}^{m}\sum_{i=1}^{i}\left(\left(\frac{2(\delta\varepsilon_{i}^{m})}{\Gamma}\right)^{2}+1\right)^{-1} dE}{\displaystyle\int_{-\infty}^{\infty} \sum_{m=1}^{m}\sum_{i=1}^{i}\left(\left(\frac{2(\delta\varepsilon_{i}^{m})}{\Gamma}\right)^{2}+1\right)^{-1} dE} \tag{5.17}$$

$E_{\min}^{bin\#}$ and $E_{\max}^{bin\#}$ are the minimum and maximum values of the photon energy of velocity bin#. The numerator of $\mathcal{R}$ is averaged for the velocity bins used to acquire the data (bin2 through bin5 for the $^{57}Fe_3Al$ data). The interference calculation described in § 5.5 uses r_{MX} as the main free parameter. Section 5.3 describes estimations of r_{MX} by modeling the $^{57}Fe_3Al$ samples.

While the primary purpose of this chapter is to describe the interference effects between the various types of photons, an examination of the case where no interference is allowed is also interesting. The scattering intensities become:

$$I_{total}^{no\ interf.} = I_{X}^{no\ interf.} + I_{M}^{no\ interf.} \quad ,$$

$$I_{X}^{no\ interf.}(\mathrm{E}) = f_{X}(\mathrm{E}) f_{X}(\mathrm{E}) = f_{X0}^{2} \quad \text{, and} \tag{5.18}$$

$$I_{M}^{no\ interf.}(\mathrm{E}) = \sum_{i=1}^{i}\sum_{j=1}^{i}\sum_{m=1}^{m}\sum_{n=1}^{m} f_{M}^{*}(\delta_{i}^{m}) f_{M}(\delta_{j}^{n}) \delta(i,j)\delta(m,n) = \frac{f_{M0}^{2}}{\displaystyle\sum_{m=1}^{m}\sum_{i=1}^{i}\left[1+\left(\frac{2(\delta_{i}^{m})}{\Gamma}\right)^{2}\right]}.$$

Note that the x-ray scattering intensity lacks a functional dependence on energy and will remain constant. The Mössbauer scattering intensity retains an energy dependence and shows the familiar Lorentzian peak shape of Mössbauer spectrometry.

5.3 Multislice calculations

This section explains the multislice computer calculations that are used to determine a value for r_{MX} and to justify the use of kinematical scattering theory. In the multislice calculation the different types of photons are transmitted through and scattered from a sequence of thin layers ("slices") of material. The ratio r_{MX} is determined by keeping track of the number and type of photons that escape the sample after scattering. The multislice calculations also determine which photon interactions are significant enough to warrant tracking, indicating whether a kinematic scattering modeling is sufficient. Multislice calculations were performed for both the ^{57}Fe and ^{57}Fe$_3$Al samples.

5.3.1 Scattering processes

Only the 14.41 keV source photons are involved in Mössbauer absorption and scattering processes. Furthermore, the diffraction pattern is formed only by photons that scatter in the sample and escape to the surface. Both the recoilless and non-recoilless 14.41 keV photons from the source must be considered, as diffraction peaks include both x-ray and Mössbauer components. All other events are assumed to create background noise but no useful diffraction peaks. This includes all other non-14.41 keV photons from the ^{57}Co source, as well as the conversion x-rays created through the decay of the excited Mössbauer nuclei.

Scattering of the 14.41 keV photons with the sample occurs by:

(1) non-recoilless from source, coherently scattered (x-ray);
(2) non-recoilless from source, incoherently scattered (x-ray);
(3) recoilless from source, coherently scattered (x-ray);
(4) recoilless from source, incoherently scattered (x-ray);
(5) recoilless from source, resonantly absorbed, recoillessly re-emitted (Mössbauer); and

(6) recoilless from source, resonantly absorbed, non-recoillessly re-emitted (Mössbauer).

While only the coherently scattered photons create the diffraction peaks, the incoherent scattering adds to the background of the diffraction pattern. Thus, it is useful to know the amount of coherent and incoherent scattering. Both are determined by the multislice calculation.

All of the above can be considered single scattering processes, as only a single interaction with the sample takes place. Double scattering processes, such as (3) from above leading to (5) or vice-versa, were found to be secondary effects that can be ignored.

5.3.2 Description of the multislice calculation

The multislice calculation tracks the photon interactions through a simulated sample with the same scattering and absorption cross sections as the real samples. The calculation divides the simulated sample into a number of slices and calculates the scattering and absorption in each slice. Slice thickness is limited by the assumption that all interactions can be handled by a linear combination of their probabilities. Nonlinear effects arise if the slice is too thick, decreasing the accuracy of the calculation.

Figure 5.4 shows a diagram of the multislice calculation. The 14.41 keV photons from the source are divided into two groups, recoilless and non-recoilless. The recoilless photons may interact in both x-ray and Mössbauer processes (x-ray coherent scattering, x-ray incoherent scattering, x-ray absorption, and Mössbauer absorption). The non-recoilless photons interact with the slice material through x-ray processes only. Photons that are x-ray absorbed are lost, since scattering is not possible. X-ray absorption includes all x-ray processes except scattering, but is primarily due to photoelectric absorption. Both x-ray coherent and incoherent scattered photons are tracked back to surface of the sample.

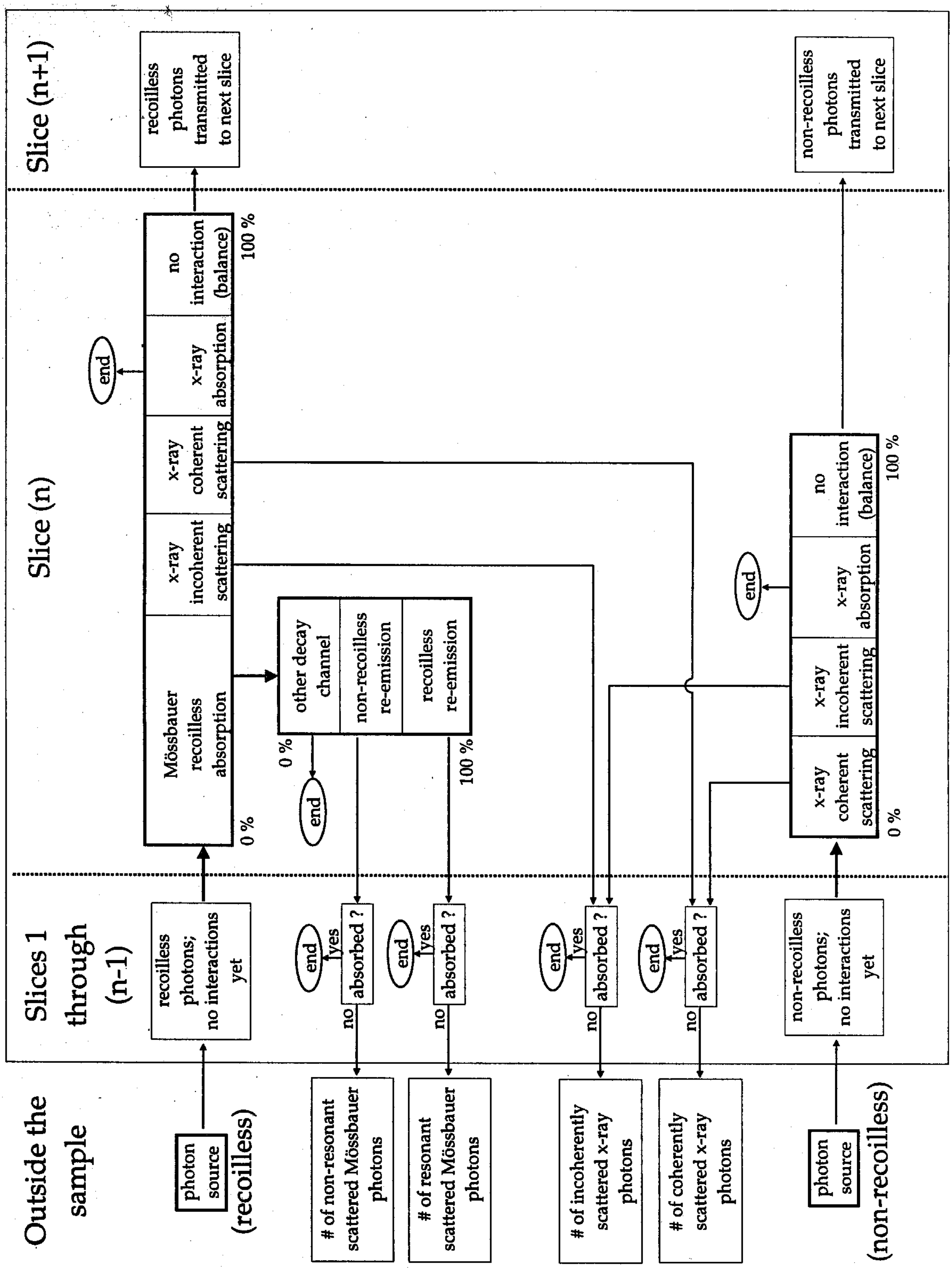

Figure 5.4 Diagram of the multislice calculation described in section 5.3.2. Only the 14.41 keV photons are tracked through the sample.

Absorption of these photons is allowed in the calculation, but further scattering is ignored. If the x-ray scattered photons are not absorbed, they are counted as scattered photons of the appropriate type.

Mössbauer-absorbed (resonant) photons are further categorized by the method of decay: recoilless re-emission, non-recoilless re-emission, and internal conversion decays. The multislice calculation tracks the re-emissions back to surface of the sample. The recoilless re-emitted photons are attenuated through both Mössbauer and x-ray absorption; the non-recoilless, by x-ray processes only. The non-recoilless re-emitted photons are treated as incoherently scattered Mössbauer photons. A more thorough calculation could consider these photons as contributing a smooth structure to the diffraction pattern by thermal diffuse scattering. If the re-emitted photons are not absorbed, they are counted as scattered Mössbauer photons of the appropriate type. The other decay channel produces are lost; these include internal conversion decays such as Auger electrons and Fe x-rays (see Fig. 3.8b).

Photons that do not interact in a slice are propagated to the next. Once a photon has propagated all the way through the sample, it is lost since it can no longer interact.

5.3.3 Multislice calculation for the $^{57}Fe_3Al$ samples

The multislice calculation for DO_3 $^{57}Fe_3Al$ samples consists of two separation calculations, one each for the 0Al and 4Al environments. The following data were used:

(1) $^{57}Fe_3Al$ sample,
(2) 95% ^{57}Fe enrichment,
(3) 5 to 7 micron sample thickness,
(4) 7.02 g/cm^3 density,
(5) 5.72 x 10^{-8} cm layer thickness (3 Fe and 1 Al atoms),
(6) 14.41 keV photons, and
(7) 80% recoil free fraction

The inverse lengths for scattering and absorption for the ^{57}Fe$_3$Al are:

(1) coherent x-ray scattering	4.77 cm^{-1}
(2) incoherent x-ray scattering	0.77 cm^{-1}
(3) total x-ray absorption	365 cm^{-1}
(4) total Mössbauer absorption	122,400 cm^{-1}
(5) 0Al Mössbauer absorption	1,432 cm^{-1}
(6) 4Al Mössbauer absorption	1,665 cm^{-1}

The x-ray scattering data are from Ref. 9.

The calculation use 25 slices of 400 layers each (0.23 microns) to approximate the real samples. At this thickness the nonlinear behavior of the interaction cross sections is less than 2%.

Double scattering processes were determined to be negligible. Double scattered Mössbauer photons amount to only 3% of the single scattered photons and the x-ray photons provide similar results. However, absorption of the single scattered photons is appreciable. (Absorption occurs as the scattered photons attempt to escape the surface of the sample). This secondary absorption results in a ~ 30% decrease in the scattering intensity.

The results of the ^{57}Fe$_3$Al multislice calculation are presented in § 5.3.5. Results are also presented for a calculation were no Mössbauer absorption is allowed.

5.3.4 Multislice calculation for the ^{57}Fe samples

A multislice calculation was also performed for the bcc ^{57}Fe foil samples. The following data were used in this calculation:

(1) ^{57}Fe sample,
(2) 95% ^{57}Fe enrichment,

(3) 2.5 micron thickness,
(4) 8.02 g/cm^3 density,
(5) 5.72 x 10^{-8} cm layer thickness (4 Fe atoms),
(6) 14.41 keV photons, and
(7) 80% recoil free fraction.

The inverse lengths for scattering and absorption for the ^{57}Fe are:

(1) coherent x-ray scattering	6.34 cm^{-1}
(2) incoherent x-ray scattering	0.80 cm^{-1}
(3) total x-ray absorption	539 cm^{-1}
(4) total Mössbauer absorption	161,500 cm^{-1}
(5) on-res Mössbauer absorption	4,457 cm^{-1}

The x-ray scattering data are from Ref. 9.

The calculation uses 25 slices of 200 layers (0.11 microns) each. Double scattering processes were again determined to be negligible.

5.3.5 Multislice calculation results and comments

Tables 5.1-2 list the results for the ^{57}Fe$_3$Al multislice calculations. The results for ^{57}Fe are listed in Table 5.3. All tables contain the calculated percentages for the coherent x-ray, incoherent x-ray, recoillessly re-emitted Mössbauer, and non-recoillessly re-emitted Mössbauer scattering. Table 5.4 presents results for x-ray scattering only for ^{57}Fe$_3$Al.

Table 5.1 Results from the ^{57}Fe$_3$Al multislice calculation in § 5.3.3 for the 0Al condition.

Result category	# of photons	ratios
starting percentage of photons:	100%	
coherent x-ray scattering:	0.1463%	5.13
incoherent x-ray scattering:	0.0285%	1.00
recoilless Mössbauer scattering:	1.8500%	64.9
non-recoilless Mössbauer scattering:	0.6153%	21.6

Table 5.2 Results from the $^{57}Fe_3Al$ multislice calculation in § 5.3.3 for the 4Al condition.

Result category	# of photons	ratios
starting percentage of photons:	100%	
coherent x-ray scattering:	0.1391%	5.05
incoherent x-ray scattering:	0.0275%	1.00
recoilless Mössbauer scattering:	1.9743%	71.7
non-recoilless Mössbauer scattering:	0.6785%	24.6

Table 5.3 Results from the ^{57}Fe multislice calculation in § 5.3.4.

Result category	# of photons	ratios
starting number of photons:	100%	
coherent x-ray scattering:	0.0865%	6.27
incoherent x-ray scattering:	0.0138%	1.00
recoilless Mössbauer scattering:	2.2546%	163.
non-recoilless Mössbauer scattering:	0.8358%	60.5

Table 5.4 Results from the $^{57}Fe_3Al$ multislice calculation in § 5.3.3 with only x-ray events allowed.

Result category	# of photons	ratios
starting number of photons:	100%	
coherent x-ray scattering:	0.2246%	6.17
incoherent x-ray scattering:	0.0364%	1

These results show two interesting features. First, x-ray scattering is suppressed when both Mössbauer and x-ray events are allowed to occur. The Mössbauer absorption steals photons that would have otherwise undergone x-ray scattering. The coherent x-ray scattering decreases 35% in the presence of Mössbauer scattering. Second, the Mössbauer to x-ray scattering ratio, r_{MX}, can be estimated from the coherent scattering results. These ratios are reported in Table 5.5. However, the accuracy of this technique is limited as the Mössbauer scattering cross section for each resonance condition has some uncertainty. While both the cross sections for x-ray absorption and scattering are tabulated and reliable, only the total Mössbauer absorption cross section is known. The Mössbauer scattering cross section was calculated assuming a knowledge of the absorption cross section and some logical assumptions.

The next subsection provides an alternate method of determining r_{MX} from the experimental data.

5.3.6 Experimental determination of r_{MX}

The experimental data provide an additional justification for the Mössbauer to x-ray scattering ratio, r_{MX}. Figure 4.1 shows the Fe_3Al95 data sets for both on-resonance and off-resonance conditions. The summed data substantially removes the interference effects by averaging them, thus providing a series of fundamental peaks, (200), (211), and (222), which can be used to determine r_{MX}. Furthermore, Mössbauer and x-ray scattering are affected similarly by sample characteristics such as crystallographic texture and peak multiplicity. Thus, these characteristics will affect peaks from all three resonance conditions in largely the same way.

Figure 5.5 plots the peak areas for the three resonance conditions along with the predicted peak intensity reductions as a function of peak order. X-ray scattering intensities decrease for increasing peak order due to two effects: the form factor[♦] for x-ray scattering [10] and the Debye-Waller (D-W) factor, e^{-2M}. Mössbauer scattering intensities decrease due to the Lamb-Mössbauer (L-M) factor, e^{-4M}. The D-W and L-M factors are described in § 2.1.2. The intensity falloff for x-ray scattering is 3.5 times greater than for Mössbauer scattering.

[♦] Mössbauer scattering is from the nucleus, which acts as a "point" scatterer; x-ray scattering is from the electron cloud, whose size is comparable to the wavelength of the 14.41 keV photon. Thus, the x-ray scattering experiences a form factor rolloff, or reduction in intensity, for higher order diffraction peaks while the Mössbauer does not.

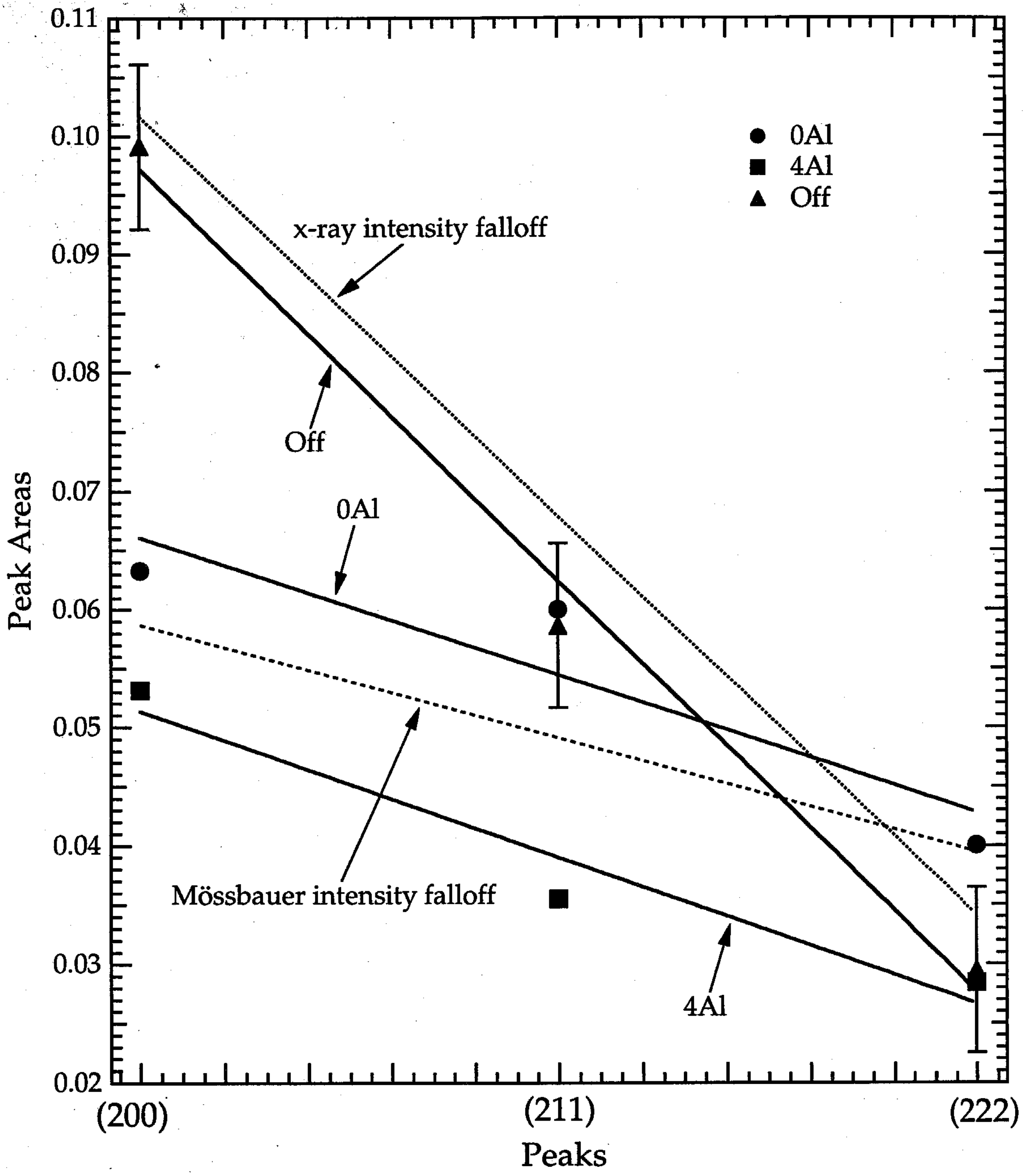

Figure 5.5 Summed peak intensities for all three resonance conditions of the $^{57}Fe_3Al95$ data set. The x-ray and Mössbauer intensity falloff lines are the predicted peak intensity reductions as a function of peak order for x-ray and Mössbauer scattering, respectively.

The slopes of the lines provide the useful information. The slopes of three resonance condition lines are assumed to be a linear combination of the slopes of the two types of intensity falloff (Mössbauer and x-ray). The ratio r_{MX} is estimated by determining the percentage of each falloff type in the resonance conditions. For example, the off-resonance condition should not contain any Mössbauer scattering. Thus, the falloff slope of the off-resonance condition line should be equal to the slope of the x-ray falloff line. Figure 5.5 shows this to be true. However, this detailed agreement is somewhat fortuitous, since sample texture could have made interpretation more difficult. The on-resonance conditions should contain a mixture of the x-ray and Mössbauer types of falloff, and the percentages of each were determined by the lever rule. The resulting percentages provide r_{MX} for the (211) peak, which can be extrapolated to the transmitted (000) peak for comparison with the multislice results.

Not much faith should be placed in this technique. First, linear fits were made to inherently non-linear processes (Lamb-Mössbauer, etc.). Second, variations in the experimental data due to texture and other effects were not taken into account. Third, using a linear combination of slopes for the falloffs may be incorrect, as changes in r_{MX} for each peak are not necessarily linear.

Table 5.5 presents the Mössbauer to x-ray scattering ratios, r_{MX}, from the multislice calculation results of § 5.3.5 and the experimental results from analysis of Fig 5.5. The experimental results have been extrapolated to the transmitted beam (000) peak to remove the intensity falloff contributions and facilitate comparison with the multislice results. The value of r_{MX} at the transmitted beam for ^{57}Fe (Table 5.3) is 26. The strong crystallographic texture of the ^{57}Fe samples prevents the experimental method from being used.

Table 5.5 Comparison of the Mössbauer to x-ray scattering ratios, r_{MX}, for the transmitted beam (000).

	r_{MX} for the (000) peak:	
Resonance Cond.	Multislice Calculation	Experimental
0Al	12.6	6.8
4Al	14.2	4.7

5.4 Monte Carlo simulation of chemical environment selective diffraction from the $^{57}Fe_3Al$ sample

Figures 4.5 and 4.7 show overlap among the absorption peaks of the different chemical environments. Because the diffraction patterns are collected from velocity bins that contain overlapping peaks, we need to know if the different chemical environments diffract in the same manner. For example, does the 1Al environment give rise to the same superlattice peaks as the 0Al environment? This question is important because Mössbauer diffraction peaks from the 0Al and 1Al environments are acquired in the same velocity bin. A Monte Carlo simulation (MCS) was performed to answer these questions.

The Monte Carlo simulation[♦] used a bcc lattice of Fe–25% Al with a total of 65536 sites and periodic boundaries (the crystal was a cube with 32 unit cells on an edge, and 2 atoms per unit cell). Atom movements occurred by a vacancy algorithm, where a solitary vacancy on the lattice changed sites with a first-nearest-neighbor atom [11-13]. The characteristic rate for an interchange of the vacancy and the $j^{\underline{th}}$ neighboring atom is ω_j, but the $j^{\underline{th}}$ atom is competing with the other neighbors of the vacancy for an atom-vacancy interchange. One of these atoms was selected to move by picking a random number, using the $\{\omega_i\}$ as weights for the different movements. An activated state rate theory was used to

---

[♦] The MCS code was written by L. Anthony [13].

calculate the characteristic transition rates, $\{\omega_i\}$. To interchange sites with the vacancy, the candidate atom must surmount a barrier of height E*. The energy required is the difference between E* and E_j, the energy of the j^th^ atom in its initial state. We determine E_j with first- and second-nearest-neighbor (1nn and 2nn) environments of the candidate j^th^ atom. If the candidate atom is of type "A," for example:

$$E_j = n_{AA1}V_{AA1} + n_{AB1}V_{AB1} + n_{AA2}V_{AA2} + n_{AB2}V_{AB2} \quad , \tag{5.19}$$

leading to a characteristic jump frequency of:

$$\omega_j \propto \exp\left(-\frac{(E^* - E_j)}{k_B T}\right) . \tag{5.20}$$

Our candidate A-atom has n_{AA1} A-atoms and n_{AB1} B-atoms in its 1nn shell and n_{AA2} A-atoms and n_{AB2} B-atoms in its 2nn shell.

The strength parameters ($V_{AA1} = 0.91$, $V_{BB1}=0.91$, $V_{AB1}=0.00$, $V_{AA2} = 0.807$, $V_{BB2}=0.807$, and $V_{AB2}=0.00$) were set to simulate the $^{57}Fe_3Al$ sample. The lattice started with random ordering progressed towards full ordering. The code was stopped after 400,000 steps, as the state of order in the alloy simulated the sample, as Table 5.6 illustrates.

Table 5.6 Comparison of the Monte Carlo simulation (MCS) state of order to the ^{57}Fe$_3$Al sample used in the experiments. The sample data are provided by the CEMS data from § 3.2.6. The 0Al and 1Al environments cannot be separated in the experimental data.

environment (Al 1nn)	^{57}Fe$_3$Al sample	MCS
0,1	29 %	33 %*
2	11.6 %	8.3 %
3	13.8 %	18.1 %
4	38.8 %	40 %
5	2.5 %	0.4 %

*The 0,1 environment is 21% 0Al 1nn and 12% 1Al 1nn.

Long range order (LRO) was measured by first obtaining the diffracted wave, $\psi(\vec{k})$, as the three-dimensional Fourier transform of the alloy, and then calculating $\psi^*\psi$. The degree of B2 order was obtained by integrating $\psi^*\psi$ in a cubical volume of edge length Δk centered around the (100) reciprocal lattice point[♦] :

$$\mathrm{I(100)} = \int_{k_x=\frac{2\pi}{a}-\frac{\Delta k}{2}}^{\frac{2\pi}{a}+\frac{\Delta k}{2}} \left[\int_{k_y=-\frac{\Delta k}{2}}^{+\frac{\Delta k}{2}} \left[\int_{k_z=-\frac{\Delta k}{2}}^{+\frac{\Delta k}{2}} \left| \sum_{\text{all sites}} f(\vec{r})\exp(-i\vec{k}\cdot\vec{r}) \right|^2 dk_z \right] dk_y \right] dk_x \quad . \tag{5.21}$$

Measuring LRO requires a decision on the spatial extent of the LRO, which is not infinite in either Monte Carlo simulations or in real alloys. We found it most meaningful to choose $\Delta k = \left(\frac{9}{32}\right)\frac{2\pi}{a}$.

The ordinary x-ray diffraction pattern was calculated by setting the atomic form factor, $f(\vec{r})$, as unity for the Fe atoms and zero for Al atoms. The chemical environment

---

[♦] An LRO parameter could be obtained by normalizing by an equivalent integral around the fundamental (110) reciprocal lattice point, and taking the square root. For convenience, however, we present the diffracted intensity directly, denoted as "I(100)."

selective diffraction patterns were calculated by setting $f(\bar{r}) = 1$ for the Fe atoms in the desired environment and zero for all other atoms (Al atoms and Fe atoms in different environments). Intensities were calculated for the three families of diffraction peaks — the $\left(\frac{1}{2}\frac{1}{2}\frac{1}{2}\right)$, (100), and (110) peaks.

Table 5.7 summarizes and Fig. 5.6 shows the results of the simulation. The contributions from the different chemical environments are shown for the three families of peaks. The (110) represents the bcc fundamental peak family, and it is found for all scattering mechanisms. The intensities for the (110) correspond directly to the percentages of each type of environment: the 4Al environment is 40% of the sample and its (110) diffraction peak has an intensity of 0.4. The important result from these simulations is that the $\left(\frac{1}{2}\frac{1}{2}\frac{1}{2}\right)$ diffractions, which represents the 0Al resonance condition, derives its scattering almost exclusively from the 0Al and 1Al environment. Thus, analysis of the $\left(\frac{1}{2}\frac{1}{2}\frac{1}{2}\right)$ superlattice peaks should be much simpler than the (100) peaks, which derive their scattering from all of the Mössbauer environments. Note, however, that the 2Al environment has much weaker superlattice peaks than suggested by the number of 2Al environments. This shows that the 2Al environment has no long range periodicity other than bcc.

Table 5.7 The results of the Monte Carlo simulation (MCS). The numbers shown have been normalized to the fundamental (110–type) peak.

environment (Al 1nn)	Diffraction peak families		
	$\left(\frac{1}{2}\frac{1}{2}\frac{1}{2}\right)$	(100)	(110)
0	0.1802	0.2063	0.2087
1	0.0544	0.1010	0.1246
2	0.0016	0.0001	0.0847
3	0.0000	0.1450	0.1830
4	0.0000	0.3970	0.4010
5	0.0000	0.0040	0.0046
(x-ray)	0.7370	0.5600	1.0000

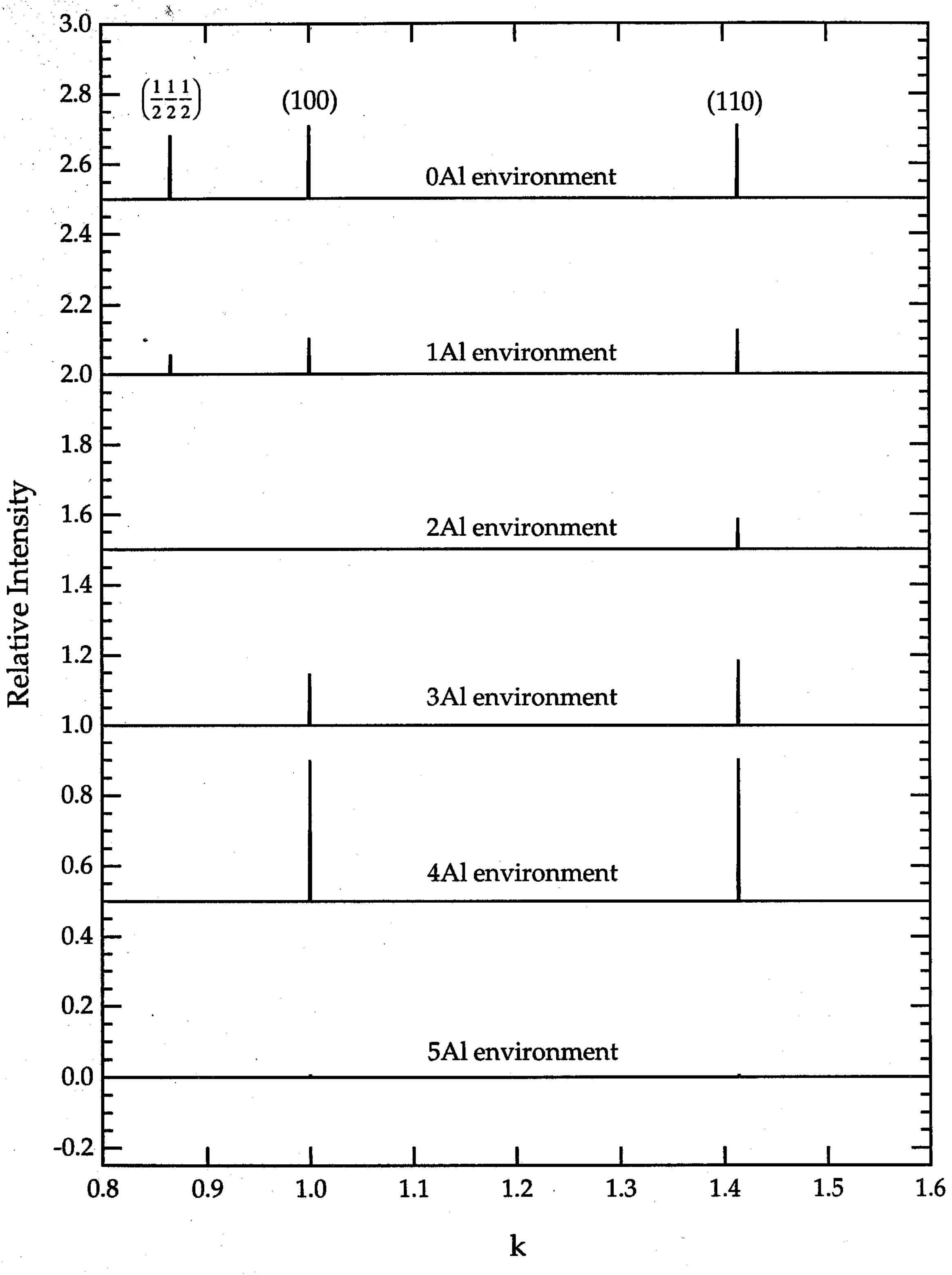

Figure 5.6 Results for the Monte Carlo Simulation. Only the chemical environment selective diffraction results are shown.

5.5 Calculation of Mössbauer scattering spectra

The model calculates coherent Mössbauer scattering spectra as a function of energy by including:

(1) normal x-ray scattering,
(2) interference between Mössbauer and x-ray scattered photons, and
(3) interference between photons scattered from different Mössbauer absorption peaks (Mössbauer self-interference).

Only the intensities of the bcc fundamental peaks were calculated. Both families of superlattice peaks, $\left(\frac{1}{2}\frac{1}{2}\frac{1}{2}\right)$ and (111), possess much smaller x-ray contributions. Thus, the superlattice peaks are formed almost exclusively from the $P_{MM}\left(\vec{R},\mathrm{E}\right)$ term of the kinematical diffraction theory (§ 5.2), and are therefore straightforward to interpret.

Crystallographic texture effects should not significantly impact the work here. Comparisons of real and modeled data will be limited to a single diffraction peak at a time, and all of the resonance conditions used to collect these peaks are affected by the crystallographic texture in the same manner.

The modeling was performed in Igor Pro♦ through the use of its macro language. Numerical functions were created for each resonant absorption peak and the x-ray scattering and were based on the Patterson functions and scattering factors described in § 5.2.1. Three types of intensity functions were calculated:

(1) no interference allowed ($P_{XX}\left(\vec{R}\right)$ of Eq. 5.10 plus a special case of $P_{MM}\left(\vec{R},\mathrm{E}\right)$ of Eq. 5.13 where i=j in the sum),
(2) interference between individual Mössbauer scattering only ($P_{XX}\left(\vec{R}\right)$ plus $P_{MM}\left(\vec{R},\mathrm{E}\right)$ of Eq. 5.13), and

---

♦ A data analysis and graphing program made by WaveMetrics, Inc., Lake Oswego, OR.

(3) all possible interference effects ($P_{XX}(\vec{R}) + P_{XM}(\vec{R},\mathrm{E}) + P_{MX}(\vec{R},\mathrm{E}) + P_{MM}(\vec{R},\mathrm{E})$).

Calculations of type (3) proved most accurate for modeling the intensities of diffraction peaks from the ^{57}Fe$_3$Al samples. The diffraction peaks from the ^{57}Fe sample show weaker interference effects and thus benefit less from the interference modeling [compared to intensity calculations of type (1)]. The ^{57}Fe Mössbauer absorption peaks are highly separated in energy (less Mössbauer - Mössbauer interference), and the x-ray scattering is much weaker for the ^{57}Fe diffraction peaks (r_{MX} is smaller). The value of r_{MX} is important only to intensity calculations of type (3).

The modeling was performed over a 20 mm/sec (9.6 x 10^{-7} eV) energy window that is wide enough to contain all of the Mössbauer absorption peaks. The absorption peaks were modeled with fits from the CEMS data (§ 3.2.6) from the experimental samples. Thus, peak shape, energy, and intensity were consistent with the samples actually used.

Figures 5.7ab and 5.8ab show modeled intensity curves as a function of energy for ^{57}Fe and ^{57}Fe$_3$Al, respectively. The velocity bins are derived from the real experiments. As these figures are meant to be illustrative, r_{MX} equals 10. The ^{57}Fe spectra shown in Figs. 5.7ab are composed of one sextet of resonant peaks. The ^{57}Fe$_3$Al curves shown in Figs. 5.8ab are composed of the five sextets of resonant peaks.

5.5.1 Comparing the interference calculation to the experimental data for ^{57}Fe$_3$Al

The calculated intensities are compared to the real data at eight points — the velocity bins for absorption peak 6 (bin2 through bin5) for the 0Al and 4Al conditions. The experimental data are derived from the diffraction peak areas corresponding to their respective velocity bins (the component diffraction patterns of Figs. 4.4 and 4.6).

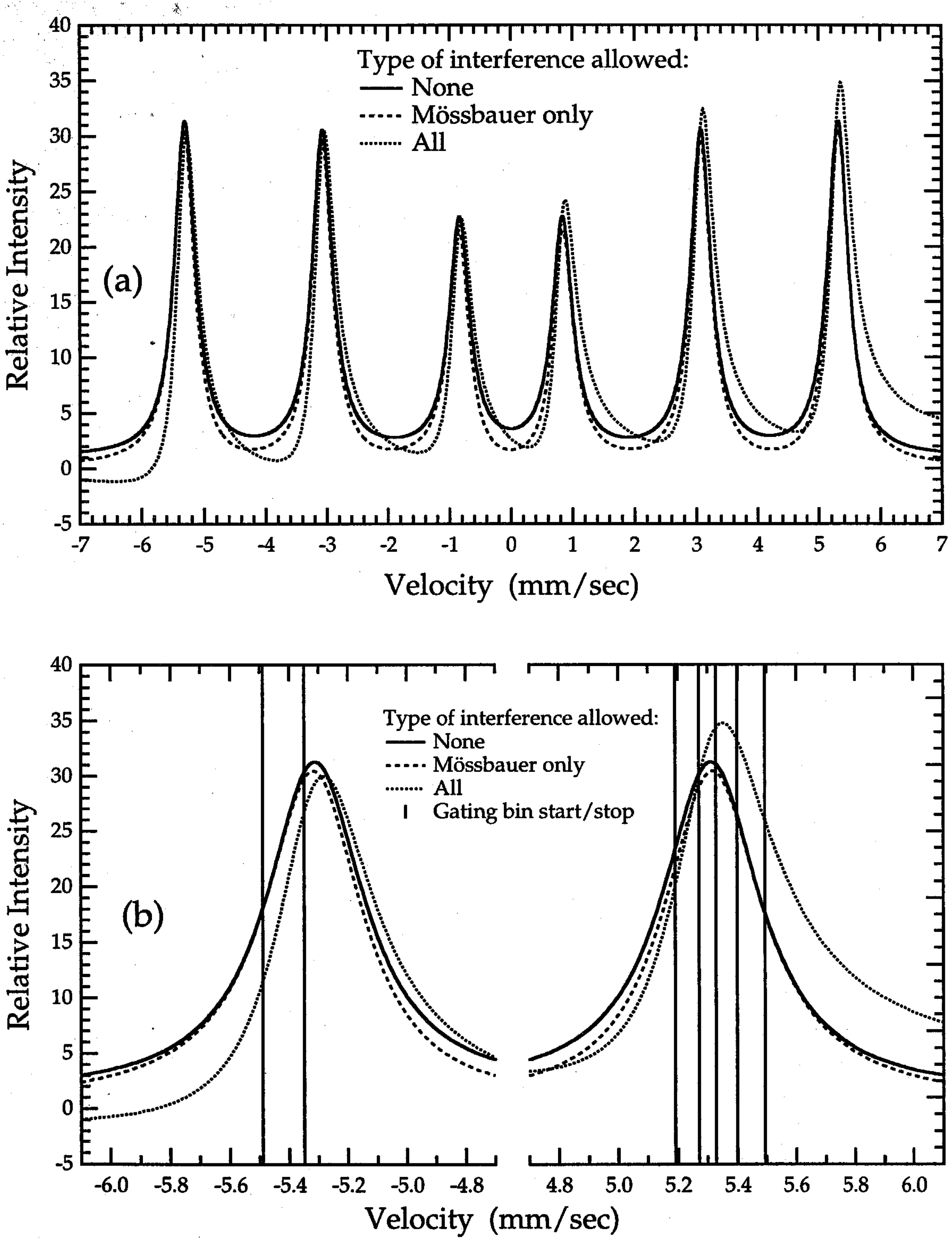

Figure 5.7 (a) Modeled intensity curves as a function of energy for the ^{57}Fe sample. A Mössbauer to x-ray scattering ratio of 10 was used.
(b) Enlargement of (a) with the 0Al velocity bins shown. While the data are modeled, the velocity ranges are those of the real experiment.

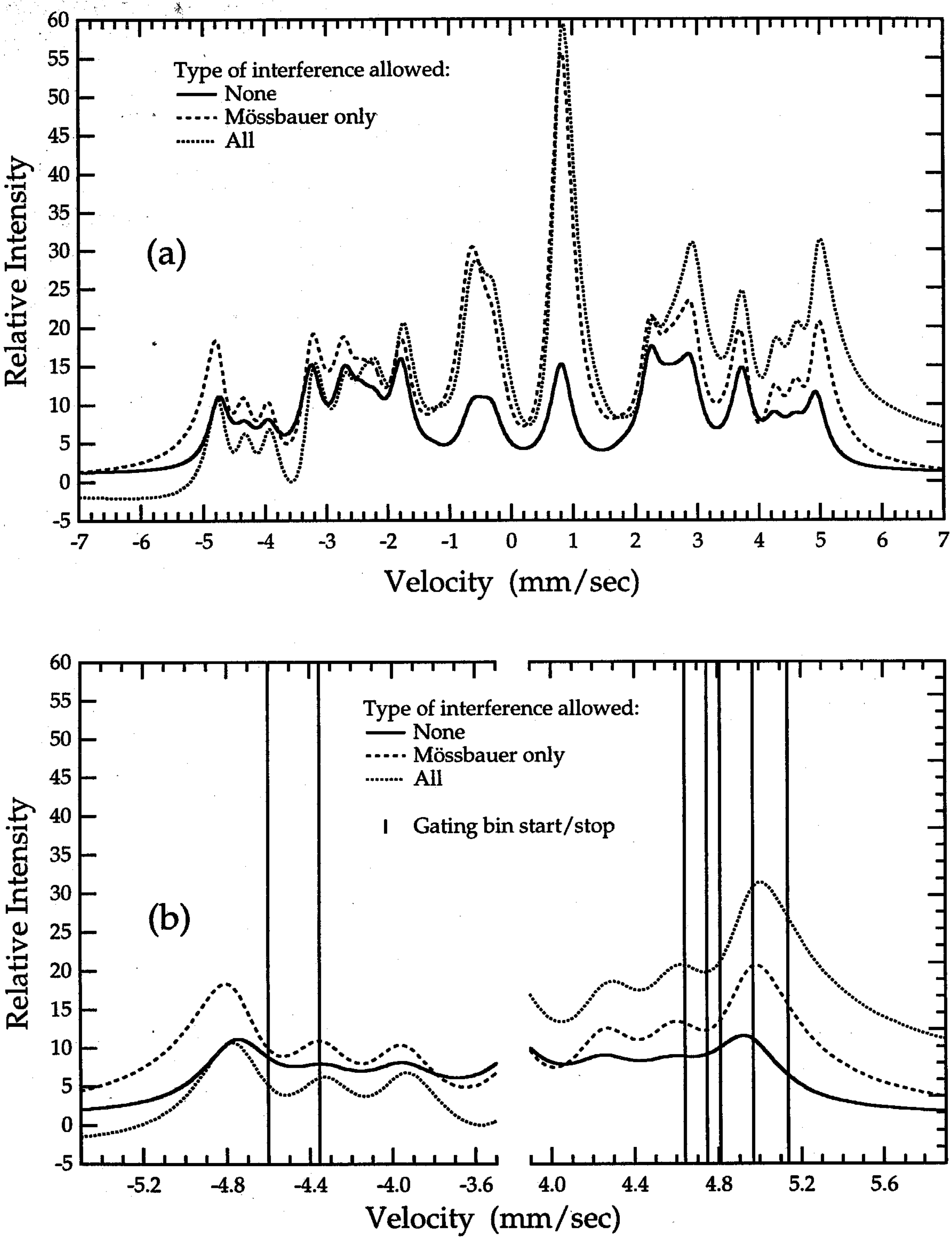

Figure 5.8 (a) Modeled intensity curves as a function of energy for the $^{57}Fe_3Al$ sample. A Mössbauer to x-ray scattering ratio of 10 was used.
(b) Enlargement of (a) with the 0Al velocity bins shown. While the data are modeled, the velocity ranges are those of the real experiment.

Figure 5.9 shows the results of the $^{57}Fe_3Al$ intensity calculation of type (3) for different values of r_{MX}. The figure also includes the no interference calculation of type (1) and the Mössbauer–Mössbauer only interference calculation of type (2) cases. The most important characteristic of this figure is that r_{MX} tends to change the scaled intensities of the different gating bins with respect to each other, but the general trends of the curves are preserved. This is particularly true for $r_{MX} > 1$. Finally, type (2) interference is the limiting case of $r_{MX} \gg 1$.

Figures 5.10ab compare the experimental data to the modeling results for the $^{57}Fe_3Al$ samples ($^{57}Fe_3Al95$ data set). Three curves are shown in each figure — the no interference calculation of type (1), the full calculation of type (3), and the experimental data. Figure 5.10a displays data for the (200) diffraction peak. The modeling used a value of $r_{MX} = 10$, based on the results from Table 5.5 with the x-ray form factor, Debye-Waller factor, and Lamb-Mössbauer factors. Figure 5.10b displays data for the (211) diffraction peak for which r_{MX} was 20. The individual component peaks for the real data are shown in Figs 4.4 and 4.6. Examining these figures shows:

(1) Both figures show better results with full modeled calculation of type (3) than the no interference calculation of type (1).
(2) The calculated intensities follow the trends in the experimental data quite well, particularly within the limits of the error bars.
(3) The upward bend in the experimental data from gating bin 4Al_4 to 4Al_5 is similar to trends seen in the curve calculated with r_{MX}=0.10 (Fig. 5.9).

From these observations we conclude that interference has an important effect on the intensities of fundamental bcc Mössbauer diffractions from $^{57}Fe_3Al$. Besides the x-ray – Mössbauer interference, the interference between Mössbauer scattering from different chemical environments is also important.

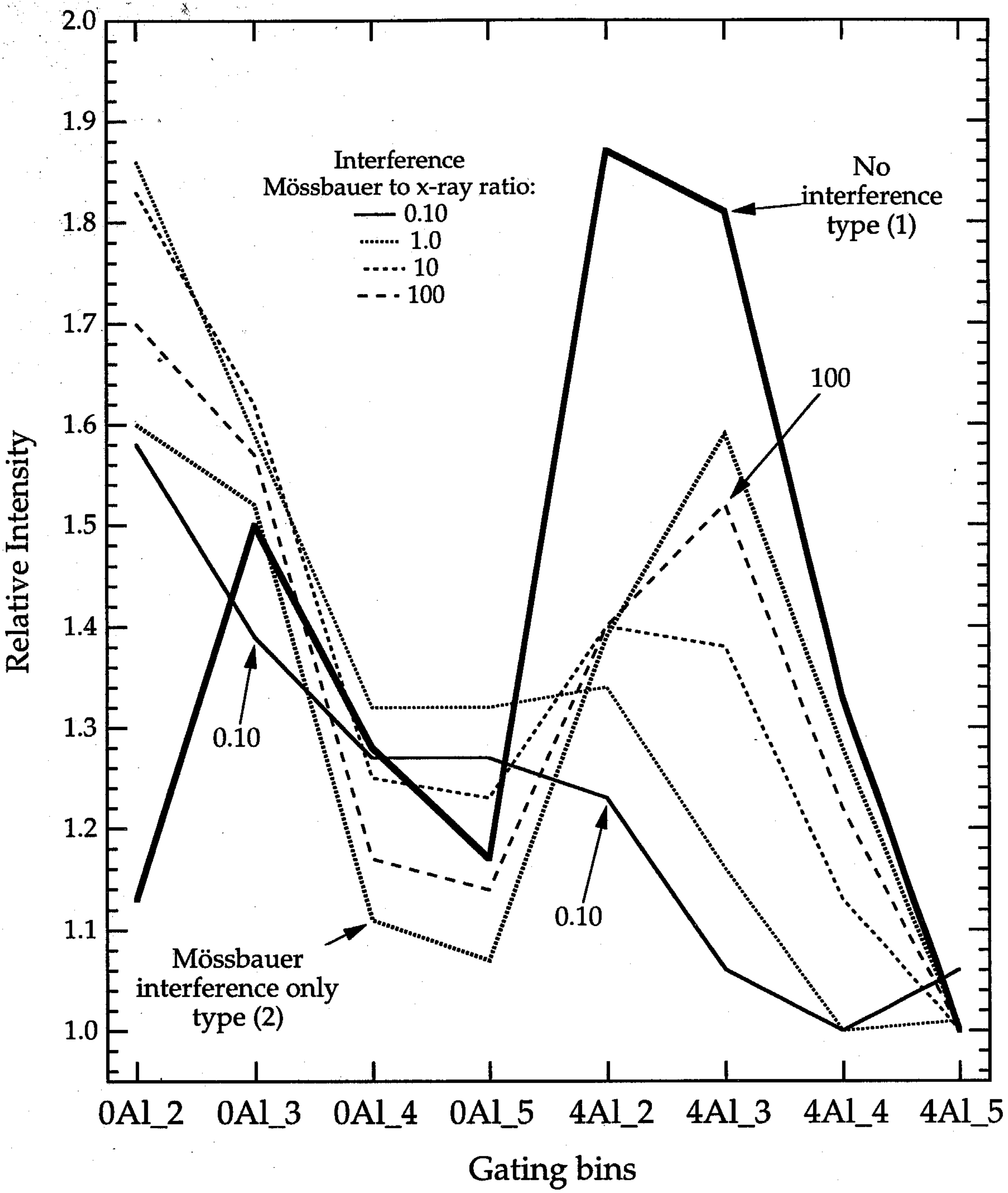

Figure 5.9 Results of the ^{57}Fe$_3$Al intensity calculation with type (3) interference for different values of the Mössbauer to x-ray scattering ratio.

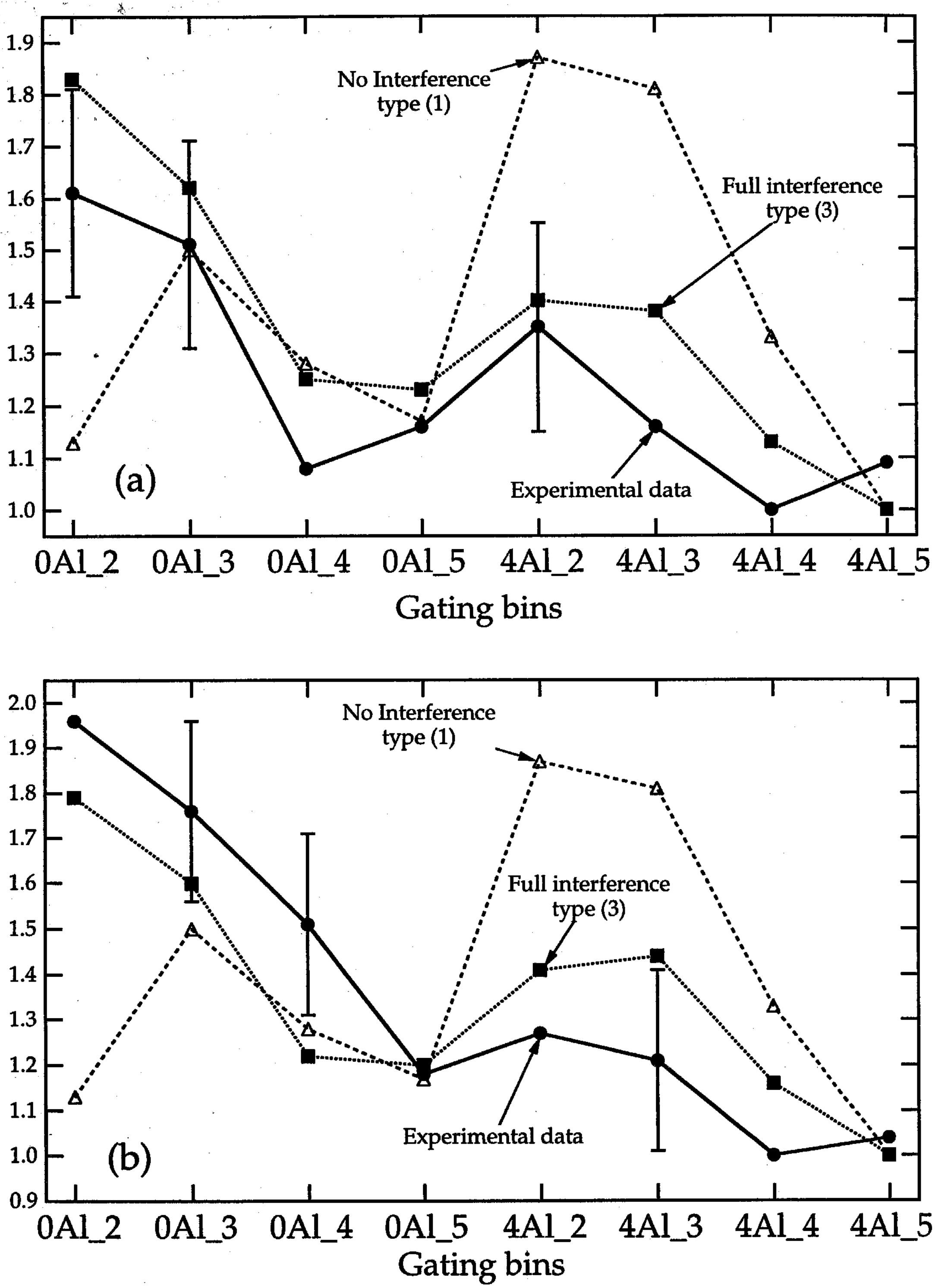

Figure 5.10 Comparison of the experimental intensities to the calculated intensities for the $^{57}Fe_3Al$ samples. (a) The (200) peak of the $^{57}Fe_3Al95$ data set (Mössbauer: x-ray = 10). (b) The (211) peak of the $^{57}Fe_3Al95$ data set (Mössbauer: x-ray = 20).

5.5.2 Comparing the interference calculation to the experimental data for ^{57}Fe

Modeling for the ^{57}Fe sample includes all five useful gating bins (bin2 through bin5 and bin7) of the ^{57}Fe on-resonance condition. Figure 5.11 shows the experimental and calculated intensities of the (400) diffraction peak for the ^{57}Fe sample (Fe95 data set). Like the case of the ^{57}Fe$_3$Al above, the full interference calculation of type (3) agrees better with the experimental data than the calculation without interference [type (1)]. The difference is not large, however. This is because the interference effects are less important — r_{MX} = 60:1 was used because of the larger Mössbauer cross section, and the strong suppression of the x-ray form factor for the higher order diffraction peak [(400) vs. (222)]. The upward kink in the experimental plot from FeON_5 to FeON_7 is similar to one seen in the ^{57}Fe$_3$Al data. Figure 4.9 shows five individual on-resonance component diffraction peaks. While the interference effects are less prevalent in the ^{57}Fe sample, the interference calculation still seems to provide the best results.

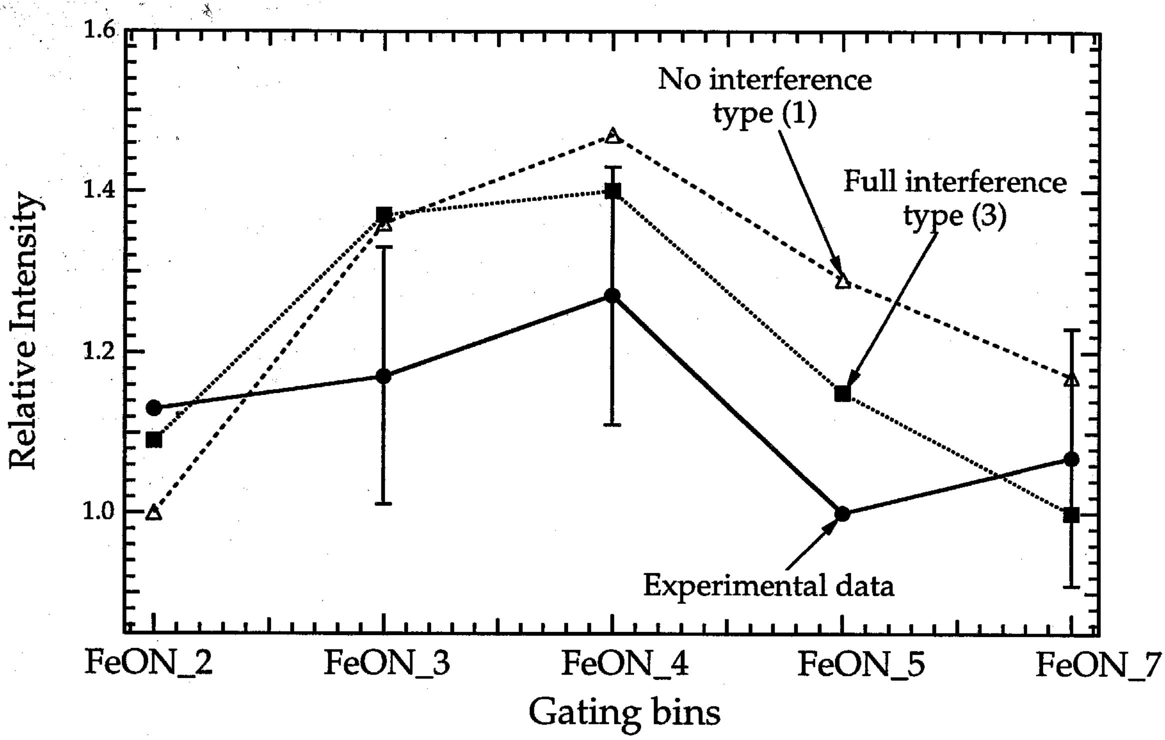

Figure 5.11 Comparison of the experimental intensities to the calculated intensities for the ^{57}Fe samples. The experimental data shown is from the (400) peak of the Fe95 data set. The full interference curve is for type (3) interference with Mössbauer: x-ray = 60.

References, Chapter 5

[1] A.P. French, Vibrations and Waves (Norton, New York, 1971) p. 77.

[2] P.J. Black and P.B. Moon, Nature **188**, 481 (1960).

[3] P.J. Black, G. Longworth, and D.A. O'Conner, Proc. Phys. Soc. **83**, 925 (1964).

[4] B.E. Warren, *X-ray Diffraction* (Dover, New York, 1990), Chap. 1.

[5] J.M. Cowley, *Diffraction Physics* (North-Holland, Amsterdam, 1975), Sec. 5.3.

[6] V.A. Belyakov, Usp. Fiz. Nauk. **115**, 553 (1975) [Sov. Phys.-Usp. 18, 267 (1975)].

[7] U. van Bürck, G.V. Smirnov, R.L. Mössbauer, F. Parak, and N.A. Semioschkina, J. Phys. C **11**, 2305 (1978).

[8] J. Arthur, G.S. Brown, D.E. Brown, and S. L. Ruby, Phys. Rev. Lett. **63**, 1629 (1989).

[9] W.J. Veigele, in *Practical Handbook of Spectroscopy*, edited by J. W. Robinson, (CRC Press, Boca Raton, 1991) p. 41.

[10] B.E.Warren, *X-ray Diffraction* (Dover, New York, 1990), Appendix IV.

[11] B. Fultz, J. Chem. Phys. **87**, 1604 (1987).

[12] H. Ouyang and B. Fultz, J. Appl. Phys. **66**, 4752 (1989).

[13] L. Anthony, *Ph.D. Thesis* (California Institute of Technology, Pasadena, 1993).

Chapter 6 Future work

The purpose of this thesis has been to test if Mössbauer diffraction, through chemical environment selective diffraction, could be used as an analytical tool for materials science. Using a low-noise, large angle position-sensitive detector, we built a Mössbauer effect Debye-Scherrer diffractometer and used it to measure diffraction patterns from polycrystalline $D0_3$-ordered $^{57}Fe_3Al$. The 0Al and 4Al environment superlattice diffraction peaks seen in the $^{57}Fe_3Al$ data (sections 4.3 and 4.4) prove that chemical environment selectivity is experimentally feasible. The successful modeling of the interference effects in chapter 5 shows that we have a good theoretical understanding of the Mössbauer and x-ray scattering mechanisms. Thus, we can acquire and analyze a new type of diffraction data that is of importance for materials science. However, we are hampered by the low signal-to-noise ratio (S/N) of our data; improvements are necessary before we attempt the experiments described in section 1.2.

This chapter will describe a number of possible improvements. Photon detection is the focus of § 6.1, while § 6.2 describes improvements in the photon flux. Finally, section 6.3 will describe a benchmark experiment that could be used to determine improvements in instrumentation.

6.1 Detector improvements

Although the present experiments were made possible by the position-sensitive detector, the INEL CPS-120 detector caused serious technical limitations. For a 2θ range of 50^0, the geometrical efficiency of the detector was less than 1%. The countrate for coherent Mössbauer scattering was only 0.25% as large as the countrate from background and x-ray fluorescences. The detector efficiency for 14.41 keV photons was 15%. Improvements in all these experimental parameters can increase the signal-to-noise ratio by

5 orders of magnitude. While an improvement factor of 100,000 seems excessively optimistic, clearly improvements can be made. Six factors are important to consider:

(1) efficiency for desired events (photons or particles),
(2) efficiency for undesired events (source noise),
(3) ambient background (non-source noise),
(4) geometric efficiency (solid angle coverage),
(5) detector quantum efficiency,
(6) position resolution, and
(7) timing capabilities.

The improvements will be discussed in terms of these items. The timing capabilities of the detector are important for synchrotron radiation experiments, as data are acquired in the time, rather than energy, domain.

6.1.1 Improvements to the INEL detector

Improvements to the INEL position sensitive detector (PSD) can be divided into two groups: those that require the detector be physically altered and those that do not. Changing the window height or length of the detector belong to the first group and are the most expensive. Electronic signal manipulation and detector gas alterations belong to the second group and are the most immediately promising.

We believe that the operational mode of the present CPS-120 detector could be changed to both improve the 14.41 keV photon efficiency and remove some of the source background. Table 3.6 shows that switching from 100% Ar to 100% Kr increases the detector efficiency for all photon energies. Proper energy discrimination would allow near 100% 14.41 keV photon efficiency without detection of the other source photons, and it would yield at least a factor of 10 improvement[•] in S/N. The energy discrimination of the

---

[•] This assumes that the energy discrimination would not decrease the ambient background.

INEL detector is not good, but there are some possibilities for energy discrimination through additional signal manipulation.

The geometric efficiency of the INEL detector was improved at the expense of the position resolution in § 3.4.4. Further improvements are not possible, as the current INEL detector is too large. While reducing the angular collection range (from a 2θ range of 120^0) would allow the detector to be moved closer to the sample, we would prefer to increase the height of the detector window, which would also increase the subtended solid angle. The height of the detector window is limited, however, as the membrane must be thin enough to be photon transparent while under 6.2 bar of gas pressure. The improvement factor is probably limited to a factor of 2 or 3.

A series of coincidence experiments have been performed that indicate the timing resolution of the INEL detector is sufficient for synchrotron work. These are described in Appendix B.

6.1.2 Alternative detectors

This section covers three possible alternative detectors that could be used with Debye-Scherrer type Mössbauer diffraction experiments: (1) CCD cameras, (2) MICE/multiwire gas proportional chamber hybrids, and (3) avalanche photodiode arrays. The advantages and disadvantages of each detector are discussed.

Digital CCD (charge-coupled device) cameras could be used as area detectors for Mössbauer diffraction experiments. The incident γ-rays would interact with a scintillation material or fluorescent screen and be converted to visible light. The light is then detected and recorded by the CCD camera. Detector efficiency, energy resolution, and noise issues are primarily a function of the scintillator; these issues are being currently explored. The CCD camera itself operates with a very low noise level and a wide dynamic range, which would allow energy discrimination if the intensity of the detected light is accurately proportional to the energy of the γ-ray. The most promising aspects of the camera are its physical size and pixel resolution. Even a modest CCD camera (512 x 512 with a 24 μm pixel resolution [1]) placed 63 mm from the sample would cover a solid angle equal to the INEL detector (2θ range of 14^0). Tapered fibre optic bundles or lens systems could also be used to focus a larger fluorescent screen onto the CCD array. However, the data acquisition speed of the camera makes it suitable only for radioisotope-based experiments.

A position sensitive microfoil conversion electron detector is another interesting type of detector. Such a detector would be constructed using microfoil conversion electron (MICE) detector technology from Mössbauer spectroscopy [2, 3] and multiwire gas proportional counter (MWPC) technology from high energy physics [4]. A microfoil conversion electron detector detects photons by resonantly absorbing the Mössbauer photons from the sample and collecting the internal conversion electrons produced (Fig. 6.1). Resonant absorption requires the detector to be made from a foil that contains the same Mössbauer isotope as the sample. Detector efficiency is very high because of the resonant absorption and the large internal conversion coefficient, α, for Fe. Noise, both ambient and source, is primarily from photoelectrons from x-ray absorption. The energies of the photoelectrons and conversion electrons overlap, but the noise can be limited through energy discrimination. Position sensitivity would be provided by MWPC technology in the form of a microstrip gas chamber (Fig. 6.2a) [5, 6] or microstrip delay line (Fig. 6.2b) [7]. In both cases, the cathode(s) would be patterned (by photolithography) onto a substrate, which would provide "pixel" resolution on the order of tens of microns or better (the resonant microfoil is the anode). Thus, spatial resolution would be excellent, allowing a correspondingly good geometric efficiency. The microstrip delay line looks promising, as the cathode also acts as a delay line, requiring only two signals to be processed for position sensitivity. Finally, a position sensitive MICE detector would share the good timing characteristics of microstrip detectors, making possible their use with synchrotron radiation sources.

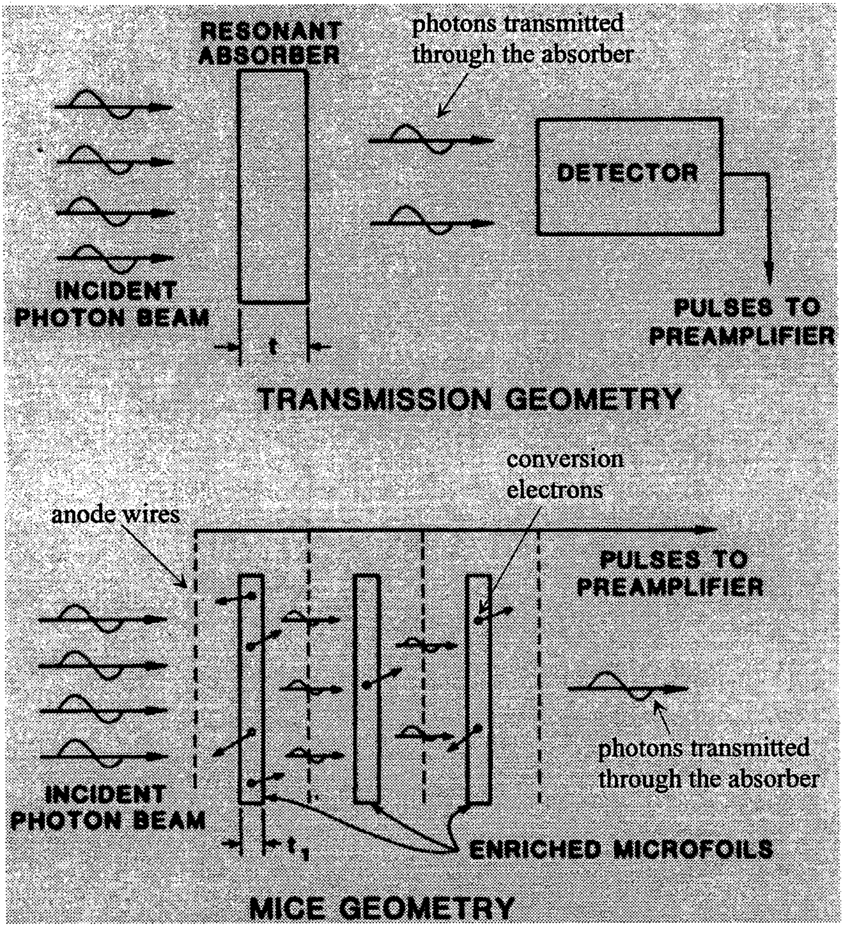

Ref. 3, p. 324

Figure 6.1 Comparison of the transmission and MICE geometries. The transmission detector registers photons that were not absorbed, while the MICE detector registers the conversion electrons produced after resonant absorption in the microfoils.

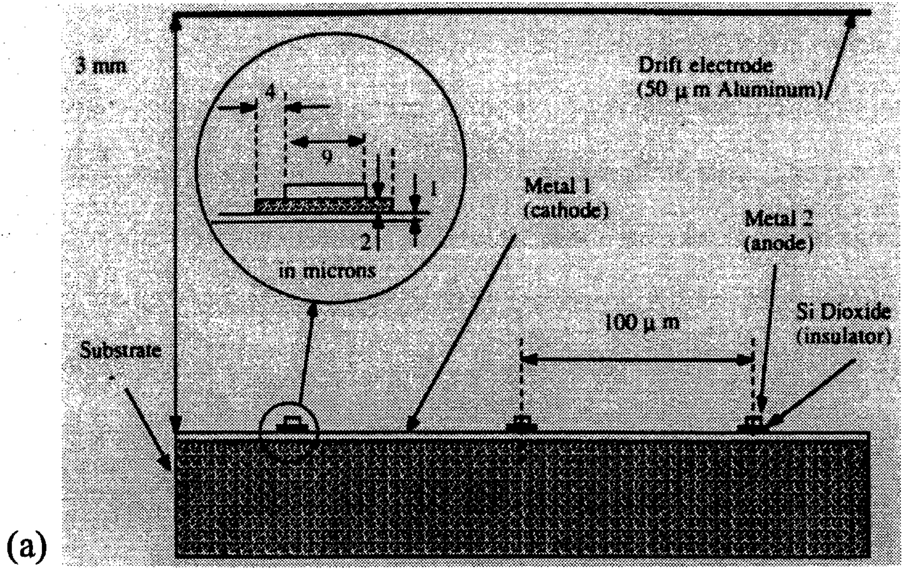

Ref. 6, p. 70

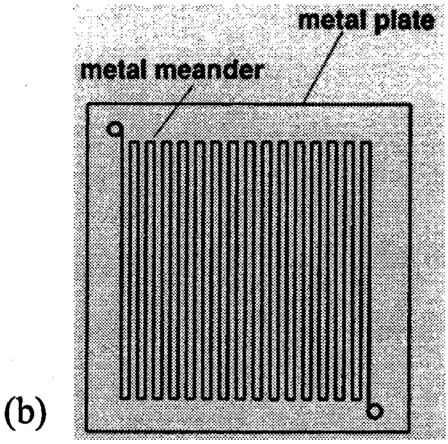

Ref. 7, p. 146

Figure 6.2 (a) Cross section of a micro-gap chamber and (b) top view of a meandering microstrip delay line.

Avalanche photodiodes (APDs) are very promising, as they possess the best timing capabilities of the detectors described here (~ 1 nsec), noise levels comparable to the INEL CPS-120, and reasonable energy discrimination [8,9]. While APDs are discrete elements, they can be converted into array detectors with a 0.5 mm pixel size. The primary limitation is their expense; each APD requires its own set of electronics for high voltage bias and signal amplification. Furthermore, a very large number of APDs are required to maintain reasonable angular resolution (~ 0.1^0) with acceptable geometric efficiency. For example, approximately 15,000 APD elements would be needed to replace the INEL detector in our current experiments. Thus, avalanche photodiode arrays are feasible only as a national resource at synchrotron radiation facilities.

6.2 Synchrotron radiation

The use of synchrotron radiation (SR) in place of radioisotope sources is another way to improve the S/N. The dedicated nuclear resonance scattering (NRS) beamline at the Advanced Photon Source (APS) in Argonne, IL, is presently coming on-line [10]. The photon flux from the undulator is 115,000 photons per Mössbauer linewidth of the ^{57}Fe isotope ($1\Gamma_s$ = 5 neV, the HWHM of the Mössbauer absorption peaks), which is approximately two orders of magnitude better than our 145 mCi ^{57}Co source. Furthermore, SR lacks the parasitic radiation of radioisotope sources (Pb fluorescence, etc). While the energy resolution of SR is inherently very poor (10^5 eV), the NRS uses a series of components to monochromate the energy resolution to the nano-eV range of the Mössbauer effect. These components include [10]:

(1) High heat load monochromator (2 eV resolution),
(2) High energy resolution monochromator (10 meV resolution),
(3) Grazing incidence anti-reflection (GIAR) films (micro-eV resolution) [11], and

(4) Multilayer structures constructed of alternating layers of nuclear resonant and nonresonant atoms (50 nano-eV resolution) [12,13].

Even the best monochromatization schemes for synchrotron radiation seem to be limited to an energy resolution of only 10 Γ_s. An energy-domain chemical environment selectivity experiment would need further improvement to be practical. On the other hand, chemical environment selectivity should be possible in the time domain by observing quantum beats between different nuclear transitions. The possibility of time-domain chemical environment selectivity experiments should be explored.

6.3 Chemical environment selective diffraction benchmark experiment

Although chemical environment selective diffraction has been proven, more work is required for technique development. An experiment using samples composed of ^{57}Fe and $^{57}Fe_2O_3$ could determine these abilities and also serve as a benchmark experiment to assess instrumentation improvements in the future. The experiment would examine a series of samples with varying amounts of ^{57}Fe and $^{57}Fe_2O_3$ (highly enriched in the ^{57}Fe isotope)♦. The intensity of diffraction peaks generated though chemical environment selectivity would then be compared to the relative ratio of ^{57}Fe and $^{57}Fe_2O_3$ in the samples. Thus, we would simulate an "ideal" two-chemical environment alloy with well-separated Mössbauer absorption peaks (peak 1 for both) and very different diffraction patterns (see Fig. 6.3). We originally considered this experiment in place of the $^{57}Fe_3Al$, but the $^{57}Fe_3Al$ experiment seemed more useful for proving the feasibility of chemical environment selectivity for "real" samples.

♦ The samples would be made by placing known quantities of $^{57}Fe_2O_3$ powder on ^{57}Fe foils, simplifying sample preparation.

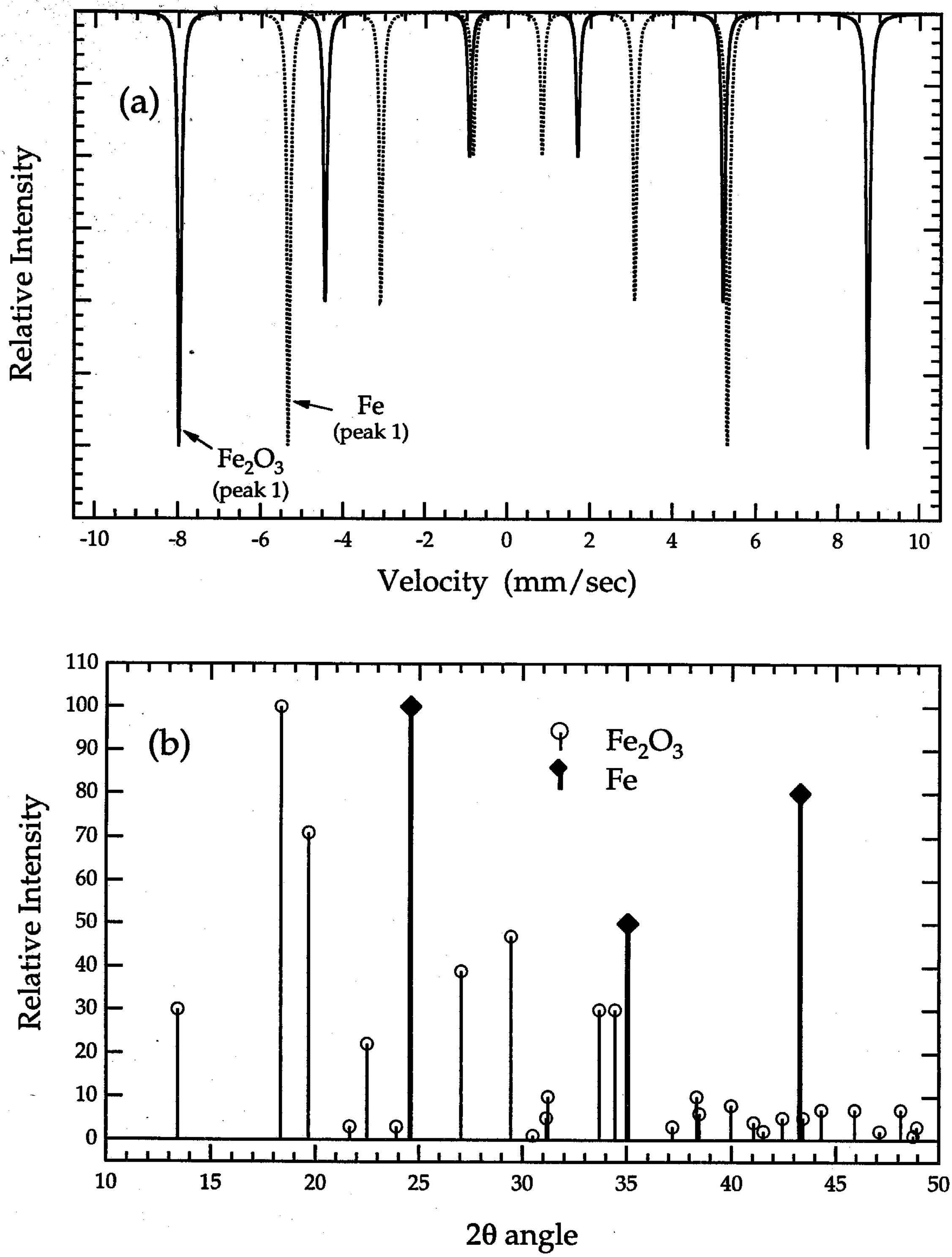

Figure 6.3 (a) Mössbauer spectra and (b) x-ray diffraction patterns for Fe_2O_3 and Fe samples. The diffraction patterns are simulated by the computer program Lazy Pulverix (section 3.2.6) with 14.41 keV photons.

References, Chapter 6

[1] Princeton Instruments, Inc, *High Performance Digital CCD Cameras* catalog (Trenton, NJ, 1994).

[2] J.G. Mullen and J. Stevenson, Nucl. Instrum. and Meth. **153**, 77 (1978).

[3] J.G. Mullen, A. Djedid, C. Holmes, G. Schupp, L. Crow, and W. Yelon, Nucl. Instrum. and Meth. in Phys. Res. B **14**, 323 (1986).

[4] G. Chapak, R. Bouclier, T. Bressani, J. Favier, and C. Zupancic, Nucl. Instrum. and Meth. **62**, 262 (1968).

[5] F. Kummenacher, C. Enz, and R. Bellanzzini, Nucl. Instrum. and Meth. in Phys. Res. A **313**, 483 (1992).

[6] F. Angelini, R. Bellanzzini, M.M. Massai, R. Raffo, G. Spandrem and M.A. Spezziga, Nucl. Instrum. and Meth. in Phys. Res. A **335**, 69 (1993).

[7] Ch. Klein, J. Trötscher, and H. Wollnik, Nucl. Instrum. and Meth. in Phys. Res. A **335**, 146 (1993).

[8] T.S. Toellner, W. Sturhahn, E.E. Alp, P.A. Montano, and M. Ramanathan, Nucl. Instrum. and Meth. in Phys. Res. A **350**, 595 (1994).

[9] E.E. Alp, W. Sturhahn, T.M. Mooney, T. Toellner, R. Blasdell, and D. Shu (unpublished).

[10] E.E. Alp, T.M. Mooney, T. Toellner, and W. Sturhahm, Hyperfine Inter. **90**, 323 (1994).

[11] H. Homma, M. Kentjana, E.E. Alp, T.M. Mooney, E. Witthoff, and T. Toellner, J. Appl. Phys. **72**, 5668 (1992).

[12] A.I. Chumakov and G.V. Smirnov, JETP Lett. **53**, 272 (1991).

[13] T.S. Toellner, W. Sturhahn, R. Röhlsberger, E.E. Alp, C.H. Sowers, and E.F. Fullerton, Phys. Rev. Lett. **74**, 3475 (1995).

Appendix A

This appendix contains the useful constants and basic information needed to perform the experimental and theoretical work. Tables A.1 through A.3 list the diffraction peak positions for $^{57}Fe_3Al$, ^{57}Fe, and the Si standard with 14.41 keV photons, respectively. Table A.4 lists the important quantities of the ^{57}Fe Mössbauer transition, while the rest of the appendix contains other various useful quantities.

h	k	l	theta	twotheta	0Al	4Al	Off	Intensity (x-ray)
1/2	1/2	1/2	7.40	14.80	✓			62.30
1	0	0	8.55	17.10	✓	✓		32.50
1	1	0	12.14	24.28	✓	✓	✓	1,000.00
3/2	1/2	1/2	14.28	28.56	✓			28.80
1	1	1	14.93	29.86	✓	✓		8.30
2	0	0	17.30	34.60	✓	✓	✓	162.50
3/2	3/2	1/2	18.91	37.82	✓			10.40
2	1	0	19.42	38.84	✓	✓		9.40
2	1	1	21.36	42.72	✓	✓	✓	305.40
5/2	1/2	1/2	22.73	45.46	✓			5.10
3/2	3/2	3/2	22.73	45.46	✓			1.70
2	2	0	24.87	49.74	✓	✓	✓	85.30
5/2	3/2	1/2	26.10	52.20	✓			5.90
3	0	0	26.50	53.00	✓	✓		2.80
2	2	1	26.50	53.00	✓	✓		0.70
3	1	0	28.05	56.10	✓	✓	✓	106.10
5/2	3/2	3/2	29.18	58.36	✓			1.90
3	1	1	29.55	59.10	✓	✓		1.90
2	2	2	31.01	62.02	✓	✓	✓	23.80
7/2	1/2	1/2	32.07	64.14	✓			1.40
5/2	5/2	1/2	32.07	64.14	✓			1.40
3	2	0	32.42	64.84	✓	✓		1.30
3	2	1	33.81	67.62	✓	✓	✓	102.50
5/2	5/2	3/2	34.83	69.66	✓			1.10
7/2	3/2	1/2	34.83	69.66	✓			2.20
4	0	0	36.50	73.00	✓	✓	✓	9.70
7/2	3/2	3/2	37.49	74.98	✓			0.90
4	1	0	37.82	75.64	✓	✓		0.90
3	2	2	37.82	75.64	✓	✓		0.90
3	3	0	39.12	78.24	✓	✓	✓	15.40
4	1	1	39.12	78.24	✓	✓	✓	30.80
7/2	5/2	1/2	40.09	80.18	✓			1.50
5/2	5/2	5/2	40.09	80.18	✓			0.30
3	3	1	40.41	80.82	✓	✓		0.70
4	2	0	41.69	83.38	✓	✓	✓	25.50
9/2	1/2	1/2	42.64	85.28	✓			1.40
7/2	5/2	3/2	42.64	85.28	✓			0.70
4	2	1	42.96	85.92	✓	✓		1.30
3	3	2	44.23	88.46	✓	✓	✓	22.00
9/2	3/2	1/2	45.18	90.36	✓			1.20
4	2	2	46.76	93.52	✓	✓	✓	19.70

Table A.1 Diffraction peaks positions for ^{57}Fe$_3$Al with 14.41 keV photons. The checkmarks indicate the peaks allowed for each of the three types of velocity conditions. The x-ray intensities shown were calculated for a powder pattern in the the computer program Lazy Pulverix (see section 3.2.6).

h	k	l	theta	twotheta	Intensity (x-ray)
1	1	0	12.25	24.50	1,000.00
2	0	0	17.46	34.92	160.00
2	1	1	21.56	43.12	297.50
2	2	0	25.11	50.22	82.70
3	1	0	28.32	56.64	103.00
2	2	2	31.31	62.62	23.20
3	2	1	34.15	68.30	100.70
4	0	0	36.88	73.76	9.60
3	3	0	39.53	79.06	15.40
4	1	1	39.53	79.06	30.90
4	2	0	42.14	84.28	25.90
3	3	2	44.73	89.46	22.60
4	2	2	47.31	94.62	20.60
5	1	0	49.91	99.82	38.60
4	3	1	49.91	99.82	19.30
5	2	1	55.26	110.52	37.50
4	4	0	58.07	116.14	9.70
5	3	0	61.03	122.06	20.50
4	3	3	61.03	122.06	20.50
4	4	2	64.19	128.38	22.40
6	0	0	64.19	128.38	5.60

Table A.2 Diffraction peaks positions for ^{57}Fe with 14.41 keV photons. The x-ray intensities shown were calculated for a powder pattern in the computer program Lazy Pulverix (see section 3.2.6).

h	k	l	theta	twotheta
1	1	1	7.89	15.78
2	2	0	12.96	25.92
3	1	1	15.25	30.50
2	2	2	15.94	31.88
4	0	0	18.49	36.98
3	3	1	20.22	40.44
4	2	2	22.86	45.72
5	1	1	24.33	48.66
3	3	3	24.33	48.66
4	4	0	26.65	53.30
5	3	1	27.98	55.96
4	4	2	28.41	56.82
6	2	0	30.10	60.20
5	3	3	31.33	62.66
6	2	2	31.74	63.48
4	4	4	33.33	66.66
5	5	1	34.49	68.98
7	1	1	34.49	68.98
6	4	2	36.40	72.80
5	5	3	37.53	75.06
7	3	1	37.53	75.06
8	0	0	39.38	78.76
7	3	3	40.47	80.94
6	4	4	40.84	81.68
6	6	0	42.29	84.58
8	2	2	42.29	84.58
7	5	1	43.37	86.74
5	5	5	43.37	86.74
6	6	2	43.73	87.46
8	4	0	45.18	90.36

Table A.3 Diffraction peaks positions for a Si powder standard with 14.41 keV photons. These values were used to calibrate the 2θ axis of the INEL detector.

Table A.4 Important quantities of the ^{57}Fe Mössbauer transition @ 14.41 keV. (a duplication of Table 2.1).

Symbol	Value (units)	Quantity
α_T	8.21	total internal conversion coefficient
f	0.9	Lamb-Mössbauer factor (average value)
$t_{1/2}$	9.77×10^{-8} sec	half-life of the excited state
Γ	4.55×10^{-9} eV	energy width of the transition
Γ_v	0.095 mm/sec	velocity equivalent of Γ
σ_0	2.38×10^{-18} cm^2	maximum absorbtion cross section
E_0	14.41 keV	energy of transition
E_R	1.95×10^{-3} eV	free atom recoil energy of nucleus
λ	0.86 Å	wavelength of transition
I_g	1/2	nuclear spin quantum # (ground state)
I_e	3/2	nuclear spin quantum # (excited state)
τ_{Co}	270 days	half-life of the ^{57}Co

Density:

sample	^{57}Fe enrichment	Density (g/cm^3)	Density (g/mole)
^{57}Fe	95%	8.02	56.95
Fe	2.2%	7.86	55.847
Al		2.7	26.98154
$^{57}Fe_3Al$	95%	7.02	49.458
Fe_3Al	2.2%	6.9	48.63

x-ray cross sections for 14.41 keV photons (in cm^2/g):

sample	coherent scattering	incoherent scattering	absorption
Al	0.34	0.12	9.36
Fe	0.79	0.10	67.15
Fe_3Al	0.68	0.11	52.70

Total Mössbauer absorption cross sections for 14.41 keV photons (in cm^2/g):

sample	^{57}Fe enrichment	Mössbauer absorption
^{57}Fe	95%	20,137
$^{57}Fe_3Al$	95%	17,436

Appendix B

B.1 2θ calibration for the INEL detector

The 2θ axis of the INEL detector was calibrated by using diffraction patterns from an x-ray Si powder standard and the ^{57}Fe foil sample. Figure B.1a shows the diffraction patterns, while Fig. B.1b shows the linear fit to diffraction peak positions. The position of the transmitted beam is also used. Thus, the linear fit provides a good 2θ calibration from 0^0 to 90^0. The calibration shown is valid for data sets Fe_3Al94, Fe_3Al95, and Fe95.

The Fe_3Al9v2 data set, which was acquired after moving the INEL detector forward (as described in § 3.4.4), required a new calibration. Moving the detector, as shown in Fig. 3.17, causes non-linearity calibration of the 2θ axis. Fortunately, the non-linearity is small enough that a linear approximation still works, as Fig. B.2 shows.

B.2 Velocity calibration for the Ranger MS-900 transducer

As discussed in § 3.3.2, the response of the Ranger MS-900 velocity transducer is consistently reproducible, but nonlinear. Thus, care must be taken to properly calibrate the velocity scales used to acquire the experimental data. Figures B.3 and B.4 show the calibration procedure for the ^{57}Fe sample. The two numbers labeling each curve are the offset and range values of the Ranger MS-900 controller used to acquire that particular data. In Fig. B.3, the two values are progressively changed to expand the desired velocity range. In this case, absorption peaks 1 (negative velocity) and 6 (positive velocity) of the ^{57}Fe sample have been chosen. The velocity range of peak 1 has been sacrificed to increase the accuracy of velocity range of peak 6. Figure B.4 shows how the accurate velocity range of (0.0; 10.0) is remapped onto the velocity setting used to acquire the ^{57}Fe diffraction patterns (23.0; 0.1). The results are shown in Fig. 3.14.

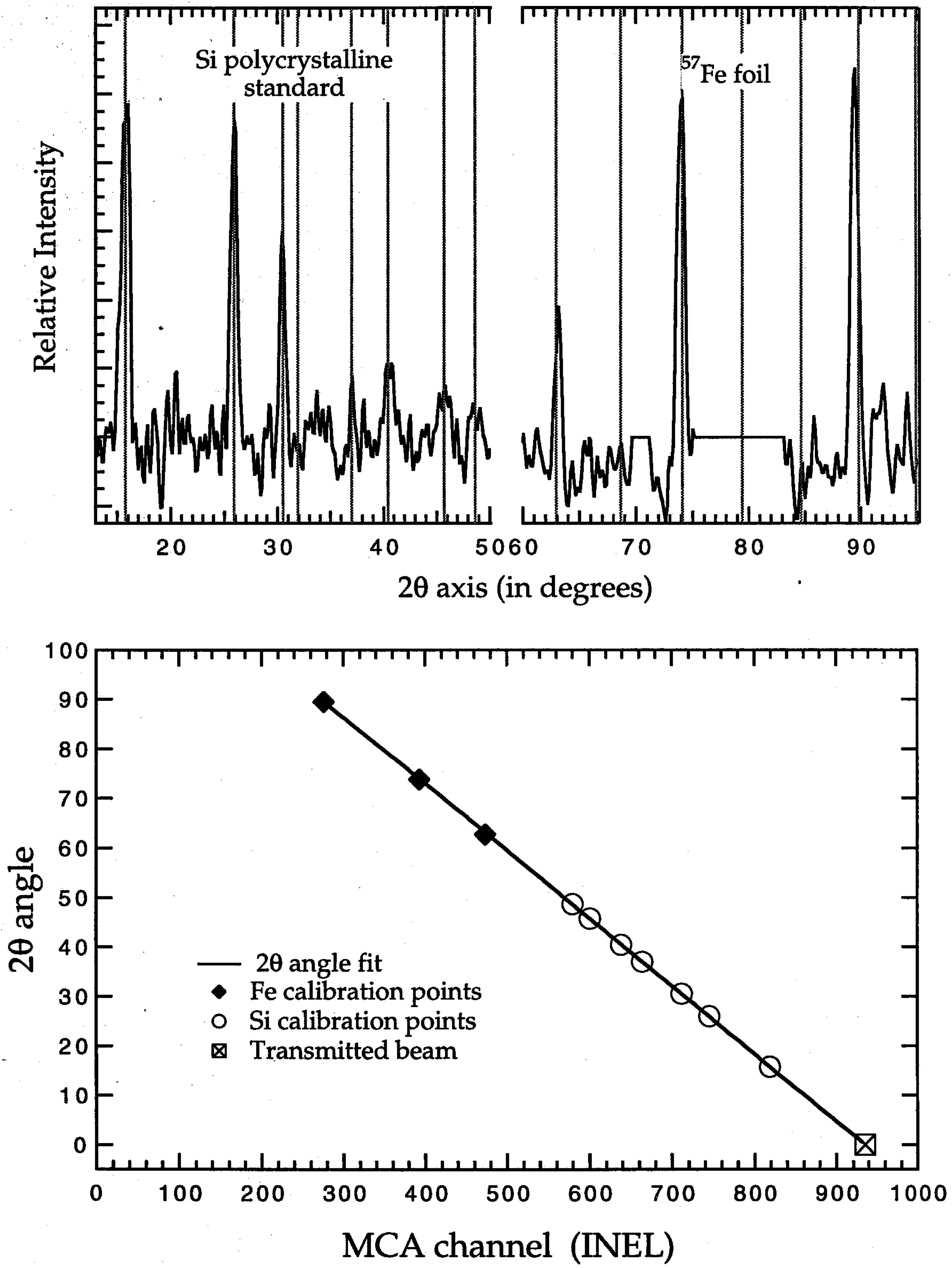

Figure B.1 2θ calibration of the INEL detector.

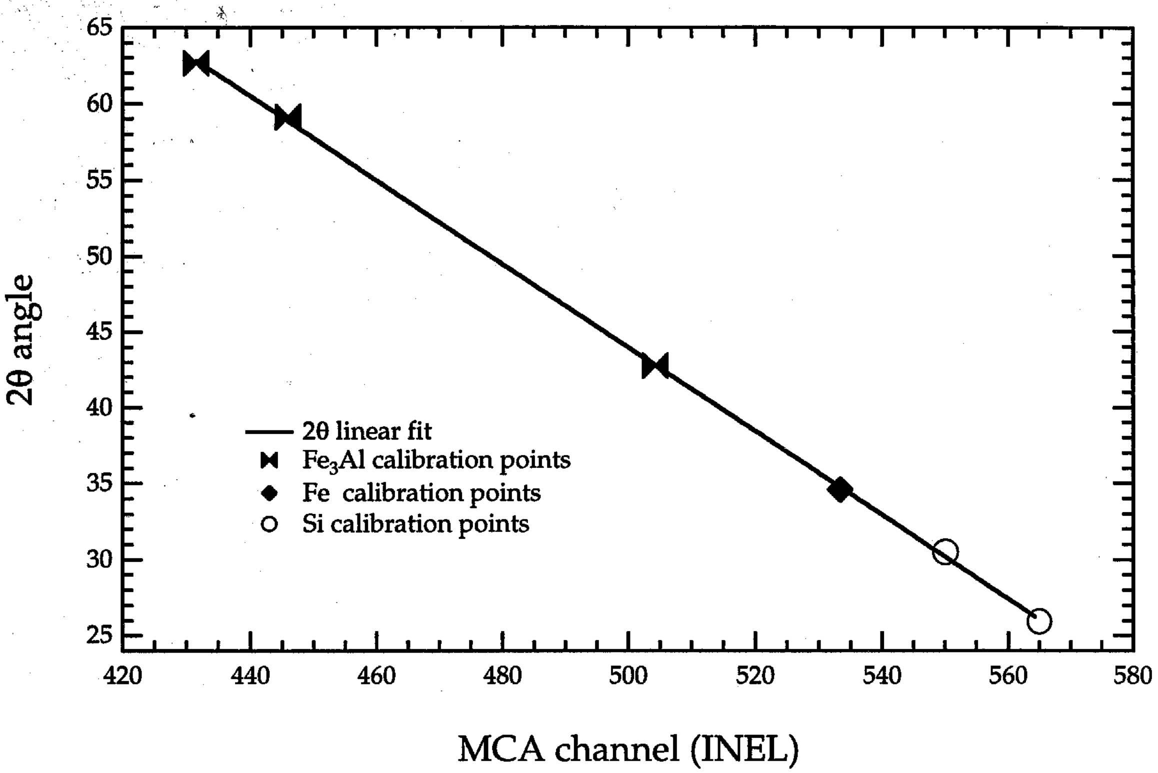

Figure B.2 2θ calibration of the INEL detector (for the $Fe_3Al95v2$ data set).

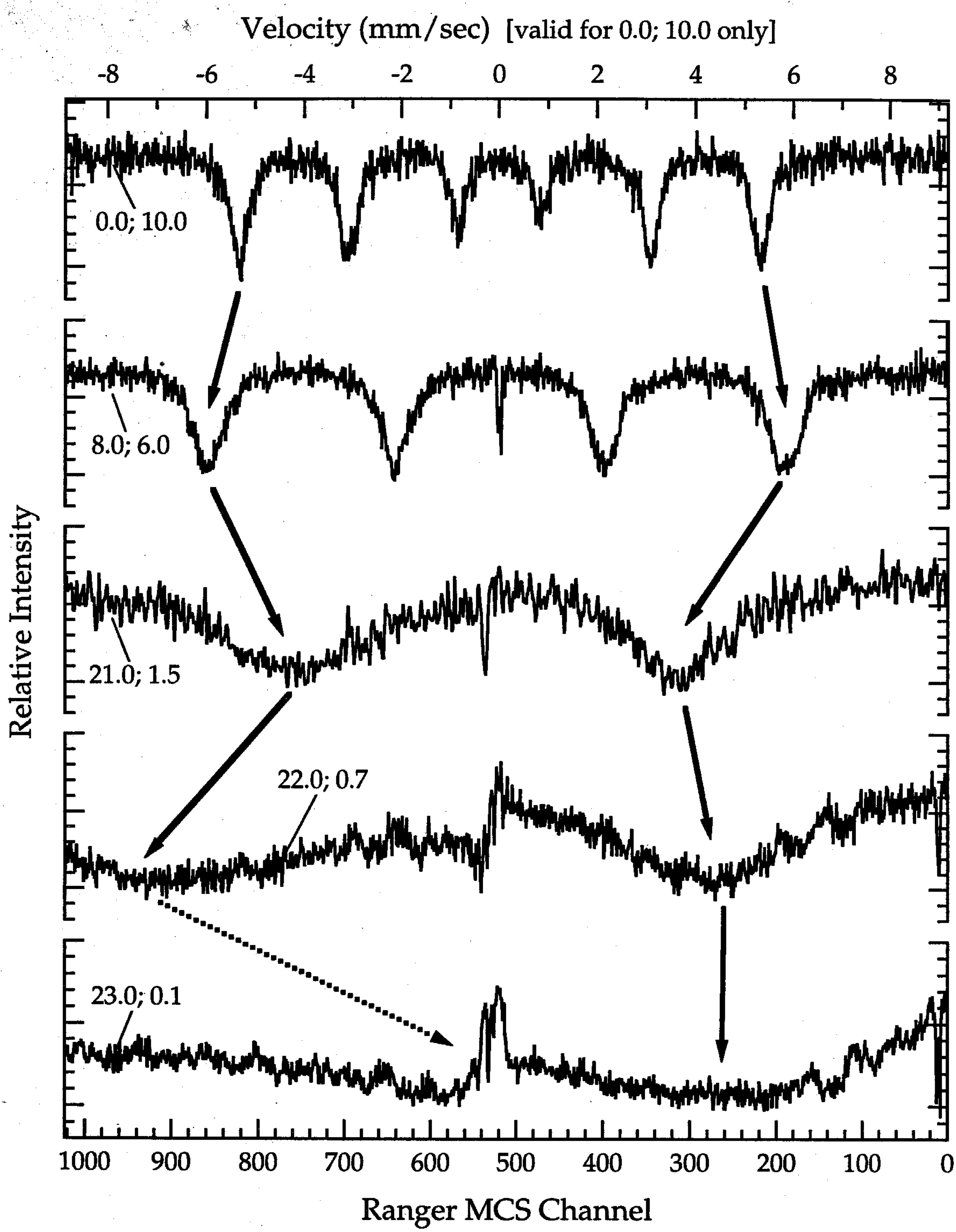

Figure B.3 Velocity calibration procedure for the ^{57}Fe sample. The numbers labeling each curve indicate offset and range values for the Ranger MS-900 controller. The dashed arrow indicates that the minimum of the peak is beyond the range of MCS.

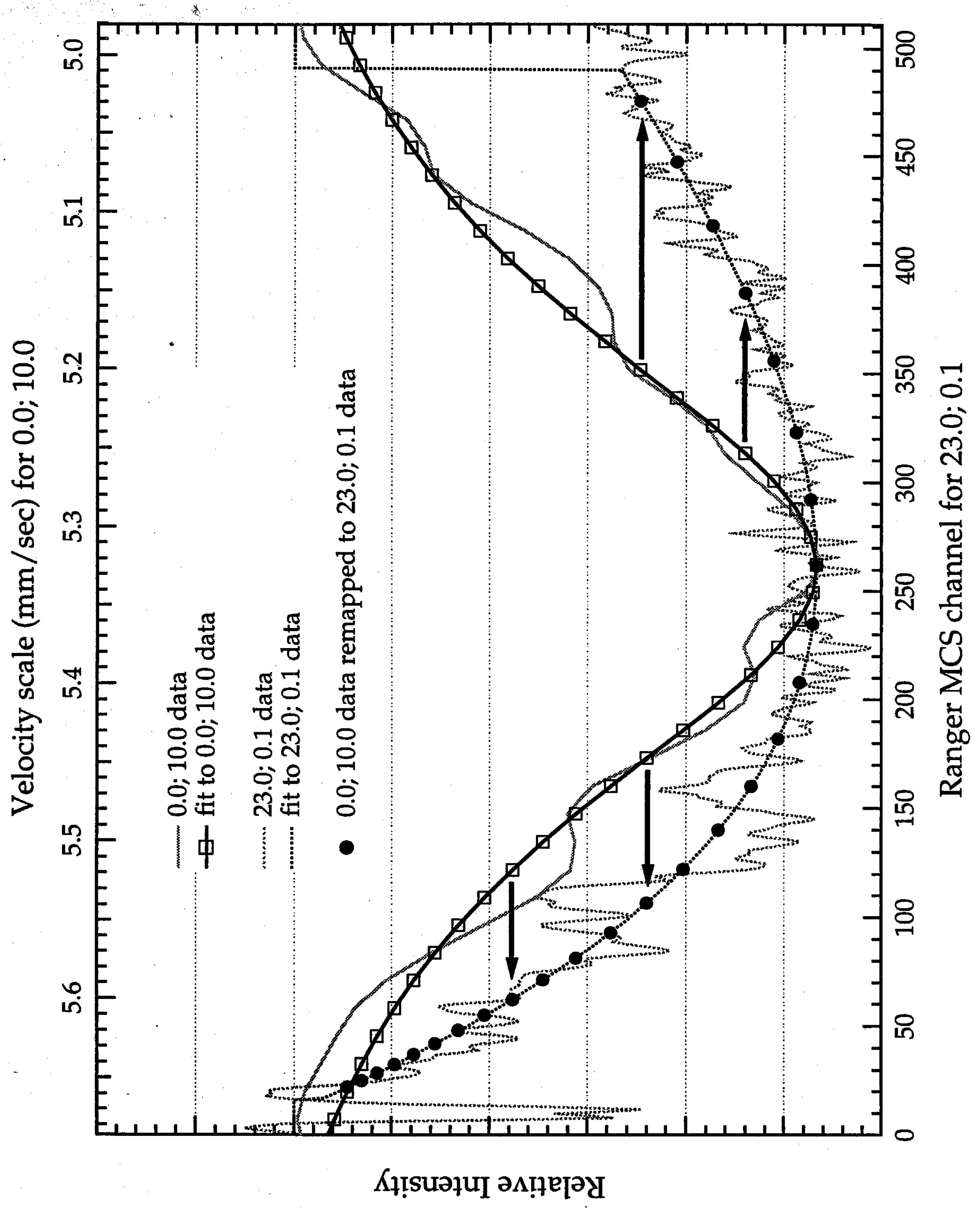

Figure B.4 Velocity calibration procedure for non-linear transducer response. The (0.0; 10.0) data possesses the correct velocity scale, and the (23.0, 0.1) data is remapped onto it for the velocity calibration. The (23.0, 0.1) data is an expansion of Mössbauer peak 6 of the ^{57}Fe sample.

B.3 Noise filtering and smoothing

This section describes the noise filtering and smoothing techniques that were used to process the data in chapter 4 (see § 4.2). To illustrate how noise affects the diffraction peaks, a simulated diffraction pattern (base pattern) was formed, and simulated "noise" was added to the pattern. Figures B.5a and B.5b show the real space and Fourier components of the diffraction patterns, respectively. The base pattern was formed by placing Gaussian peaks (FWHM = 0.67^0) at the positions of the Fe_3Al diffraction peaks for 14.41 keV photons. The area of each peak is equal to the standard deviation of the noise (1σ). The (base + noise) pattern was treated by both a Fast Fourier Transform (FFT) filter and the Igor smoothing (§ 4.2.3). The FFT filtering was performed by Fourier transforming the (base + noise) pattern, multiplying the resulting Fourier components by the filter, then back transforming to obtain the FFT filtered pattern shown in Fig. B.5a. The diffraction peaks can be seen in the resulting filtered data, but they are too small to be reliable. For example, possible peaks can be seen at 40.2^0 and 47.1^0, but these are clearly results of the noise. Also, the FFT filtering is more harsh than the smoothing, since a larger amount of the high frequency components have been removed. As a result, the background diffraction patterns used to treat the experimental data are treated with the FFT filtering, while the experimental data is smoothed (to facility easier peak identification).

Since the 1σ diffraction peaks (1σ, FWHM = 0.67^0) were difficult to identify, Figs. B.6ab show simulated diffraction peaks for various widths and areas. As expected, peaks are easier to identify for narrower peaks and larger areas. The widths of the diffraction peaks in our experimental data are approximately 2/3 of a degree, so the simulated peaks with FWHMs of 0.67^0 are particularly relevant. The 3σ area peaks in Fig. B.6a are easily distinguishable; thus, we can be confident in the superlattice diffraction peaks of chapter 4.

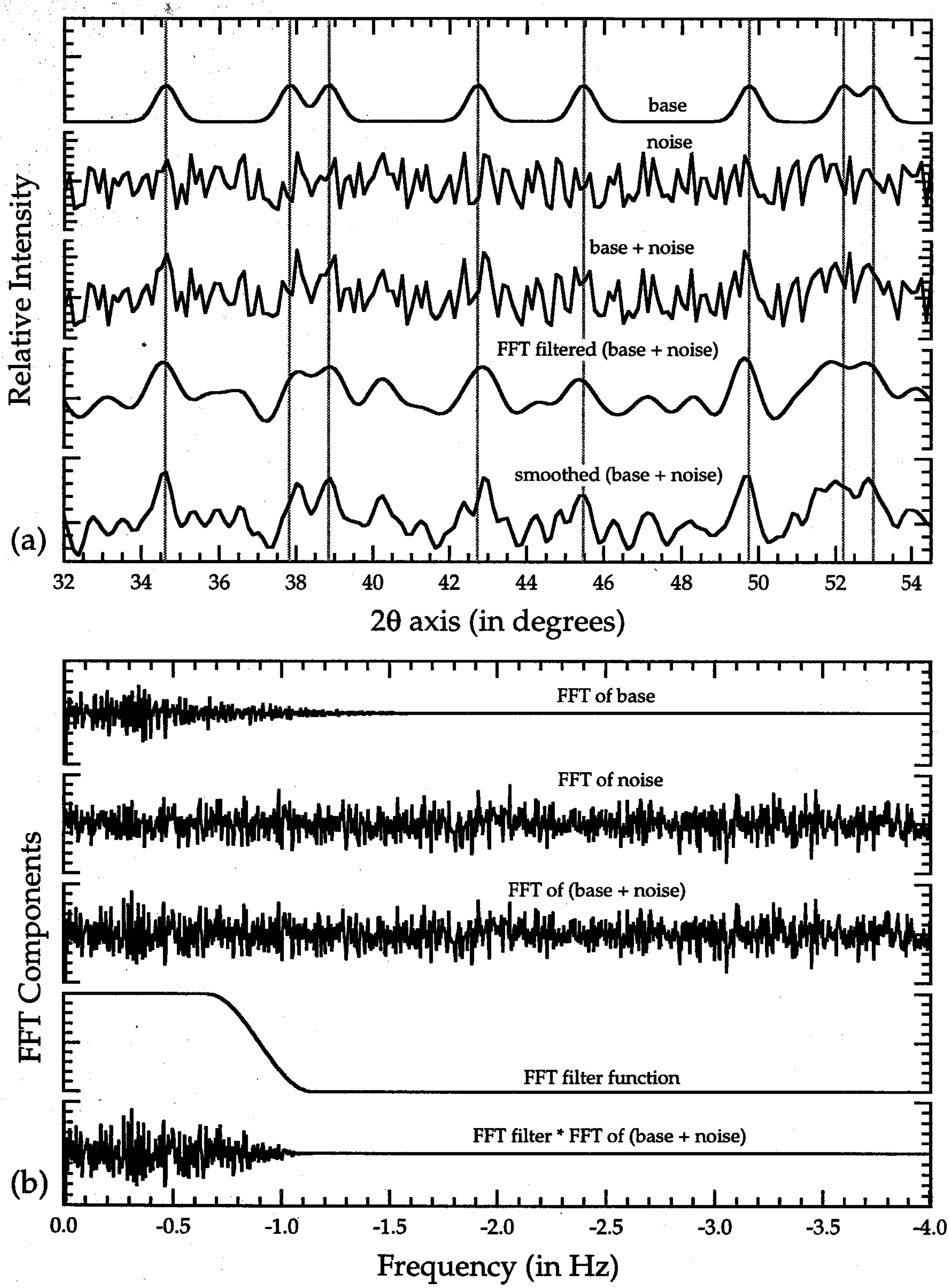

Figure B.5 FFT filtering of simulated diffraction peaks. Diffraction patterns are shown in (a), while the Fourier components are shown in (b). Each peak is Gaussian with a FWHM of 0.67^0 and an area of 1σ (where σ is the standard deviation of the noise).

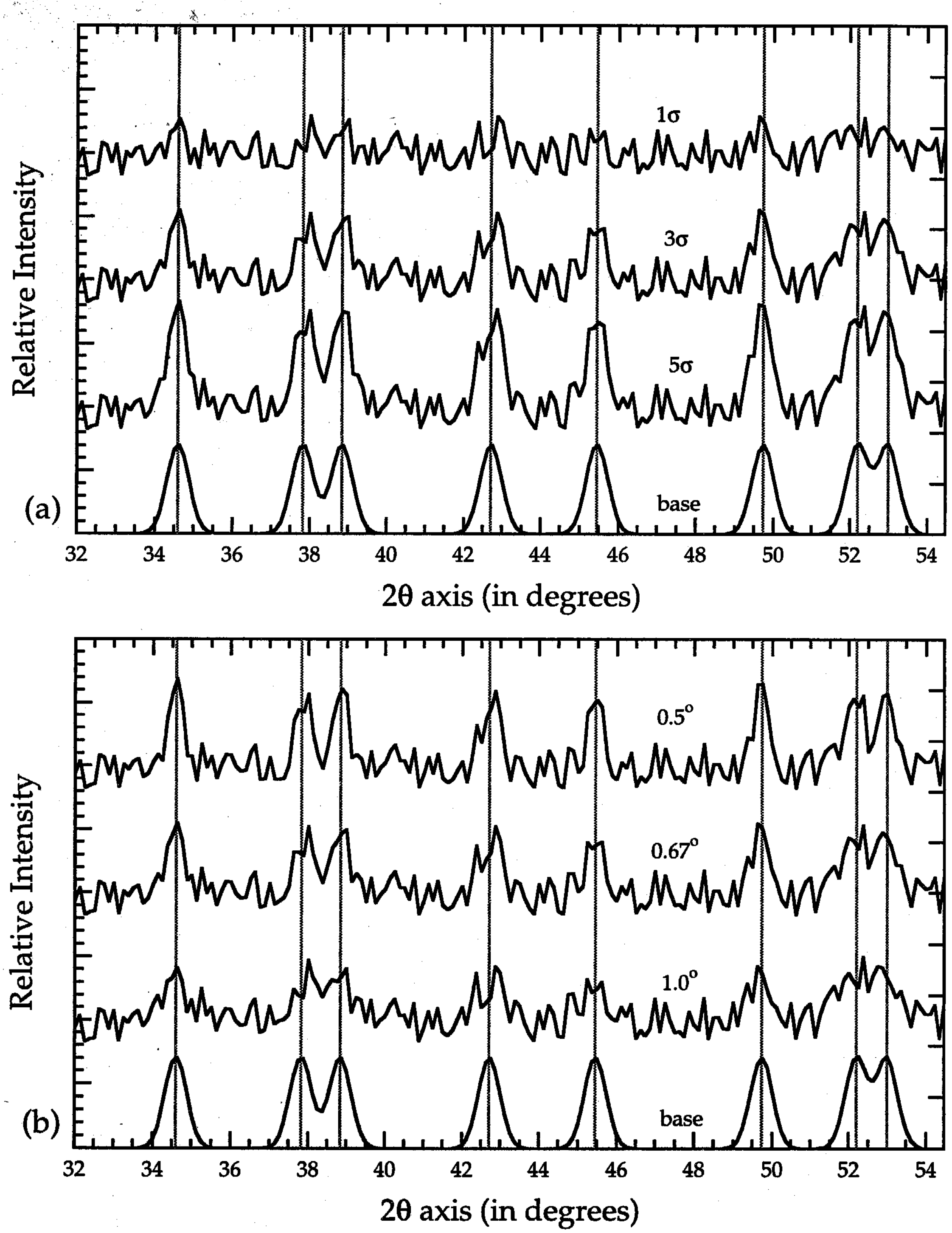

Figure B.6 Simulated diffraction patterns as a function of peak width and area. (a) The peak areas are changed, while the width is fixed (FWHM is 0.67°). (b) The peak widths are changed, while the area is fixed (3σ). In both cases, the base pattern has a FWHM of 0.67° and an area of 3σ.

B.4 Coincidence experiment with the INEL detector

We performed a simple coincidence experiment to test the timing capabilities of the INEL CPS-120 detector. The experiment was used to measure the decay of the Mössbauer excited state of a ^{57}Co radioisotope by the photon-photon coincidence method [1]. The 122 keV γ-ray photon indicates the creation of the Mössbauer excited state in ^{57}Fe, with approximately 10% of the decays producing a 14.41 keV γ-ray photon. Because of the large difference in the number of photons, we triggered the start signal of the time to amplitude converter (TAC) with the detection of the 14.41 keV photons. Detection of the 122 keV photons was time-delayed and used as the stop signal for the TAC.

The INEL detector was used to detect the 14.41 keV photons. Unfortunately, we could not limit photon detection to a single INEL channel as the photon flux was too low. Thus, the start signals for the TAC were acquired over a small range of INEL channels. Because of the delay line of the INEL, the signals varied in time over a 30 nsec range (the effective instrument function of the INEL detector). The 122 keV γ-ray photons were detected with a LSO (cerium-doped lutetium oxyorthosilicate) single crystal scintillator [2] coupled to a Hamamatsu R329-01 photomultiplier and its associated electronics. The lifetime of the LSO excited state is 12 nanoseconds [3].

Figure B.7 shows the result of the coincidence experiment. The rising edge of the observed peak (left side) indicates the timing resolution of the INEL detector, while the right side of the peak shows the decay of the Mössbauer excited state ($\tau_{1/2} = 100$ nsec). The slope of the rising edge should be close to vertical for nanosecond timing resolution, but it is clearly not (the rising edge is approximately 44 nsec wide). The culprits are the instrument function of the INEL detector and the LSO excited state lifetime mentioned above. The solid trace displayed against the data is the convolution of an exponentially decaying function for the Mössbauer excited state, the LSO excited state decay function,

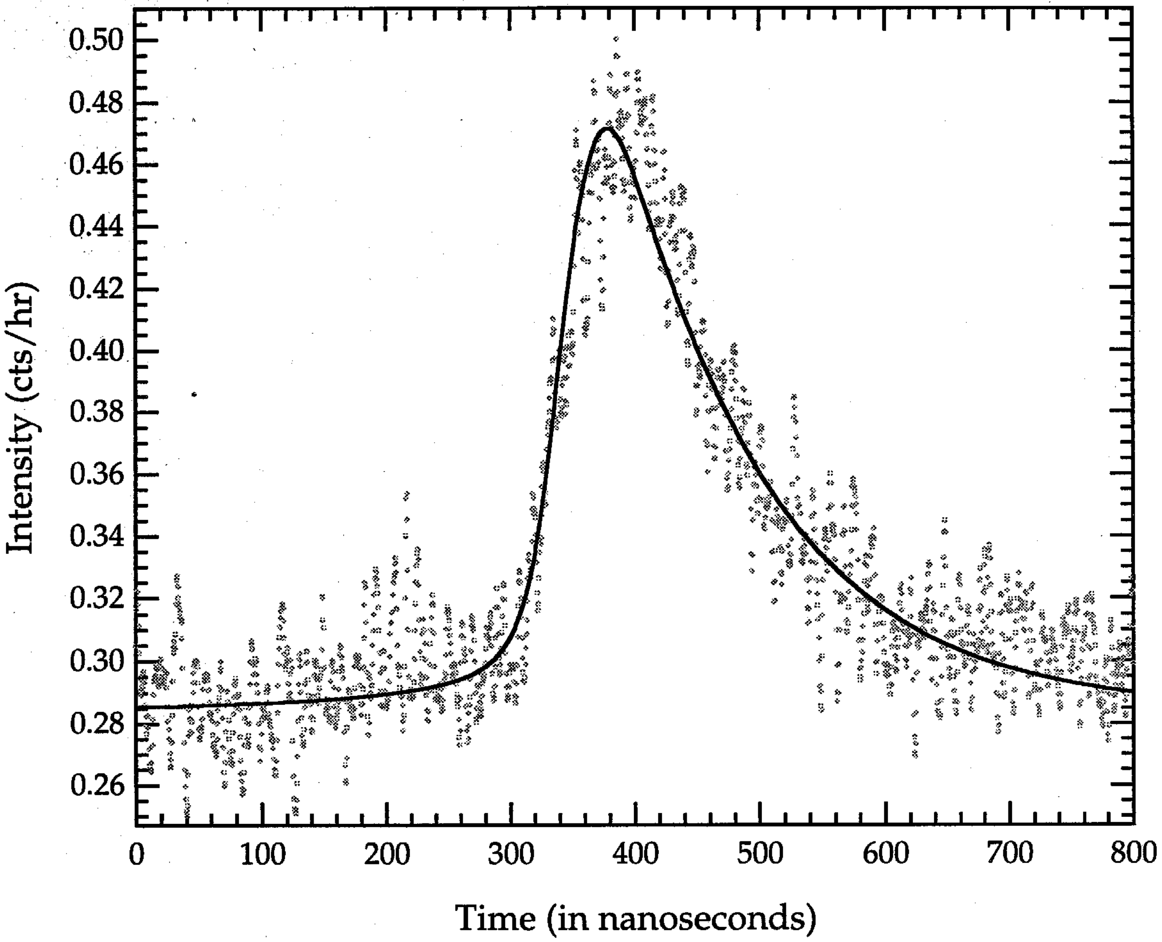

Figure B.7 Results of the INEL coincidence experiment. The right side of the peak shows the decay of the Mössbauer excited state.

and the INEL instrument function. The convolution fits the data well, indicating that we have correctly diagnosed the problem.

While our coincidence experiment was crude, it indicates that the INEL detector should have sufficient timing resolution for synchrotron work. The problem of the instrument function caused by the delay line will not occur, since the synchrotron-based photons will be detected by single channels in the INEL detector. Furthermore, the 4096 channels of the INEL detector are spread over the 1.2 μs delay line, resulting in sub-nanosecond timing resolution.

[1] R.E. Imhof and F. H. Read, Rep. Prog. Phys. **40**, 1 (1977).

[2] C.L. Melcher and J.S. Schweitzer, Nucl. Instrum. Methods Phys. Res. **A314**, 212 (1992).

[3] H. Suzuki, *Ph.D. Thesis* (California Institute of Technology, Pasadena, 1994).

Appendix C

This appendix contains information on the older data sets collected for the $^{57}Fe_3Al$ and ^{57}Fe samples. Chapter 4 contains the newer, more important data sets. The naming scheme used to differentiate the data sets and explained in § 4.1 is repeated here for clarity. The $^{57}Fe_3Al$ sets use the letters Fe_3Al as a prefix; the ^{57}Fe sets, Fe. The numbers in the names indicate the year when collection started for the data set. The data sets described in chapter 4 are;

(1) Fe_3Al95	$^{57}Fe_3Al$ data set collected using the 145 mCi source; fully described in § 4.3,
(2) $Fe_3Al95v2$	a repeat of Fe_3Al95 with the INEL detector moved closer to the sample, fully described in § 4.4, and
(3) Fe95	the best ^{57}Fe data set to date; fully described in § 4.5.

The data sets described in this appendix are:

(4) Fe91	the first good ^{57}Fe data set; acquired with a simple electronic gate,
(5) Fe_3Al93	the first $^{57}Fe_3Al$ data set; the milled collimator was introduced, and
(6) Fe_3Al94	the second $^{57}Fe_3Al$ data set; the improved gating system was implemented.

C.1 The Fe91 ^{57}Fe data

The Fe91 [1] was the first data set which proved that Mössbauer powder diffraction could be seen. This data set preceded the synchronous router, the machined Pb collimator, the 145 mCi source, and a number of other improvements. The average source strength was 38 mCi.

Figure C.1 shows the on-resonance, off-resonance, and difference diffraction patterns for the Fe91 data. The left-hand side of the figure displays the data collected with the sample incident angle at 17^0 to maximize the (200) peaks. The right-hand side was set to maximize the (400) peak with a 37^0 incident angle. The form factor rolloff can very clearly be seen, as the x-ray diffraction peaks fade to insignificance as the order of the peaks increases. The (400) and (332) peaks are of sufficiently high order to be completely from Mössbauer scattering, at least within the limits of the noise. Table C.1 lists the areas of the diffraction peaks found in Fig. C.1. A comparison of this data to the Fe95 data can be found in § 4.5.

Table C.1 Peak areas for the Fe91 data in Fig. C.1. The question marks indicate the peak was too small to fit.

resonance condition	(200)	(222)	(400)	(332)
on	4.0 σ	3.5 σ	2.8 σ	5.6 σ
off	3.2 σ	1.1 σ	? σ	? σ

C.2 The earlier $^{57}Fe_3Al$ data sets: Fe_3Al94 and Fe_3Al93

This section describes the two earlier $^{57}Fe_3Al$ data sets: Fe_3Al94 and Fe_3Al93. Fe_3Al94 was collected prior to receiving the 145 mCi source, but includes most of Fe_3Al95 data set's advantages, including the synchronous router. Fe_3Al93 preceded Fe_3Al94: it lacks the synchronous router, but it does include improved shielding and the machined Pb collimator. It was also our first attempt at Mössbauer diffraction on an $^{57}Fe_3Al$ sample.

Figures C.2 through C.5 show the Fe_3Al94 and Fe_3Al93 data set diffraction patterns and differences. These data sets are clearly not as good as the Fe_3Al95 ($^{57}Fe_3Al$) data, but the improvements made between the data sets are reflected in diffraction patterns.

Figures C.2 and C.3 show the Fe_3Al94 diffraction patterns for the three resonance conditions and their differences, respectively. Only the $^{57}Fe_3Al$ #2(A) sample (rolled from ingot) was used to acquire the Fe_3Al94 data set, so the crystallographic texture favors the (200) bcc fundamental peak. The other fundamental peaks of the Fe_3Al95 set, the (211) and (222), can be seen in the off-resonance data but are very small. The average diffraction pattern intensity is 13,000 mCi·hr. Table C.2 lists the peak areas for the Fe_3Al94 data.

Table C.2 Peak areas for the Fe_3Al94 data in Fig. C.2. The question mark indicates the peak was too small to fit.

resonance condition	(200)	(222)
OAl	4.5 σ	1.5 σ
4Al	4.4 σ	? σ
off	7.6 σ	3.0 σ

While both of the superlattice peaks described in § 4.3, $\left(\frac{3}{2}\frac{3}{2}\frac{3}{2}\right)\left(\frac{5}{2}\frac{1}{2}\frac{1}{2}\right)$ at 45.5 degrees and (300)(221) at 53 degrees, can be seen in Fig. C.3, they are small. The peaks have areas of ~1.2 σ.

Figures C.4 and C.5 display the Fe_3Al93 diffraction patterns for the three resonance conditions and their differences, respectively. The Fe_3Al93 data set was acquired using both types of samples (rolled from ingot and rolled from splat). The (200) and (211) fundamental peaks can be seen, but the peaks are very wide and small. Clearly, all of the peaks have fairly low confidence levels (for fundamental peaks). This set was collected before the improved background and data handling procedures were implemented, and the data set suffers from their absence. The average intensity of the patterns is 13,000 mCi·hr. Table C.3 lists the peak areas for the Fe_3Al93 data.

Table C.3 Peak areas for the Fe_3Al93 data in Fig. C.4.

resonance condition	(200)	(211)
OAl	1.3 σ	1.9 σ
4Al	2.0 σ	2.3 σ
off	2.1 σ	2.8 σ

It is possible that the $\left(\frac{3}{2}\frac{3}{2}\frac{3}{2}\right)\left(\frac{5}{2}\frac{1}{2}\frac{1}{2}\right)$ superlattice peak can be seen in Fig. C.5, but it is very small (peak area is ~0.5 σ). Thus, the confidence in this peak is very low.

In summary, the $^{57}Fe_3Al$ data sets have continually improved. The total area of the fundamental peaks for the Fe_3Al95 data is a factor of 3 better than the Fe_3Al94 data and a factor of 4.7 better than the Fe_3Al93. The superlattice peaks have also shown great improvements: peaks are barely seen in the Fe_3Al93, and the Fe_3Al94 data shows only small ones. The Fe_3Al95 and $Fe_3Al95v2$ data sets clearly demonstrate chemical environment selectivity.

References

[1] T.A. Stephens, W. Keune, and B. Fultz, Hyperfine Interact. **92**, 1095 (1994).

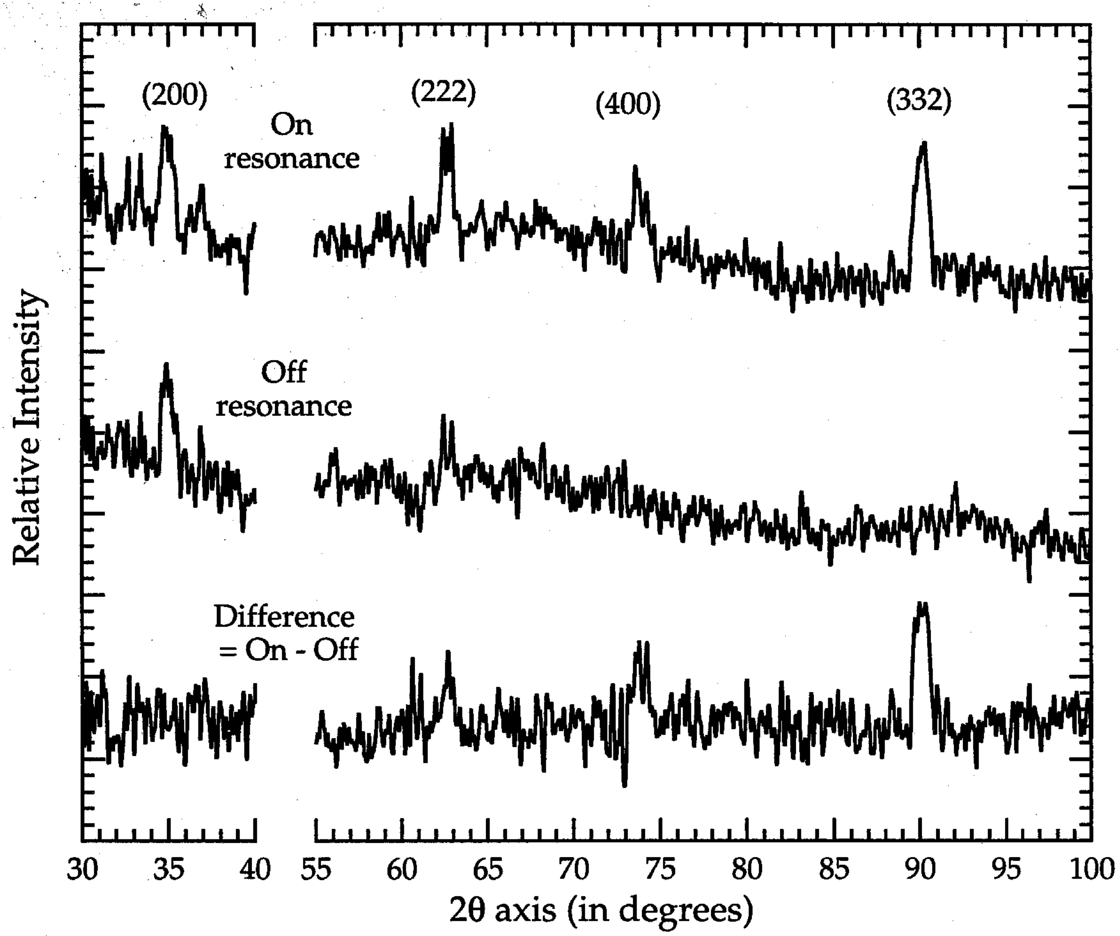

Figure C.1 The Fe91 ^{57}Fe data. Left side data used a sample incident angle of 17°. The right side data used an incident angle of 37°.

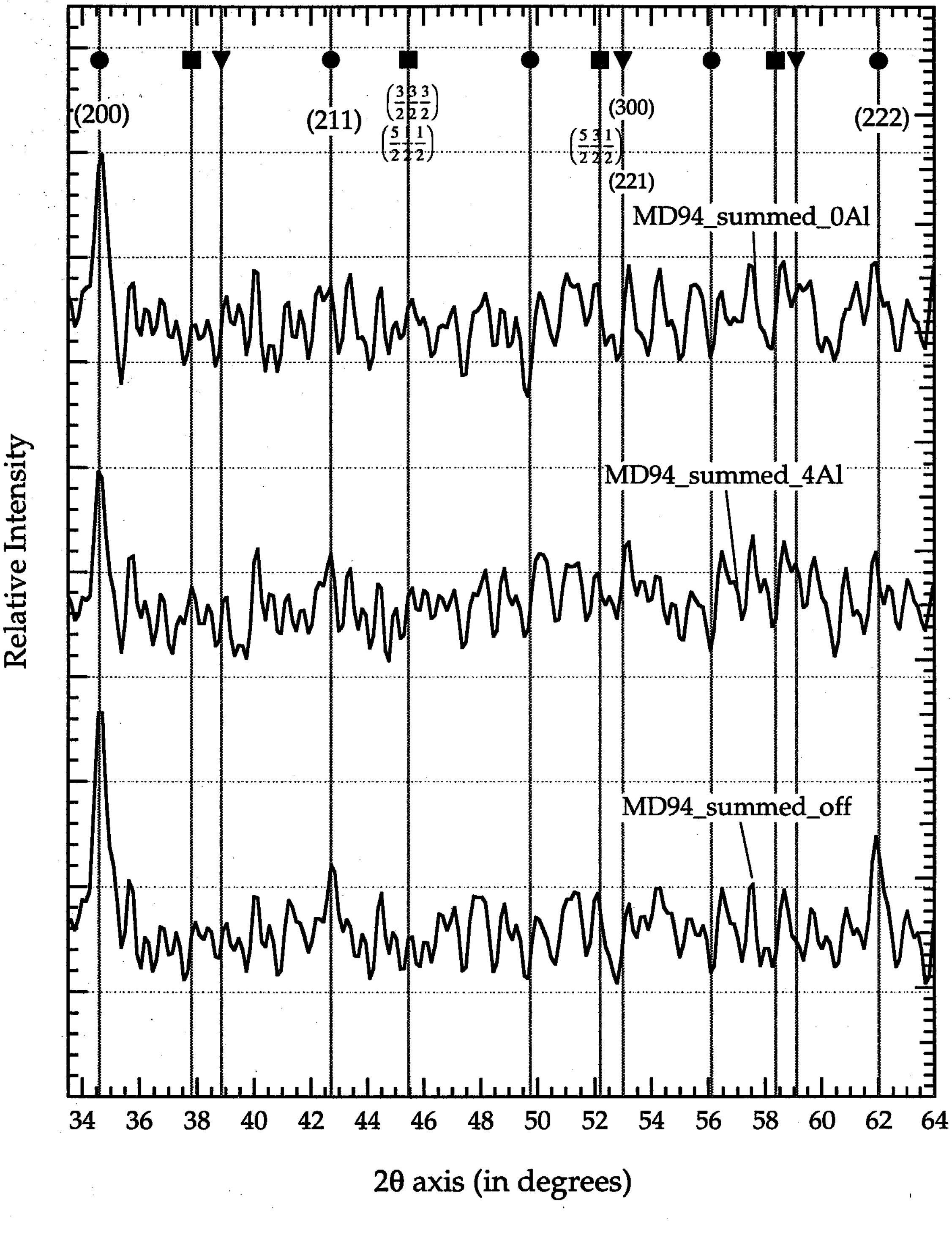

Figure C.2 Diffraction patterns for the summed Fe_3Al94 data sets.

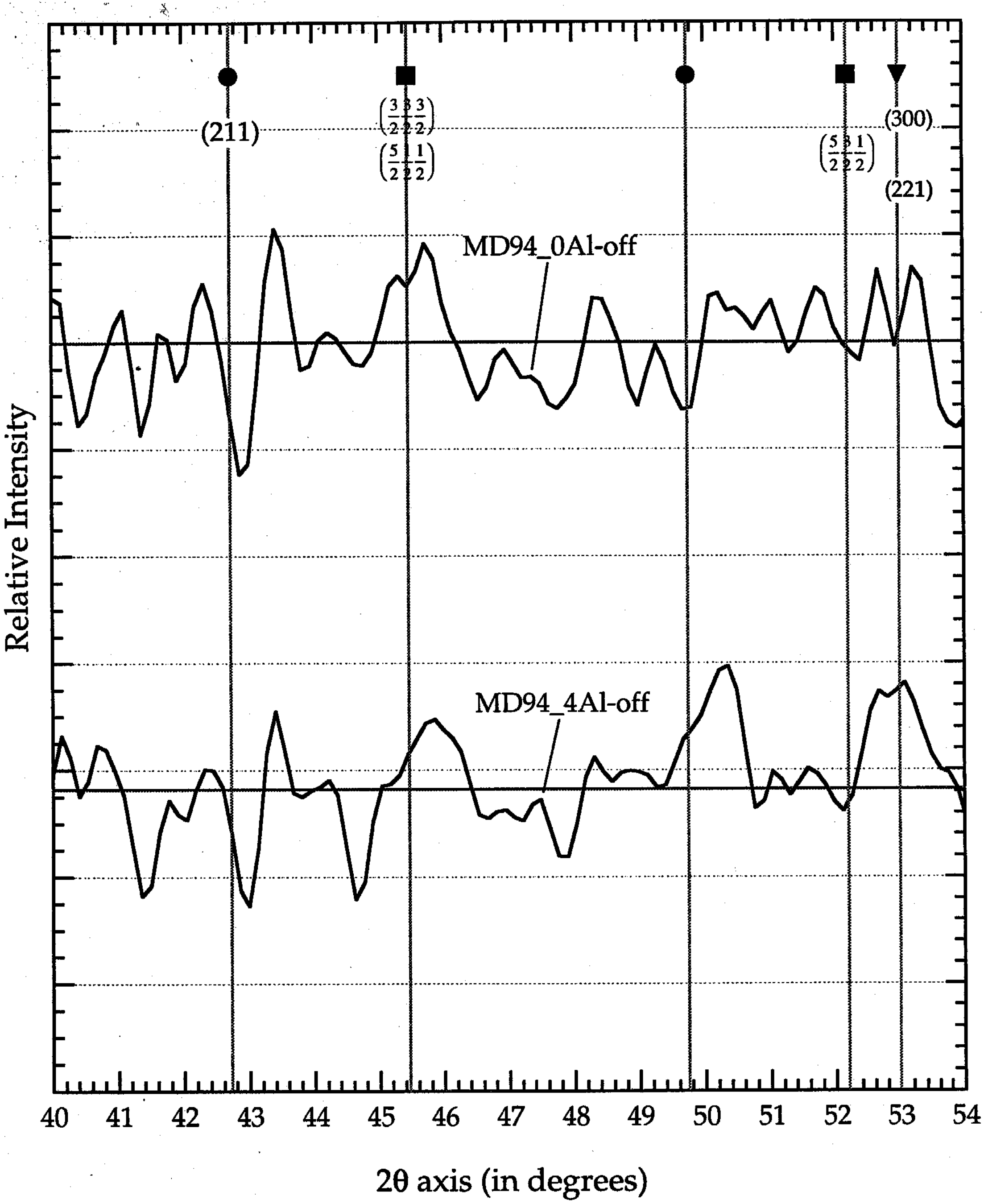

Figure C.3 Diffraction pattern differences for the summed Fe_3Al94 data sets.

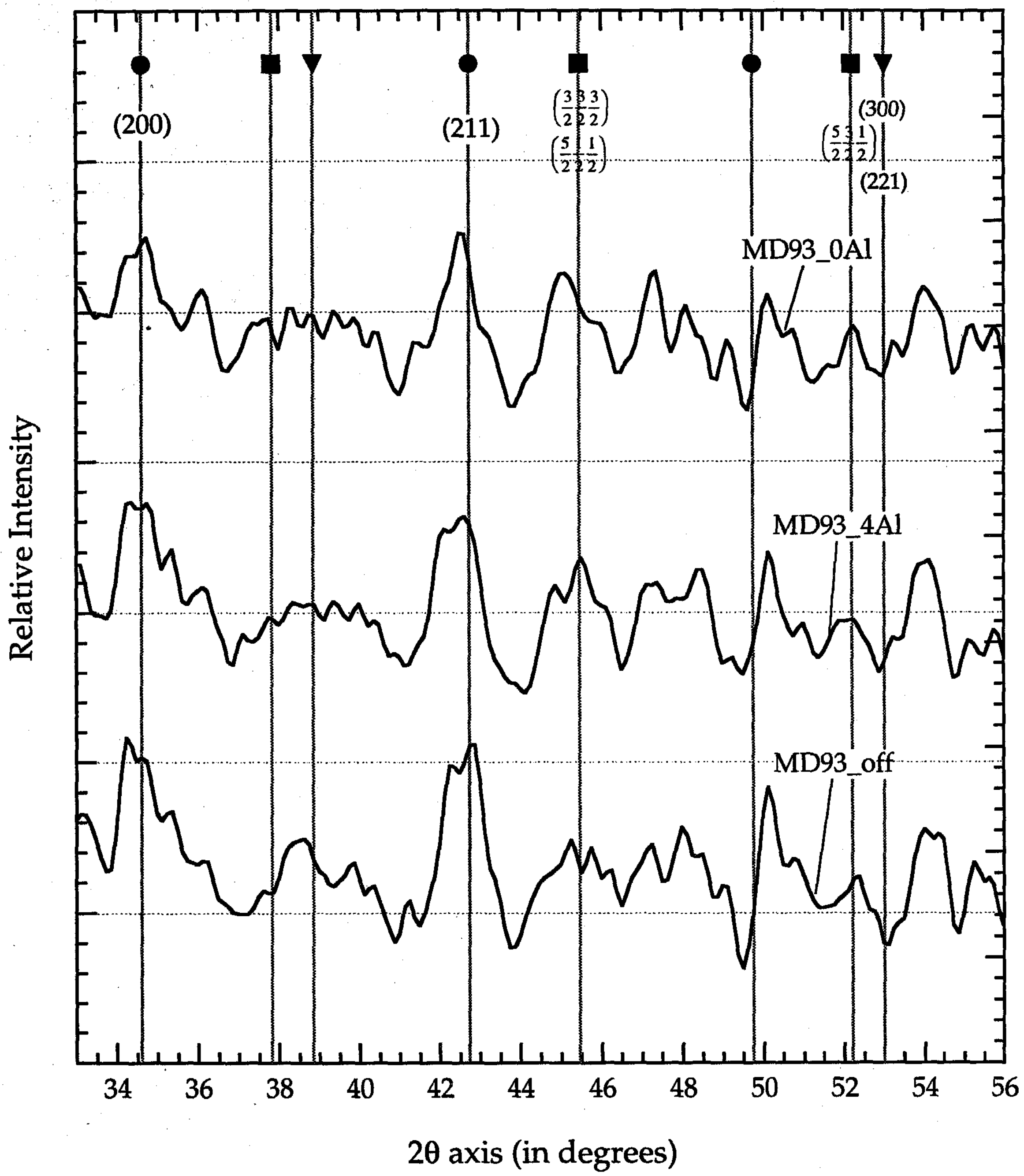

Figure C.4 Diffraction patterns for the summed Fe_3Al93 data sets.

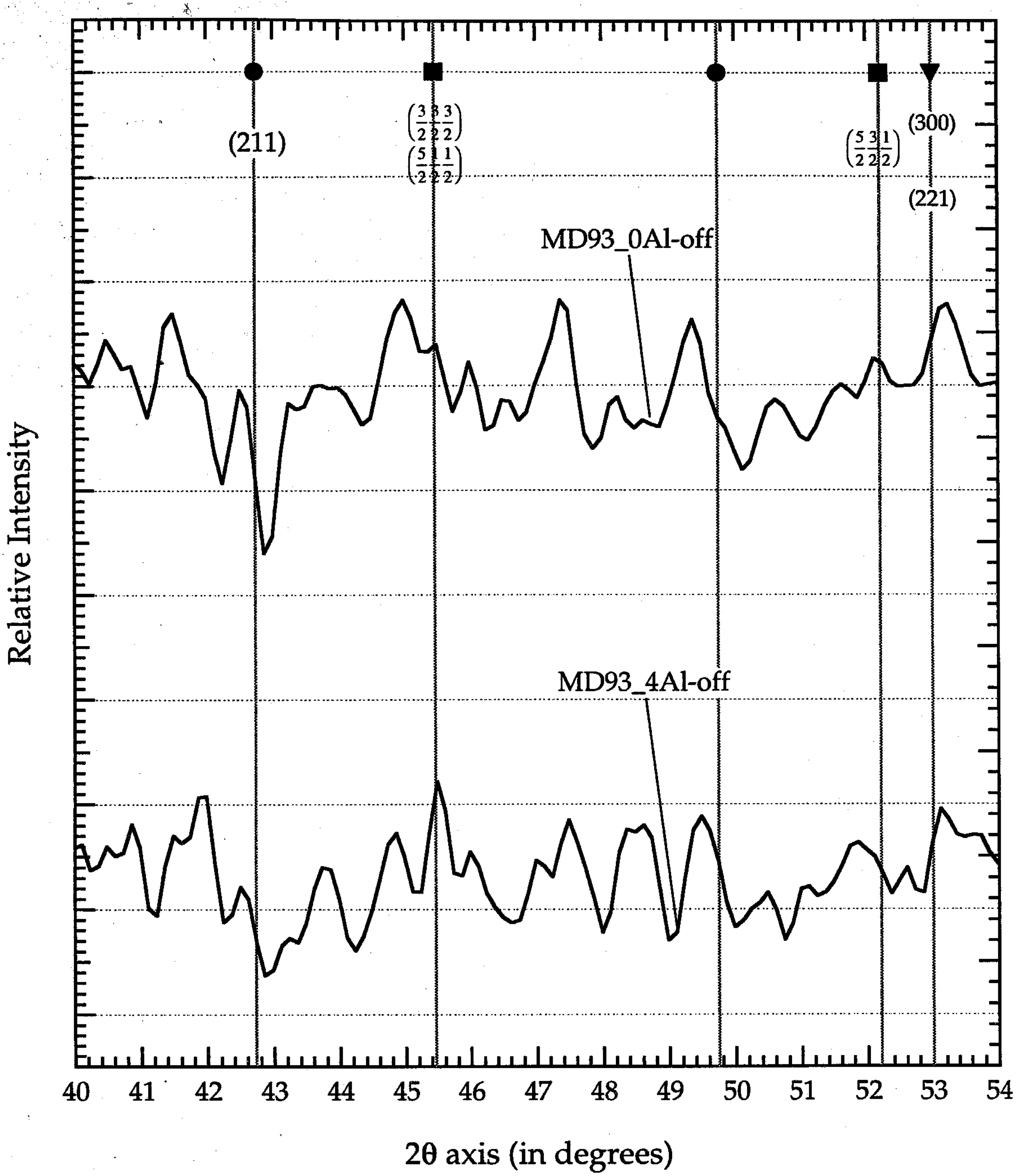

Figure C.5 Diffraction pattern differences for the summed Fe_3Al93 data sets.